VCU

Virginia Commonwealth University

VCU Scholars Compass

2016

Beyond conventional c-plane GaN-based light emitting diodes: A systematic exploration of LEDs on semi-polar orientations

Morteza Monavarian
Virginia Commonwealth University

Ph.D. Dissertation

Beyond conventional *c*-plane *GaN*-based light emitting diodes: A systematic exploration of LEDs on semi-polar orientations

A Ph.D. dissertation submitted in partial fulfillment of the requirements for the degree of Doctor of Philosophy at

Virginia Commonwealth University

by

Morteza Monavarian

Director: Prof. Vitaliy Avrutin[1]

Committee Members:

Prof. Hadis Morkoç[1]
Prof. Ümit Özgür[1]
Prof. Shiv Khanna[2]
Prof. Michael Reshchikov[2]
Prof. Denis Demchenko[2]

[1]*Department of Electrical and Computer Engineering, Virginia Commonwealth University*
[2]*Department of Physics, Virginia Commonwealth University*

Abstract

Despite enormous efforts and investments, the efficiency of InGaN-based green and yellow-green light emitters remains relatively low, and that limits progress in developing full color display, laser diodes, and bright light sources for general lighting. The low efficiency of light emitting devices in the green-to-yellow spectral range, also known as the "Green Gap", is considered a global concern in the LED industry. The polar c-plane orientation of GaN, which is the mainstay in the LED industry, suffers from polarization-induced separation of electrons and hole wavefunctions (also known as the "quantum confined Stark effect") and low indium incorporation efficiency that are the two main factors that contribute to the Green Gap phenomenon. One possible approach that holds promise for a new generation of green and yellow light emitting devices with higher efficiency is the deployment of nonpolar and semi-polar crystallographic orientations of GaN to eliminate or mitigate polarization fields. In theory, the use of other GaN planes for light emitters could also enhance the efficiency of indium incorporation compared to c-plane.

In this thesis, I present a systematic exploration of the suitable GaN orientation for future lighting technologies. First, in order to lay the groundwork for further studies, it is important to discuss the analysis of processes limiting LED efficiency and some novel designs of active regions to overcome these limitations. Afterwards, the choice of nonpolar orientations as an alternative is discussed. For nonpolar orientation, the $\left(1\bar{1}00\right)$-oriented (m-plane) structures on patterned Si (112) and freestanding m-GaN are studied. The semi-polar orientations having substantially reduced polarization field are found to be more promising for light-emitting diodes

(LEDs) owing to high indium incorporation efficiency predicted by theoretical studies. Thus, the semi-polar orientations are given close attention as alternatives for future LED technology.

One of the obstacles impeding the development of this technology is the lack of suitable substrates for high quality materials having semi-polar and nonpolar orientations. Even though the growth of free-standing GaN substrates (homoepitaxy) could produce material of reasonable quality, the native nonpolar and semi-polar substrates are very expensive and small in size. On the other hand, GaN growth of semi-polar and nonpolar orientations on inexpensive, large-size foreign substrates (heteroepitaxy), including silicon (Si) and sapphire (Al_2O_3), usually leads to high density of extended defects (dislocations and stacking faults). Therefore, it is imperative to explore approaches that allow the reduction of defect density in the semi-polar GaN layers grown on foreign substrates.

In the presented work, I develop a cost-effective preparation technique of high performance light emitting structures (GaN-on-Si, and GaN-on-Sapphire technologies). Based on theoretical calculations predicting the maximum indium incorporation efficiency at $\theta \sim 60°$ (θ being the tilt angle of the orientation with respect to *c*-plane), I investigate $(11\overline{2}2)$ and $(1\overline{1}01)$ semi-polar orientations featured by $\theta = 58°$ and $\theta = 62°$, respectively, as promising candidates for green emitters. The $(11\overline{2}2)$-oriented GaN layers are grown on planar *m*-plane sapphire, while the semi-polar $(1\overline{1}01)$ GaN are grown on patterned Si (001).

The *in-situ* epitaxial lateral overgrowth techniques using SiN_x nanoporous interlayers are utilized to improve the crystal quality of the layers. The data indicates the improvement of photoluminescence intensity by a factor of 5, as well as the improvement carrier lifetime by up to

3

85% by employing the *in-situ* ELO technique. The electronic and optoelectronic properties of these nonpolar and semi-polar planes include excitonic recombination dynamics, optical anisotropy, exciton localization, indium incorporation efficiency, defect-related optical activities, and some challenges associated with these new technologies are discussed. A polarized emission from GaN quantum wells (with a degree of polarization close to 58%) with low non-radiative components is demonstrated for semi-polar $(1\bar{1}01)$ structure grown on patterned Si (001). We also demonstrated that indium incorporation efficiency is around 20% higher for the semi-polar $(11\bar{2}2)$ InGaN quantum wells compared to its *c*-plane counterpart. The spatially resolved cathodoluminescence spectroscopy demonstrates the uniform distribution of indium in the growth plane. The uniformity of indium is also supported by the relatively low exciton localization energy of $E_{loc} = 7 meV$ at 15 K for these semi-polar $(11\bar{2}2)$ InGaN quantum wells compared to several other literature reports on *c*-plane. The excitons are observed to undergo radiative recombination in the quantum wells in basal-plane stacking faults at room temperature. The wurtzite/zincblende electronic band-alignment of BSFs is proven to be of type II using the time-resolved differential transmission (TRDT) method. The knowledge of band alignment and degree of carrier localization in BSFs are extremely important for evaluating their effects on device properties. Future research for better understanding and potential developments of the semi-polar LEDs is pointed out at the end.

Acknowledgements

In the name of God, the most Compassionate, the most Merciful. My first and deepest appreciation must go to my adviser Professor Vitaliy Avrutin. It has been a privilege to have been educated by him. I would like to extend my appreciation to him for his invaluable help, guidance and encouragement. I appreciate the efforts that he has made in my personal development as a researcher and numerous discussions required by this study. I am also very grateful to Professor Hadis Morkoç for his consistent and valuable effort to encourage me during my research, and also his valuable suggestions and constant support. I would also like to acknowledge Professor Ümit Özgür for his helps and guidance in class as well as during my research. In addition, I would like to thank Dr. Natalia Izyumskaya for her supports and helps as well as sharing her opinions for developing ideas along the projects. I also acknowledge financial support from National Science Foundation (NSF). Moreover, I would like to thank VCU School of Engineering for providing me with this opportunity.

Special thanks go to my colleagues, Dr. Daniel Rosales and Professor Bernard Gil from University of Montpellier in addition to Dr. Sebastian Metzner, Dr. Macus Müller, Professor Frank Bertram and Professor Jürgen Christen from University of Magdeburg. Our monthly videoconferences helped me to increase my understanding on different aspects of the projects. I also want to thank Professors Shiv Khanna, Denis Demchenko, and Michael Reshchikov from VCU department of physics for their valuable comments and guidance.

I am also grateful to my friends at microelectronic materials and devices laboratory (MMDL) at VCU, Dr. Fan Zhang, Dr. Serdal Okur, Dr. Romualdo Ferreyra, Dr. Nuri Can, Dr. Shopan Hafiz, Dr. Mykyta Toporkov, Dr. Ismail Altuntas, Mr. Barkat Ullah, Mr. Saikat Das, and

Mr. Tanner Nakagawara for all their helps and supports. I am also indebted to Dr. Behnam Moradi for his suggestions, guidance, and constant supports during my PhD. I would also like to thank my aunt (Tahereh Balani) and my uncle (Saeed Fallah) and their families for their supports during my PhD.

I am very grateful to my parents (Hossein Monavarian and Marzieh Fallah Balani), and my family for their invaluable encouragement and support during my whole educational life. I would not be able to reach my goals without them. Finally, and most importantly, I would like to thank my wife, Elnaz Sadeghi for her constant understanding, love, and self-sacrifice without which this thesis would not have been possible.

Table of Contents

List of Figures

13

14

15

16

17

18

19

21

25

28

30

31

Figure 9.7.   *(a) Low-temperature and (b) room-temperature PL spectra for in situ double nano-ELO GaN samples with SiNx interlayers deposited for 1 min (blue) and 2 min (green) in comparison with spectra for $\left(11\overline{2}2\right)$ GaN/m-sapphire template without SiNx interlayer (red) and state-of-the-art c-plane nano-ELO GaN film (black).*   *282*

List of Tables

Chapter 1

1. Introduction

Development of blue light emitting diodes (blue LEDs) in early 1990s was made possible by utilizing InGaN/GaN and InGaN/AlGaN double heterostructures (DH). Efficient blue LEDs together with green and red colored ones established earlier by means of InGaAsP material systems could potentially make a complete set of colors.[1] This breakthrough leading to substantial progress in full color display technology as well as cost effective white light generation, brought three Japanese fellows -Shuji Nakamura, Hiroshi Amano, and Isamu Akasaki the 2014 Noble Prize in physics.[2]–[5] Nowadays, InGaN based LEDs have surrounded us in almost every instrument as well as traffic lights, cell phone displays and energy efficient TV/monitors, white lamps, car lighting applications and so on which after all makes us feel like life can't be imagined without them. LEDs are more useful than other sources of lighting in terms of energy efficiency, device lifetime, and probably most importantly, environmental friendliness.[6]

Due to the above-mentioned numerous applications of GaN based light-emitters, there is a growing market, demand, and production on them.[7] It has been recently predicted that the global LED lighting market is expected to reach $25.7 Billion dollars in 2015.[8] Considering the overall lighting market will grow to almost $82.1 Billion dollars in 2015, as reported by LED Inside,[8] the penetration of LED technology will increase to about 31%. These figures are

34

predicted to increase further in next few years, first of all, due to rapid population growth, large number of private-sector LED projects, and governmental supports.[8] LED Inside has predicted the global market to become as large as $36 Billion dollars in 2018.[9] Shares of LED demand for various applications for the years 2013, 2014, and 2015 are shown in Figure 1.1.[9] The tangible increase in general lighting application of high brightness LEDs which can be clearly seen from the diagram for this three year period illustrates the enormous role of this technology in future of our planet, Earth, reducing the demand for destructive, less efficient sources of energy. To summarize, LEDs play a very important role in almost everybody's daily life and most of this development is performed after inventionof InGaN based emitters in less than 20 years.
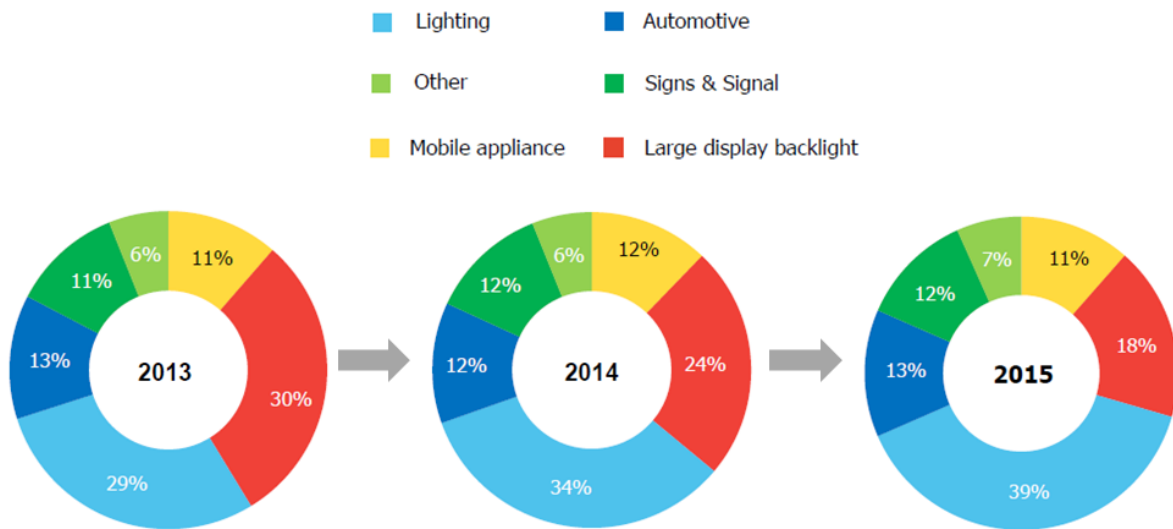
Figure 1.1. Lighting Market demands specified for different applications for 2013, 2014, and predicted for 2015. The clear increase in general lighting and reduction in display backlight can be seen from 2013 to 2015 from the diagram. [Data from Ref. [9]]

Despite of numerous applications of GaN-based LEDs and enourmous investigations which provided such a wide global market in various applications, the LEDs still have limited

efficiency especially at high injected current densities. External quantum efficiency (EQE) of LEDs typically reaches the maximum at moderate current densities (5 to 100 A/cm^2, depending on the device design and emission wavelength) and then degrades with further inleasing injection. The real mechanism behind this efficiency degradation at high injection levels also known as "efficiency droop", *i.e.* referred to as the gradual reduction in efficiency as a function of injection current level, has not been clearly understood yet.[10] Asymmetry in carrier distribution due to large effective mass of holes in multiple-quantum wells (MQWs) structure is another problem limitting efficiency at different injection levels. In adition to the above-mentioned mechanisms, presence of defects acting as non-radiative recombination centers and effect of polarization field known for polar structures are also responsible for efficiency limitations that requires to be addressed.[10] Moreover, the efficiency of LEDs reduce dramatically with increasing operation wavelength to the extent that there is a gap in efficiency for green LEDs operating at about 560nm (see Figure 1.2) - a problem known as "green gap" phenomenon.

36
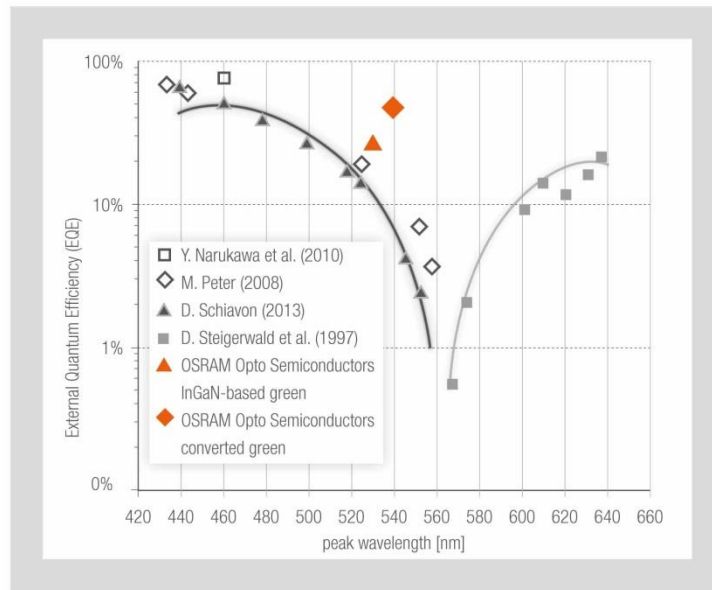
Figure 1.2. Luminous efficacy as a function of peak operational wavelength demonstrating a gap in luminous efficacy in about 560nm range (Image source: OSRAM). [11]

Let us discuss first the mechanism behind efficiency limitation mechanisms in conventional LEDs. One of the main factors which limit performance of LEDs is the separation of electron and hole wave-functions in active region due to the polarization field acting as perturbation to the initial rectangular well system.[12] This effect is more pronounced for long wavelength emitters in which lattice mismatch and, therefore, piezoelectric field is higher thus contributing to the green gap issue.[12] Also, the polarization at the hetero-interfaces can enhance the barriers for electrons and holes and aggravate asymmetry in distributions of the carriers across the active regions for multi quantum well (MQW) systems with resultant reduction in efficiency.[13] Degradation of structural quality for high indium content heterostructures is another factor which can have a dramatic effect on the LED efficiency especially for green-light sources.[14] These altogether have encouraged researchers to search for alternative solution to overcome the obstacles for furher improvement of the LED

37

performance: low recombination efficiency at moderate current level, efficiency retention at high injection, and poor efficiency of green LEDs.

Theoretically, in polar crystals such as GaN, the spontaneous polarization is the maximum along the (0001) (or c-) direction. It decreases for the planes which make angles $0^o < \theta < 90^o$ with this plane (referred as "semi-polar planes") and drops to zero for planes perpendicular to the polar plane (nonpolar planes). Piezoelectric polarization in the InGaN/GaN structures behaves in the similar manner because of polarization discontinuity and this makes the piezoelectric polarization to differ from that in the polar c-plane variety. Figure 1.3 shows the theoretical curves representing this phenomenon $i.e.$ changes in piezoelectric polarization and total polarization charge as well as wave function overlap (based on quantum confined Stark effect) versus inclination angle to the c-direction.[15] Obviously, in semi-polar and nonpolar planes the absolute values of polarization charge and electron-hole wavefunction overlap is diminished compared to conventional c-plane demonstrating the potential benefits of choosing them as substrates for light emitting applications.
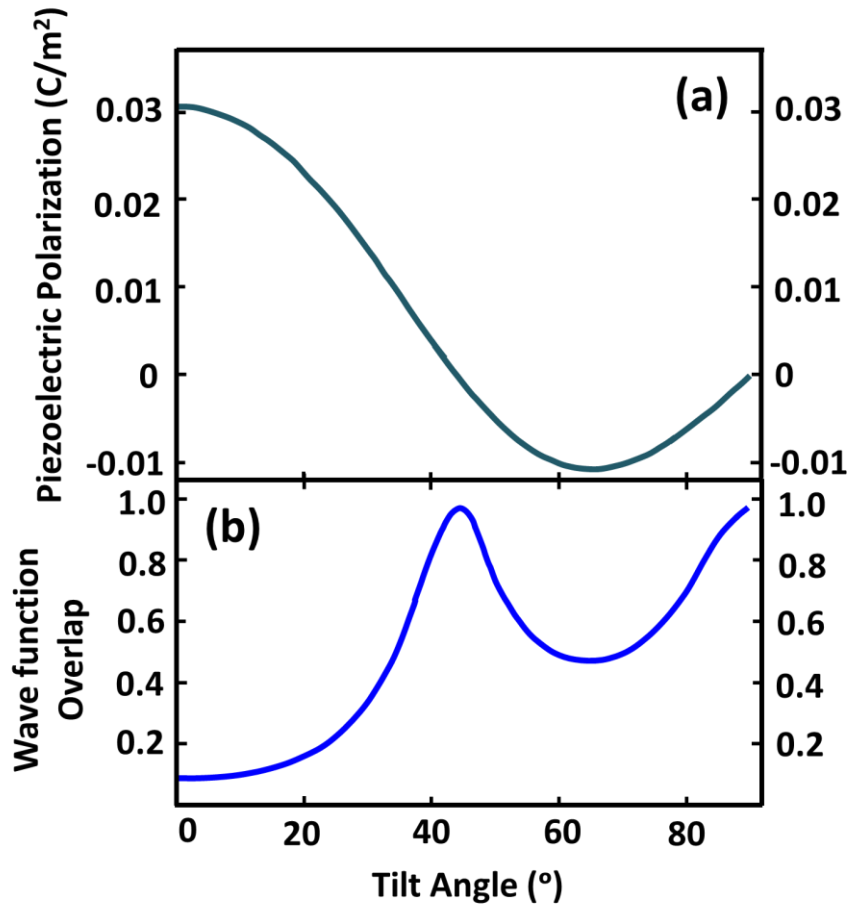
Figure 1.3. (a) Piezoelectric polarization and (b) wave function overlap of electrons in conduction and holes in valence bands as a function of tilt angle with respect to the *c*-direction for a 3nm $In_{0.25}Ga_{0.75}N$/GaN quantum well system. [Data from Ref. [15]]

Therefore, as an alternative to c-plane conventional LEDs, nonpolar structures with no polarization fields were proposed in early 2000.[16], [17] Later report by Yamada *et al.*[18] on reduced indium incorporation efficiency by a factor of about three compared to c-plane and consequently reduction in LED output power for devices emitting above 400nm[19] As will be discussed in more detailes in next chapter, supported theoretically[20], [21] and experimentally[22] in some other groups, the observation of low incorporation efficiency into

nonpolar planes turned attention more to semi-polar planes as potential alternatives for green emitters. Reduction/elimination in polarization field for semi-polar and nonpolar structures was interesting as could pave the way for further improvement of LED efficiencies. Moreover, such suppression in polarization field could result in some degrees of freedom in design of LEDs which could result in better performance in terms of lower efficiency droop. From crystallographic point of view, the idea of studying and looking for planes with potentially higher indium incorporation efficiency was giving additional motivation for researchers to address the green gap problem as well. The latter was motivated by theoretical predictions on improved indium incorporation efficiency for some semi-polar planes based on the effect of strain[20] and surface atomic configurations[21] with some experimental verifications[22] (more detailed discussions will be brought in Chapters 2 and 4).

After all, it seems that use of nonpolar (mainly for higher energy emitters) and semi-polar planes of GaN heterostructures could potentially result in improvement in next generation of light emitters. However, the major problems are related to the technological limitations on growing high quality nonpolar and/or semi-polar GaN structures by means of either homo- or heteroepitaxially. Consequently, the low optical and structural quality negates the improvement due to reduction in QCSE and potential reduction in efficiency droop, *etc.* and thus makes the *c*-orientation yet the winner. It is noteworth to mention that utilizing nonpolar/semipolar substrates due to eliminated/suppressed QCSE could pave the way for new designs of single well active regions with thicker widths that negates the carrier spillover at high current densities as main cause of efficiency droop.

However, the recent advances in growth of nonpolar and semi-polar GaN are giving promises for future of this technology. This can be inferred from recently reported external

quantum efficiency (EQE) values for semi-polar and nonpolar LEDs on native and non-native substrates as brought together in Figure 1.4. This figure illustrates the reported values for external quantum efficiency of InGaN LEDs with three emission colors (blue, green and yellow-green) as a function of crystal inclination angle with respect to c-axis. Since the reported data in Figure 1.4 are mainly based on bulk substrates prepared by cutting the HVPE grown c-plane layers at different angles (what is frequentky referred in literature as "second generation" LEDs[19]), the improved efficiencies of semi-polar LEDs that approach those of the conventional c-plane devices can be attributed to the ability to prepare high quality layers. Although this approach for preparation of non-basal-plane GaN substrates seems to be promising, it is a costly method and dictates the final product to become expensive. Heteroepitaxy of semi-polar and nonpolar films, on the other hand, could be of more interests due to relatively low costs of preparation.

41
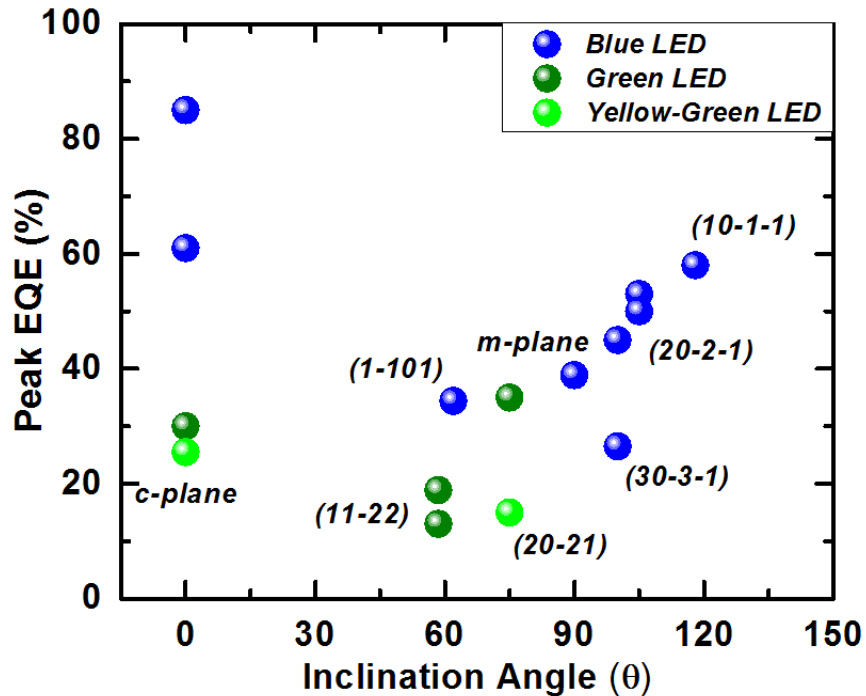
Figure 1.4. Reported peak EQE values for various substrate orientations (inclination angle with respect to *C*-axis).[23]–[35] The blue, green and yellow-green spheres indicate blue, green and yellow-green LEDs, respectively.

As mentioned, growth of semi-polar and nonpolar GaN layers on non-native and relatively inexpensive foreign substrates such as sapphire and Si using relatively inexpensive techniques is of great interest. However, these layers often suffer from high density of extended defects due to relatively high mismatch with the substrate. The further development of these LEDs require further investigations in order to find suitable growth conditions as well as develop defect reduction techniques which could enable high efficiency semi-polar and nonpolar LEDs at low cost. In addition to that, better understanding of properties of GaN light emitters which are orientation-dependent could be possible when growth of high quality semi-polar and nonpolar layers will be developed, similar to the evolution of conventional *c*-plane light emitters.

In this thesis we intend to go over these nonpolar and semi-polar orientations in details systematically. The discussion will contain comparison of nonpolar/semipolar with c-orientation in terms of structural and optical properties, their promises based on theoretical predictions, growth limitations, and potential techniques for improving quality of the heteroepitaxial layers grown on some of these orientations. Finally, considering the promises and limitations of the heteroepitaxial technologies ("GaN on Sapphire", "GaN on Si") together with "GaN on GaN", the potential technologies for future lighting applications will be discussed briefly.

The work is organized as follows. In Chapter 2, we investigate a bit on physical background behind orientation-dependence of optical and structural properties of LEDs, theoretical predictions, and future promises given by the semipolar generation of GaN LEDs. I briefly discuss my methodology in systematic investigations of this wide area of light emitting diodes in Chapter 3. In Chapter 4, conventional c-plane LEDs, the efficiency improvements, potential methods for enhancement of indium incorporation efficiency, and the challenges will be discussed. The nonpolar LEDs as alternatives for c-plane-based light emitting structures and the limitations will be addressed in Chapter 5. Later on, heteroepitaxial semipolar LEDs with planes having particular tilt angles with respect to basal plane will be investigated both on patterned (Chapter 6) and planar substrates (Chapter 7). At the end, the work will be summarized (Chapter 8) and some future research for semipolar GaN on Sapphire and Si technologies will be proposed (Chapter 9).

Chapter 2

2. Orientation dependent properties of GaN based light emitting structures

In this chapter, physical and optical properties of selected semi-polar and nonpolar crystallographic planes of GaN-based heterostructures will be discussed. In the view of orientation dependent properties of GaN, some of the main differences which could be most effective in determining the LED performances will be considered. The content of this chapter is organized as follows. First a general overview of the crystallographic planes of GaN and their identifications will be provided. The discussion will be followed by brief description of the most influential characteristics of various planes of GaN including strain and polarization fileds and their effects on related quantum confined Stark effect (QCSE), carrier transport properties, light emission characteristics, and indium incorporation. The discussion will mainly contain theoretical predictions and will be followed by experimental verifications if available in literature.

2.1. Selected crystallographic planes of GaN: A General Overview

Owing to its wurtzite hexagonal crystal structure featured by 6 fold rotation and 2 mirror planes, a primitive Bravais lattice containing only one lattice point in the unit cell, and screw 6_2 axis (two step, 60 degrees each), GaN belongs to the point group of 6mm and space group of C^4_{6v} in Hermann-Mauguin and $P6_3mc$ in Schoenflies notation.[36] Within GaN structure, each atom of Ga is surrounded by four N and each N atom surrounded by four Gallium atoms in tetrahedral coordination. As a result, along polar axis, *i.e. c*-direction, the relative numbers of Ga and N atoms change going from one parallel plane to the other which gives rise to a net polarization known as spontaneous polarization. The situation can be different at other planes that do not contain polar axis of symmetry which can be obtained by changing the angle with respect to *c*-direction providing other sets of parallel planes with different characteristics. Later on, we will discuss the differences in characteristics for the non-*c*-oriented planes of GaN.

As known, the planes of a hexagonal lattice can be represented by four indices h, k, i, l as in (h, k, i, l). Having a constraint between indices *i.e.* $h + k + i = 0$, one can write each plane of (h, k, i, l) in hexagonal system as a unique (h, k, i) in a cubic system. There are certain relations governing these indices that define general properties of the corresponding planes. For instance, $h = k = i = 0$, $l \neq 0$ defines *c*-plane giving rise to sets of parallel planes with interplanar distance that is determined by index l only. As will be demonstrated later in this subsection, these planes are polar planes as a result of unequal numbers of N atoms and Ga atoms in the double-monolayer plane. In case in addition to nonzero l index any of the h or k indices being nonzero, the plane is featured by reduced spontaneous and dubbed by convention as "semipolar". If $l = 0$, the plane is featured by zero polarization field and teramed as a "nonpolar" plane. As examples

for this general rule, planes (0001), $(10\bar{1}0)$, and $(10\bar{1}1)$ represent polar *c*-plane, nonpolar *m*-plane, and semipolar *s*-plane crystallographic planes, respectively.

It turns out that the characteristics are dependent on tilt angle of a plane with respect to polar axis. This inclination angle (θ) *i.e.* the angle between a plane of interest (h,k,i,l) and the *c*-plane can be determined from the four indices and lattice constants with the following relationship

$$\theta = \cos^{-1}\left(\frac{\sqrt{3}al}{\sqrt{4c^2\left(h^2+k^2+hk\right)+3a^2l^2}} \right)$$

(2.1)

Where a and c are in-plane and out of plane lattice parameters of the hexagonal structure, respectively. Some of the semipolar and nonpolar planes and the calculated value for the inclination angles are shown in Figure 2.1.[36], [37] The distance between the parallel planes (d) of a given orientation which can be calculated having h, k, and l indices using a 3-dimensional geometrical method is unique for a certain orientation and so is the Bragg angle. Thus, XRD analysis using the following relation can be used to identify the orientations

$$\frac{Sin(\Theta)}{\lambda} = \frac{n}{2d}$$

(2.2)

Where Θ is the Bragg angle, λ is the incident x-ray wavelength (for $\kappa\alpha_1$ and $\kappa\alpha_2$), n is an integer and d is the inter-planar distance in the orientation.[7] Therefore, one to one correspondence of each set of plane with a certain inclination angle (θ) and corresponding Bragg angle (Θ) resolved by XRD could act as a fingerprint identifying the orientations of a film for a single or multiple phase layers.

46
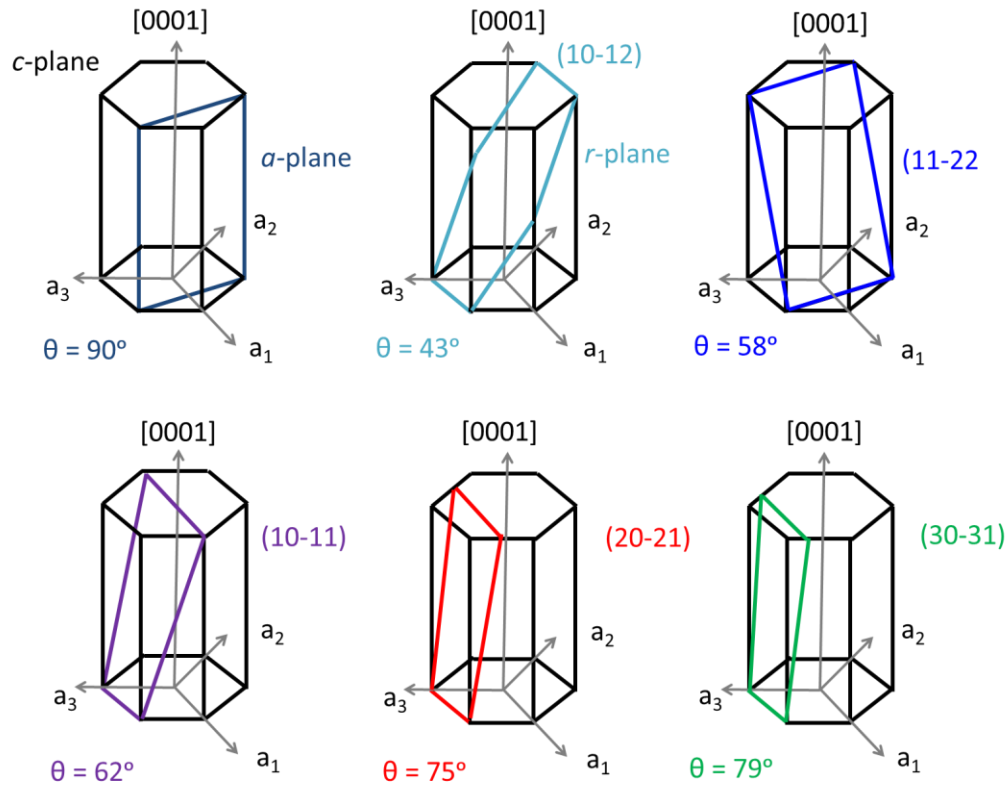
Figure 2.1. Schematic Representation of some of the nonpolar, semipolar and polar planes for Wurtzite GaN. The θ angles for each plane is calculated assuming $a = 318.6\,pm$ and $c = 518.6\,pm$ for GaN.

As seen above, for a crystallographic orientation of interest, the inclination angle is important in identifying characteristics and the corresponding properties of the particular plane. Some of these characteristic properties such as polarization and strain in multilayer structures identified by the substrate inclination angle with respect to *C*-axis will be discussed in details in next section.

47

2.2. Characteristics of various orientations of GaN heterostructures

The properties of heterostructures such as strain, polarization charge, carrier dynamics and transports, optical activities, impurity and alloy incorporations, *etc.* depend on their orientation. This means that the corresponding parameters for the properties are variable under rotation of substrate orientation with respect to *c*-axis. The dependence of some of the properties in GaN heterostructures will be treated theoretically and/or experimentally in this section.

2.2.1. Stress and polarization

Presence of tensile or compressive strain induced in layers thinner than the critical thickness grown on a substrate with larger or smaller in-plane lattice constant, respectively, is known to affect the band-structure and thus emission properties and efficiencies.[7] The strain for various orientations of substrate can be taken into consideration. In polar coordinate system in which ϑ and φ are rotational angle with respect to *c*-axis (polar axis) and azimuthal angle, respectively, the derivation of different strain components can be carried out utilizing the rotation transformation matrix as follows

$$U = \begin{pmatrix} \cos\vartheta\cos\varphi & \cos\vartheta\sin\varphi & -\sin\vartheta \\ -\sin\varphi & \cos\varphi & 0 \\ \sin\vartheta\cos\varphi & \sin\vartheta\sin\varphi & \cos\vartheta \end{pmatrix}. \qquad (2.3)$$

Assuming strained InGaN layer on a GaN substrate as in blue and green light emitting diodes, the in-plane strain (for two orthogonal in-plane directions) for a semipolar plane would be [38]

$$\varepsilon_{m1} = \varepsilon_{y'y'} = \frac{a_S - a_L}{a_L} \qquad (2.4)$$

48

$$\varepsilon_{m2} = \varepsilon_{x'x'} = \frac{a_S c_S - \sqrt{\left((a_L c_S)^2 \cos^2 \vartheta + (a_S c_L)^2 \sin^2 \vartheta\right)}}{\sqrt{\left((a_L c_S)^2 \cos^2 \vartheta + (a_T c_L)^2 \sin^2 \vartheta\right)}} \qquad (2.5)$$

Where a_S and c_S are substrate in-plane and out of plane lattice constants while c_L and a_L are in-plane and out of plane lattice constants for InGaN layer. The calculation is performed for InGaN and AlGaN systems by Romanov *et al.*[38] the results of which is brought in Figure 2.2. At polar orientation ($\vartheta = 0$) the in-plane strain anisotropy will be zero (for both AlGaN and InGaN epilayer systems) that means unlike semipolar and nonpolar heterostructures, for *c*-plane the in-plane strain will be isotropic. As we will demosntrate in subsection 2.2.3, this leads to a different optical polarization behavior for semipolar, nonpolar and polar structures.
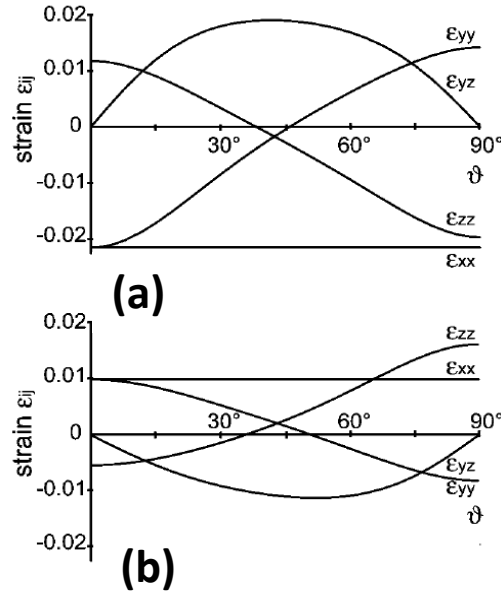
49

Being strong piezoelectric, III-nitride semiconductor heterostructures saffer from both in piezoelectric and spontaneous polarization,[37] whereas the former exists for strained layers while the latter is present even for fully relaxed structures as a result of anisotropy in electronegativity of atoms in multi atomic crystals along a specific direction. The polarization induced charges can be used to induce two-dimentional electron gas (2-DEG) required in heterostructure field effect transistors (HFETs),[39] but they can also decrease electron and hole wavefunctions overlap and thus reduce recombination efficiency which is crucial in light emitters.[12] Therefore, in the ternary AlN-GaN or InN-GaN systems which are mainly used for UV and visible light emitters, these polarization needs to be understood.

Following the strain calculation, the piezoelectric polarization can be calculated as[38]

50

$$P^{pz} = \begin{pmatrix} 0 & 0 & 0 & 0 & e_{15} & 0 \\ 0 & 0 & 0 & e_{15} & 0 & 0 \\ e_{31} & e_{31} & e_{33} & 0 & 0 & 0 \end{pmatrix} \begin{pmatrix} \varepsilon_{xx} \\ \varepsilon_{yy} \\ \varepsilon_{zz} \\ \varepsilon_{yz} \\ \varepsilon_{zx} \\ \varepsilon_{xy} \end{pmatrix} = \begin{pmatrix} e_{15}\varepsilon_{zx} \\ e_{15}\varepsilon_{yz} \\ e_{31}\left(\varepsilon_{xx} + \varepsilon_{yy}\right) + e_{33}\varepsilon_{zz} \end{pmatrix} \tag{2.6}$$

Where e_{ij} is the piezoelectric, and ε_{ij} is the strain tensor elements.[38] For different orientations

of InGaN/GaN structure the total polarization Charge at the interface would be

$$\Delta P_{z'} = P_{Lz'}^{pz} + (P_L^{sp} - P_S^{sp})\cos\vartheta \tag{2.7}$$

Where P_L^{sp} and P_S^{sp} are spontaneous polarization for the layer and substrate, respectively.[36] As it

was demonstrated elsewhere,[38] the piezoelectric polarization for different inclination angle can

be expressed as:

$$\begin{aligned} P_{Lz'}^{pz} &= e_{31}\cos\vartheta\,\varepsilon_{x'x'} + \left(e_{31}\cos^3\vartheta + \frac{e_{33} - e_{15}}{2}\sin\vartheta\sin 2\vartheta\right)\varepsilon_{y'y'} \\ &+ \left(\frac{e_{33} + e_{15}}{2}\sin\vartheta\sin 2\vartheta + e_{33}\cos^3\vartheta\right)\varepsilon_{z'z'} \\ &+ \left[(e_{31} - e_{33})\cos\vartheta\sin 2\vartheta + e_{15}\sin\vartheta\cos 2\vartheta\right]\varepsilon_{y'z'} \end{aligned} \tag{2.8}$$

The piezoelectric and change in total polarization for both $In_xGa_{1-x}N$/GaN QW and $Al_yGa_{1-y}N$/GaN QW structures strain is plotted as a function of inclination angle (ϑ) for various molar

fractions of InN and AlN in Figure 2.3.[38] Comparison of the piezoelectric component and total

polarization for InGaN and AlGaN QW systems reveal the significant role of spontaneous

polarization in case of AlGaN system (compare plots Figure 2.3 (c) and (d)). In contrast, it

appears that piezoelectric polarization is dominant in case of InGaN QW (compare plots Figure

2.3(a) and (b)). Another interesting observation is the cross-over of the total polarization plots at

$\vartheta = 45°$ and $\vartheta \sim 70°$ for InGaN and AlGaN systems, respectively regardless of indium or Al

51

contents. Vanishing of the total polarization is favorable due to the elimination of quantum confined stark effect (QCSE).[12]
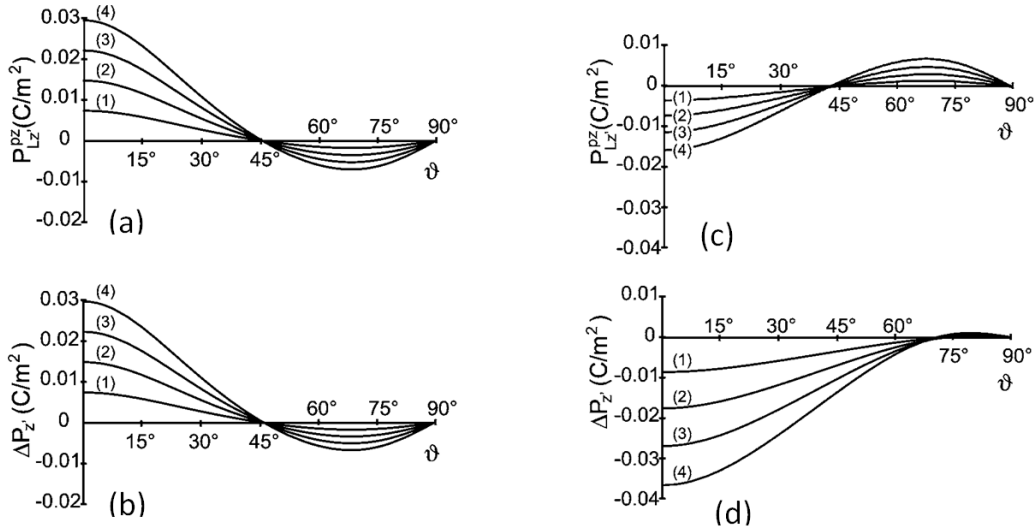
Figure 2.3. Piezoelectric polarization (a,c) and change in total polarization (b,d) as a function of inclination angle (ϑ) with respect to *c*-axis of $In_xGa_{1-x}N/GaN$ (a,b) and $Al_yGa_{1-y}N/GaN$ (c,d) quantum well structures with different compositions. Compositions x=0.05 (1), 0.1 (2), 0.15 (3), 0.2 (4) and y = 0.1 (1), 0.2 (2), 0.3 (3), and 0.4 (4).[Reprinted with Permission from Ref.[38]]

The polarization induced internal electric field associated with spontaneous and piezoelectric components can be determined from the calculated polarization charges using

$$E_{z'} = -\frac{P_{z'}}{\varepsilon_r . \varepsilon_0} , \qquad (2.9)$$

where ε_r and ε_0 are relative dielectric constants of the material and vacuum permittivity, respectively. The calculations can be performed more accurately considering two-way (coupled) piezoelectric interaction between electric field and strain with incorporation of spontaneous polarization[40] *i.e.* utilizing the models described in Refs.[41], [42] by adding SP polarization.[40] For wurtzite GaN structure, elastic stiffness and piezoelectric constant matrices appear as follows

52

$$C_{ij} = \begin{pmatrix} C_{11} & C_{12} & C_{13} & 0 & 0 & 0 \\ C_{12} & C_{11} & C_{13} & 0 & 0 & 0 \\ C_{13} & C_{13} & C_{33} & 0 & 0 & 0 \\ 0 & 0 & 0 & C_{44} & 0 & 0 \\ 0 & 0 & 0 & 0 & C_{44} & 0 \\ 0 & 0 & 0 & 0 & 0 & \dfrac{C_{11}-C_{12}}{2} \end{pmatrix}, \tag{2.10}$$

$$e_{ki} = \begin{pmatrix} 0 & 0 & 0 & 0 & e_{15} & 0 \\ 0 & 0 & 0 & e_{15} & 0 & 0 \\ e_{31} & e_{31} & e_{33} & 0 & 0 & 0 \end{pmatrix} \tag{2.11}$$

and using stress equation

$$\sigma_i = C_{ij}\epsilon_j - E_k e_{ki}, \tag{2.12}$$

where σ , ϵ , and E_k are stress, strain and the kth component of the electric field, and using the known electrostatic equation

$$D_m = \varepsilon_{mk}E_k + P_m, \tag{2.13}$$

where D_m and P_m , being the mth component of the electric displacement field and polarization charge, respectively. Knowing that $\nabla.D = 0$ in direction perpendicular to plane of the QW (z-direction assuming the coordinate frame similar to what is shown in Figure 2.3(c)) in the absence of free charges, the strain and electric field (ϵ , and E_k) can be found in a coupled form as

$$E_{coup} = \frac{2\varepsilon_0(C_{13}e_{33} - C_{33}e_{31}) + C_{33}(D - P^{SP})}{C_{33}\varepsilon_{33} + e_{33}^2} \tag{2.14}$$

$$\epsilon_{3,coup} = \frac{-2\varepsilon_0(C_{13}\varepsilon_{33} + e_{31}e_{33}) + e_{33}(D - P^{SP})}{C_{33}\varepsilon_{33} + e_{33}^2} \tag{2.15}$$

53

This is known as coupled equation for internal field.[42] Ignoring the converse piezoelectric effect the equations will become uncoupled as

$$E_{uncoup} = \frac{2\varepsilon_0(C_{13}e_{33} - C_{33}e_{31}) + C_{33}(D - P^{SP})}{C_{33}\varepsilon_{33}} \tag{2.16}$$

$$\epsilon_{3,uncoup} = \frac{-2\varepsilon_0 C_{13}}{C_{33}} \tag{2.17}$$

In case of a single QW system, the displacement field would be spontaneous polarization in the barrier[43] except for the surface. In case of multi-quantum wells, on the other hand, the following periodic boundary condition demonstrated by Bernardini et al. [43] needs to be applied

$$\sum_q l^{(q)} E^{(q)} = 0 \tag{2.18}$$

where l being the thickness of a layer noting that the summation is operating over all layers including the barriers. Following calculations in Ref.[40], the strain and electric field in growth direction for n^{th} layer in MQW structure can then be derived as a solution of the coupled equations[40]

$$E_{coup}^{(n)} = \frac{A^{(n)}\sum_q \dfrac{l^{(q)}C^{(q)}}{B^{(q)}} - C^{(n)}\sum_q \dfrac{l^{(q)}A^{(q)}}{B^{(q)}}}{B^{(n)}\sum_q \dfrac{l^{(q)}C^{(q)}}{B^{(q)}}} \tag{2.19}$$

$$\epsilon_{3,coup}^{(n)} = \frac{G^{(n)}\sum_q \dfrac{l^{(q)}C^{(q)}}{B^{(q)}} - e^{(n)}\sum_q \dfrac{l^{(q)}A^{(q)}}{B^{(q)}}}{B^{(n)}\sum_q \dfrac{l^{(q)}C^{(q)}}{B^{(q)}}} \tag{2.20}$$

Where

$$A = 2\varepsilon_0(C_{13}e_{33} - C_{33}e_{31}) + C_{33}P^{SP},$$
$$B = C_{33}\varepsilon_{33} + e_{33}^2,$$
$$C = C_{33}, \tag{2.21}$$
$$G = -2\varepsilon_0(C_{13}\varepsilon_{33} + e_{31}e_{33}) - e_{33}P^{SP},$$
$$e = e_{33}.$$

Takeuchi *et al.*[44] have performed the calculations for strained InGaN layers the result of which is plotted as a function of polar angle θ (denoting the same angle as inclination angle) in Figure 2.4 (a). The transition energy and probability of transition as a function of inclination angle can be calculated assuming triangular potential well in which the internal electric field is taken as perturbation to the rectangular well[45] that is shown in Figure 2.4 (b) and (c), respectively. The variation in the QCSE for various InN molar fractions is demonstrated in Figure 2.5.[46]
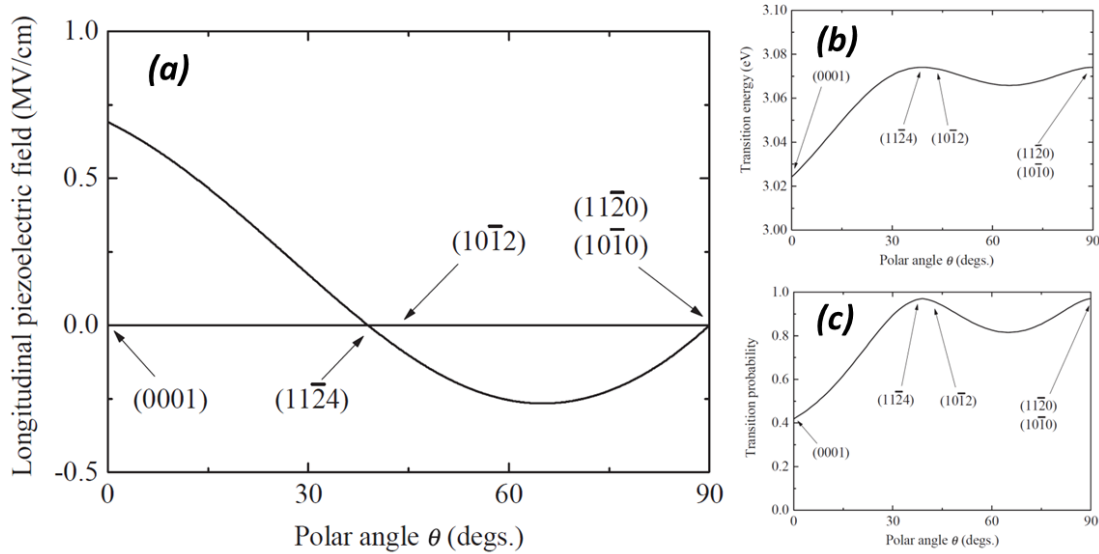
Figure 2.4. Calculated longitudinal internal electric field induced by piezoelectric polarization for a strained In$_{0.1}$Ga$_{0.9}$N layer on GaN (a) and the transition energy (b) and probability (c) for a 3nm In$_{0.1}$Ga$_{0.9}$N/GaN QW as a function of inclination angle (polar angle) with respect to (0001) direction.[Reprinted with Permission from Ref.[44]]
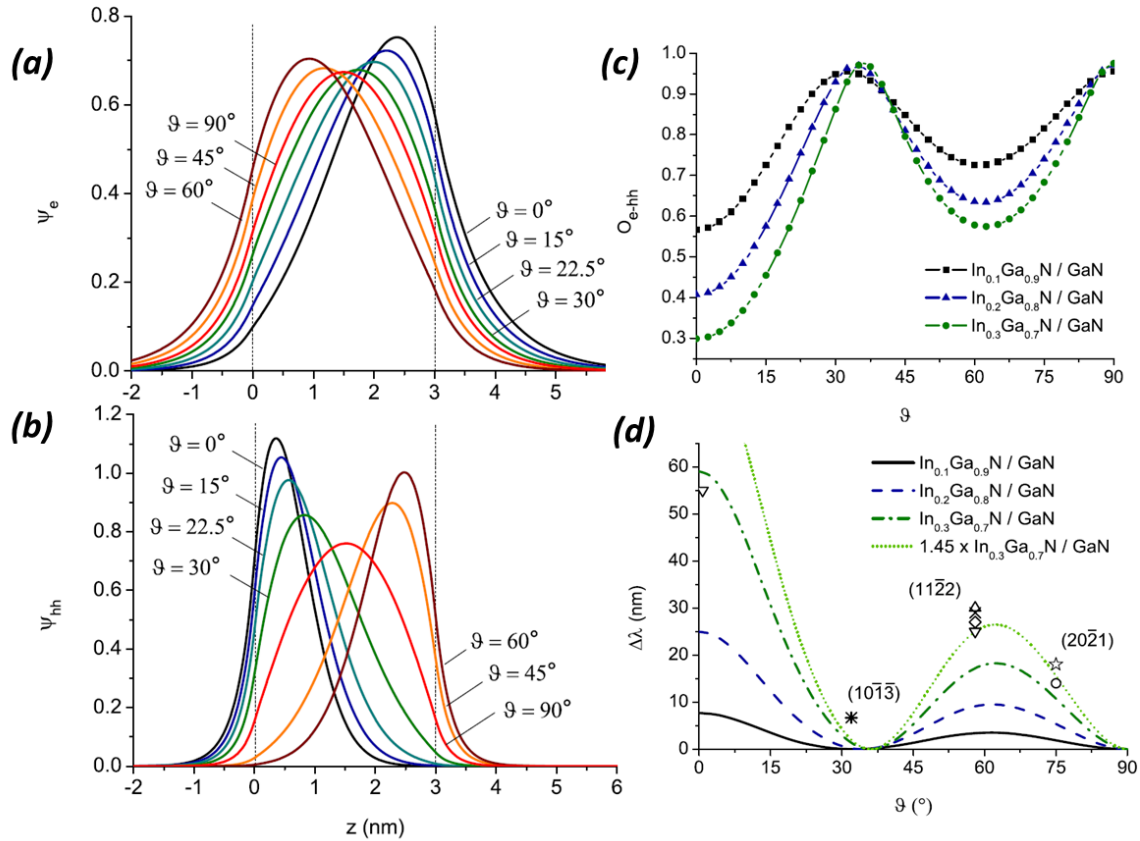
Figure 2.5. Theoretically determined ground state electron (a) and heavy-hole (b) wave function for a 3.0nm $In_{0.2}Ga_{0.8}N$/GaN QW for some discrete values of inclination angles (ϑ) leading to the wave –function overlap (O_{e-hh}) in (c) and the QCSE induced shift in emission spectra ($\Delta\lambda$) as a function of inclination angle for various indium contents. [Reprinted with Permission from Ref.[46]] The points in the plot (d) corresponds to the reported experimental values for $In_{0.3}Ga_{0.7}N$/GaN QW which is followed by theoretical fitting multiplied by 1.45 shown as green dotted line that.[28], [29], [47]–[51]

The internal electric field for GaN-based heterostructures can also be extracted using a set of experiments as performed earlier [52] for *c*-plane by photoluminescence evaluation of QWs with varied thicknesses. Leroux *et al.*[52] reported estimation of internal electric field along *c*-oriented $Al_{0.17}Ga_{0.83}N$/GaN QWs with various widths of 4MLs, 8MLs, 12MLs, and 16MLs and different barrier thicknesses from 5nm to 50nm. Emission analysis of QWs with varied

56

thicknesses based on shift caused by QCSE for estimation for the internal electric field along the wells. Figure 2.6 depicts the emission energy analysis of low temperature photoluminescence using the fitting curves obtained from following equation written for case of superlattice (or MQWs) [52]

$$E_w = \frac{L_b \left(P_b - P_w \right)}{\left(\varepsilon_b L_w + \varepsilon_w L_b \right)} \tag{2.22}$$

Where L_w and L_b denotes well and barrier thicknesses, P_w, and P_b are the zero-field polarization in QW and barrier, respectively. Static dielectric constants in wells and barriers are shown by ε_w, and ε_b, respectively. Similar approach can be performed to estimate electric fields in InGaN and AlGaN heterostructures grown on other crystallographic orientations.
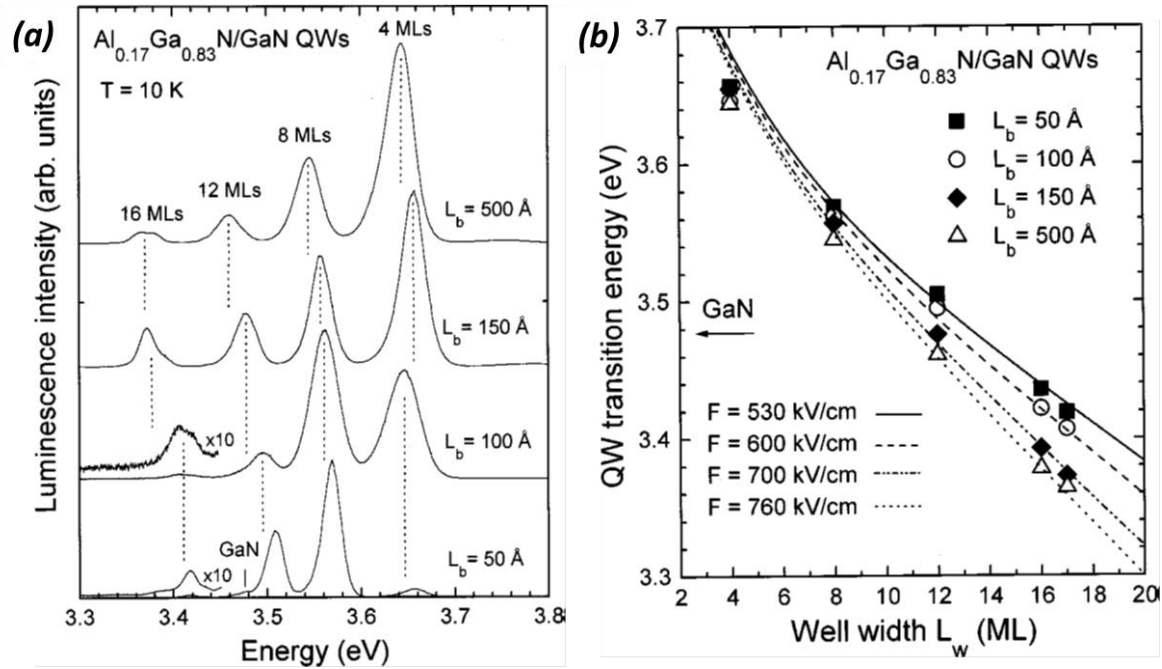
Figure 2.6. Low temperature PL spectra of $Al_{0.17}Ga_{0.83}N$/GaN MQWs with different well widths from 4MLs to 16MLs (a) and dependence of the measured transition energy as a function of well width (b) for different barrier thicknesses from 5nm to 50nm fitted using various electric fields from 530 kV/cm to 760 kV/cm, respectively.[Reprinted with Permission from Ref.[52]]

57

2.2.2. Transport Properties

Transport of carriers in bulk or quantum well systems can be strongly orientation dependent due to variation in strain anisotropy and polarization fields. Unlike optical properties, carrier transport in semipolar and nonpolar structures has remained unexplored as there are only a few studies on this topic to date. Except some studies on semipolar $(11\overline{2}2)$,[53]–[55]$(20\overline{2}1)$ as well as $(20\overline{2}\overline{1})$,[13] and nonpolar $(11\overline{2}0)$[55] structures, there is no significant studies reported on the topic. There are some others reports on carrier transport of ohmic contacts to non-conventional substrate orientations[56] which is not our main topic discussion here. Nevertheless, the investigation of carrier transport is very important for determining desired device performance particularly in MQW systems. Thus, we present a short but comprehensive overview of charge transport properties as well as the potential orientation-dependence.

In the growth plane, *i.e.* the plane perpendicular to growth direction, the scattering mechanisms in semipolar and nonpolar structures could be different from those in *c*-plane mainly due to presence of in-plane polarization and extended defects such as stacking faults.[57] According to literature reports, for nonpolar structures the mobility of carriers in the in-plane directions parallel to $[0001]$ is significantly lower than that in $[11\overline{2}0]$ direction.[58]–[60] The in-plane anisotropy in electron and hole mobility for nonpolar and semipolar structures can be understood considering the carrier transport across basal plane stacking faults (BSF) in the presence of polarization.[61]

The transport problem could be solved assuming two tunneling processes through delta function barriers induced by QW-like band-structures in BSF *i.e.* a zincblende segment inserted between two wurtzite GaN layers, as demonstrated schematically in Figure 2.7 (we will provide

58

more detail discussion of BSFs later in sub-subsection 4.4.2.2 when discussing their optical activities). The strength of the barriers can be found as $S_1 = eV_\pi x_d$, $S_2 = (\Delta E_c + eV_\pi)d$, where $V_\pi = \sigma_\pi d / 2\epsilon_s$ [61] and the total coefficient of incoherent transmission across BSF consisting of coefficients for barrier ($T_{tr,1}(\epsilon)$) and QW ($T_{tr,2}(\epsilon)$) can be written as

$$T_{tr}(\epsilon_k) = \left[\frac{1}{1 + \dfrac{m^* S_1^2}{2\hbar^2 \epsilon_k}} \right] \times \left[\frac{1}{1 + \dfrac{m^* S_2^2}{2\hbar^2 \epsilon_k}} \right] \tag{2.23}$$

Where, ϵ_k and m^* are the electron energy before entering the well and band edge effective mass, respectively. In the absence of SFs, the elemental current component of $j_x^k = ev_x^k \delta f_k$ can be assumed for electrons moving in x-direction with velocity of v_x^k and with perturbation of equilibrium Fermi-Dirac distribution of δf_k in the presence of an electric field. Presence of SFs reduces this current due to partial blocking of the carriers from transmission through the barrier and the QW. The effective current density in x-direction and in the presence of SFs will be $J_k^{eff} = T_{tr}(\epsilon_k) j_k^x$ and, therefore, the total current density in the presence of BSF will be derived as [61]

$$J_x = 2e \int \frac{d^3 k}{(2\pi)^3} T_{tr}(\epsilon_k) v_k^2 \delta f_k \tag{2.24}$$

and conductivity in the x-direction is

$$\sigma_{xx}(T,n) = \frac{3ne^2}{8\pi} \frac{\int d\epsilon \epsilon^{1/2} \cosh^{-2}(\epsilon / 2k_B T) T_{tr}(\epsilon) \tau(\epsilon) \left(v_x^k \right)^2}{\int d\epsilon \epsilon^{3/2} \cosh^{-2}(\epsilon / 2k_B T)}. \tag{2.25}$$

Thus,

59

$$\sigma_{xx}(T,n) = \frac{3ne^2}{8\pi} \frac{\int d\epsilon_k \epsilon_k^{1/2} \cosh^{-2}(\epsilon_k/2k_BT) T_{tr}(\epsilon_k) \tau(\epsilon_k) \left(v_x^k\right)^2}{\int d\epsilon_k \epsilon_k^{3/2} \cosh^{-2}(\epsilon_k/2k_BT)}.$$ (2.26)
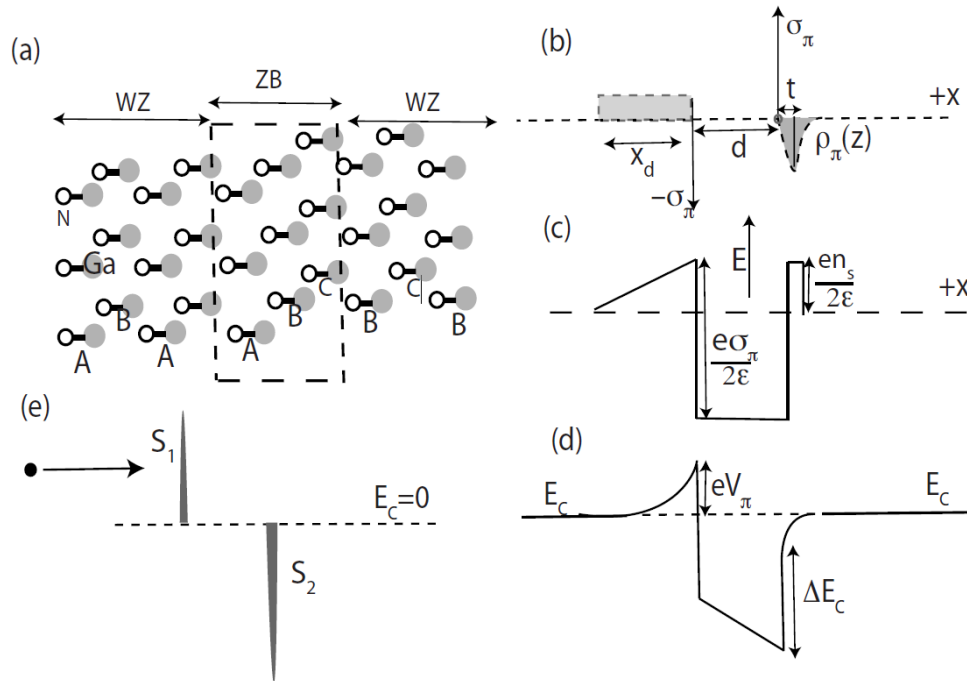
Figure 2.7. (a) Schematic structure of BSFs, (b) charge distribution across BSFs, (c) electric field diagram, (d) conduction band profile of BSFs, and (e) modeling of the QW/Barrier system with delta functions.[Reprinted with Permission from Ref.[61]]

Figure 2.8 represents theoretically calculated together with experimental verification of dependence of film mobility and conductivity on carrier density for two perpendicular directions for *p*-doped *m*-plane substrates. The plots clearly indicate the adverse effect of basal plane stacking faults on carrier transport, as the electrical data shows anisotropic behavior for directions parallel and perpendicular to the basal plane in the presence of BSF.
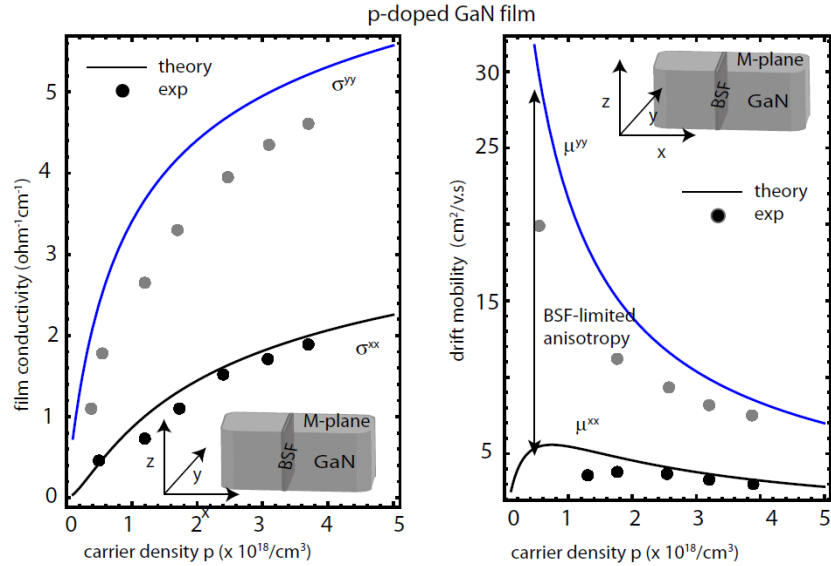
Figure 2.8. Theoretically calculated (solide lines) and experimental data (solid circles) for film conductivity (left) and drift mobility (right) for direction parallel (blue) and perpendicular (black) to the plane of BSF *i.e. c*-plane. [Reprinted with Permission from Ref.[61]]

For out-of-plane transport, since polarization-induced electric field in polar structures and resulting band bending is orientation dependent (see subsection 2.2.1), it is reasonable to assume transport of electron and holes in a multi quantum well system being affected by choice of substrate orientation.[37] Based on the calculated plots for piezoelectric and total polarizations (discussed in previous section), at inclination angles of above 45° the polarization direction switches and thus direction of band bending in the structure changes as well. This phenomenon can be better understood by considering the band structures simulated for selected orientations and selected indium content in InGaN/GaN MQWs as shown in Figure 2.9.
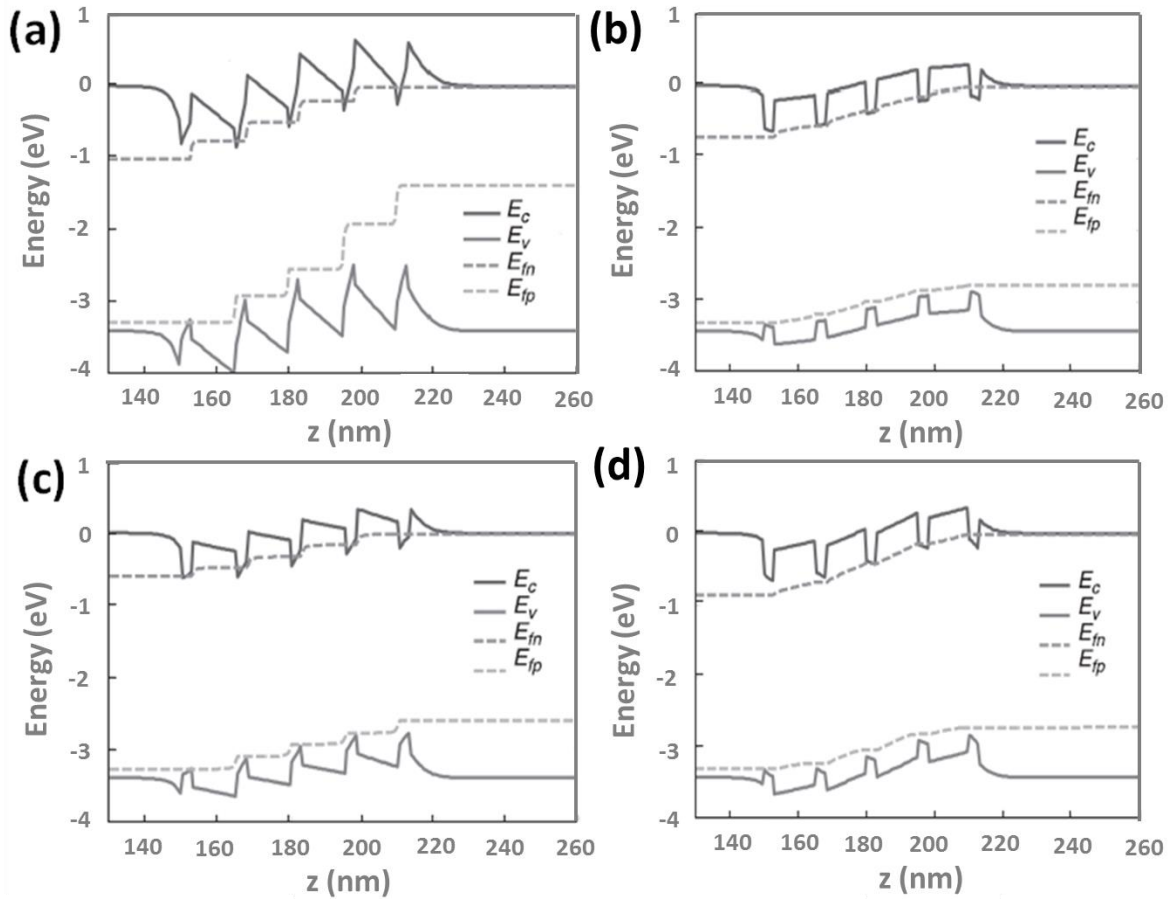
Figure 2.9. Simulated band structure of InGaN/GaN MQWs for (a) *c*-plane, (b) *m*-plane, (c) for $(10\bar{1}3)$, and (d) $(20\bar{2}1)$. The conduction (E_C) and valence band energy (E_v) and electron (E_{fn}) and hole quasi Fermi levels (E_{fp}) are shown in the plots. [Data from Ref.[37]]

In multi quantum well structures, when the polarization changes the sign [the case of $(11\bar{2}2)$ or $(20\bar{2}1)$], the carriers escaping from one quantum well would face an additional barrier on their path to the next quantum well. This is, in contrast to the case of nonpolar heterostructures ($\theta = 90°$) in which there should not be effectively any band bending. In that case, the escaped carriers would be more easily injected to the next quantum well (see Figure 2.9). Therefore, for the same forward bias voltage, the output power will be lower in case of

62

nonpolar structures, which means decrease in efficiency. This has been experimentally demonstrated by Kawaguchi *et al.*.[13] According to their study, the distribution of carriers is more uniform in semipolar $(20\overline{2}\,\overline{1})$ MQW InGaN structures than that in $(20\overline{2}1)$ counterpart with opposite polarity and thus the forward bias voltage needed to have same optical power is lower in case of $(20\overline{2}\,\overline{1})$ than that in $(20\overline{2}1)$ InGaN light emitting diodes.[13] Therefore, consideration of carrier transport properties is essential in choosing orientation and and in design of InGaN LEDs for high efficiency.

2.2.3. Light Emission Properties

The optical properties of a material system are determined by its energy-momentum relation as it controls transition states for charge carriers. Therefore, in order to understand the effect of inclination angle on optical properties it is necessary to start from E-k dispersion curve. Using first-principle calculations to obtain the electronic band structure parameters (such as effective masses and splitting energies) by a full-potential linearized augmented plane wave (FLAPW) method[62] within local density functional approximation (LDA)[63] the electronic band structure (E-k diagram) can be determined.[64] The result of the calculation at around the Γ point which leads to dispersion curve for GaN is shown in Figure 2.10. In this calculation, it is assumed that charge density in valence band is strongly localized and the hybridization of Ga 3d is non-negligible.[64]
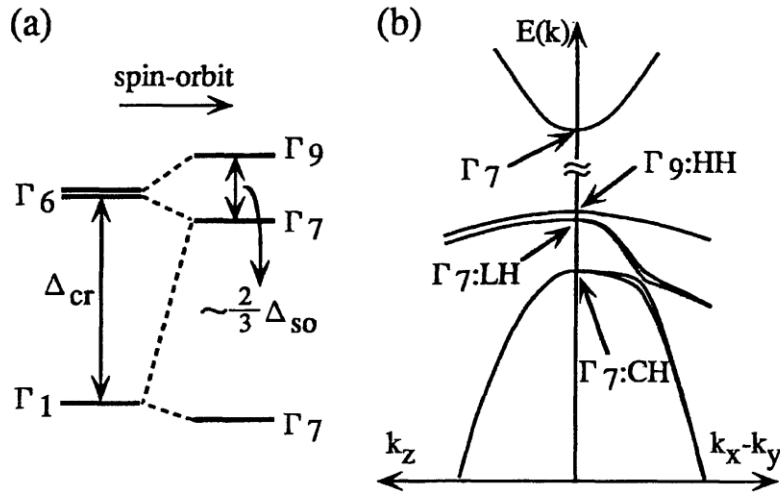
Figure 2.10. Schematic electronic band structure (E-k diagram) of wurtzite GaN. (a) Spin orbit splitting of the bands in valence band maximum. (b) The energy dispersion along k_z and in k_x-k_y plane where HH, LH, and CH represents heavy holes, light holes, and crystal-field split-off hole bands, respectively.[Reprinted with Permission from Ref.[64]]

In order to understand the optical properties of wurtzite GaN crystal the realization of momentum matrix are also required.[62] For diamond-structure materials such as Si, and Ge parabolic function is assumed for conduction band and 4×4 and/or 6×6 Hamiltonian are used to describe valence bands. For the valence band together with the conduction band, 8×8 Hamiltonian can be used. For wurtzite GaN structure assuming 8×8 $k.p$ Hamiltonian using the following basis functions:

$$|S,\alpha\rangle, |S,\beta\rangle, \left(1/\sqrt{2}\right)|(X+iY),\alpha\rangle, \left(1/\sqrt{2}\right)|(X+iY),\beta\rangle, |Z,\alpha\rangle, |Z,\beta\rangle, \qquad (2.27)$$

$$\left(1/\sqrt{2}\right)|(X-iY),\alpha\rangle, \left(1/\sqrt{2}\right)|(X-iY),\beta\rangle \qquad (2.28)$$

where $|S\rangle, |X\rangle, |Y\rangle, |Z\rangle$ Relates with s, p_x, p_y, p_z orbital functions, respectively and $|\alpha\rangle, |\beta\rangle$ are spin up and down functions, respectively. Later we will discuss that the light emission

64

polarization for a certain orientation is dependent on these basis.[37] The Hamiltonian would have the form

$$H(k) = \begin{pmatrix} H_{cc} & H_{cv} \\ H_{cv}^{\dagger} & H_{vv} \end{pmatrix}, \tag{2.29}$$

Where H_{cc}, H_{vv}, and H_{cv} are matrices (2×2, 6×6, and 2×6, respectively) describing conduction band, valence, and the interaction between conduction and valence bands, respectively with matrix elements as follows:

$$H_{cc} = \begin{pmatrix} E_c & 0 \\ 0 & E_c \end{pmatrix}, \tag{2.30}$$

$$H_{cv} = \begin{pmatrix} Q & 0 & R & 0 & Q^* & 0 \\ 0 & Q & 0 & R & 0 & Q^* \end{pmatrix}, \tag{2.31}$$

$$H_{vv} = \begin{pmatrix} F & 0 & -H^* & 0 & K^* & 0 \\ 0 & G & \Delta & -H^* & 0 & K^* \\ -H & \Delta & \lambda & 0 & I^* & 0 \\ 0 & -H & 0 & \lambda & \Delta & I^* \\ K & 0 & I & \Delta & G & 0 \\ 0 & K & 0 & I & 0 & F \end{pmatrix}, \tag{2.32}$$

Where the parameters can be found as

$$
\begin{aligned}
& E_c = E_s^0 + \frac{\hbar^2 k_z^2}{2m_c^{\parallel}} + \frac{\hbar^2 k_{\perp}^2}{2m_c^{\perp}}, \\
& Q = \frac{1}{\sqrt{2}} P_{\perp} k_+, R = P_{\parallel} k_z, \\
& F = \Delta_1 + \Delta_2 + \lambda + \theta, G = \Delta_1 - \Delta_2 + \lambda + \theta, \\
& H = iA_6 k_z k_+ - A_7 k_+, I = A_6 k_z k_+ + A_7 k_+, \\
& K = A_5 k_+^2, \Delta = \sqrt{2}\Delta_3, \\
& \lambda = E_P^0 + A_1 k_z^2 + A_2 k_{\perp}^2, \theta = A_3 k_z^2 + A_4 k_{\perp}^2, \\
& k_{\pm} = k_x \pm ik_y, k_{\perp}^2 = k_x^2 + k_y^2.
\end{aligned}
\tag{2.33}
$$

65

Where $E_{s,p}^0$ is energy levels for *s*, and *p* states for $k = 0$. $\Delta_1, \Delta_{2,3}$ are crustal-field and spin-orbit splitting, respectively. The momemtum matrix elements for parallel and perpendicular to *c*-directions ($P_{\parallel,\perp}$) can be expressed as

$$P_{\parallel} = \frac{\hbar}{m_0}\langle S | p_z | Z \rangle, P_{\perp} = \frac{\hbar}{m_0}\langle S | p_x | X \rangle.$$ (2.34)

Unlike zincblende structures, for wurtzite $P_{\parallel}$ and $P_{\perp}$ are not normally the same.

In case of strained layers, the strain tensor plays an important role in Hamiltonian matrix elements, E-k relation, momentum matrix elements and as a result, optical polarization. Knowing the fact that valence band states mixing, the separation energy between the two valence bands CH$_1$, CH$_2$ and the effective mass ratio of these bands will have significant effect on quantum confinement, the 6×6 *k.p* Hamiltonian for valence band considering strain tensor would have the following form[65]

$$H_{vv} = \begin{pmatrix} F & 0 & -H^* & 0 & K^* & 0 \\ 0 & G & \Delta & -H^* & 0 & K^* \\ -H & \Delta & \lambda & 0 & I^* & 0 \\ 0 & -H & 0 & \lambda & \Delta & I^* \\ K & 0 & I & \Delta & G & 0 \\ 0 & K & 0 & I & 0 & F \end{pmatrix},$$ (2.35)

Where the parameters can be found as

$$F = \Delta_1 + \Delta_2 + \lambda + \theta, G = \Delta_1 - \Delta_2 + \lambda + \theta,$$

$$\lambda = \frac{\hbar^2}{2m_0}\Big[A_1 k_z^2 + A_2 \big(k_x^2 + k_y^2 \big) \Big] + D_1 \epsilon_{zz} + D_2 \big(\epsilon_{xx} + \epsilon_{yy} \big),$$

$$\theta = \frac{\hbar^2}{2m_0}\Big[A_3 k_z^2 + A_4 \big(k_x^2 + k_y^2 \big) \Big] + D_3 \epsilon_{zz} + D_4 \big(\epsilon_{xx} + \epsilon_{yy} \big),$$

$$K = \frac{\hbar^2}{2m_0} A_5 \big(k_x + ik_y \big)^2 + D_5 \big(\epsilon_{xx} - \epsilon_{yy} + 2i\epsilon_{xy} \big), \qquad (2.36)$$

$$H = \frac{\hbar^2}{2m_0} i \Big[A_6 k_z \big(k_x + ik_y \big) + A_7 \big(k_x + ik_y \big) \Big] + iD_6 \big(\epsilon_{xz} + i\epsilon_{yz} \big),$$

$$I = \frac{\hbar^2}{2m_0} i \Big[A_6 k_z \big(k_x + ik_y \big) - A_7 \big(k_x + ik_y \big) \Big] + iD_6 \big(\epsilon_{xz} + i\epsilon_{yz} \big),$$

$$\Delta = \sqrt{2}\Delta_3,$$

Here, D_i, A_i, k_i, and ϵ_{ij} are deformation potentials, fitting parameters, wave-vector, and strain tensor, respectively. All the parameters and more extended discussion can be found elsewhere.[65]

With technique similar to what we used in calculations of strain and polarization in subsection 2.2.1, the light emission polarization for InGaN/GaN in different planes can be understood by rotation of the coordinate system with respect to c-axis by an angle corresponding to their inclination angle. As demonstrated earlier in this section, the transformation matrix as a function of inclination (ϑ) and azimuthal angles (φ) would have the following form:

$$U = \begin{pmatrix} \cos\vartheta\cos\varphi & \cos\vartheta\sin\varphi & -\sin\vartheta \\ -\sin\varphi & \cos\varphi & 0 \\ \sin\vartheta\cos\varphi & \sin\vartheta\sin\varphi & \cos\vartheta \end{pmatrix}. \qquad (2.37)$$

The E-k diagrams calculated using the transformed coordinate system for valence band in In$_{0.2}$Ga$_{0.8}$N QWs for polar, nonpolar m-plane, and semipolar $\left(11\bar{2}2\right)$ plane are shown in Figure

67

[2.11](#) which is patterned after Ref.[37]. In the original plot which is in color (see the figure in Ref. [37]), red, green, and blue colors represent $|X'\rangle, |Y'\rangle$, and $|Z'\rangle$ states, respectively and mixed color represents mixed states. The strength of emission for any interband transition can be calculated from momentum matrix elements. For instance, in case of *c*-plane substrate orientation where the basis in valence band is made by mainly $|X \pm iY\rangle$ states, momentum matrix element appears as follows[37]

$$\left| \langle f_e(z) | f_h(z) \rangle \langle S | \cdot \left(i\hbar\vec{\nabla} \right) \| X \pm iY \rangle \right|^2 . \tag{2.38}$$

Here $\left| \langle f_e(z) | f_h(z) \rangle \right|$ is the overlap between conduction and valence band wave functions. Since *c*-oriented structure has mostly $|X\rangle$ and $|Y\rangle$ states, the radiating dipole is in the *x-y* plane, which is the plane of the InGaN quantum well. In case of nonpolar *m*-plane, the first sub-band would be $|X\rangle$-like (X') state, the second sub-band would be $|Z\rangle$-like (Y') state and the $|Y\rangle$-like (Z') state would be the final subband. In semipolar QW, due to strain anisotropy and shear strain, we can have mixed states $|X\rangle$, $|Y\rangle$, and $|Z\rangle$-like states in valence band. Depending on the indium content and inclination angle of the plane, the polarization can be different. For $\left(11\bar{2}2\right)$ orientation for which the inclination angle is calculated in previous section to be $\theta = 58°$ (see [Figure 2.1](#)), using the rotated coordinates, the first sub-band would be $|Y'\rangle$-like state, the second subband would be a mixed $m|X'\rangle + n|Z'\rangle$-like state. The second sub-band may elevate and become the first for high indium content QWs as a result of enhancement of anisotropic strain[37] causing out of plane polarization. These theoretical predictions are supported by experimental data presented by Koslow *et al.*[66]. They have experimentally demonstrated that

68

the emission corresponding to out of plane polarization will be suppressed when using strain reduction layers for $In_{0.4}Ga_{0.6}N/GaN$ structures on $(11\bar{2}2)$ orientation. Therefore, based on reports of Refs.[37], [65], for InGaN/GaN structures with Indium content below 20%, the emitting dipole would be in-plane. The increase of the Indium composition will increase the out-of-plane dipole contribution.
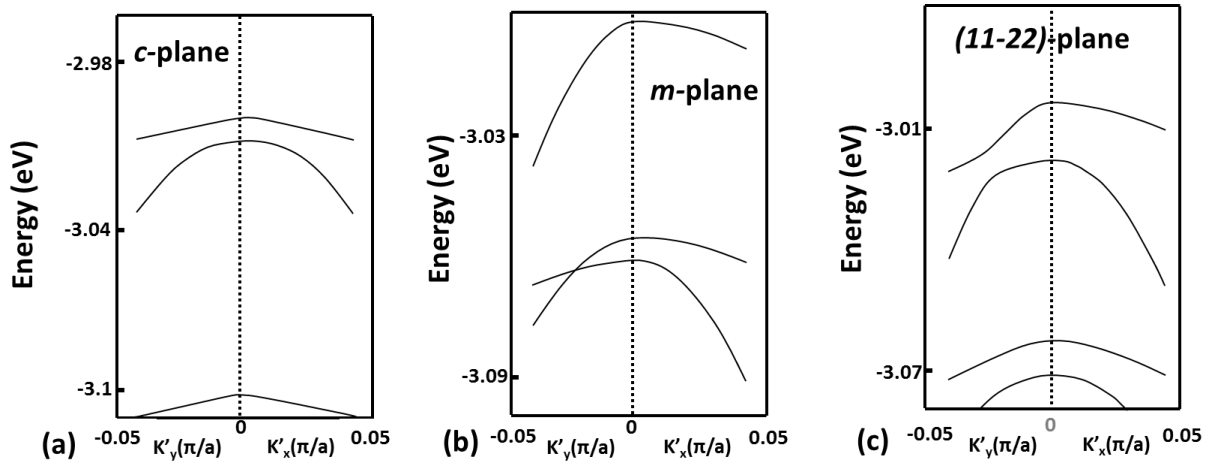
Figure 2.11. Calculated valence band dispersion around the Γ point for (a) *c*-plane, (b) *m*-plane and (c) semipolar $(11\bar{2}2)$ $In_{0.2}Ga_{0.8}N$ QWs with band gap of 2.7eV. Note that conduction band of GaN is assumed as zero potential. [Patterned After Ref.[37]]

2.2.4. Indium Incorporation Efficiency

One of the main challenges for development of green LEDs based on InGaN systems is highly defective layers due to poor indium incorporation efficiency for the conventional systems. Not only the large lattice mismatch between InN and GaN but also the difficulties in MOCVD growth of high Indium content InGaN structures (because of increase in possibility of indium desorption at elevated substrate temperature) have made the growth of high quality long-

69

wavelength LEDs challenging.[37] In order to have high indium composition for a given orientation, growth temperature should be reduced to reduce the probability of Indium desorption.[37] While the surface diffusivity of adatoms at low temperatures is suppressed the quality of the InGaN layers degrades. Feng Wu *et al.*[67] demonstrated the reduction in recombination rate for longer wavelength devices ($\lambda > 500nm$) which has been attributed to the formation of I_1 type BSF bounded by partial dislocations as revealed by observated increase in dislocation density by 3 orders of magnitude compared to the GaN template.[67]

Besides the effect of growth conditions,[37] the indium incorporation efficiency is mainly determined by substrate orientation due to its dependence on strain[20] and surface atomic configurations.[21] This fact has made researchers eager to find an orientation that enhances the incorporation of indium into the InGaN layers. Theoretically, based on calculation of strain[20] and formation energy,[21] it has been demonstrated that among the semipolar and nonpolar planes of GaN, the nonpolar *m*-plane exhibits the lowest and semipolar plane with inclination angle of $\theta \sim 60°$ has the highest indium incorporation efficiency. Experimental reports are also in agreement with the theoretical predictions indicating lowest indium incorporation for *m*-plane[18], [22], [67]. Zhao *et al.*[22] reported that semipolar $\left(11\overline{2}2\right)$ orientation with $\theta = 58°$ to have the highest incorporation among all others with inclination angles above $\theta = 60°$ (see Figure 2.12) which supports the theoretical prediction presented by Durnev et al.[20] Unfortunately, the results of comparison with *c*-plane (and other orientations with $\theta < 60°$) is missing in experimental study by Zhao *et al.*[22].

70
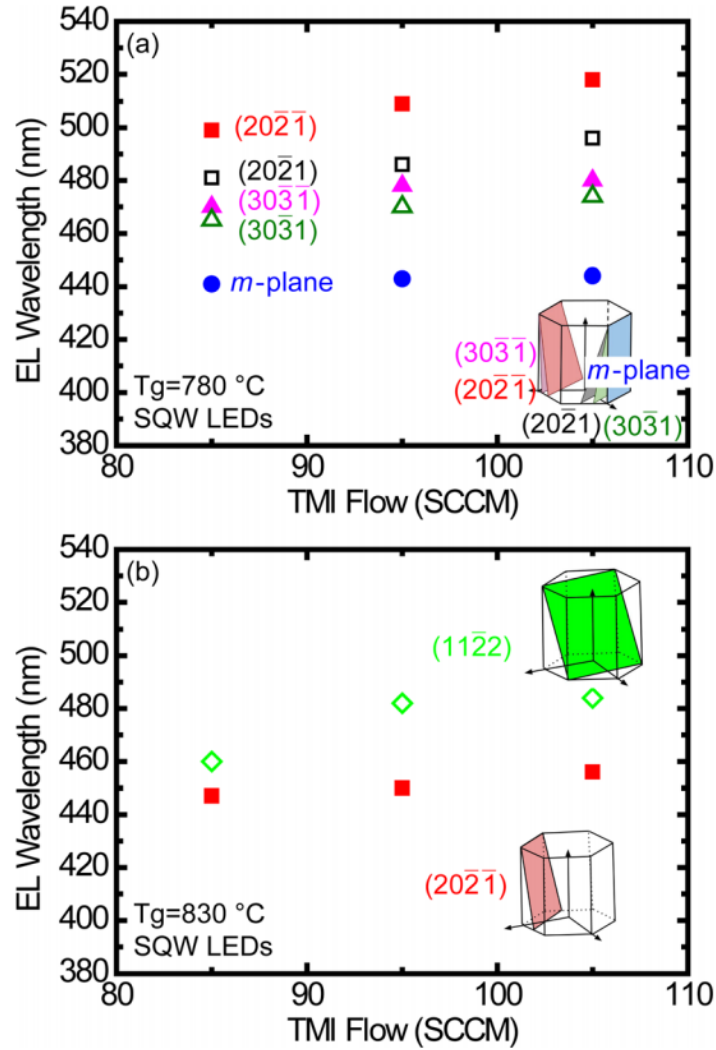
Figure 2.12. Electroluminescence peak wavelength for 3nm single QW LED for (a) $(20\bar{2}\bar{1})$, $(20\bar{2}1)$, $(303\bar{1})$, $(30\bar{3}1)$, and *m*-plane at 780˚C of growth temperature and (b) for $(20\bar{2}\bar{1})$ and $(11\bar{2}2)$ at growth temperature of 830˚C. The inset demonstrate schematics of the planes used in the experiment. [Reprinted with Permission from Ref.[22]]

Moreover, it has been shown that the incorporation of indium is also affected by surface polarity.[22] As examples, indium incorporation is found to be higher in case of $(20\bar{2}\bar{1})$, $(30\bar{3}\bar{1})$, and finally $(000\bar{1})$ orientations compared to their metal-polar counterparts $(20\bar{2}1)$,

71

$(30\overline{3}1)$ [22] (see Figure 2.12), and (0001) [68] with virtually identical strain conditions. This phenomenon can be explained by higher binding energy between In species and N-polar surface compared to Ga-polar surface which prevents the indium atoms from desorption as revealed by first principle calculation reported in Ref. [69].

Density functional theory (DFT) calculation with pseudopotential assumption for InGaN layers with various orientations is performed to determine total energy [21], [70], [71] and thus stability of the layers. Ga 3d, and In 4d electrons will be considered as core electrons in valence band for pseudo-potential assumption in this calculation. By calculating the difference in formation energy of surface states of GaN occupied by indium atoms, the relative stability of GaN surface can be understood using the following equation

$$\Delta\Omega = \Delta E - \Delta n_{Ga}\mu_{Ga} - \Delta n_{N}\mu_{N} - \Delta n_{In}\mu_{In} \qquad (2.39)$$

where $\Delta\Omega$, ΔE, and Δn_i (i = Ga, N, In) are the difference in formation energy, total energy, and number of atoms, respectively and μ is the chemical potential[21], [72], [73]. Using the above equation, one can compare various orientations in terms of indium incorporation.

Northrup[21], [73] compared theoretically the indium incorporation on $(11\overline{2}2)$ and $(10\overline{1}0)$ orientations for a relaxed In$_{0.25}$Ga$_{0.75}$N layer (see Figure 2.13). based on the relative energy curve versus chemical potential for $(11\overline{2}2)$ substrate orientation, the indium can incorporate below the adlayer at much lower chemical potential than in case of *m*-plane (compare the chemical potential at which the black horizontal line crosses the colored tilted lines

72

in both orientations), which essentially means that growth is favorable for a wider growth condition window.[21]
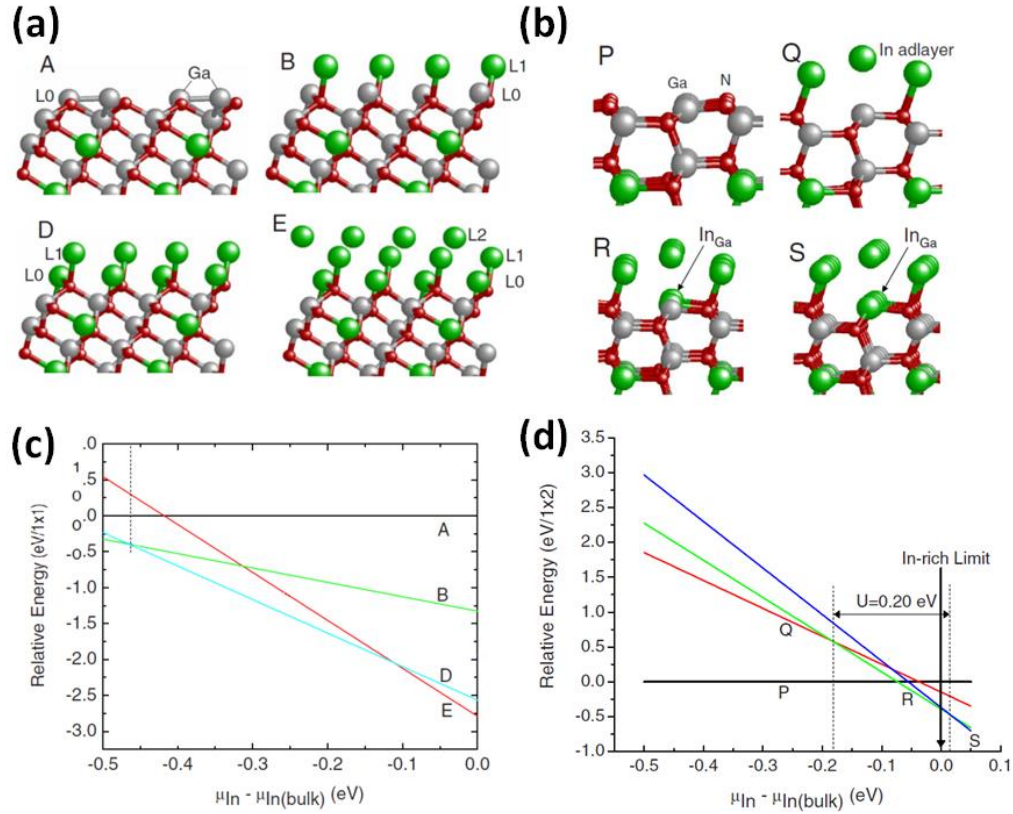
Figure 2.13. Schematic representation of InGaN surface for (a) $(11\bar{2}2)$ plane where A (Ga terminated surface), B, D, and E surfaces contain more indium atoms in turn, and (b) $(10\bar{1}0)$ plane with P, Q, R, and S having more indiums successively. Note that green, gray and red atoms are indium, Ga, and N, respectively in this representation. Plots in (c) and (d) illustrate formation energy for different layers with respect to the reference sample for $(11\bar{2}2)$ and $(10\bar{1}0)$ samples, respectively. [Reprinted with Permission from Ref.[21]]

As a conclusion to this subsection, Indium incorporation efficiency is another parameter which appears to be orientation dependent. The theoretical calculation suggests the highest incorporation into semipolar planes with $\theta \sim 60°$. Experimental data seems to agree with the theory that is studied for some substrates with inclination angles above 58°. Comparison with *c-*

plane which is critical was not conclusive based on literature reports and will be discussed in more details in Chapter 4.

Chapter 3

3. Methods and Approach

3.1. Overview

Following the above discussion, the methodology for investigation of physical properties of polar, nonpolar and semi-polar light emitting heterostructures and their will be discussed in this Chapter. The general approach to systematic investigation of heterostructures on nonpolar and semi-polar crystallographic planes described in section 3.1 will be followed by developed methods classified into five main categories in section 3.2: Theoretical calculations, growth techniques, optical/structural characterization, fabrication, and electrical characterizations.

Part of the work (mainly in material characterization and recombination dynamics parts) is being performed through an international collaboration with Otto-von-Guericke University of Magdeburg (Germany) and University of Montpellier-2 (France). The diagram in Figure 3.1 illustrates the interactions and contributions of the teams participating in the Material World Network (MWN) project supported by NSF.
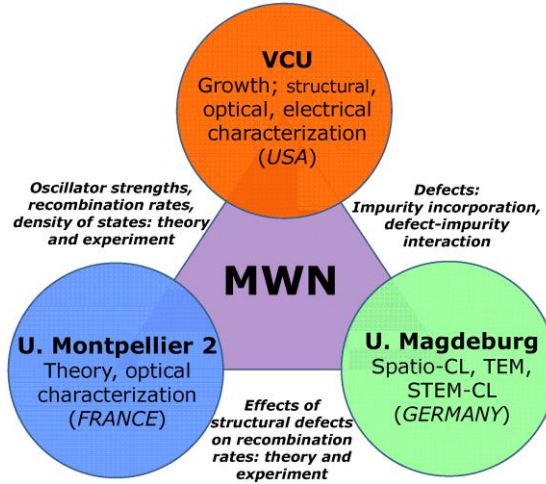
Figure 3.1. Contributions and interactions of the three teams for the Material World Network (MWN) project as part of the research being performed and will be proposed in this proposal.

3.2. Investigation of polar, nonpolar, and semi-polar LEDs: A systematic approach

Exploration of semi-polar GaN heterostructures in all aspects from physical and crystallographic properties to suitable growth conditions for high performance and device properties could only be performed through a systematic approach.

Along with general aspect of systematic approach, we first demonstrate efficiency improvements by novel LED designs for *c*-plane orientations to overcome the efficiency degradations and understanding of the mechanisms limiting the device efficiency. Discussion of the challenges for conventional *c*-plane LEDs as well as nonpolar structures as alternatives will be brought into attention. The investigations of nonpolar structures and their limitations will guide us to semi-polar orientations as more promising candidates for efficient LEDs, particularly for long wavelength emitters. Among all the semi-polar planes, the attention will focused on two

75

planes due to their relatively low cost of preparation (through heteroepitaxy) and substantial potentials for improved long wavelength emitters. One of the semi-polar orientations obtained by heteroepitaxy will be chosen for further investigations as it features planar surface morphology unlike the other one that is obtained on patterned substrate.

The systematic approach incorporates as necessary part the theoretical calculations followed by simulation of the desired structure design. Theoretical analysis provides the knowledge which is required before proceeding to any experiment. Thereafter, experiment comes to picture starting from growth procedures. Challenges related to material quality which caused by the presence of defects and their optical activity as well as effects on electrical properties have to be considered in association with methods to reduce the defect density in the layers. Methods of optical and structural characterization which include photoluminescence (PL), cathodoluminescence (CL) X-ray diffraction (XRD), and transmission electron microscopy (TEM), are used to evaluate the quality of the GaN layers grown with semipolar orientations.

Attaining high crystal quality of the GaN layers, we perform optical investigations in order to characterize the structures. Such investigations will also allow us to better understand the intrinsic properties of the orientation under study (and compare with theory) and evaluate the structure in terms of emission properties and efficiency. The fabrication and device characterization will be the next step. During this step, we will prepare *n*-type as well as *p*-type contacts on the layers which is required for electrical injection. Finally, electroluminescence for determination of external quantum efficiency (EQE) of the devices in relative and absolute scheme will be performed. The latter requires over-layer metal deposition followed by wire bonding. Design of device structures needs to be optimized for high efficiency devices with improved EQE retention at high injection levels.

76

Various optical techniques are involved for parameter determination as another part of the approach. These parameters of interest include internal electric field perpendicular to growth plane as well as along structural defects (stacking faults), carrier diffusion constants, excitonic recombination, localization parameters, *etc.* Comparison of the obtained characteristics with those for the conventional *c*-plane structures is of great importance especially when supported by theoretical analysis.

During the following sections, the utilized methods and approaches classified into five groups will be treated in more details including theoretical calculations, growth techniques, optical/structural characterization, fabrication, and electrical characterization. The method descriptions will be followed by schematics in case it is necessary and will be referred in the next Chapters when discussing my contributions to the field and future proposed researches.

3.3. Theoretical methods

The first thing to start with before running any experiment is the theoretical calculations which help to design effective structures. Group theoretical calculations and simulation using Silvaco Atlas software are the main calculations tools required for this investigation. The former is used for determining optical transition parameters for different orientations and the latter is utilized for calculation of band structure and related parameters.

Group theory methods are used to determine Bloch states, dispersion curves, optical transition probabilities, and oscillator strength for the InN-GaN and AlN-GaN quantum well systems grown on semi-polar and nonpolar orientations in comparison to *c*-plane. More detailed discussion of the theretical approaches and the assumptions made were provided in Chapter 2 and will be discussed in more details for each case prior to experimental results in Chapter 4.

77

On the other hand, band structure calculations of the design structures are calculated using SILVACO Atlas simulation package. More information such as electron and hole wavefunctions and populations, position of quasi Fermi levels, and could also be extracted.

However, in order to simulate the polarization charges in the interfaces (it can also be inserted as percentile of maximum calculated polarization) and carrier concentrations in each layer need to be inserted. The former requires calculations of spontaneous and piezoelectric contributions which are definitely reduced in case of semi-polar heterostructures compared to *c*-plane based on polarization charge plots as a function of crystal inclination angle (θ) with respect to *c*-axis discussed in detail in Chapter 2. In literature reports, the value of polarization charge used for *c*-plane structures was 40-50% of the maximum calculated values without mentioning why this value was chosen. Thus, the choice of the polarization percentile requires more investigations and potential experiment which need a separate work for confirmation and will not be brought in this proposal. The carrier concentration is inserted based on values obtained from hall measurement performed on *n*-GaN and *p*-GaN layers grown in separate experiments.

3.4. Growth Technique

The layers have been grown in a vertical design low pressure metal-organic chemical vapor deposition (MOCVD) system, where trimethylaluminum (TMA), trimethylgallium (TMG), trimethylindium (TMI), and NH_3 are used as Al, Ga, and In, N sources, respectively and H_2 used as precursors. Triethylgallium (TEG) is another source of Ga which is used for the growth of high quality structures at relatively lower substrate temperatures, *e.g.* in case if InGaN growth which requires temperatures of the order of 700 C. SiH_4 and CP_{MG} are used as sources of Si and

78

Mg to dope structures *n*-type and *p*-type, respectively. The simplified schematics and the image

of our MOCVD system are shown in Figure 3.2.
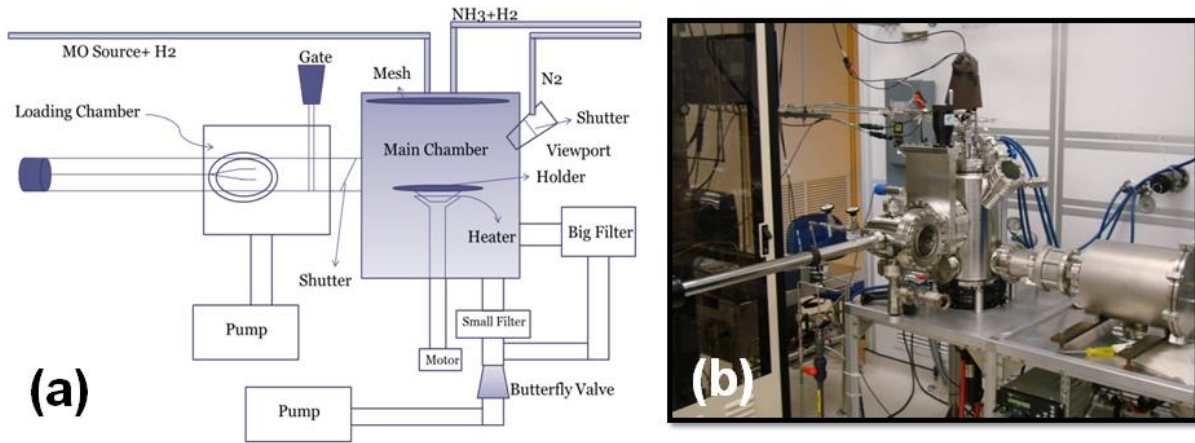
Figure 3.2. (a) Simplified schematics and (b) photograph of our home-made vertical design MOCVD system at microelectronic materials and device laboratory (MMDL) at VCU. The system includes four main parts: loading chamber, reactor, Gas cabinet (not shown here), and exhaust.

The quality and surface morphology of the semi-polar GaN layers was examined with

scanning electron microscopy (SEM), optical microscopy imaging, steady state and time-

resolved photoluminescence (PL), etc. Based on the analysis, the growth parameters such as

substrate temperature, V/III ratios, and growth pressure are modified to optimize the growth

conditions for the best optical and structural properties as well as surface morphology.

The research in this section of the project includes application and optimization of novel

viable defect reduction techniques to obtain the favorable layer properties which is required for

device application and investigations of intrinsic properties of the heteroepitaxial as well as

homoepitaxial material systems. The MOCVD was used also to grow AlGaN/GaN quantum well

structures on non-polar m-plane free-standing substrates (see sub-section 4.3.2) provided by Kyma Tech.

3.5. Optical and Structural Characterizations

The characterization of the heterostructures on planar and patterned substrates have been performed with SEM and atomic forced microscopy (AFM) to study surface morphology of the films, X-ray diffraction (XRD) to examine structural quality as well as verifying the structural design, and steady state and time-resolved photoluminescence (PL) in order to investigate optical quality of the films. Cathodoluminescence (CL) measurements performed at Magdeburg using highly spatially and spectrally resolved CL system built around JEOL 6400 scanning electron microscope.[74] and Near field scanning optical microscopy (NSOM) measurements at low and room temperature (at VCU) were utilized to study defect distribution and optical activity of the defects as well as to see the uniformity of impurity and alloy incorporation in the structures. The NSOM setup were being performed using a Cryoview 2000 system (N anonics Imaging Ltd). The 325-nm line from a HeCd laser through a Cr-Al coated near-field optical fiber probe with a 100 nm aperture was used as an excitation source. During NSOM scans the distance between the sample surface and the NSOM tip was being controlled by a force feedback system. In order to perform NSOM photoluminescence intensity mapping, the light from the sample surface was being collected with a long working distance 50x UV-visible microscope objective and detected by a photomultiplier tube. A short-pass optical filter was used to block the HeCd laser light reflected from the sample surface. In order to spectrally analyze the detected light, long pass and band pass optical filters were used.

Wavelength-degenerate time-resolved differential transmission (TRDT) technique also will be used to study band-alignment of stacking faults (section 5.3 discusses the details of the proposed research that will be performed based on this technique). Figure 3.3 shows the typical setup for the degenerate TRDT experiment. These measuremens performed as follolws: each pulse emitted by frequency doubled mode-locked Ti:sapphire laser is split into two beams, the pump and the probe, where the pump is usually at least 10 times stronger than the probe. The pump beam is reflected from a retro-reflector mounted on a translational stage. The time delay between the pump and the probe is varied by changing the path length of the pump beam using the translational stage. Both the pump and probe beams are focused and overlapped on the sample. To eliminate the stray pump light on the detector, pump and probe beams are usually cross-polarized. The pump beam is usually modulated using a mechanical chopper, and the change in the probe beam transmission (ΔT) is measured by lock-in detection to improve the signal-to-noise ratio. In order to compute the differential transmission (DT $\equiv \Delta T/T_0$), the bare probe transmission (T_0) is also measured by chopping the probe beam and using the lock-in amplifier when the pump beam is blocked.

81
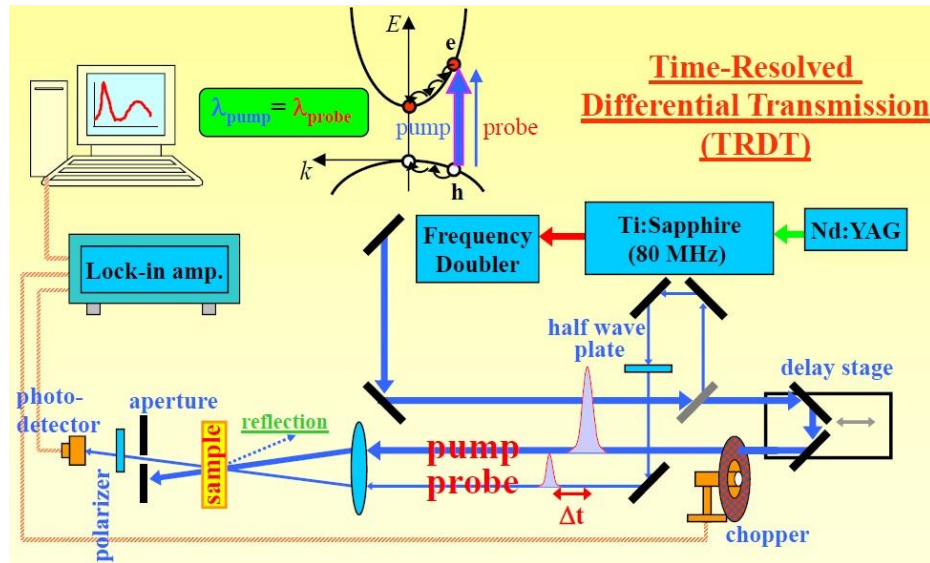
Figure 3.3. Experimental setup of time-resolved differential transmission (TRDT).

Figure 3.4 illustrates the unique equipment used for the characterization of defects related emissions using STEM-CL at helium temperatures at our collaborators' lab (University of Magdeburg, Germany). Utilizing this setup, the optical properties of single basal plane stacking faults formed in a single nano-coloumn was explored for the first time in another work. [75] This setup is also utilized in our work to study defect distribution and to identify type of defects and their optical properties. The STEM images and the corresponding CL intensity and wavelength mapps of the layers could also be used to evaluate the quality of the layers in terms of dislocation and stacking faults.
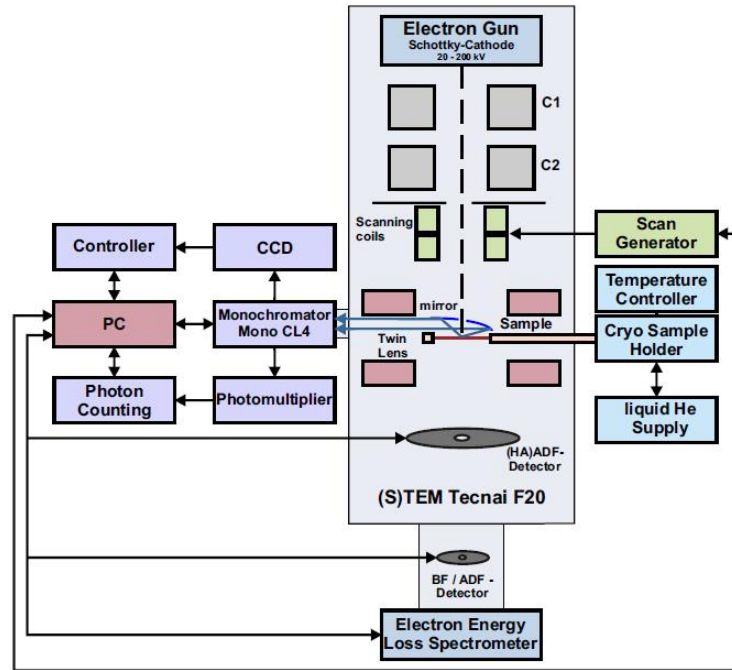
Figure 3.4. The actual image (left) and simplified schematics (b) of the low temperature (S)TEM-CL setup located in University of Magdeburg, Germany which is being utilized in order to study spatial features and defect distributions as well as their optical properties in our project as a collaboration at University of Magdeburg, Germany.

Exploration of the optical, and structural properties of the polar, nonpolar and semi-polar structures which are critical for LED performance is carried out mainly by optical measurements. Moreover, nature of extended defects (stacking faults) and their optical activity, their effects on optical transitions as well as transport properties of the LED device based on the abovementioned characterization techniques will be treated in the following chapters. The preliminary results are presented in Chapter 4, and the future work is discussed in Chapter 5.

83

3.6. Fabrication Processes

Mg *p*-dopant activation, mesa etching, metal deposition for *n*-type contacts followed by annealing, and finally *p*-type metal deposition are the main processes of LED fabrication. Normally, we form square mesa patterns (400×400 μm^2) using conventional photolithography technique followed by Ti/Al/Ni/Au (30/100/40/50 nm) metallization annealed at 860 °C for 60 seconds for *n*-type ohmic contacts, and semi-transparent 5 nm/5 nm thick Ni/Au with 40 nm/50 nm Ni/Au contact pads served as *p*-contacts. The mesa pattern is formed using mask aligner followed by dry etching in out inductively-coupled plasma (ICP) etching system. The metal deposition (Ti, Al, Ni, Au, etc.) is performed in an evaporator system. A rapid thermal annealing (RTA) system is utilized to anneal the contacts and also for *ex-situ* Mg dopant activation. Figure 3.5 demonstrates the image of the systems used for fabrication processes (photolithography, dry etching, metal deposition and annealing) in our lab.
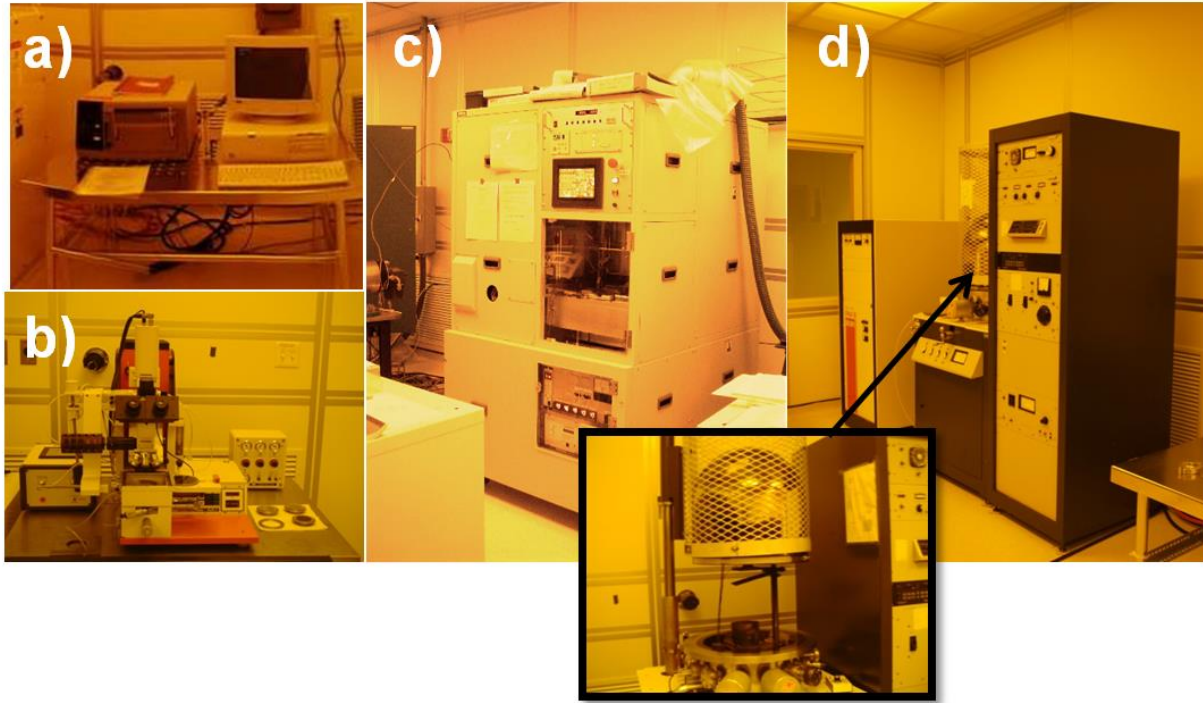
Figure 3.5. Images of (a) rapid thermal annealing (RTA) system, (b) mask aligner, (c) inductively coupled plasma (ICP) etching, and (d) e-beam evaporator systems which are utilized for the device fabrication at microelectronic materials and device laboratory (MMDL) cleanroom. The (d) inset in shows the opened evaporator chamber.

3.7. Electrical characterization

Some of the characterization methods including electroluminescence (EL), photo-current measurements have to be performed on the fabricated layers as they require electrical connections for carrier injection/detection. Relative and absolute external quantum efficiency (EQE) as a function of injection current can be obtained using integrated EL and will give us information about the efficiency peak, current density corresponding to peak EQE, and efficiency droop. Utilizing photocurrent setup as well as hall measurements will also be

85

informative when studying carrier transport properties as well as the effect of structural defects (mainly stacking faults) on electrical and optical properties of the layers.

Chapter 4

4. Conventional *c*-plane GaN-based light emitting diodes: Efficiency improvements and Challenges

4.1. Overview

As mentioned, the conventional *c*-plane GaN-based LEDs suffer from efficiency limitations mainly at long wavelengths (the green gap) and at high injection levels (efficiency droop). For the past couple of years, our group has been working on understanding the causes of efficiency degradations leading to novel structure designs for efficient blue InGaN LEDs. Application of stair-case electron injectors[76] (SEI) with optimized design[77] instead of electron blocking layer (EBL)[78] and compared with EBL in terms of hole distribution and efficiency,[79] and optimization of multi-double-heterostructures (DHs) in the active region design (number and size of DH widths)[80] are some of the previous works done in our group to improve efficiency of LEDs in terms of reduction in carrier spillover, improving carrier injection symmetry, and to enhance overall efficiency. In this chapter, we will demonstrate some studies performed to understand and methods applied for realization of efficiency improvements.

The Discussion will include understanding and estimation of carrier overflow as potential candidate for cause of efficiency droop (section 4.2), designs for reducing efficiency droop by improvement in carrier injection symmetry (Section 4.3), and methods to enhance indium

87

incorporation efficiency by minimizing compressive strain in InGaN layers (section 4.4). At the end, the limitations and alternatives (section 4.5) for the LEDs on conventional *c*-plane GaN substrates will be briefly pointed out.

Despite of the improvements for conventional *c*-plane LEDs that will be demonstrated in this chapter, the abovementioned limitations are still significantly affecting device performance. Alternatively, nonpolar (Chapter 5) and semipolar (Chapter 6 and 7) structures will be presented in next chapters as candidate for high efficiency LEDs at green due to eliminated/reduced polarization-induced QCSE.

4.2. Estimation of carrier spillover from photocurrent measurements

4.2.1. Overview

As mentioned above, recently, we have tried to take some steps toward improving LED efficiency especially at high injection levels by better understanding of the mechanisms behind efficiency droop. Different mechanisms such as Auger recombination,[81] electron overflow,[82]–[84] carrier delocalization and nonradiative recombination at defects,[85], [86] junction heating effects,[87] have been proposed to be responsible for this efficiency loss. However, among these proposed mechanisms, carrier overflow is considered to be one of the most possible one. Carrier escape from the active region of devices in forward bias is known as carrier overflow (or also called carrier spillover). In reverse bias, however, it is termed as carrier

leakage. Calculation of carrier overflow from band structure simulation had already been reported in our group.[77] In this section, we demonstrate quantifications of the carrier leakage as well as correlation of the information derived from carrier leakage to carrier overflow for InGaN LEDs with quad (4x) double heterostructure (DH) active regions and various electron injector thicknesses.[88] The work presented in this section was leaded by Dr. Fan Zhang and Dr. Shopan Hafiz and I was mainly involved in MOCVD growth of the layers.

4.2.2. Experimental Details

As shown in Figure 4.1, the active region for all the structures used in this investigation was composed of four 3nm-thick $In_{0.15}Ga_{0.85}N$ active regions separated by 3nm $In_{0.06}Ga_{0.94}N$ barriers (quad 3 nm DH). A Si-doped (2×10^{18} cm^{-3}) $In_{0.01}Ga_{0.99}N$ underlying layer with designed thickness of 60nm was grown beneath the active regions for the sake of improving the quality of the overgrown layers. All the structures utilize a staircase electron injector (SEI) structure to enhance the efficiency of thermalization of hot carriers before reaching the active region. The SEI consists of two InGaN layers with each 30nm (Figure 4.1(a)), 20nm (Figure 4.1(b)), and 4nm (Figure 4.1(c)) widths with 4% and 8% Indium compositions inserted below the active layers in the given order. The LED structures were capped with Mg-doped p-GaN layer with 100-nm thickness and hole density of 4×10^{17} cm^{-3}, as determined by Hall measurements on a separate sample grown as calibration.
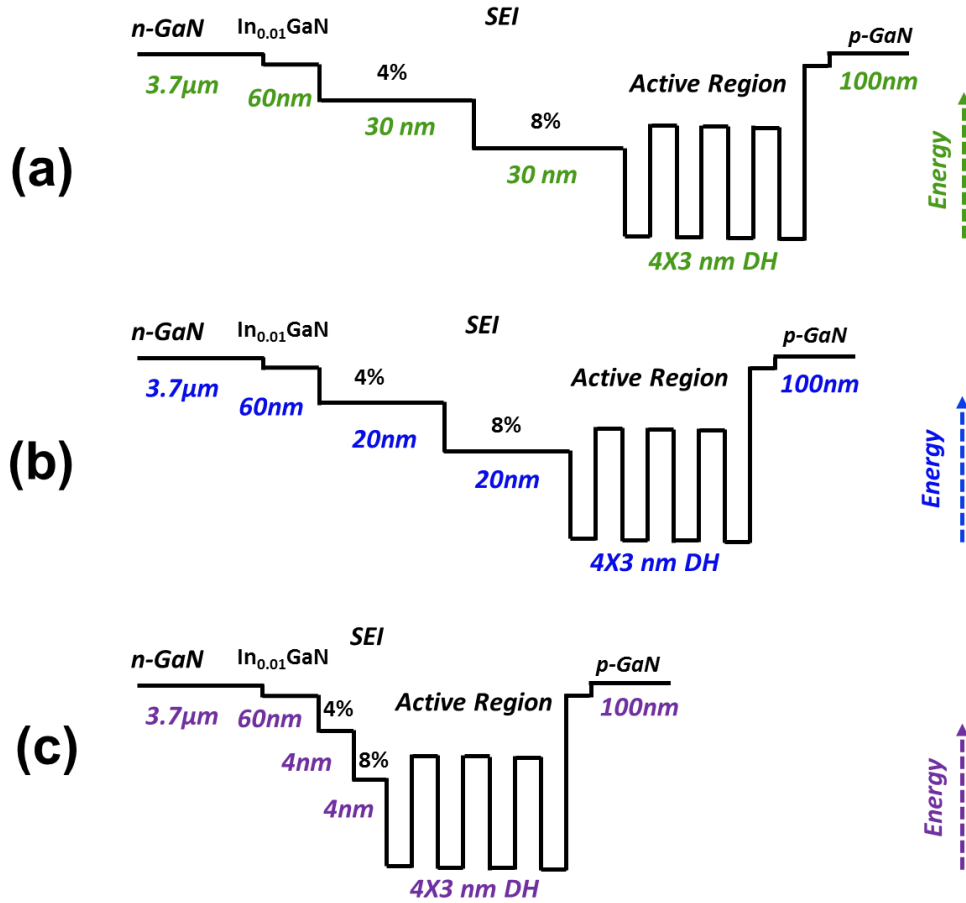
Figure 4.1. Flat band conduction band schematic of the InGaN 4×3nm DH LEDs with two step 30nm (a), 20nm (b), and 4nm (c) stair-case electron injectors (SEI) employed for estimation of carrier leakage from photo-current measurements.

For devices, square mesa patterns (400×400 μm^2) were formed by conventional lithography and chlorine-based inductively coupled plasma (ICP) etching. For *n*-type ohmic contacts Ti/Al/Ni/Au (30/100/40/50 nm) metallization annealed at 800°C for 60 s, and for the semi-transparent *p*-contact Ni/Au electrodes (5 nm/5 nm) was used (see Figure of the equipment in section 3.5). At last, 40/50 nm Ni/Au electrodes were deposited on part of the mesas as contact pads.

4.2.3. Experimental Results and Discussions

I-V measurements for the three LED structures were performed with and without CW HeCd (wavelength 325 nm) laser excitation. No significant variation was observed for multiple devices measured across each LED sample. According to the plots in Figure 4.2(a) which demonstrates the representative data from all the devices measured, reverse current increases as the excitation density increases from 0 to 280 Wcm^{-2}. This can be due to increased photo-current (as a result of carrier leakage). Thus, the rate of carrier leakage was calculated based on photo-current measurements. The injected carrier rate, on the other hand, was calculated using absorption and minority carrier diffusion profile of top *p*-GaN layer. The carrier escape (leakage) to generation rate ratio as a function of reverse bias voltage is plotted in Figure 4.2(b) for various excitation densities and for the three structures with schematics demonstrated in Figure 4.1. For identical bias voltage and excitation density, the percentage of carrier leakage increases with the increase of the SEI thickness. At -3V bias voltage and optical excitation density of 280 Wcm^{-2}, for instance, carrier leakage percentile increased from 24 % to 55 % when SEI thickness was increased from 4 nm + 4 nm to 30 nm + 30 nm.
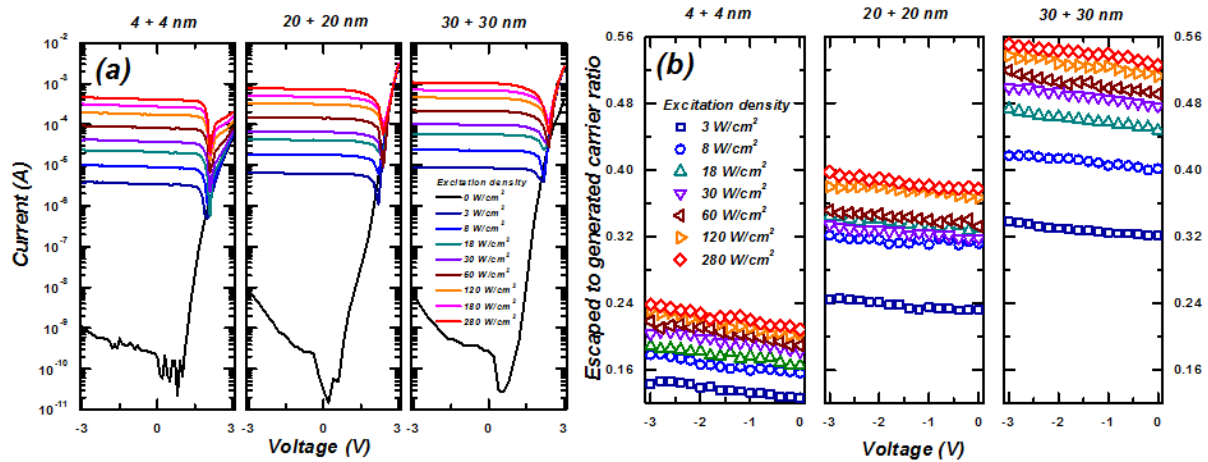
Figure 4.2. I-V measurements for structures under study in this subsection at different optical excitation densities (a) and the carrier leakage percentile (that is derived using escaped to generated carrier ratio) (b) for the layers with various SEI thicknesses.

In order to have explanation for the observed increase in carrier leakage with increasing SEI thickness, we performed energy band structures simulation using Silvaco Atlas. As shown in Figure 4.3, by increasing the SEI thicknesses from 4 + 4 nm to 30 + 30 nm, the effective barrier that opposes the escape of photo-generated carriers from the active region reduces by 346 meV assuming that carriers are thermalized in the last active layer.

92
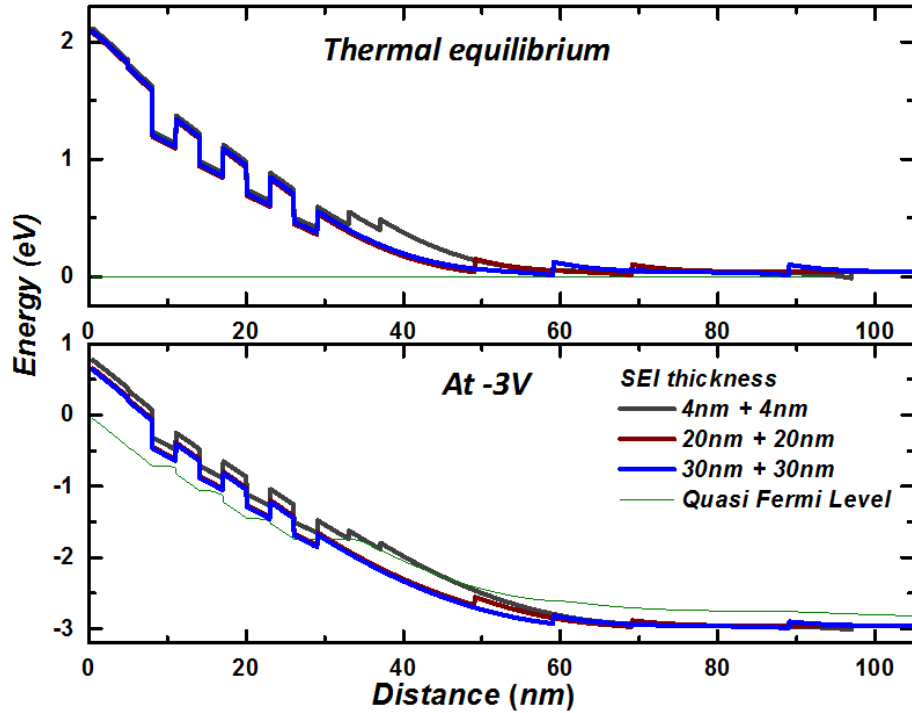
Figure 4.3. Simulated conduction band structure and position of quasi Fermi level for the LED structures with various SEI designs under thermal equilibrium (top) and under 3V reverse bias (bottom).

There are two main mechanisms responsible for electron overflow (spillover) in semiconductor heterostructures. The first mechanism is thermionic emission of electrons that are thermalized in the active region over the barrier into the *p*-layer and the second one is the ballistic and quasi-ballistic transport of the electrons injected across the active region. Contribution of the first mechanism to the electron overflow is very small in the InGaN system owing to the large band discontinuities[76] and thus, ballistic and quasi-ballistic transport (the second mechanism) of hot electrons (non-equilibrium electrons) will be the dominating factor in estimation of electron overflow.

Hot electrons escape from recombination in the active region passing from *n*-GaN to *p*-GaN under forward bias. Under reverse bias, the LED structures were illuminated with HeCd

excitation (325nm excitation wavelength). This resulted in generation of electron-hole pairs both in the active region and throughout the whole structure depending on the penetration depth (83 nm). Top *p*-GaN is the layer in which most of the carriers were generated and then electrons start to diffuse from *p*-GaN to *n*-GaN (diffusion length in *p*-GaN is 92 nm). Therefore, in reverse bias, the situation of carrier leakage is quite similar to carrier overflow in forward bias. As a result, the trend observed in this work *i.e.* the increase of carrier leakage with increasing SEI thickness will also be applicable for carrier overflow.

4.2.4. Conclusions

As a conclusion of this investigation, carrier leakage in InGaN LEDs with various electron injector designs (different thicknesses) was estimated from photocurrent measurements. Percentage of carrier leakage at -3V bias and 280 Wcm-2 optical excitation density increased from 24 % to 55 % by increasing SEI thickness from 4 nm + 4 nm to 30 nm + 30 nm. The photocurrent method is found to be applicable in estimation of carrier overflow in LEDs with different structural designs.

4.3. Improvement of carrier Injection symmetry and quantum efficiency of InGaN *c*-plane LEDs with Mg delta-doped barriers

4.3.1. Overview

As discussed earlier on mechanisms behind efficiency droop, one obvious cause of the efficiency rollover is the asymmetrical doping in GaN. Under electrical injection, this deficiency could result in an insufficient supply of holes to the active region. Since electron injection is typically much more efficient than hole injection, the radiative recombination cannot match with increasing carrier injection. This causes either carrier escape from the active region to *p*-GaN or accumulation in the active layers (which induces internal bias that opposes further carrier injection) both of which reduces radiative recombination efficiency. Moreover, in multi-well LEDs, as the wells near the *n*-type GaN contain relatively low density of holes owing to the poor hole transport, recombination mainly occurs in the wells adjacent to *p*-GaN.[89], [90] In order to address this issue, one may think of either increasing hole concentration in *p*-type GaN or *p*-type doping of the barriers in the multi-well systems.[84], [91]–[93] In case of applying the latter approach, there is a reduction in LED efficiency associated with the presence of Mg in the active region which has been manifested by diminishing band edge emission with increasing Mg content.[94]

In this section, we demonstrate Mg *p*-type δ-doping of the barriers with in order to improve the LED efficiency in which Mg was deposited in the middle of barrier growth while growth was interrupted.[95] This approach is helpful in reducing possible Mg diffusion into the

active layers which potentially reduce the deficiency associated with presence of Mg and improve the near band edge emission. The experimental data in this work are followed by results of numerical simulations of electron and hole concentrations in the active regions of LED structures. The work presented in this section was leaded by Dr. Fan Zhang and I was mainly involved in MOCVD growth, analysis and fabrications of the layers.

4.3.2. Experimental Details

Three InGaN LED structures emitting at ~430 nm on *c*-plane orientations were grown on *n*-type GaN/*c*-sapphire with 4 µm-thickness utilizing our MOCVD system (see section 3.3 for more information about growth technique). Two step SEI with each step 15nm-thick and 4% and 8% indium contents is grown underneath the active region to efficiently cool the injected hot electrons as mentioned in previous subsection.[10], [77] Similar to the structures presented in the last subsection, a 60-nm *n*-type (2×10^{18} cm^{-3}) In$_{0.01}$Ga$_{0.99}$N as underlying layer was situated beneath the SEI to reduce the probability of strain relaxation in the active region due to its compliance action owing to its softer lattice compared to GaN. As demonstrated in Figure 4.4, all three LED structures contain hex (6x) 3-nm In$_{0.15}$Ga$_{0.85}$N double heterostructure (DH) active regions separated by In$_{0.06}$Ga$_{0.94}$N barriers. The barriers are designed to have relatively low height to help with the hole transport across the active region. The first two barriers close to *n*-type GaN are 6 nm-thick while the remaining ones are designed as 3 nm-thick. The Mg δ-doping was applied in two of the LED structures in either one or both of the 6 nm-thick barriers. The third and last LED sample (reference), on the other hand, was grown without any Mg doping in the barriers. The first two barriers that are located closest to *n*-GaN layer were designed to be

96

thicker than the others to avoid possible out-diffusion of Mg from the *p*-type doped barriers into the active regions and thus reducing the LED efficiency.
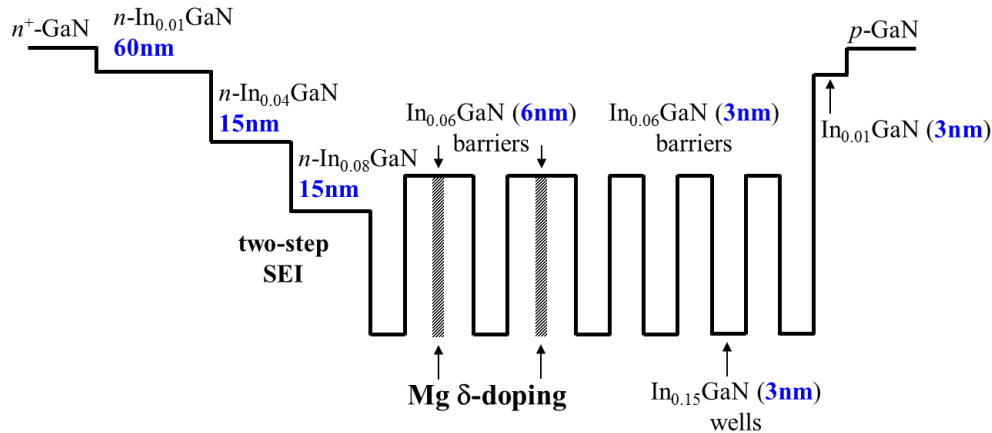
Figure 4.4. The flat-band conduction band schematic of 6×3 nm (hex 3nm) DH LEDs indicating the position at which Mg delta doping is applied for either only the first or the first two nearest barriers to the *n*-GaN layer (6nm-thick $In_{0.06}Ga_{0.94}N$). The rest of the barriers are kept 3nm thick and are unintentionally doped. A reference sample without any δ-doped barriers is used as comparison. [Reprinted with Permission from Ref.[95]]

The *p*-type δ-doping with Mg was implemented as follows: the growth was interrupted after the deposition of 3 nm of the 6 nm-thick barrier was finished and the Cp2Mg source (as Mg precursor) was supplied to the reaction chamber for 20 seconds with flow rate of 100 sccm, followed by the growth of the rest of the barrier layer keeping the same growth conditions as the rest of the barriers. The hole concentration of $4\times10^{17}cm^{-3}$ in the doped barrier was estimated based on Hall measurements performed on separate δ-doped *p*-GaN thin film samples grown using identical growth conditions. No significant degradation of the optical performance of the LEDs with Mg δ-doped barriers as compared to the reference sample (without Mg δ-doped barriers) was observed from photoluminescence measurements performed under resonant excitation of the InGaN active regions[10] which reveals insignificant Mg out-diffusion to the

97

active region wells in amounts detrimental for the LED performance. Thereafter, Mg-doped *p*-GaN layers with thickness of 100 nm and hole concentration of 6×10^{17} cm^{-3} was grown on top of the structures. Here again, the hole concentration is determined from Hall measurements performed on separate samples having identical experimental conditions.

Similar to the experiment demonstrated in previous subsection, for this experiment, again we formed square mesa patterns (400×400 μm^2) using conventional photolithography technique. Ti/Al/Ni/Au (30/100/40/50 nm) metallization annealed at 860 °C for 60 seconds was used for *n*-type ohmic contacts, and semi-transparent 5 nm/5 nm thick Ni/Au with 40 nm/50 nm Ni/Au contact pads served as *p*-contacts.

4.3.3. Simulation Results and Discussions

Electron and hole distributions were simulated using the Silvaco to verify the effectiveness of Mg δ-doping of barriers in improving hole injection. The simulation parameters appropriate for nitride material system was used for this calculation; Shockley-Read-Hall recombination coefficient $A = 10^7 s^{-1}$, bimolecular recombination coefficient $B = 10^{-10} cm^{-3} s^{-1}$, Auger recombination coefficient $C = 10^{-30} cm^{-6} s^{-1}$, electron and hole motilities are assumed to be 250 and 5 cm^2 /V s, respectively, determined from measurements on separate samples, and polarization charge assumed to be 40% of the theoretical value.[79] Figure 4.5(a) illustrates the electron distribution in the active layers of all three mentioned LED structures under injection current density of 35 A/cm^2. As manifested in the figure, the distribution of electrons is relatively uniform in the reference LED as a result of efficient cooling of the injected electrons in the SEI. Moreover, it can be inferred from the simulation results that δ-doping of barriers does not have significant effect on the distribution of electrons while it increases substantially the hole

98

concentrations in the wells near the *n*-side in the active regions, as demonstrated in Figure 4.5(b) and discussed below.
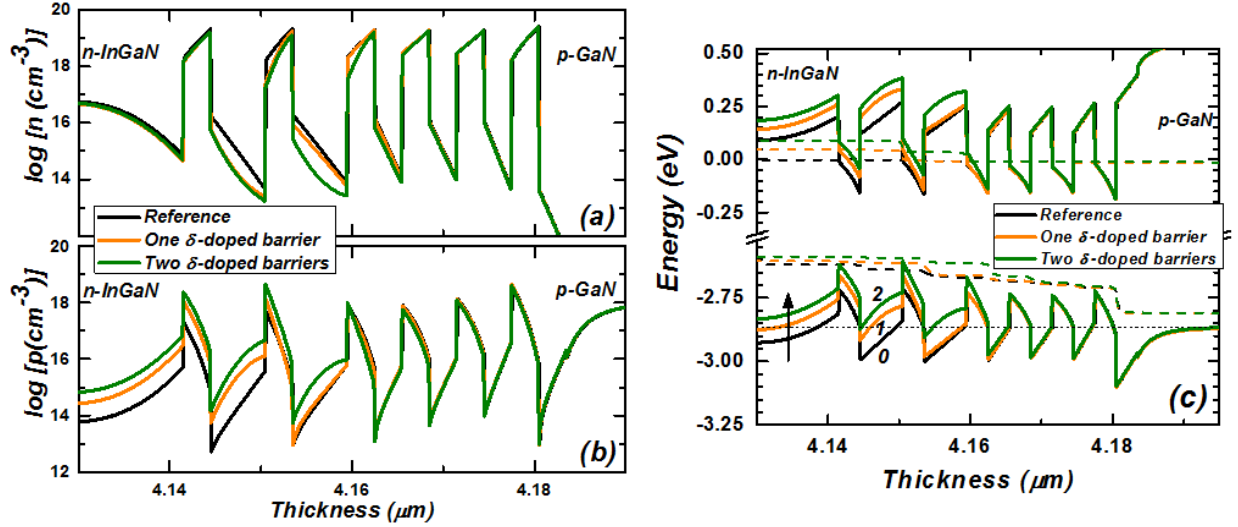
Figure 4.5. Numerical simulation results for Electron (a) and hole concentrations (b) (in logarithmic scale) and the energy band structures (c) for the reference LED (black, curve 0) and LEDs with one (orange, curve 1) or two (green, curve 2) Mg δ-doped barriers at an injected current density of 35 A/cm^2 using SILVACO ATLAS. The dashed lines in (c) show the quasi-Fermi levels. Left side of the figures are *n*-InGaN with 15 + 15 nm-thick SEI. The horizontal dotted line in (c) indicates the energy corresponding to the valence band maximum in *p*-type GaN.

Owing to their relatively large effective mass and low mobility, holes transport deeper into the active region is impeded. Thus, even without considering hot electron overflow, radiative recombination is limited by the density of holes, as the minority carriers in the active region under bias. Under these conditions, as indicated in Figure 4.5(b), the hole distribution across the active region for the reference sample is very non-uniform. The holes seem to be more populated in the InGaN well closest to *p*-GaN, and the concentration decreases rapidly towards the *n*-side of the structure. Therefore, for structures with multi-well active region designs, electron and hole recombination happens mainly in the active layers adjacent to *p*-GaN. The rest

99

of the active region, however, lacks enough number of holes to have efficient recombination with the existing electrons. Mg δ-doping of the barrier closest to *n*-GaN greatly enhances the hole concentration in the nearby active regions (by nearly one order of magnitude) [Figure 4.5(b)], and thus reducing substantially the asymmetry of electron and hole concentrations and improving the recombination efficiency as a result.

For the structure that includes two δ-doped barriers, the further enhancement of hole concentration in the active layers near *n*-GaN can be observed [Figure 4.5(b)], in particular in the second well closest to *n*-GaN resulting in further improvement in LED output power. In addition, δ-doping of barriers near the *n*-side of LEDs introduces band bending that provides more favorable hole transport across the active region. The simulated energy band structure for the three LED structures at a current density of 35 A/cm^2 (see Figure 4.5(c)) indicates the effect of δ-doping of the InGaN barriers closest to *n*-GaN on reduction of the effective barrier height for holes. According to the simulation results demonstrated in Figure 4.5(c), the effective barrier height for the holes with respect to the valence band maximum drops from 120 meV in the reference LED to 50 meV in the single barrier doped sample and further to -10 meV for the sample with first and the second barrier doped. At higher injection current density of 100 A/cm^2 (not shown), the effective barrier height reduces down to -40 meV and -80 meV for LEDs with one and two δ-doped barriers, respectively, while the corresponding value for the reference LED is as high as 70 meV.

4.3.4. Experimental Results and Discussions

To experimentally illustrate the effect of *p*-type Mg δ-doping of InGaN barriers on LED performance, we performed electroluminescence (EL) measurements on the samples under

100

pulsed excitation with 0.1% duty cycle to eliminate heating effects. The results of EL intensities and relative external quantum efficiencies (EQEs) are demonstrated in Figure 4.6(a). It can be clearly observed in the plots shown in Figure 4.6(a) that layers with δ-doped barriers exhibit higher integrated EL intensities at high current injection levels (>50 A/cm^2), indicating no significant material degradation as a result of Mg out-diffusion and incorporation to the active regions compared to the reference structure. The peak relative EQE for the LED with single δ-doped barrier is about 20% higher than that for the reference LED structure (see Figure 4.6(b)). However, the δ-doping of the second barrier in addition to the first one adjacent to the *n*-side of the structure did not result in a significant enhancement of the peak EQE. This can be due to slight degradation of the active region quality caused by increase in the amount of Mg incorporated into the structure which partially negates an additional improvement resulting from enhancement of hole injection induced by δ-doping of the barrier. It is noteworthy to mention that LEDs with δ-doped barriers exhibit lower efficiency degradation percentile (14% at 400 A/cm^2) with increasing injection level compared to the reference LED (23% at 400 A/cm^2). Moreover, the EQE roll over for the δ-doped barrier LEDs occurs at higher injection current densities (120 A/cm^2) compared to that for the reference structure (80 A/cm^2). For a given active region design of a LED, the more the roll-over current density, the more improved is the hole supply and injection symmetry. This is due to the fact that the electrons start to escape from the active region when hole injection cannot keep up with the electron supply and thus causing the reduction in the LED efficiency. After all, these findings suggest that, in addition to enhancement of the peak EQE, improved hole injection and thus carrier injection symmetry partly suppresses the efficiency degradation at high injection levels.

101
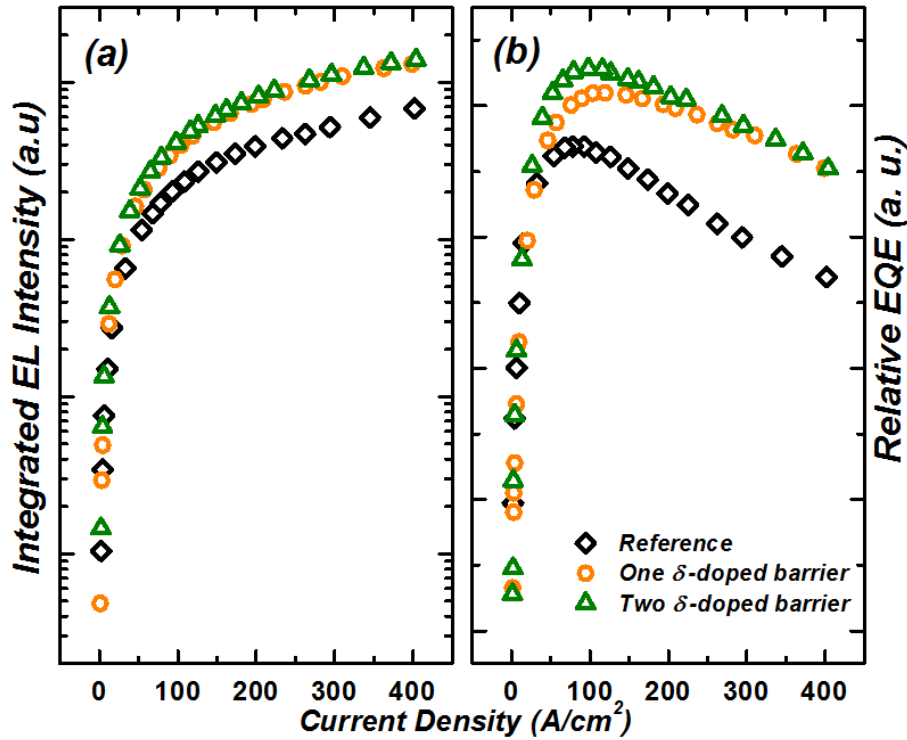
Figure 4.6. Integrated EL intensities (a) and the relative EQE (b) as a function of injected current density for the three LEDs under investigations in this study.

4.3.5. Summary and Conclusions

As a conclusion to the presented work in this subsection, the *p*-type δ-doping of barriers with Mg significantly improves the quantum efficiency of LEDs with multi-well active region designs. The improvement of 20% in EQE for the barrier doped samples compared with the reference structure which is supported by numerical simulation results is found to be due to enhanced hole injection and more symmetrical carrier injection to the active regions. However, Mg delta doping of an additional barrier on the *n*-GaN side induces only a small increase in the peak EQE in contrast to the simulation results. Seemingly, the slight degradation of the active region quality induced by more incorporation of Mg in case of structure with dual δ-doped

102

barrier partially negates the additional improvement expected as a result of enhanced hole injection.

4.4. Enhancement of indium incorporation to InGaN MQWs on AlN/GaN periodic multilayers

4.4.1. Overview

One promising approach to improve the In incorporation and thus efficiency of long wavelength InGaN emitters is tailoring strain in InGaN heterostructures through modification of in-plane lattice parameter of buffer layers for strain-compensation and/or enhanced indium incorporation efficiency. Application of GaN buffer layer under tensile strain reduces the total strain of the structure and thus improve radiative recombination efficiency of the InGaN active layers while the situation is opposite in case of compressively-strained GaN under-layer. On the other hand, amount and sign of strain in InGaN heterostructures has a strong effect on indium incorporation; tensile strain enhances while compressive strain reduces the incorporation efficiency.[96], [97] Even though increase in compressive strain could significantly improve performances for certain applications[98], in light emitting devices the increase in compressive strain reduces indium incorporation and enhance polarization-induced QCSE at the same time.[97], [99] Strain re-laxations, on the other hand, improves the indium incorporation efficiency but at the expense of reduced radiative recombination efficiency due to defect generation.

103

In this section, we explore the effect the strain in underlying layer on indium incorporation and polarization-induced QCSE in InGaN multi-quantum well (MQW) active regions.[100] We also demonstrate that a variety of emission wavelengths, from purple to green, can be achieved by modifying only amount of strain in the templates.

4.4.2. Experimental Details

The structures were grown using our MOCVD system (see section 3.3 for more information about growth technique). In this work, InGaN active regions were grown concurrently on the same holder on strained 10-pair AlN/GaN periodic multilayers and GaN templates, which were prepared by *in situ* epitaxial later overgrowth through SiNx nanoporous mask[101], [102]. The GaN and the multilayer templates were located at the same radial positions to avoid any possibility of radial temperature non-uniformity affecting indium incorporation and to ensure fair comparison of indium incorporations. For these experiments, we used two different AlN/GaN templates with different strain conditions (see Figure 4.7): (1) periodic multilayer 1 (ML_1) composed of 14-nm AlN and 4.5-nm GaN and (2) multilayer 2 (ML_1) composed of 14-nm AlN and 2.5-nm GaN. The InGaN active regions consisted of ten 3-nm $In_{0.15}Ga_{0.85}N$ QWs separated by 8-nm $In_{0.02}Ga_{0.98}N$ barriers (the indicated compositions are nominal) have been grown side by side on the relaxed GaN and strained ML templates in two separate growth runs. Thus, 4 samples were involved into this investigations; the active regions of samples A and C were grown at substrate temperature of 810ºC on relaxed GaN and strained ML_1, respectively, while samples B and D were deposited at substrate temperature of 790ºC on relaxed GaN and strained ML_2 (See Table 4.1). The schematics of the structures are shown in Figure 4.7.

104
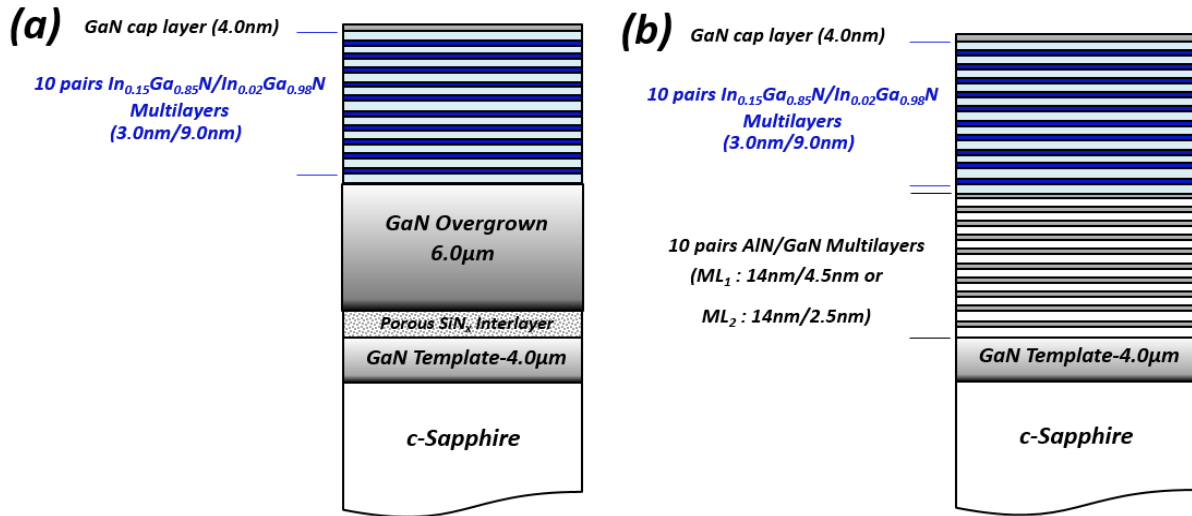
Figure 4.7. (Color online) Schematics of the InGaN multi-quantum wells structures with nominal compositions grown on (a) relaxed GaN and (b) strained AlN/GaN multilayers.[100]

Table 4.1. Descriptions of samples used for studying the effect of strain on indium incorporation efficiency.[100]

Sample	Substrate	AlN/GaN Thicknesses in MLs	InGaN Growth Temperature
A	Relaxed GaN	--	810 ºC
B	Relaxed GaN	--	790 ºC
C	ML_1 (10 pairs)	14nm/4.5nm	810 ºC
D	ML_2 (10 pairs)	14nm/2.5nm	790 ºC

High resolution X-ray diffractometry (XRD) was utilized to evaluate the interface quality and to verify layer thicknesses in the AlN/GaN periodic multilayers and determine the degree of relaxation of GaN layers. The surface morphologies of the periodic multilayer templates were studied using atomic forced microscopy (AFM). The optical properties of the InGaN active layers were characterized using steady-state photoluminescence (PL) and time-resolved photoluminescence (TRPL) using a frequency doubled Ti-sapphire laser with 150 fs pulse width

105

and period of 12.5 ns as an excitation source. A Hamamatsu streak camera was used for the TRPL measurements and to study the temporal evolution of emission lines and the QCSE induced shift in the emission wavelengths. The peak positions of the PL emission lines at the highest excitation (immediately after the pulsed excitation in time-dependent PL measurements) were used to assess the actual indium contents in the QWs.

4.4.3. Determination of Strain

The ω-2θ HRXRD scans (see Figure 4.8) reveal multiple satellite peaks indicating smooth interfaces between the AlN and GaN multilayers. The ML period defined as $t_{AlN} + t_{GaN}$, (where t_{AlN} and t_{GaN} represent respectively the thickness of AlN and GaN) was found to be about 18.5nm and 16.5nm for ML_1 and ML_2 structures, respectively. The thicknesses of individual AlN and GaN were determined by fitting simulated HRXRD patterns to the measured ones. The results of simulations also indicate that the degree of relaxation of AlN and GaN layers are 100% and 60%, respectively, in ML_1 (Figure 4.8 (b)) and are 100% and 0.0% in ML_2 (Figure 4.8 (c)).
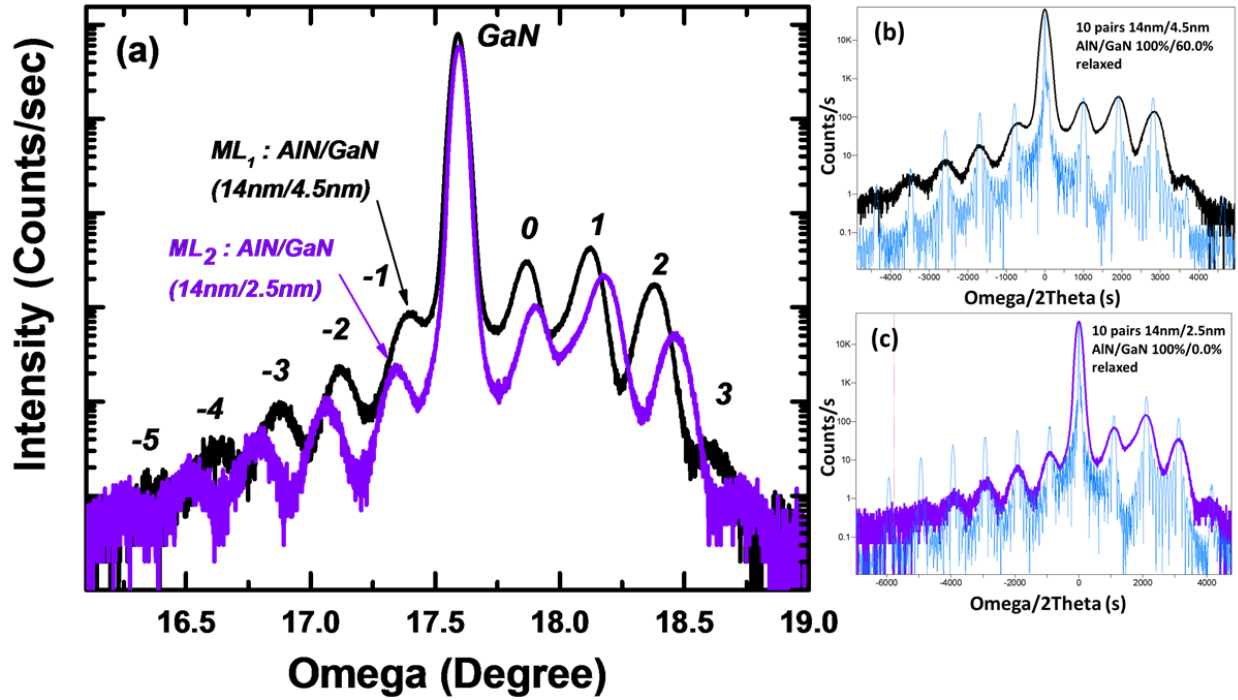
Figure 4.8. (Color online) (a) Measured ω-2θ HRXRD patterns from both AlN/GaN periodic multilayers used in this study. Large number of satellite peaks is indicative of relatively smooth interfaces between the AlN and GaN layers. The simulation results and fitting curves for the structure ML$_1$ (b) ML$_2$ (c) indicate degree of relaxation of 100%/60% and 100%/0.0% for AlN/GaN in ML$_1$ and ML$_2$, respectively.[100]

The in-plane lattice parameters, a, and amount of strain in GaN layers in the multilayers were calculated [103] using the degrees of relaxation (R) obtained from the analysis of HRXRD patterns under assumption that the degree of relaxation in 14-nm AlN layers is 100%

$$R = \frac{a - a_s}{a_l - a_s} \times 100\%$$

(4.1)

where a_{AlN}, a_{GaN}^{b}, and a_{GaN}^{f} are the in-plane lattice constants of AlN acting as a substrate for thin GaN layers, bulk GaN, and measured in-plane lattice constants of the layer (GaN), respectively. Therefore, strain in GaN layers can be calculated as follows [103], [104]

107

$$\varepsilon = \frac{a - a_l}{a_l} \times 100\% \qquad (4.2)$$

The calculated values of strain in the periodic multilayer structures as well as the GaN template are summarized in Table 4.2.

Table 4.2. Calculated strain for the relaxed GaN and AlN/GaN multilayers.[100]

Structure Design	GaN Relaxation	Strain
Relaxed GaN	100.0%	0.0%
ML_1 (10 pairs)	60.0%	1.11%
ML_2 (10 pairs)	0.0%	2.78%

4.4.4. Surface Morphologies

The AFM images of ML_1 and ML_2 layers are shown in Figure 4.9. The surface of both multilayers are found to contain micro-cracks and some surface undulations. The structure with thinner GaN thickness (ML_2) exhibits smoother surface morphology despite having weaker satellite peaks in XRD data in Figure 4.8. The weaker satellite peaks in ML_2 could also be due to thinner GaN layers compared to that in ML_1 structure.
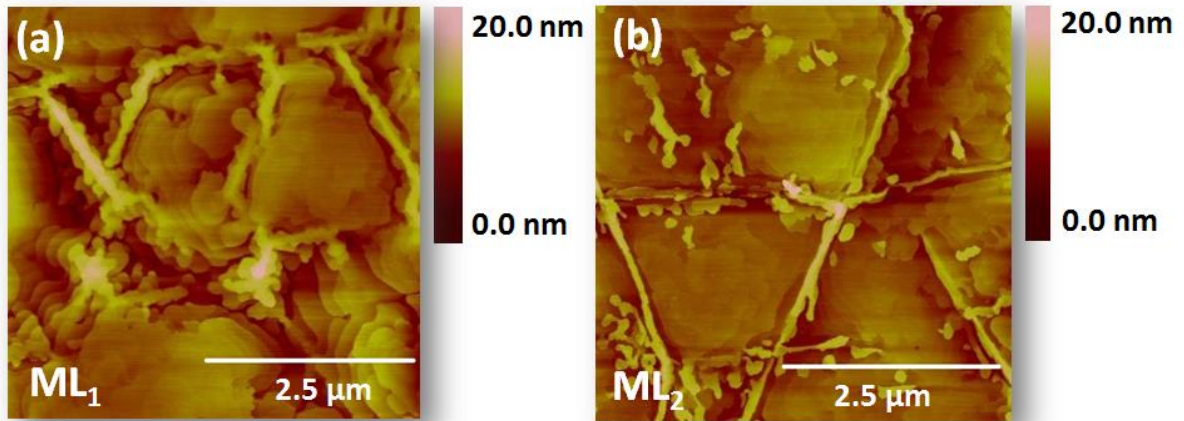
The origin of the surface undulations in the periodic multilayer structures may also be related to strain relaxations. On the other hand, the surface undulation by itself will facilitate strain relaxations in the overgrown InGaN MQWs for samples C and D. In this case, the relieve of compressive strain in InGaN layers should enhance the indium incorporation according to the published data reporting the negative effect of compressive strain on indium incorporation [96], [97], [99]

4.4.5. Optical Properties

Room temperature PL spectra from the InGaN MQWs structures grown on relaxed (samples A and B) and compressively strained (samples C and D) templates are shown in Figure 4.10 (a). It worth to restate here that the active regions of A and C structures are grown at 20ºC higher substrate temperatures (810 ºC) compared to those of B and D (790 ºC). Thus, the difference in observed PL peak positions for samples A and B is related to the difference in substrate

temperatures. Nevertheless, the data clearly show longer emission wavelengths for the structures grown on AlN/GaN multilayers (C and D) compared to the ones on relaxed GaN (A and B). Moreover, significantly longer emission wavelength for sample D with thinner GaN layers in the multilayer template compared to sample C (2.5 nm vs. 4.5 nm) can be attributed to higher value of strain in the GaN causing deeper strain relaxation in InGaN layers. Another interesting finding is the comparable integrated PL intensities from InGaN MQWs of different emission wavelength on strained periodic multilayers and GaN templates. Figure 4.10 (b) shows selected emissions from the InGaN active regions of the samples in this study. Interestingly the layer emissions cover a wide wavelength range from purple to green. It is intriguing to see that using modification in mainly strain (with only 20 ºC change in substrate temperature in InGaN growth stages), one can obtain light emission in variety of wavelengths from purple to green.
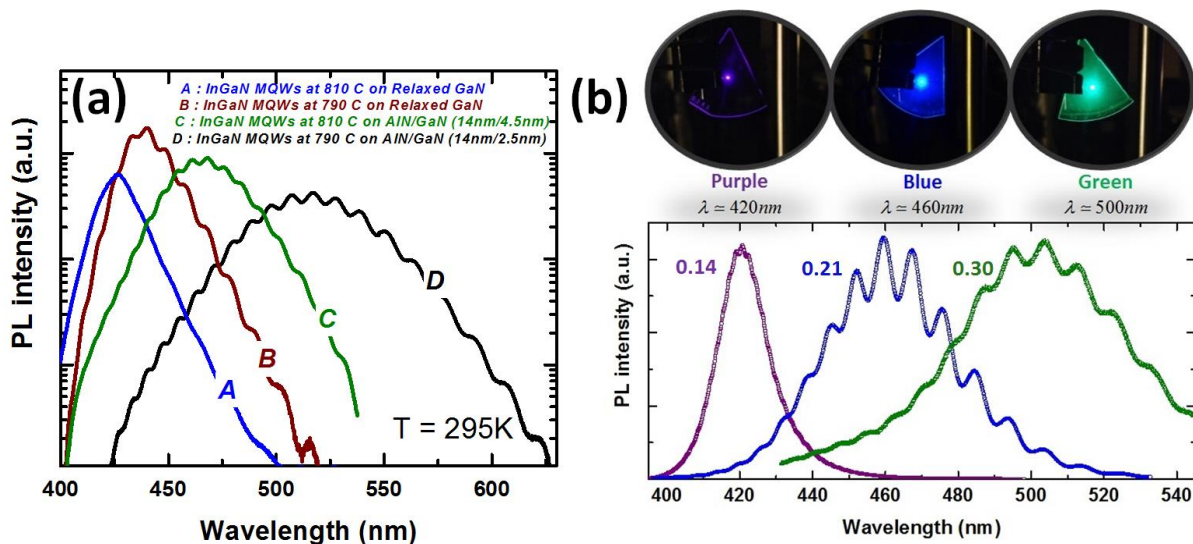
Figure 4.10. (Color online) Room temperature photoluminescence (PL) comparison from InGaN MQWs grown on GaN (A and B) and AlN/GaN multilayers (C and D). The thicknesses of GaN in the multilayer are 4.5nm (C) and 2.5nm (D). (b) Selected normalized PL spectra for $In_xGa_{1-x}N$ QWs with 0.14, 0.21, and 0.30 InN molar fractions obtained mainly by modifying strain relaxations using AlN/GaN MLs.[100]

110

Room temperature PL transients integrated over active region emission for the structures under investigation are displayed in Figure 4.11. The data indicate single exponential decay for InGaN MQWs grown on relaxed GaN templates (samples A and B), while the decay is bi-exponential for the structures grown on MLs (samples C and D). The longer decay times for the layers C and D compared to A and B can be attributed to larger spatial separation of electrons and holes wave function for the active regions with higher indium content. The double exponentional decay behavior for InGaN MQWs on MLs (C and D) can be attributed to presence of localization sites with different indium contents while the indium distribution is uniform in the MQWs grown on the smooth GaN templates. This observation is in agreement with the dot-like surface morphologies revealed by the AFM for the active regions grown on the periodic multilayer templates (not shown).

111
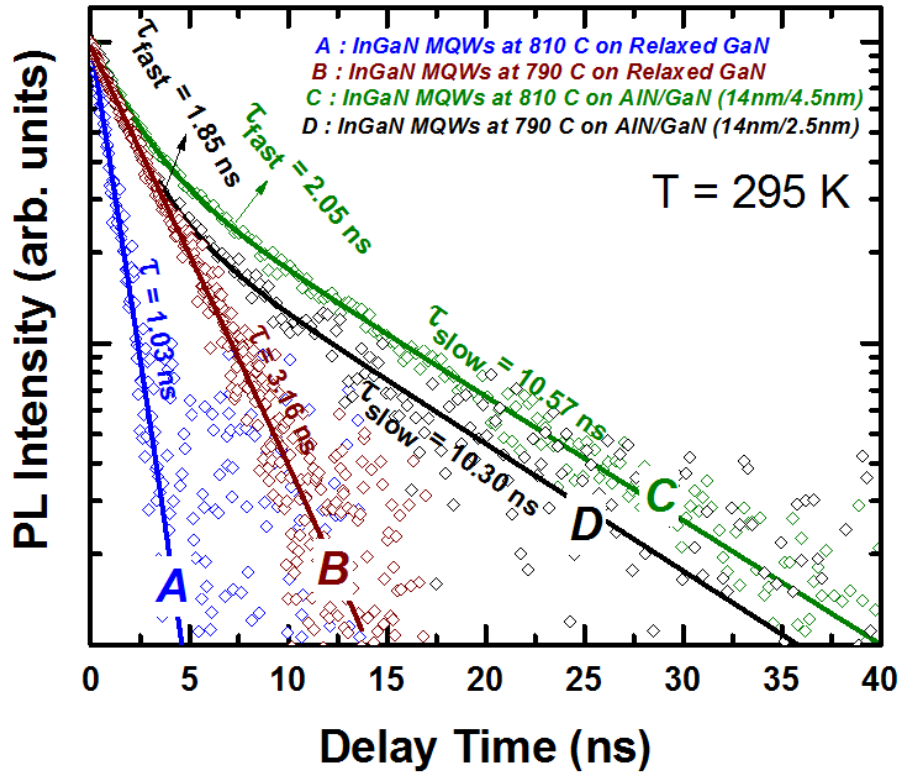
Figure 4.11. (Color online) Room temperature PL transient (integrated over active region emission) comparison of InGaN multi-quantum well structures grown on GaN (A and B) and AlN/GaN multilayers (C and D). The solid lines indicate the single exponential (A and B) and bi-exponential (C and D) fitting of the data. The thicknesses of GaN in the multilayer structures are 4.5nm (for layer C on ML_1) and 2.5nm (for layer D on ML_2).[100]

4.4.6. Determination of Indium Contents

While the effect of strain on InGaN growth rate was found to be negligible based on HRXRD data, there are two main parameters contributing to the large difference in PL emission wavelengths: strain induced enhanced band bending and corresponding shift in the emission wavelength and increased indium incorporation. Therefore, a reliable separation of these contributions is imperative for the correct interpretation of the experimental findings.

In order to evaluate the above-mentioned contributions to the observed emission wavelengths, we performed ultra-fast optical spectroscopy on the layers using pulsed excitation and compared the emission wavelengths at pulse arrival and when photo-excited carrier concentration was significantly reduced through carrier recombination. For the used excitation power density and pulse width, the estimated density of photo-generated carriers at the peak is $n = 4.54 \times 10^{19} cm^{-3}$ which results in complete screening of the polarization induced electric field. With time, the carrier density reduces due to recombination and thus, the screening effect gradually vanishes. As a result, the band bending and associated separation of electron and hole wavefunctions increase. Therefore, time evolution of PL spectra allows one to isolate the contribution to the redshift of emission lines associated with the presense of the polarization field. Figure 4.12 compares the 300-K PL spectra recorded for the highest and the lowest photo-excited carrier concentrations for all the samples investigated. The structures grown on MLs (samples C and D) exhibit significantly larger red shifts (ΔE) with reducing photo-generated carrier density compared to the structures on the relaxed GaN templates (samples A and B).
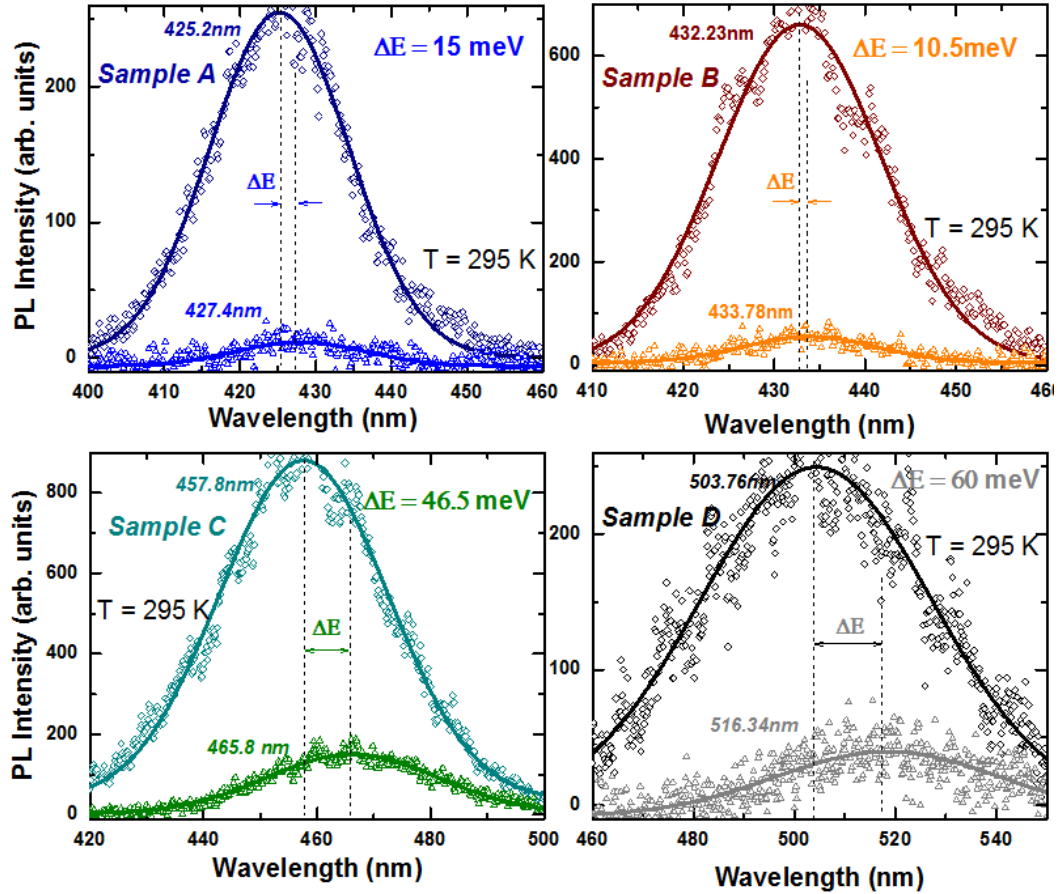
Figure 4.12. Room temperature PL spectra for the highest and the lowest photo-generated carrier density in InGaN MQWs on relaxed GaN (A and B) and AlN/GaN MLs (C on ML$_1$ and D on ML$_2$) recorded using ultra-fast optical spectroscopy. The PL spectrum tends to shift to longer wavelengths with increasing the delay time. This shift is much more pronounced for MQWs on MLs (C and D) compared to those on relaxed GaN (A and B).[100]

The average indium compositions in InGaN active regions were determined from the PL peak positions at the highest photo-generated carrier concentrations, which eliminated the contribution from the internal electric field. Considering the quantum confinement, the PL emission energy can be written as

$$E_{PL} = E_g^{InGaN}(x) + E_{Confinement} \qquad (4.3)$$

Where E_{PL} denotes the MQW PL peak emission energy, and $E_g^{InGaN}(x)$ is the InGaN bandgap calculated using[105], [106]

$$E_g^{InGaN}(x) = xE_g^{InN} + (1-x)E_g^{GaN} - bx(1-x) \qquad (4.4)$$

Where b is the bowing parameter, E_g^{InN} and E_g^{GaN} are the room temperature bandgaps for InN and GaN, respectively. The bowing parameter (b) is assumed to be dependent on indium content as predicted by Moses et al.[107] The bandgap values of 0.7 eV [108] and 3.42 eV [104] were used in the calculation for InN and GaN, respectively. The confinement component of the PL emission energy ($E_{Confinement}$) can be found considering solution for ground state energy of electrons and heavy holes in a finite rectangular potential well having width of $L = 3.0nm$.[109]

The calculated indium concentrations are shown in Table 4.2 together with the PL emission properties including the redshift associated with polarization-induced QCSE. It can be inferred from the data shown in Table 4.3 that high indium content (up to green emission) can be achieved with no significant drop in the integrated PL intensity by employing of AlN/GaN MLs. The results obtained for AlN/GaN periodic MLs with 60% and 0.0% relaxation GaN layers reveal 6.7 % and 14.5 % higher indium contents, respectively, for the structure grown on MLs compared to those grown side by side on relaxed GaN layers.

115

Table 4.3. Estimated parameters, PL properties, and calculated indium contents for the structures used in this investigations emitting from purple to green.[100]

Sample	Emission Wavelength	QCSE induced PL shift	FWHM in PL	Normalized Integrated PL Intensity	Indium Content	Emission Color
A	425.2 nm	15.0 meV	126 meV	0.38	14.4 % (±0.2%)	Purple
B	432.2 nm	10.5 meV	148 meV	0.80	15.7 % (±0.2%)	Purple-Blue
C	457.8 nm	46.5 meV	218 meV	1.00	21.1 % (±0.3%)	Blue
D	503.8 nm	60.0 meV	273 meV	0.71	30.2 % (±0.5%)	Green

4.4.7. Summary of Findings

In summary, employment of AlN/GaN periodic MLs is found to efficiently enhance indium incorporation efficiency in the InGaN MQWs by promoting the strain relaxations. The inhomogeneity of indium distribution cannot be ruled out. The indium contents in the active layers on the periodic multilayers with two different values of compressive strain in GaN (1.11% and 2.78 %) were found to be higher by absolute composition values of 6.7 % to 14.5 % compared to the layers grown side by side on relaxed GaN templates (0.0% strain). The enhanced indium incorporation could be originated from the role of AlN/GaN MLs as strain relaxation layer for the overgrown InGaN MQWs reducing the compressive strain. Presence of deep and shallow band-gap regions due to spatial non-uniformity of indium distribution could also be assumed due to bi-exponential decay behavior of PL transients as well as surface undulation for active layers grown on MLs (C and D). The optical properties (integrated PL) of the structures containing high indium contents (> 20%) were not significantly degraded. Efficient PL emissions from purple to green was obtained using this approach which could be a potential candidate to alleviate the efficiency limitations for long wavelengths emitters.

116

4.5. Limitations and Alternatives

Despite of great improvements of *c*-plane LED performance and attempts to understand and reduce the efficiency degradations at high injection levels and long wavelengths (mentioned in previous sections), the efficiency of LEDs are still limited due to polarization induced quantum confined Stark effect (QCSE), especially for emitters emitting at long wavelengths. One solution is to reduce the total strain of the structures (as partially shown in section 4.4) and thus piezoelectric polarization by means of strain compensating layers[110], [111] or to grow the layers on nonpolar planes of GaN in which the spontaneous and piezoelectric polarization are absent.[112], [113] The latter solution will be more effective in efficiency improvement as it completely eliminates the polarization induced electric field. Moreover, the growth on nonpolar planes has been demonstrated to be strongly polarized[113] compared to un-polarized emission in case of *c*-plane.

The change in substrate crystallographic orientation (which is required for growth of nonpolar heterostructures) could provide many new concepts as well as challenges which opens a whole new window to study and understand the potential new properties. The possibility to have enhanced indium incorporation in other crystallographic planes, polarization charge, optical anisotropy, potential designs based on nonpolar structures to diminish efficiency droop along with growth challenges are some of the subjects to be considered when studying nonpolar and semipolar LEDs. In next chapters, a systematic analysis of growth, characterization and realization of theoretical predictions for nonpolar and semipolar structures will be provided in a way described fully in chapter 3 (in methods and approaches).

Chapter 5

5. Nonpolar GaN-Based Light Emitting Structures

5.1. Overview

As mentioned earlier, there is a great interest in nonpolar GaN substrates[16], [44], [112]–[117] for light emitting heterostructures owing to the absence of spontaneous and piezoelectric polarization. Unlike the structures grown in [0001] direction in polar wurtzite material, in the case of the wurtzite crystal with nonpolar orientation, there should be no polarization charges appeared at the quantum well interfaces. Therefore, the band structure should remain unaffected by the polarization field in the nonpolar structures. In this sense, GaN of nonpolar orientations holds great promise for new material physics and the production of LEDs with high efficiency and high power.

However, there is a lack of suitable substrates for growth of the nonpolar GaN epilayers. GaN freestanding substrates with nonpolar orientations are available but expensive, small in size, and of low crystal quality. Hence, there is a great interest in growing nonpolar GaN with reduced defect density on low-cost substrates such as Si and Sapphire. In this section, our investigations on nonpolar *m*-plane GaN and heterostructures on both native and foreign substrates (patterned Si (112)) will be demonstrated.

5.2. Nonpolar *m*-plane GaN on Si substrate; a two-step growth method

5.2.1. Overview

In this section, our attempts toward quality improvement of nonpolar GaN layers on patterned Si (112) have been considered. Based on the previous studies done in our group[115], [118] we demonstrate here the significant effect of the reactor pressure during metal-organic chemical vapor deposition (MOCVD) on the GaN growth on Si(112) patterned substrates.[119] It turns out that a low reactor pressure of 30 Torr is necessary for the the $(1\bar{1}00)$ top facets (for *m*-plane GaN) to be formed. However, enhanced carbon incorporation into the layers as a result of the low-pressure growth led to poor optical quality of the non-polar material, which demonstrated low PL intensity and fast non-radiative recombination rate.[118] The contribution in this subsection reports on a two stage growth method that is developed with the aim of improving optical quality of the *m*-plane GaN on Si (112) substrates. The procedure involves a low pressure (30 Torr) first stage followed by a high pressure (200 Torr) GaN overgrowth. As mentioned, the former is to ensure formation of the *m*-plane facet while the latter is utilized to enhance optical properties of the layers.

5.2.2. Experimental Details

Nonpolar *m*-plane GaN layers were grown by MOCVD (see section 3.3. for images and schematic of our home-built MOCVD system) on patterned Si (112) substrates. The patterning of the Si (112) is to form grooves aligned parallel to the <110> Si direction. Details of the

119

substrate patterning procedures and preparation is described elsewhere.[115] In this study, MOCVD growth was performed at an NH3 flow rate of 500 sccm, a TMG flow rate of 16 sccm, and a substrate temperature of about 1030 ℃. As discussed above, the *m*-plane layers were grown using a two-step growth procedure. Another $\left(1\bar{1}00\right)$ GaN (*m*-GaN) sample was grown in one step at a pressure of 30 Torr as a reference.

m-plane GaN layers were characterized by scanning electron microscopy (SEM), near-field scanning optical microscopy (NSOM) at room temperature, steady-statephotoluminescence (PL) with He-Cd laser excitation (325 nm wavelength), and cathodoluminescence (CL) at 6 K. For details about the measurements setups see section 3.4.

Figure 5.1 shows a cross-sectional SEM imgae of the non-coalesced GaN stripes grown on the patterned Si (112) substrate. GaN growth started on the Si{111} sidewalls and then advanced laterally first along the Ga-polar [0001] direction (*c*+ wing) and then, once the vertical growth had advanced above the level of Si(112) surface, also along the N-polar $[000\bar{1}]$ direction (*c*− wing). As seen from Figure 5.1, the *c*+ wing is much wider than the *c*− wing. This is due to the fact that the growth rate of GaN in the *c*+ direction is much higher than that in *c*− direction.

120
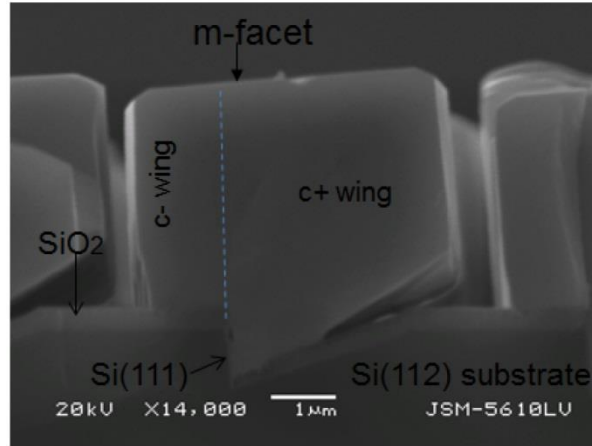
Figure 5.1. Cross-sectional SEM image of the nonpolar *m*-plane GaN grown on patterned Si (112) substrate. The c^+ and c^- wing regions are indicated in the figure.[119]

5.2.3. Optical and Structural Characterization

Figure 5.2(a) demonstrates comparison of room-temperature PL spectra from the *m*-plane GaN samples grown in two steps (30 + 200 Torr) and the reference one grown at a low pressure of 30 Torr. In this plot, the spectra from semipolar $(1\bar{1}01)$ GaN (*s*-plane) layer grown on patterned Si (001) substrate at 200 Torr[120] and polar *c*-plane GaN layer grown on the state-of-the-art GaN templates using *in-situ* epitaxial lateral overgrowth (ELO) technique applying a SiN_x nano-network mask to block defect propagation[101] are also brought for comparison. It can be inferred from the plot that the *m*-plane GaN layer grown at low pressure shows rather weak near band edge emission (NBE) and a strong defect-related deep level emission at around 550 nm. The shoulder that appears at 373 nm is related to excitons bound to prismatic stacking faults (PSFs). The sample grown in two steps, on the other hand, demonstrates improved optical quality compared to the single step (at 30 Torr) grown *m*-plane GaN with higher PL intensity by a factor of 3 and considerably lower intensity of the deep level emission. However, the emission

from m-plane GaN is still more than one order of magnitude lower compared to that of the semipolar GaN grown under the similar conditions. Our investigations on growth of semipolar $(1\bar{1}01)$-plane GaN on patterned Si (001) will be discussed in details in Chapter 6.
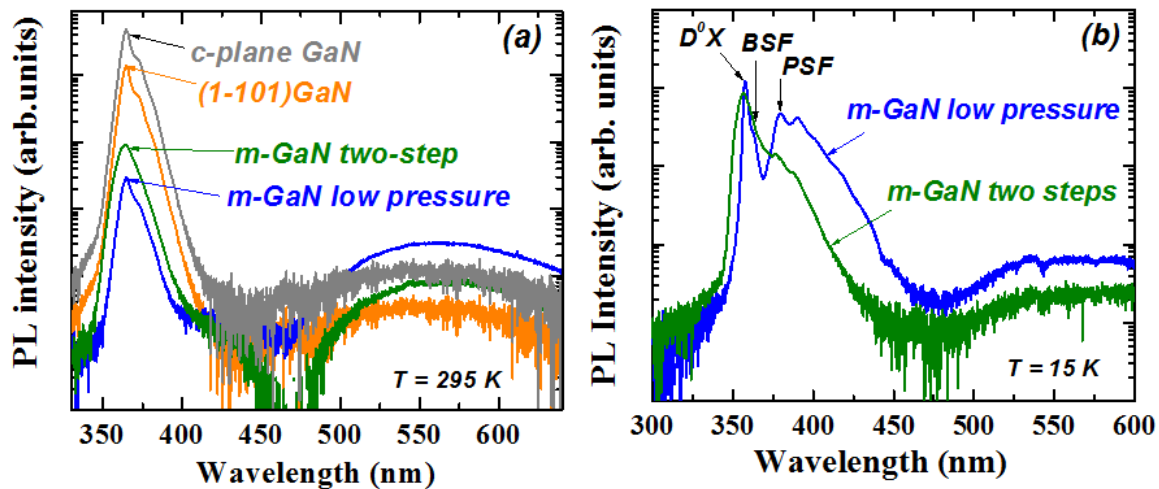
Figure 5.2. (a) Room-temperature steady-state PL spectra for m-plane GaN layers grown at 30 Torr (blue) and in two steps (30 Torr followed by 200 Torr) (green). The spectra from c-plane GaN nano-ELO layer (gray) and $(1\bar{1}01)$ GaN semipolar sample (orange) are also demonstrated for the sake of comparison. The plots in (b) indicate the PL spectra at low-temperature (15 K) for m-plane GaN layers grown in 30 Torr (blue) and using two step growth approach (green).[119]

Figure 5.2(b) presents PL spectra at 15 K measured for the two m-plane samples: low-pressure sample and the sample grown in two steps. In addition to narrow donor-bound exciton emission line (D^0X) at 357.6 nm, the low-pressure sample demonstrates a strong peak at 380 nm related to PSFs followed by its phonon replicas at longer wavelengths and a shoulder of the D^0X line at about 362 nm which can be assigned to basal stacking faults (BSFs).[121] in the spectrum of the two-step-grown sample, a broad NBE emission line at 356.4 nm can be observed, while PSF-related emission line can be seen only as a weak shoulder.

Low-temperature cathodoluminescence (CL) data are in good agreement with the low temperature PL results demonstrated above. Figure 5.3 illustrates spatially integrated CL spectra measured for the *m*-plane GaN layer grown at low pressure (Figure 5.3(a)) and for the one grown in two steps (Figure 5.3(b)). The first spectrum shows a strong donor-bound exciton emission (D^0X) line followed by a peak associated with prismatic stacking faults (PSF)[121] and its phonon replica, and a deep level yellow emission (YE) band at ~560 nm central wavelength (Figure 5.3(a)). On the other hand, the spectrum in Figure 5.3(b) that is from the sample applying two step growth approach is composed of a strong and broad NBE line and the deep level YE band which is quite different from the CL spectrum demonstrated in Figure 5.3(a). Selected-area CL spectra (not shown) reveal that NBE line from the layer grown in two steps is broad as it is composed of D^0X lines and electron-hole plasma emission. Another interesting point is that there is no sign of stacking fault-related emission in the CL spectra of the sample grown in two steps shows (Figure 5.3(b)), and there is simply a weak shoulder which can be assigned to PSFs (Figure 5.3(b)). As we have reported earlier,[115] high density of stacking faults in the $c-$ wing regions of *m*-plane GaN is present as revealed by spectrally and spatially resolved CL studies.

123
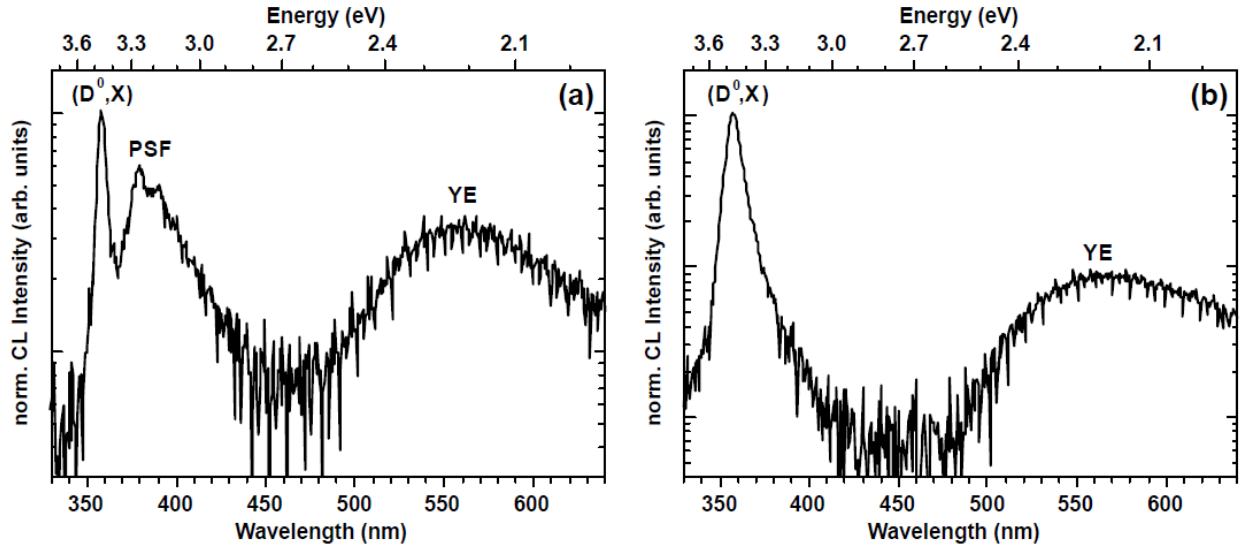
Figure 5.3. CL spectra measured at low-temperature (6 K) for the samples grown (a) at low pressure and (b) in two steps (low pressure + high pressure).[119]

In order to investigate on PL intensity distribution in the $c+$ and $c-$ wings of the nonpolar m-plane GaN layers, micro PL and NSOM measurements were performed. Figure 5.4(a) shows the μ-PL spectra from $c+$ and $c-$ wings of the m-plane GaN layer grown in two steps, where the intensity of PL emission from $c+$ and $c-$ wing regions is almost the same. Figures 5.4(b) and (c) show the spatial distribution of PL intensity integrated for near band edge emission (NBE) and yellow emission (YE), respectively, measured by NSOM over the surface of the m-plane GaN layer grown in two steps. The results of NSOM measurement are in agreement with the micro PL data showing that distribution of PL intensity indicates no clear difference between the $c+$ and $c-$ wings.

www.manaraa.com
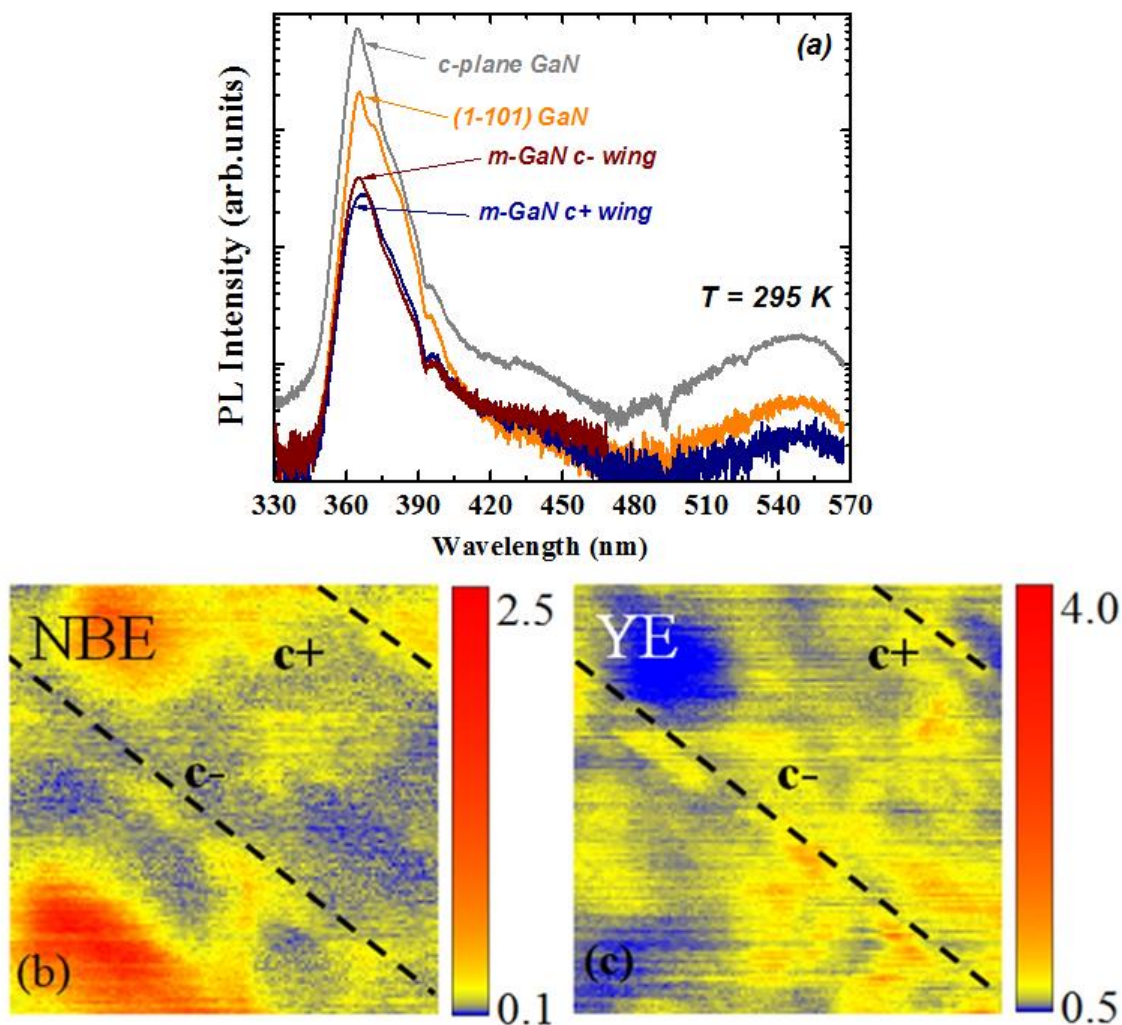
Figure 5.4. (a) Room-temperature micro-photoluminescence spectra for *m*-plane GaN layers measured on $c+$ (blue) and $c-$ (wine) wing regions. The micro-PL spectra of *c*-plane GaN nano-ELO layer (gray) and $(1\bar{1}01)$-oriented semipolar GaN sample (orange) are illustrated for comparison. NSOM images obtained at room-temperature from the nonpolar *m*-plane GaN sample grow in two steps with the scan area of 20×20 μm demonstrating local intensity distribution in the linear scale for (b) near-band edge (NBE) integrated between 350-370nm and (c) yellow emissions (YE) integrated above 450nm . Dashed lines in the images indicate the boundaries of GaN stripes.[119]

To further probe the spatial distribution of intrinsic as well as defect related optical processes, $c+$ and $c-$ wing regions of the *m*-plane GaN stripes were directly imaged utilizing

highly spatially and spectrally resolved CL microscopy. Figure 5.5(a) represents a cross-sectional SEM image of the *m*-plane sample grown in two steps. CL wavelength image that shows the distribution of the local CL peak wavelength is illustrated in Figure 5.5(b) which clearly indicates that yellow emission (YE) centered at 550 nm dominates the near-surface regions in the middle of the GaN stripes. This is visible as yellow-green triangular areas located below the surface on Figure 5.5(b). As seen from Figure 5.5(c) and (d), that are CL intensity image integrated in the NBE and YE regions, respectively, spatial distribution of CL intensities of NBE and YE are locally anti-correlated, meaning that for instance, no NBE is observed where the YE dominates. As the YE is known to be mainly due to presence of point defects, we expect these regions to contain high density of point defects. As the formation of the mentioned defective regions can be related to the growth evolution, the investigations of initial stages of the epitaxial growth are necessary to shed light on their origin.
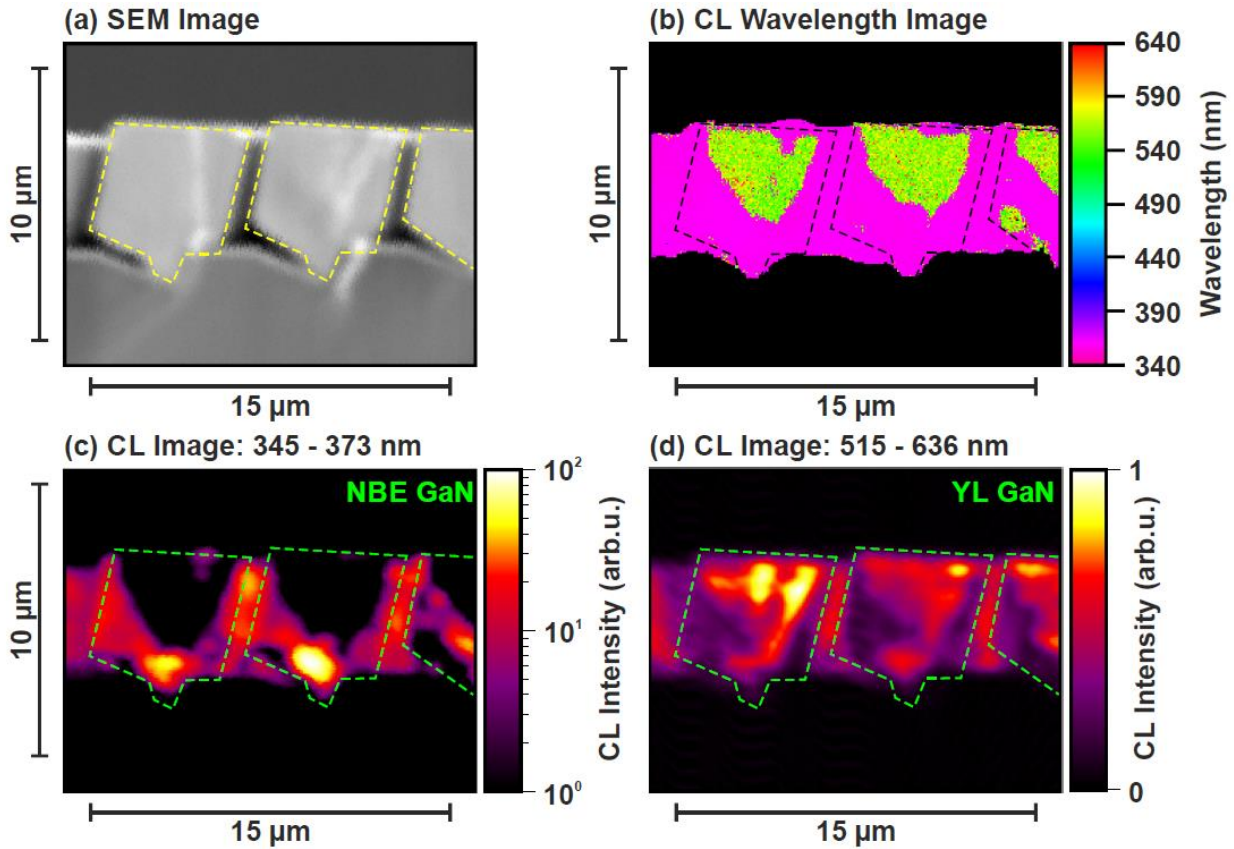
Figure 5.5. (a) Cross-sectional SEM image of the nonpolar *m*-plane sample grown using a two-step approach and corresponding (b) CL wavelength image and intensity images integrated between (c) 345 – 373 nm and (d) 515 – 636 nm.[119]

5.3. Nonpolar *m*-plane AlGaN/GaN heterostructures on native substrates

5.3.1. Overview

In this section, the optical examination and properties investigation of the heterostructures grown on bulk *m*-plane GaN will be discussed.[122] Even though the quality of bulk *m*-plane freestanding substrates grown in nonpolar directions are still not optimal and hetero-epitaxy of

127

non-polar [123]–[125] GaN layers can be used as an alternative approach[126], the optical investigations of structures grown on bulk *m*-GaN are still of significant importance.

Up to now, most of the investigations in this field have focused on InGaN QWs widely utilized as active regions in visible LEDs and laser diodes (LDs). It has been shown that, in the case of InGaN QWs, excitonic recombination dynamics are mainly governed by localized states, rather than demonstrating the intrinsic properties of the material system.[123], [127] Only few studies had been focused on detailed investigation of excitonic recombination dynamics in non-polar GaN[128], [129] and GaN/AlGaN QWs.[130]

In the work presented in this section, that is performed as a collaboration with the group at Montpellier University, France, we examined the optical properties of GaN/AlGaN multi-quantum wells (MQWs) grown on free-standing *m*-plane $(10\overline{1}0)$ GaN substrates using MOCVD (see section 3.3 for specifications of our MOCVD growing system). We first provide evidence of the experimental anisotropy of the in plane optical response. Then, the discussion will be followed by study of the excitonic emission. It is found here that the excitonic recombination is dominantly radiative for temperatures below 80K in our moderately shallow quantum wells. However, at higher temperatures, the recombination dynamics and the robustness of the photoluminescence are influenced by non-radiative recombination channels and the thermally induced de-trapping of the photo-generated carriers in the barrier layers.

5.3.2. Layer Schematics and Experimental Details

Five 1.5 nm thick GaN quantum wells (QWs) separated by 8.5 nm $Al_{0.15}Ga_{0.85}N$ barrier layers were grown on free-standing bulk m-plane $(10\bar{1}0)$ GaN substrates at a substrate temperature of $T_s = 1045°C$ by MOCVD. The m-plane bulk substrates were provided by our industrial collaborator, Kyma Technologies. Underneath the QWs, a GaN buffer with thickness of about 400 μm was grown at $T_s = 1050°C$ followed by a 30nm AlGaN layer. The multiple QW (MQW) structure was ended with 20 nm AlGaN (top barrier) and 3nm GaN (cap layer). The schematic of the sample structure is shown in Figure 5.6.
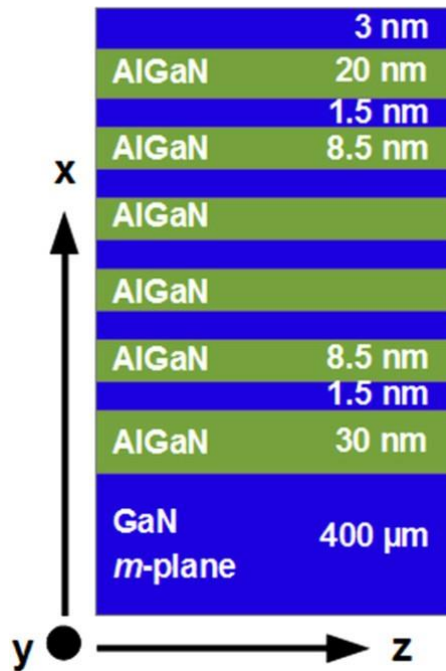
Figure 5.6. Schematic of the sample under investigation including five periods of the quantum well basic building blocks. The Cartesian coordinate system with the x, y and z axes are also indicated at the bottom corner of the figure indicating x as growth direction. [Reprinted with Permission from Ref.[122]]

The sample was mounted in a helium flow cryostat for all the measurements and the temperature varied from 8K to room temperature. The optical excitation for this study was provided by a mode-locked frequency tripled Ti-Sapphire laser, with wavelength of 266 nm and pulse width of 2 ps. The focused laser spot diameter was 100 μm and the estimated photo-generated carrier concentration was about $3-4\times10^{10} cm^{-2}$. Owing to the relatively long values of PL decay times, using an acousto-optic modulator, we have adapted a laser repetition rate of 4MHz. The PL signal was temporally resolved by a streak camera with an overall time resolution of 8 ps.

5.3.3. Evidence for Optical Anisotropy in QW Emission

Based on group theory, the optical response for the *m*-plane is expected to be anisotropic in the growth plane. Experiments performed on nonpolar *a*-plane GaN/AlGaN quantum wells[131], [132] have also reported it. Funato *et al.*[133] have recently reported on optical anisotropy in *m*-plane AlGaN/AlN quantum wells with AlGaN being the QW layer. This optical anisotropy for the nonpolar heterostructures is also confirmed by the data presented in Figure 5.7(a). According to this plot which is a series of 8K photoluminescence spectra for different orientations of the electric field of the emitted photon radiation obtained using a polarization analyzer in the emitted beam path before reaching the detector. We wish to emphasize that the spectra does not contain emission in the 3.42 eV region (corresponding to structural defects) which is typical for growth of non-polar GaN layers grown on lattice mismatched foreign substrates[121] and is not observed for our sample grown on *m*-plane bulk GaN substrates. The intensity of donor-bound exciton emission line at an energy slightly below 3.480 eV at 8K is maximum when one probe

130

the Γ_9 hole for the electric field of the emitted photon parallel to the $\vec{y}$ direction in the Cartesian coordinate system. The $\vec{y}$-polarized emission is observed to emit at lower energy by about 5meV compared to that corresponds to $\vec{z}$-polarizations. The inhomogeneously broadened PL band at higher energies corresponding to the emission of confined excitons is observed at 3.616 eV with a full width at half maximum (FWHM) of 61 meV. However, emission of excitons localized in the barrier layers is observed at 3.709 eV with a FWHM of 69 meV. Using the energy of the emission in the barrier layer and including the Stokes-shift which is normally observed between the PL and a reflectance experiment,[134] the aluminum content is estimated in the barrier to be about 14%.[135] Figure 5.7(b) represents the normalized intensities of the photoluminescence from the GaN donor-bound exciton, the MQW, and the barrier layers in polar coordinates. The crystallographic axes $\left(\vec{a}_1, \vec{a}_2, \vec{c}\right)$ in the Cartesian basis $\left(\vec{x}, \vec{y}, \vec{z}\right)$ with respect to the unity vectors are indicated on the schematic in top corner of Figure 5.7(b). The degree of polarization is defined as

$$DOP = 100 \times \frac{I_y - I_z}{I_y + I_z} \tag{5.1}$$

where I_u is the PL intensity of the emitted photon with electric field parallel to the direction $\vec{u}$. The values of degree of polarization for the quantum wells and barriers are 38% and 39%, respectively which means they have similar anisotropic behavior. The AlGaN barriers and GaN quantum wells are both crystals with macroscopic C_{2v} orthorhombic symmetry. For the AlGaN barriers, the degeneracy between $\vec{x}$ and $\vec{y}$ is lifted by strain and thus it is anisotropic strain that reduces the symmetry. For the MQW systems (MQWs), on the other hand, the breaking of

131

translational symmetry in the $\vec{x}$ direction (growth direction) is responsible for reducing the symmetry.
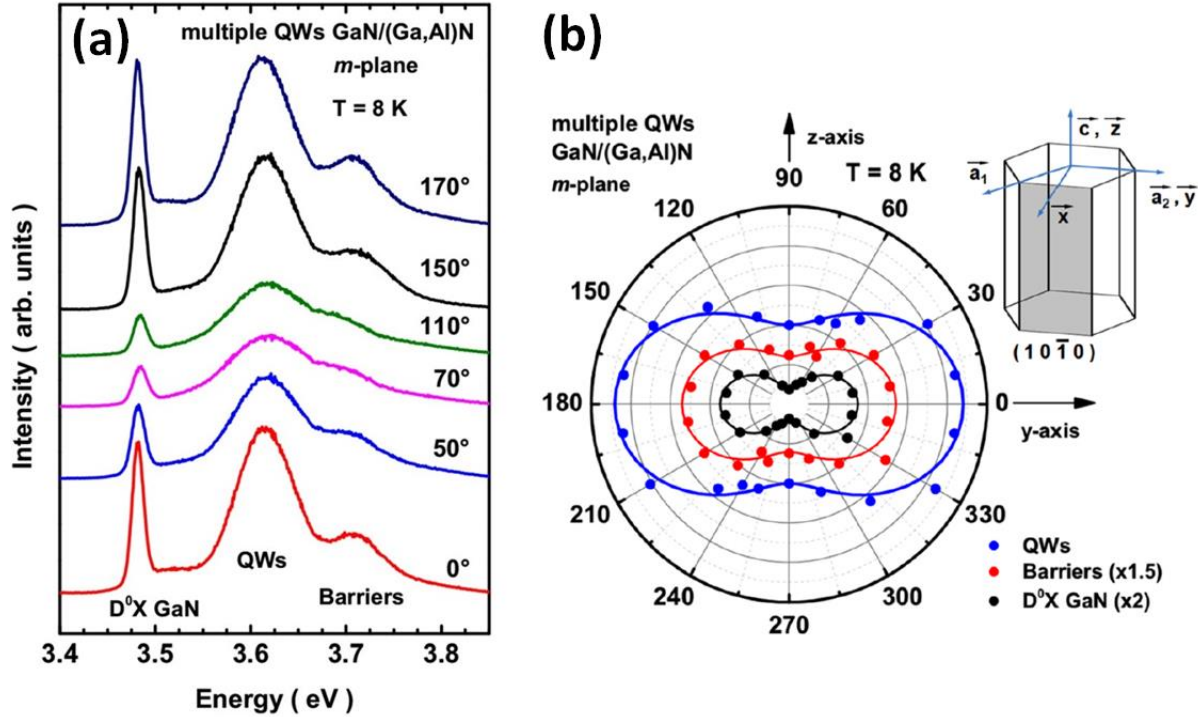
Figure 5.7. (a) Photoluminescence spectra for various polarizations of the emitted photons with 0° being taken parallel to the $\vec{y}$ direction of the Cartesian coordinate system. (b) Polar plot of the PL intensity for the MQWs (blue), for the barrier layers (red) and for the GaN (black). The orientation of the crystal is shown at the top corner of the figure. [Reprinted with Permission from Ref.[122]]

The calculation based on theoretical analysis of crystal orientation effects in wurtzite semiconductors[136], [137] and using the literature values of matrix elements[138] and Luttinger parameters[139] for GaN was performed and the dispersion of the eigenvalues in case of an infinitely deep GaN well for k_x values between 0 and $1\,nm^{-1}$ is plotted in Figure 5.8(a). It can be pointed out that starting from the Γ_9, Γ_7 and Γ_7 ordering for $k_x = 0$, increasing k_x made a complicated behavior with anti-crossings for high values of k_x to the relative ordering of the

132

valence bands: x, z, and y. Also, y and z states are almost parallel to each other for high values of k_x. For the band to band transition, the symmetry of the photon polarization may be Γ_1' $\left(\vec{E} \parallel \vec{z}\right)$, $\Gamma_2'\left(\vec{E} \parallel \vec{y}\right)$ or $\Gamma_4'\left(\vec{E} \parallel \vec{x}\right)$ in orthorhombic environment. It can be inferred from group theory that matrix elements (non-vanishing ones) for the band-to-band transitions will be transformed as z^2 or y^2 or x^2. In our experiment, transitions can be recorded for $\Gamma_1'\left(\vec{E} \parallel \vec{z}\right)$ and $\Gamma_2'\left(\vec{E} \parallel \vec{y}\right)$ polarizations for photons with Poynting vectors parallel to $\vec{x}$ direction (light emitted through the *m*-plane surface or along growth direction). Therefore, our experimental configuration should not be able to allow the transition between the *x*-type confined hole state and the confined electron state. Apparently, that the first dipole allowed transition is *z*-type for high values of k_x corresponding to thin wells, while *y*-type is allowed for low values of k_x corresponding to wide wells. The oscillator strengths are calculated as the squared components of the coefficients of the eigenvectors that are projected over $\vec{z}$ and $\vec{y}$ directions.

133
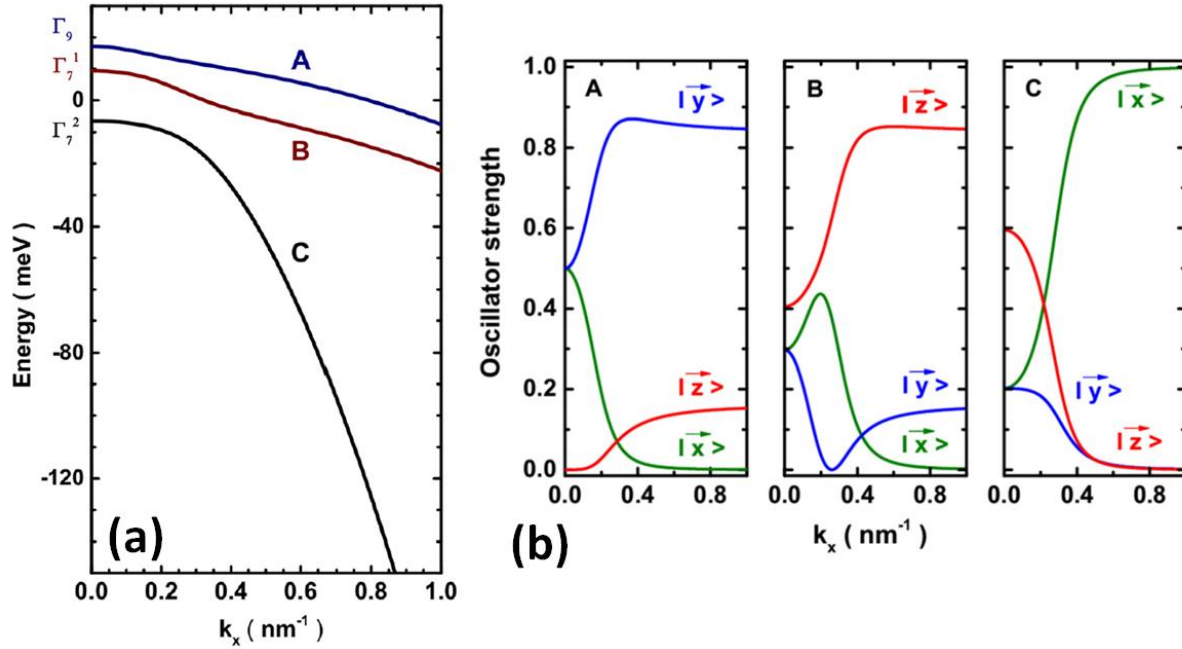
Figure 5.8. (a) The dispersion curves for the three valence band levels at $k_x \neq 0$ and $k_y = k_z = 0$. For high values of k_x A and B are almost parallel but C rapidly separates from both of them. (b) The expansion of A (left), B (middle), and C (right) levels versus k_x. At high values of k_x, the A valence band level dominantly contains $|\vec{y}\rangle$ state and about 15 percent $|\vec{z}\rangle$ state while for the B level it dominantly contains $|\vec{z}\rangle$ Bloch state and about 15 percent $|\vec{y}\rangle$ state. Also, it appears that the C is only built of $|\vec{x}\rangle$ Bloch state at high values of k_x. These expansions affect the selection rules for band to band transitions. [Reprinted with Permission from Ref.[122]]

The oscillator strengths for z, y, and x polarization are plotted in Figure 5.8(b) for the three band to band transitions; between the first confined electron states and the three (A, B, and C) confined valence bands. Here, we mention that both the lowest confined levels from the Γ_9 and the highest Γ_7 valence bands allow the $\vec{E} \parallel \vec{z}$ and $\vec{E} \parallel \vec{y}$ polarizations which is qualitatively in agreement with the theoretical prediction of Park.[140]

134

5.3.4. Excitonic Recombination Dynamics

Figure 5.9 shows the PL spectra for various temperatures ranging from 8K to 295K for $\vec{E} \parallel \vec{y}$ and $\vec{E} \parallel \vec{z}$ polarizations. The PL intensities remain constant at low temperature up to 40–50K and then start to decrease with further increase in temperature. The peaks associated with QW and barrier emissions can be fitted using a Gaussian fit function. However, It is hard to separate the contributions of the barriers and QWs especially for the $\vec{E} \parallel \vec{z}$ polarization due to overlapping of the peaks.
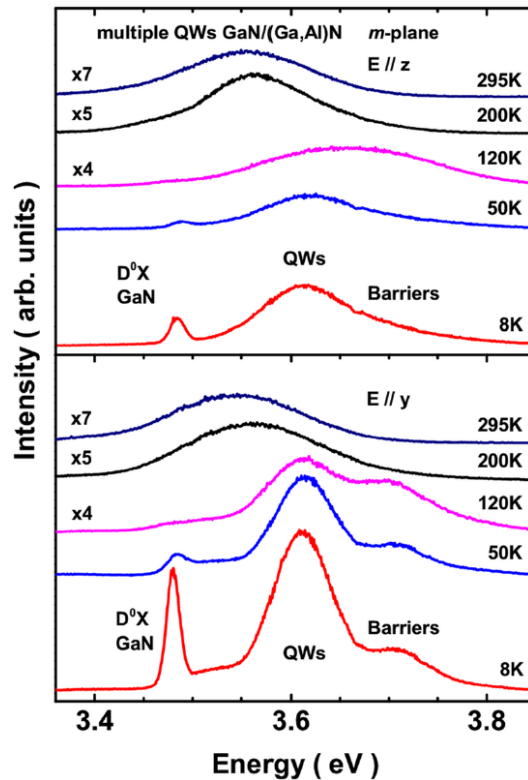
Figure 5.9. Photoluminescence spectra for the *m*-plane AlGaN/GaN MQWs structure for $\vec{E} \parallel \vec{z}$ (top) and $\vec{E} \parallel \vec{y}$ (bottom) polarizations. [Reprinted with Permission from Ref.[122]]

135

The changes of the PL energy in the temperature range of 8K to 295K t for $\vec{E} \parallel \vec{y}$ and $\vec{E} \parallel \vec{z}$ polarizations are demonstrated in Figure 5.10. At first glance, the luminescence for the quantum wells and barrier layers exhibit fairly similar behaviors for both y and z polarizations. However, the energy is more stable in both polarizations for the quantum wells compared to that in case of barrier layers with increasing temperature. The energy associated with PL peak of the quantum wells is found to be virtually unchanged up to about 150 K while for barrier related emission there is are slight blue shifts up to temperatures of about 50 K, above which it drops rapidly. This can be due to the thermal de-trapping of the carriers from aluminum poor regions to aluminum-rich ones. Using model by Vina *et al.*[141], [142]

$$E_g(T) = E(0) - \frac{\alpha_B \Theta_B}{\exp(\Theta_B / T) - 1}, \tag{5.2}$$

We fitted the data which indicates an average phonon bath temperature (Θ_B) in the range of 335–340K for the barrier layers while $\Theta_B \simeq 500K$ for the MQWs, for both polarizations. Apparently, there is no remarkable influence of the polarization on the phonon bath temperature.

136
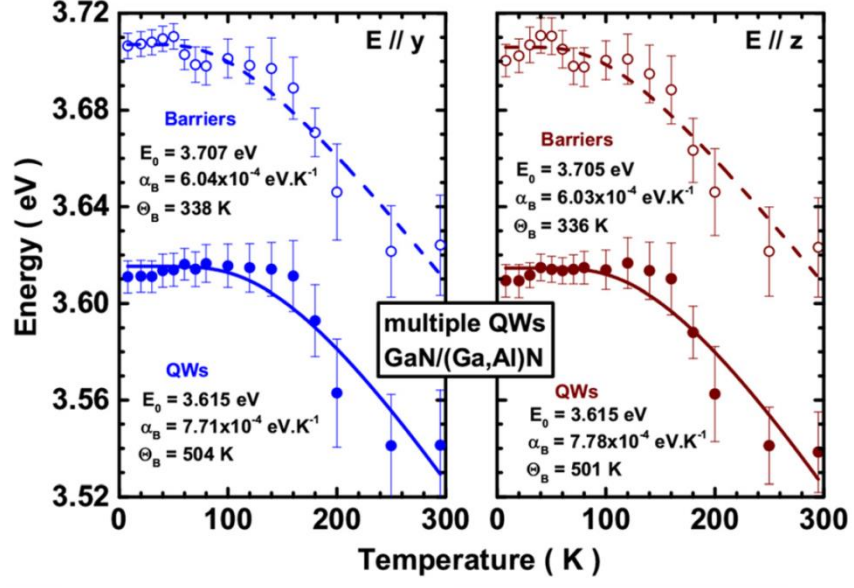
Figure 5.10. PL energy position as a function of temperature for the *m*-plane AlGaN/GaN MQWs for $\vec{E} \parallel \vec{y}$ (left) and $\vec{E} \parallel \vec{z}$ polarizations (right). PL energies in the barrier layers as well as QWs are fitted using Vina's equation. [Reprinted with Permission from Ref.[122]]

Here we want to calibrate the relative contributions of radiative and non-radiative recombination processes in the *m*-plane MQWs sample. We know that the PL intensity varies proportional with ratio of non-radiative to radiative lifetimes via the following relation:

$$I(T) \propto \frac{\tau_{nonrad}}{\tau_{nonrad} + \tau_{rad}} \propto \frac{1}{1 + \dfrac{\tau_{rad}}{\tau_{nonrad}}} \, . \tag{5.3}$$

The radiative recombination rate $G(T)$ (the inverse of the radiative decay time) is proportional to the relative number of excitons having the wave-vector in the light cone (wave-vector smaller than $\dfrac{E}{\hbar c}$)[143] which can be expressed as:

137

$$G(T) = \frac{1}{2\tau_{rad}} \propto \frac{\int_0^{E/\hbar c} \exp\left(-\frac{\hbar^2 k^2}{2M(k)k_B T}\right) d^n k}{\int_0^{\infty} \exp\left(-\frac{\hbar^2 k^2}{2M(k)k_B T}\right) d^n k} \qquad (5.4)$$

where $d^n k$ is the n-dimensional elemental volume in the k space. This dimension will be $n = 3, 2, 1, 0$ for bulk material, quantum well, quantum wire, and quantum dot or impurity, respectively. Here, $M(k)$ is excitonic translation mass which is direction-The radiative lifetime in an n-dimensional integration can be derived and expressed as:

$$\tau_{rad} = \tau_0 T^{\frac{n}{2}} \qquad (5.5)$$

The thermally activated non-radiative decay time can be shown as:

$$\tau_{nonrad} = \tau_1 \exp\left(\frac{E_a}{k_B T}\right) = \tau_1 \exp\left(\frac{T_a}{T}\right) \qquad (5.6)$$

where E_a (T_a) depicts activation energy (temperature). Higher value of E_a (T_a) gives better robustness of PL with increasing temperature. Finally, the variation of the PL intensity with change of temperature could be fitted using

$$I(T) \propto \frac{1}{1 + \frac{\tau_0}{\tau_1} T^{\frac{n}{2}} \times \exp\left(-\frac{T_a}{T}\right)}. \qquad (5.7)$$

Figure 5.11(a) illustrates the photoluminescence intensities as a function of temperature for quantum wells and barrier layers in the $\vec{E} \parallel \vec{y}$ and the $\vec{E} \parallel \vec{z}$ polarizations. The PL intensity of the barrier layers were fitted using a three-dimensional model for exciton propagation while a two dimensional model was used to fit the data for QWs related PL intensities. The fitting

138

parameters indicated more robustness of PL in $\vec{E} \| \vec{y}$ polarization than in the $\vec{E} \| \vec{z}$ polarization for both barrier and QW-related emission. In addition, the activation temperature is found to be smaller for barriers than for QWs. Note that ratios $\dfrac{\tau_0}{\tau_1}$ are named as W_2 for wells and B_2 for barriers. The logarithm of the PL intensity versus T^{-1} (Arrhenius plot) is also given in Figure 5.11(b). The inset of Figure 5.11(b) demonstrates the experimental and theoretical values of energy splitting between the photoluminescence associated with barriers and the wells.
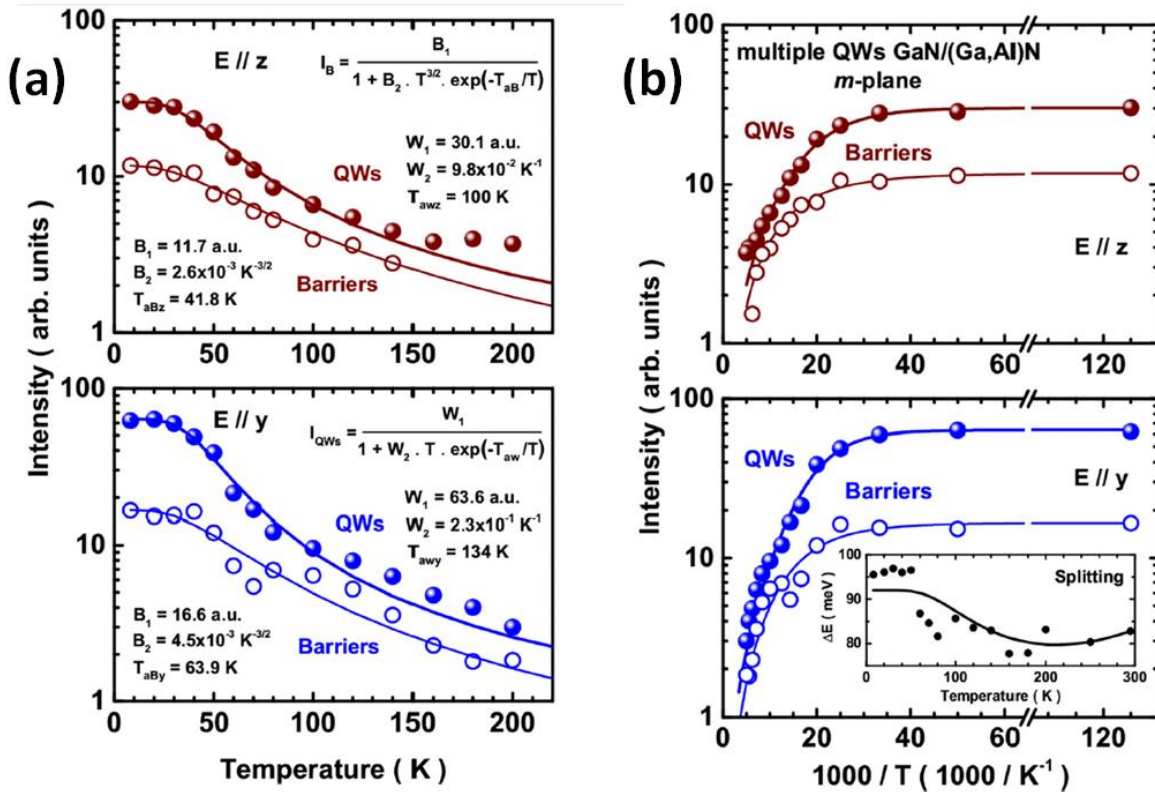
Figure 5.11. (a) photoluminescence intensities and (b) Arrhenius plots of the PL intensities for the *m*-plane AlGaN/GaN MQWs sample in case of $\vec{E} \| \vec{z}$ polarization (top) and $\vec{E} \| \vec{y}$

139

polarization (bottom) and. The data for QWs related PL intensities are full dots and data for the barrier related emission intensity data are open dots. The results of the fitting are reported using continuous lines with the fitting parameters indicated for the corresponding cases as well as the fitting functions for QWs and barriers. W and B letters are used as the parameters of fits. The inset in the bottom part of (b) is the experimental (dots) and theoretical (continuous line representing the differences of the fits of energies using Vina's model) values of energy splitting between the PL associated with barrier layers and the QWs. [Reprinted with Permission from Ref.[122]]

We examined the temperature dependent PL transients to obtain the values of the radiative and nonradiative decay times knowing the relationship between the PL decay time τ and the nonradiative (τ_{nonrad}) and radiative (τ_{rad}) components which is

$$\frac{1}{\tau} = \frac{1}{\tau_{rad}} + \frac{1}{\tau_{nonrad}} \ . \tag{5.8}$$

Figure 5.12(a) shows the the QW-related PL transients measured at various temperatuers below 70K where a mono-exponential decay is noted. We make the assumption that non-radiative recombination processes are slower than the radiative ones at low temperature to extract the radiative and non-radiative decay times. We also normalize the PL intensity to unity at low temperature. Figure 5.12(b) demonstrated the radiative and non-radiative decay times as a function of temperature together with the measured values of the PL decay time. As the temperature reaches 80K the decay times saturate for the quantum wells in both y and z polarizations, while the "saturation temperature" is around 150 K for case of barriers which means more temperature robustness. From the change of PL intensity with temperature, the radiative and nonradiative decay times can be extracted. For the barriers, the radiative part increases with the temperature and is fitted non-linearly with $\tau_0 T^{\frac{3}{2}}$ where $\tau_{0y} = 1.6 \times 10^{-1} \, ps.K^{-3/2}$

for $\vec{E} \parallel \vec{y}$ and $\tau_{0z} = 9.8 \times 10^{-2} \, ps.K^{-3/2}$ for $\vec{E} \parallel \vec{z}$ with the activation temperatures (T_a) being 64K

and 42 K, respectively, giving $\tau_{1y} = 36 ps$ and $\tau_{1z} = 38 ps$.
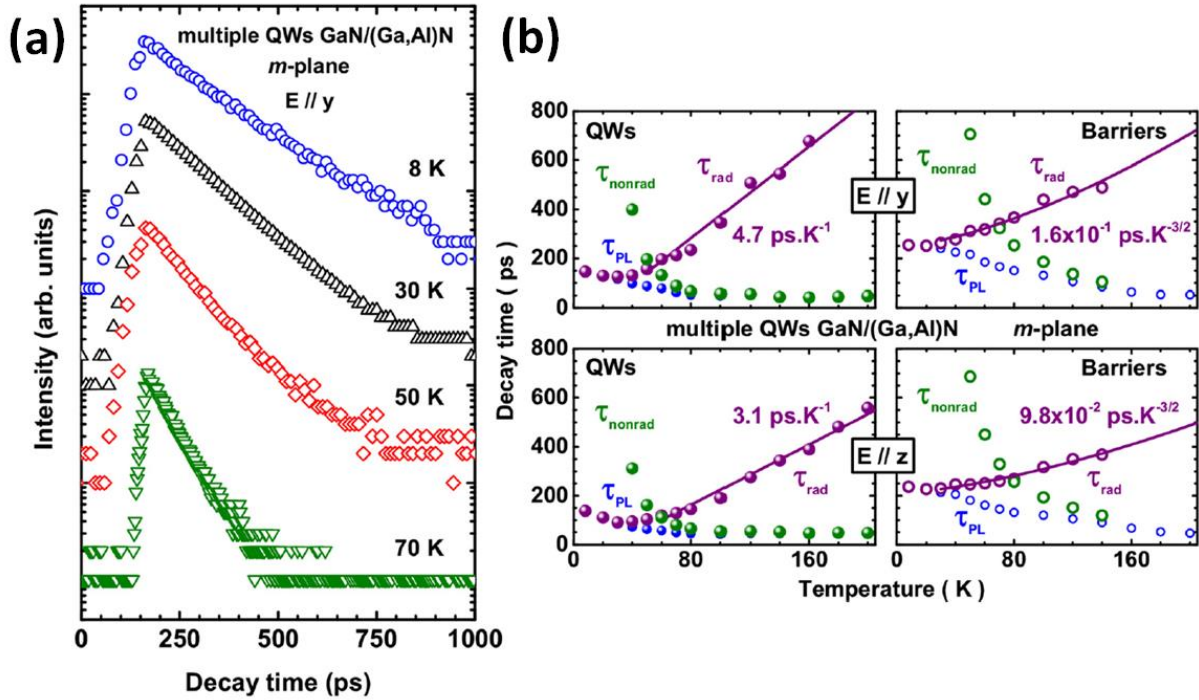
Figure 5.12. (a) photoluminescence transients of the QWs measured for different temperatures ranging from 8K up to 70 K. (b) PL decay times (green dots) with non-radiative (green dots) and radiative (wine dots) components for the *m*-plane MQWs structure for $\vec{E} \parallel \vec{y}$ (top) and $\vec{E} \parallel \vec{z}$ (bottom) polarizations for the quantum wells (full dots) and the barriers layers (open dots). The solid lines indicate the fit of radiative decay times. [Reprinted with Permission from Ref.[122]]

In case of QW-emission, existence of a constant decay time up to 50–60K is indicative of exciton localization. This is in agreement with intensity versus temperature. Further increase in temperature makes the excitons to become mobile in the quantum well planes and thus we observe the expected linear dependence with temperature.

141

Activation temperatures of $T_a = 134K$ for $\vec{E} \parallel \vec{y}$ and $T_a = 100K$ for $\vec{E} \parallel \vec{z}$ were obtained for non-radiative components in agreement with temperature dependence of PL intensities which gives $\tau_{1y} = 20ps$ and $\tau_{1z} = 32ps$ for $\vec{E} \parallel \vec{y}$ and $\vec{E} \parallel \vec{z}$ polarizations, respectively. Activation temperature (T_a) is higher in case of QWs compared to that of the barrier layers. Based on the relative time dependent behavior, the recombination dynamics in the QWs are governed by non-radiative recombination at higher temperatures and the decay of the QW-related emission is ruled by carrier feeding from the barrier layers.

The radiative decay time for quantum wells grown on *m*-plane substrates can be written as[144]

$$\tau_{rad}(T) \approx \frac{2c^2 k_B}{\hbar \omega_{LT} a_B{}^3} \left(\frac{1}{m_{ey} + m_{hy}} + \frac{1}{m_{ez} + m_{hz}} \right)^{-1} \frac{\lambda^2}{\omega^3 I_{eh}{}^2} T \ , \tag{5.9}$$

where c is the velocity of light, k_B is the Boltzmann constant, ω is the light angular frequency, a_B is the bulk Bohr radius , λ is the in-plane exciton Bohr radius in the quantum well and ω_{LT} is the angular frequency of the longitudinal splitting of the exciton. The quantity $m_{ei} + m_{hi}$ is the exciton translation mass in the i direction and I_{eh} is the overlap of electron and hole envelope functions. The equation will also hold for *c*-plane quantum wells, where $m_{ez} + m_{hz}$ will be replaced by $m_{ex} + m_{hx}$. It is noteworthy to mention that the Quantum Confined Stark Effect is responsible for the strong dependence of τ_{rad} on well-width via quantities λ , ω and I_{eh}. It is also interesting to see that quantity $\dfrac{\lambda^2}{\omega_{LT} \omega^3 I_{eh}{}^2}$ in the above Equation contains all the information

required for determining the polarization dependence as well as well-width dependence of the slope of τ_{rad} as a function of temperature for a given orientation.

Compared to other orientations, there are other reports in literature for for *c*-plane[145] and $(11\bar{2}2)$-oriented GaN/Al$_{0.5}$Ga$_{0.5}$N quantum wells,[146] indicating $\tau_0 = 20\,ps.K^{-1}$ and $\tau_0 = 8\,ps.K^{-1}$ respectively, and $\tau_0 = 20\,ps.K^{-1}$ for homopitaxial *m*-plane ZnO/ZnMgO quantum wells.[144] Our report here indicates $\tau_0 = 4.7\,ps.K^{-1}$ for $\vec{E} \parallel \vec{y}$ and $\tau_0 = 3.1\,ps.K^{-1}$ for $\vec{E} \parallel \vec{z}$ polarization that is in agreement with other experimental values (for instance, see Confdir *et al.*[147]) and in accordance with the predictions of the simple theory although the slope is a little bit smaller than the expected value. The smaller value of slope compared to prediction could be due to the competition between the localized and delocalized excitons for the whole range of temperature of this experiment.

5.3.5. Summary and Conclusions

As a summary of the reports in this section, the experimental anisotropy of the in plane optical response for GaN/AlGaN multi-quantum wells grown on *m*-plane freestanding GaN substrate has been demonstrated. The sample did not feature emission related to excitons bound to basal plane staking faults that is typical of heteroepitaxial non-polar GaN epilayers (No PL line at 3.42 eV was observed). The excitonic recombination dynamics has been investigated and shown that excitonic recombination is dominantly radiative up to 80 K for our moderately shallow QWs while it is dominated by non-radiative recombination at higher temperatures. The thermally induced carrier de-trapping from the barrier layers at higher temperatures affects the robustness of the photoluminescence as well as recombination dynamics.

143

5.4. Limitations and alternatives for nonpolar structures

In spite of great promises of nonpolar heterostructures mainly due to elimination of quantum confined Stark effect (QCSE) as well as the ability to have polarized emission, these structures started to loose popularity due to the low quality of available substrates for homoepitaxy and poor optical quality of the heteroepitaxial films grown on this orientations. Moreover, in 2008, Yamada *et. al.*[18] demonstrated the reduction in indium contents by a factor of two to three for the layers grown on nonpolar *m*-plane compared to those on conventional *c*-plane substrates under similar growth conditions. This caused significant reduction in LED output power for devices emitting above 400nm[19] and thus made the nonpolar choice of substrate no more a solution to the green gap issue.

Semipolar orientations with substantially reduced polarization fields represent another alternative to the polar structures for producing efficient LEDs in wide range of wavelengths from blue to yellow. In next section, our investigation on heteroepitaxial semipolar $(10\bar{1}1)$ and $(11\bar{2}2)$ GaN layers on patterned and plannar substrates, defect reduction methods and optical and structural characterizations of the AlGaN/GaN and InGaN/GaN heterostructures will be discussed in details.

Chapter 6

6. Semi-polar GaN-based Light Emitting Structures on Patterned Substrates

6.1. Overview

As mentioned, due to relatively low quality of nonpolar heterostructures and the observations on reduced indium incorporation to nonpolar m-plane,[18] semi-polar orientations with substantially reduced polarization fields gained attention for producing efficient LEDs emitting above blue,[19] in particular in the light of theoretical predictions of enhanced indium incorporation efficiency relying on effect of strain[20] and surface atomic configurations.[21] According to the theoretical studies, planes with inclination angle of $\theta \sim 60°$ with respect to c-axis should exhibit the highest In incorporation among all the planes of GaN.[20] Zhao et $al.$[22] reported experimental verifications of the theoretical predictions[20] for layers grown on high quality bulk substrates. They concluded on the highest incorporation efficiency for semipolar $\left(11\overline{2}2\right)$ orientation with inclination angle of $\theta = 58°$. Detailed discussion about the dependency of indium incorporation on substrate orientation can be found in

In this chapter and , we will focus our attention to two semipolar orientations with inclination angles close to $\theta \sim 60°$ that is optimum for indium incorporation efficiency as

predicted by theory[20]: $(10\bar{1}1)$-plane with inclination angle of $\theta = 62°$ and semipolar $(11\bar{2}2)$ with inclination angle of $\theta = 58°$. Moreover, these orientations can be grown as single phase on foreign substrates; the former is grown on patterned Si (001) while the latter is on *m*-sapphire substrates. The Structural and optical properties of the GaN as well as heterostructures grown on these orientations will be discussed and some intrinsic properties of the semipolar planes of GaN including indium incorporation will be studied. Investigation of fabricated LED performances on these orientations especially planar semipolar $(11\bar{2}2)$ layers on *m*-sapphire which is very important as it offers a relatively in-expensive solution to the green gap issue will be discussed as proposed works in next chapter.

In this chapter, our investigations on semipolar $(10\bar{1}1)$ structures grown on patterned Si (001) substrate will be discussed. The content of this chapter is organized as follows. A brief description of substrate and heteroepitaxial GaN layer preparation at first will be followed by investigations of optical anisotropy and excitonic recombination dynamics of AlGaN/GaN heterostructures grown on the prepared GaN layers (in a similar way as demonstrated in section 5.3 for *m*-plane AlGaN heterostructure). Following the result of study of indium incorporation efficiency to this emipolar plane, the limitations of this growth method and the choice of orientation will be discussed at the end.

6.2. Substrate preparation and GaN growth

Wurtzitic GaN grows epitaxially on Si(111) in *c*-direction, with the epitaxial relationships GaN<0001>||Si<111> and GaN<$2\bar{1}\bar{1}0$> || Si<011>. Therefore, the growth of nonpolar and

semipolar GaN on Si is possible if a Si substrate of proper orientation is patterned to expose {111} Si facets for GaN nucleation, as shown schematically in Figure 6.1(a) and (b) for the $(1\bar{1}00)$ and $(1\bar{1}01)$ GaN cases, respectively. For *m*-plane GaN growth, we used Si(112) substrates as discussed in section 5.2. In order to obtain semipolar $(1\bar{1}01)$ GaN surface, we used Si(001) substrates that are miscut 7° toward the Si<110> direction. The substrates were patterned to expose vertical (111)Si facets for growth initiation, with the grooves aligned parallel to the <110> Si direction. For this investigation, the SiO_2 mask was removed in order to increase the surface coverage of GaN and thus enhanced emission intensity with reduce growth time.
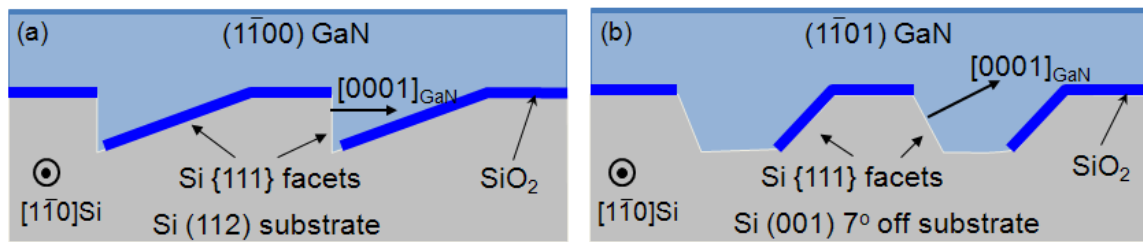
Figure 6.1. (a) Schematic of nonpolar *m*-plane $((1\bar{1}00))$ GaN on patterned Si(112) substrate. In these schematics, top Si(112) surface and the tilted Si(111) facet are both masked with SiO2, so that the GaN growth is initiated at the vertical Si$(\bar{1}\bar{1}1)$ facets. (b) Schematic of semipolar $(1\bar{1}01)$ GaN on patterned Si(001) 7° off-cut substrate. The top Si(001) surface and one of the tilted Si(111) facets are masked with SiO2, so that the GaN growth is initiated at the open Si $(\bar{1}\bar{1}1)$ facets.

Figure 6.2 shows schematically the patterning procedure for case of nonpolar *m*-plane GaN growth on Si (112). First, 100-nm-thick SiNx layer was deposited by plasma enhanced chemical vapor deposition (PECVD) on the entire surface. The SiNx layer was then patterned by using inductively coupled plasma (ICP) etching after standard photolithography to form a mask for subsequent Si wet etching. Anisotropic wet etching of Si was performed in a KOH solution

147

(4.16 M) at 40 °C to form Si {111} facets. After removal of the remaining SiNx mask, a 50-nm-thick AlN layer was grown in a vertical low-pressure MOCVD system on the patterned Si substrate to serve as a seed layer for the GaN growth followed by GaN growth. Similar processes were done for preparation of s-plane GaN on patterned Si (001) with 7° offcut. Figure 6.3 demonstrates SEM images of the coalesced (Figure 6.3(a)) and un-coalesced (Figure 6.3(b)) $\left(1\,\overline{1}01\right)$-plane GaN substrates prepared using this method under different growth and fabrication conditions.
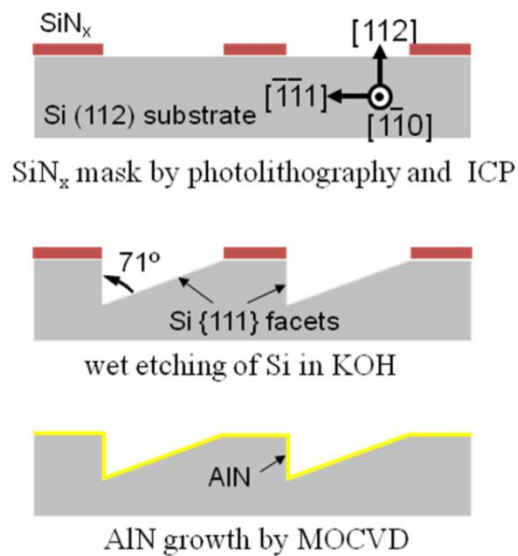
Figure 6.2. Fabrication sequence of Si(112) patterned substrate.
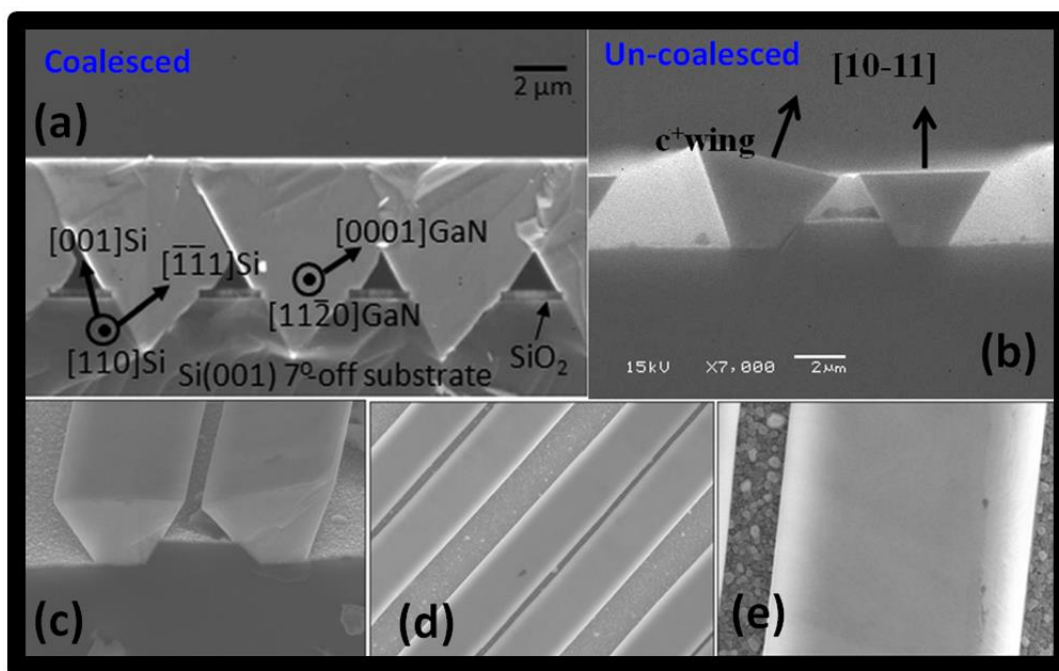
Figure 6.3. Cross-sectional SEM images of (a) coalesced and (b) un-coalesced $(1\bar{1}01)$ GaN on patterned Si(001) substrate with 7° offcut. The inclined (c), and top view (d,e) SEM images of the un-coalesced layers are also shown.

6.3. Excitonic recombination dynamic in $(10\bar{1}1)$ AlGaN/GaN heterostructures

6.3.1. Overview

In this part, similar to what has been demonstrated for nonpolar m-GaN in section 5.3, we examine and demonstrate the temperature dependence and the recombination dynamics in semi-polar $(10\bar{1}1)$-oriented GaN/Al$_{0.2}$Ga$_{0.8}$N multi-quantum wells (MQW).[148] Unlike the study which was performed and described in section 5.3 which was performed on bulk m-plane

substrates, the semi-polar structure was grown on heteroepitaxial GaN on patterned 7º-off silicon (001) substrates. The details about substrate preparation for this study including patterning and growth of GaN buffer layer can be found in section 6.2.

Here, after describing the sample growth procedure and structure schematics, we investigate the emission properties at different temperatures in terms of optical anisotropy followed by some theoretical calculations of oscillator strength. Then, we proceed to temperature dependent photoluminescence measurements, and present experimental results followed by quantitative analysis. At the end, a simple model is developed which enables us to determine the relative populations of free and localized excitons.

6.3.2. Layer Schematics and optical characterizations

Before deposition of the quantum wells, the $(10\bar{1}1)$-oriented GaN (s-plane GaN) buffer was grown on the patterned Si (001) substrate with 7°-off as described in previous sub-subsection, followed by a 30 nm $Al_{0.25}Ga_{0.75}N$ bottom barrier layer. The structure consisted of five GaN QWs with thickness of 1.2-nm separated by 8.5-nm-thick $Al_{0.2}Ga_{0.8}N$ barriers. The structure was completed with 20 nm $Al_{0.2}Ga_{0.8}N$ (top barrier) and 3 nm GaN (cap layer). The schematic of the structure is shown in Figure 6.4. The electron-hole confinement is critical in this multi-quantum well structure as the energy splitting between the confined excitons in the QWs and the ones trapped in the barriers is fairly small. This allows us to simultaneously study the localization of photo-generated carriers in the barriers as well as their delocalization induced by temperature. The sample was mounted in a cryostat (similar way as described in section 5.3) and the temperature varied from 8 to 295 K. The excitation wavelength of 264nm with a 2 ps pulse width and focused laser spot diameter of 100 µm was utilized as described in section 5.3 Similar to

150

measurements performed in section 5.3, owing to the relatively long photoluminescence decay times, laser repetition rate of 4MHz was adapted by means of an acousto-optic modulator. More details about the setup can be found in section 5.3.
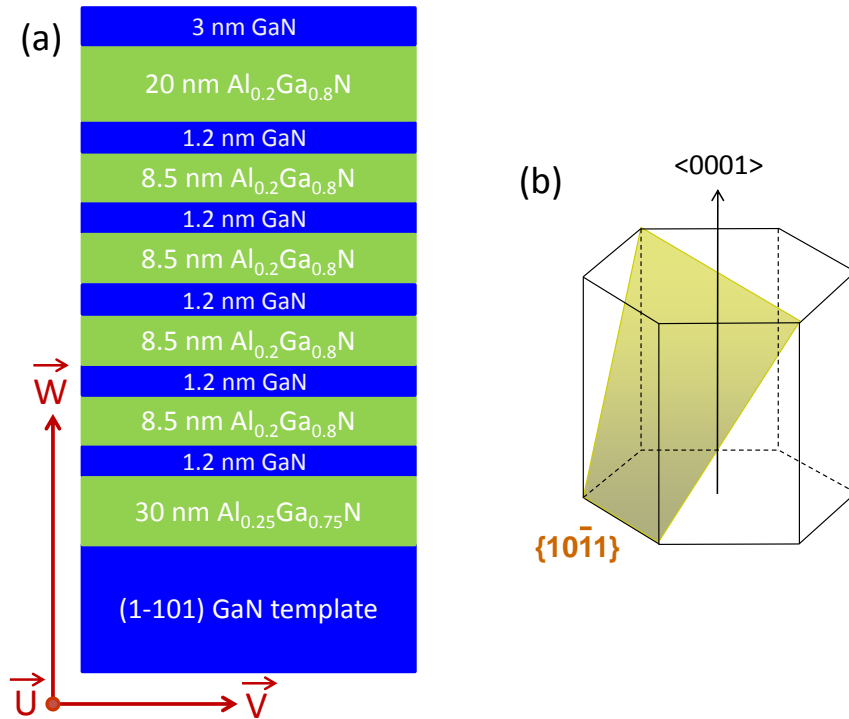
Figure 6.4. (a) Schematic of the semipolar AlGaN/GaN MQW structure and (b) position of $(1\bar{1}01)$ crystallographic plane in GaN wurzite lattice. [Reprinted with Permission from Ref.[148]]

Figure 6.5 demonstrates PL spectra measured at various temperatures in the range from 8 to 295 K. The spectra at low temperature contains two overlapping peaks that correspond to excitons confined in the QWs and the ones localized in the barrier layers.[135] The peak corresponding to AlGaN barriers is quickly suppressed by increasing the temperature. The full-width at half maximum (FWHM) of the PL peaks are moderately large which can be due to

www.manaraa.com

inhomogeneity of compositions and thicknesses. Also, the fluctuations in the alloy composition, and well width and depth fluctuations in the five-period QWs at the position excited by the laser spot could be the reasons behind the large broadening of the quantum well-related PL emission spectra. The broadening in PL is supported by non-uniformity in emission across the stripes which are observed in CL measurement results demonstrated in Figure 6.6. As will be shown below, the Quantum Confined Stark Effect (QCSE) is quite small for such semi-polar orientation but it does not disappear completely. The carrier confinement does not take place in the triangular part of the well for such thin wells (1.2nm). The localization of electrons and holes near opposite sides of the wells caused by internal electric field may also induce inhomogeneous broadening thru slight red-shift of the quantum well-related emission. The presence of such localization can be verified by examination of the PL lifetime in a various set of samples with different orientations.

152
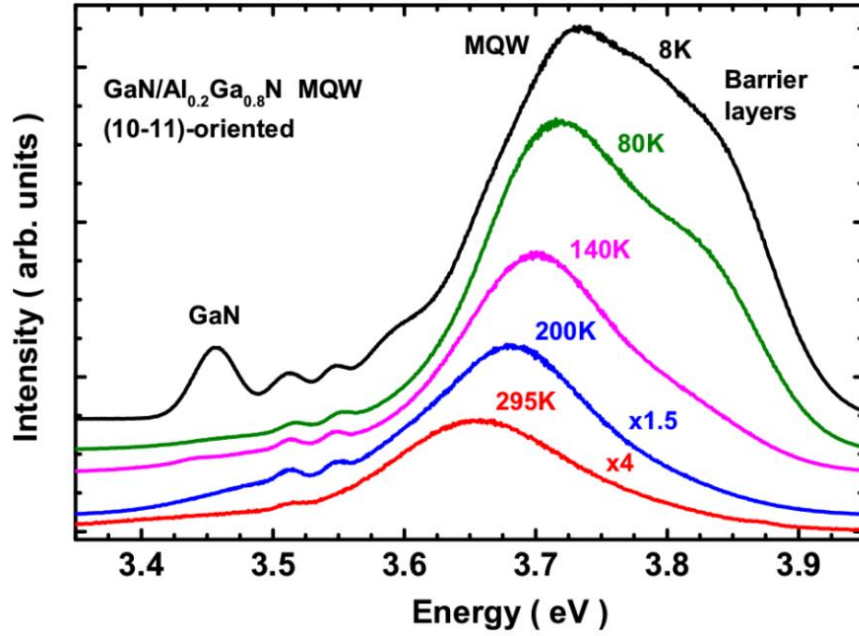
Figure 6.5. Photoluminescence spectra at different temperatures ranging from 8K to 295K. Note the temperature-induced de-trapping of excitons from the barriers to the QWs. [Reprinted with Permission from Ref.[148]]
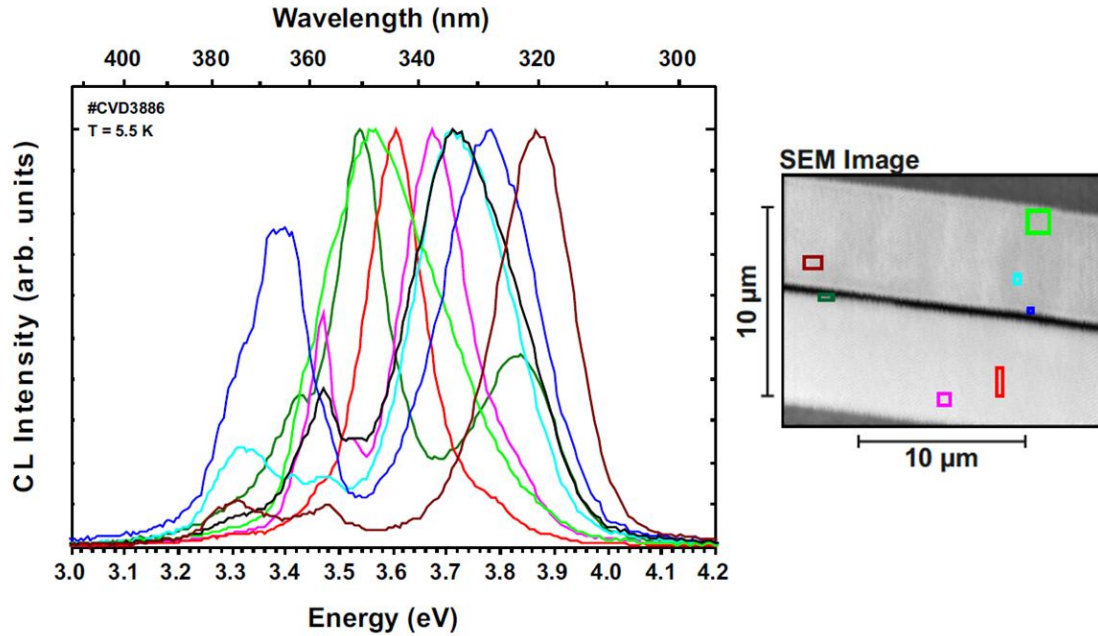
Figure 6.6. CL spectra for the *s*-plane AlGaN/GaN MQWs structure for various regions across the stripes. The figure in the right indicates the corresponding positions at which the CL measurements are performed.

Figures 6.7(a) and (b) represent temperature dependences of the PL peak energy and PL intensity, respectively. As the temperature increases to 300 K, the PL intensity reduces by nearly an order of magnitude. This relative decrease in PL intensity with temperature for semi-polar MQWs is substantially smaller than that observed earlier for nonpolar *m*-plane MQWs, which is indicative of a reasonably good crystalline quality and a fair density of non-radiative defects. The exciton localization energy of ~12 meV was estimated based on the difference between the low-temperature PL data and a fitting using Vina function describing the bandgap variation with temperature.[141]
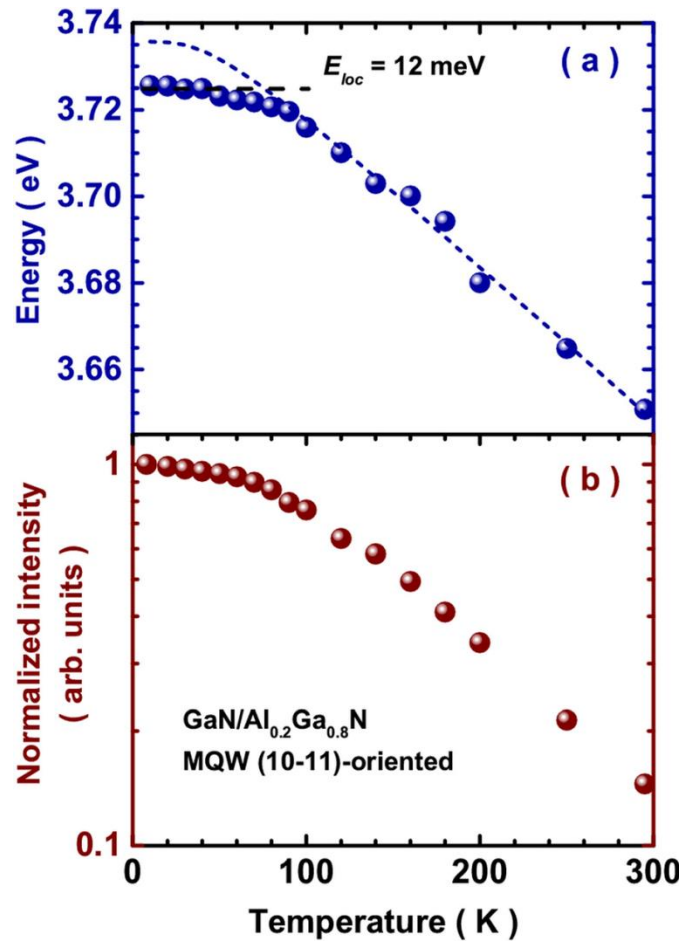
Figure 6.7. Temperature dependent PL (a) peak energy and (b) intensity associated with multi-quantum well emission for the s-plane AlGaN/GaN MQWs. [Reprinted with Permission from Ref.[148]]

6.3.3. Optical Anisotropy

Similar to what we reported on subsection 5.3.2 in case of non-polar *m*-plane, optical anisotropy of the QW related emission is illustrated in Figure 6.8. The experimental value for degree of polarization was found to be 58% which is higher than that the case of *m*-plane which was about 38%. The optical anisotropy for these orientations are expected based on the theory of light interaction with anisotropic medium and can be more quantitatively considered by examination

155

of the physics of the valence band (not shown here). The calculated degree of polarization for this orientation is found to be slightly higher (64%) than the experimental value observed here.
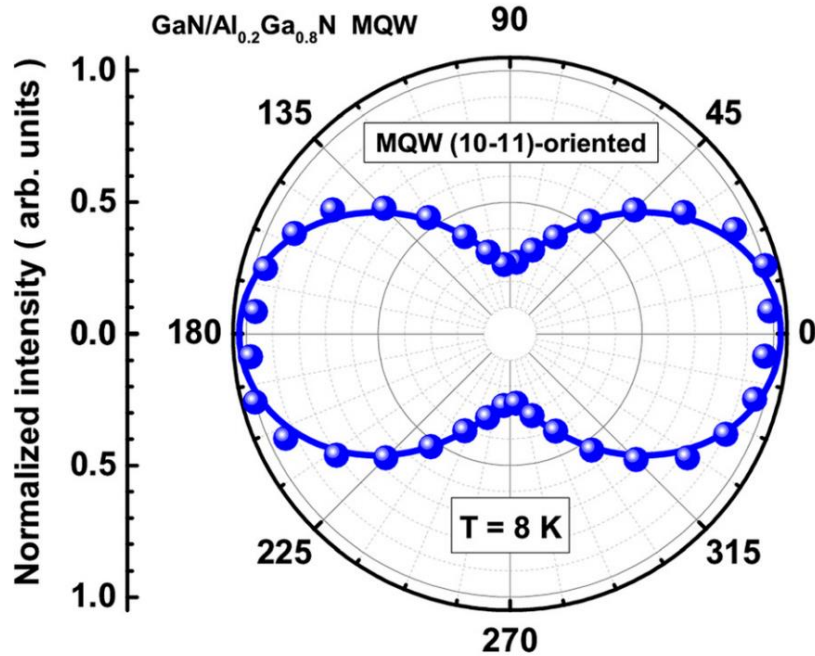
Figure 6.8. Polar plot of normalized PL intensity from the MQWs. The light polarization associated with maximum PL intensity is along <001> direction. [Reprinted with Permission from Ref.[148]]

The valence band dispersion as a function of wave-vector (k) is calculated and plotted in Figure 6.9 the similar way as described and discussed for m-plane structure in subsection 5.3.2. A complex anti-crossing behavior for small values of κ can be observed and the dispersion curve becomes almost parabolic at large values of κ. The dispersion relations for the two low energy hole states (levels 1 and 2) clearly indicate heavier holes compared to those in the higher energy hole state (level 3).
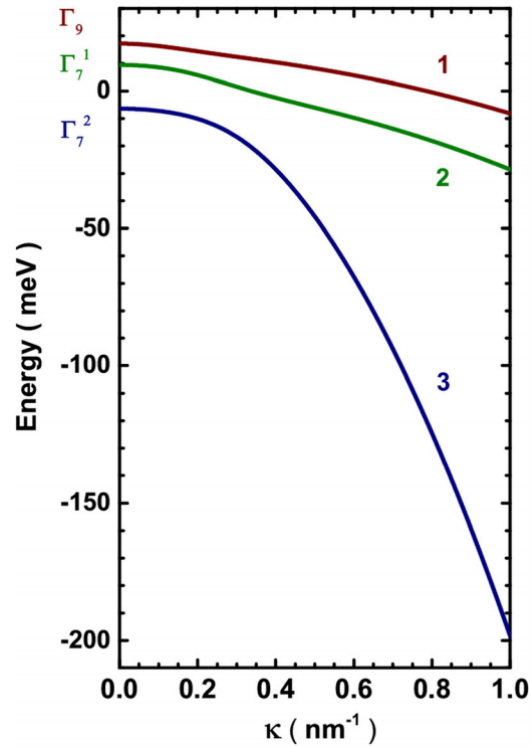
Figure 6.9. E-k diagram (dispersion curve) for the three GaN valence bands and for wavevector orthogonal to the semi-polar $(10\bar{1}1)$-plane (growth plane). [Reprinted with Permission from Ref.[148]]

The eigenvectors can be written in terms of the Bloch states $|\vec{x}\rangle$, $|\vec{y}\rangle$ and $|\vec{z}\rangle$ as $|\Psi_j\rangle = \sum_{i=1}^{i=3} c_{ij}|u_i\rangle$. Figure 6.10 shows the relative proportions of $|\vec{x}\rangle$, $|\vec{y}\rangle$ and $|\vec{z}\rangle$ Bloch states as a function of κ for the valence eigenstates, with hole energy increasing from left to right (1 to 3).

157

www.manaraa.com
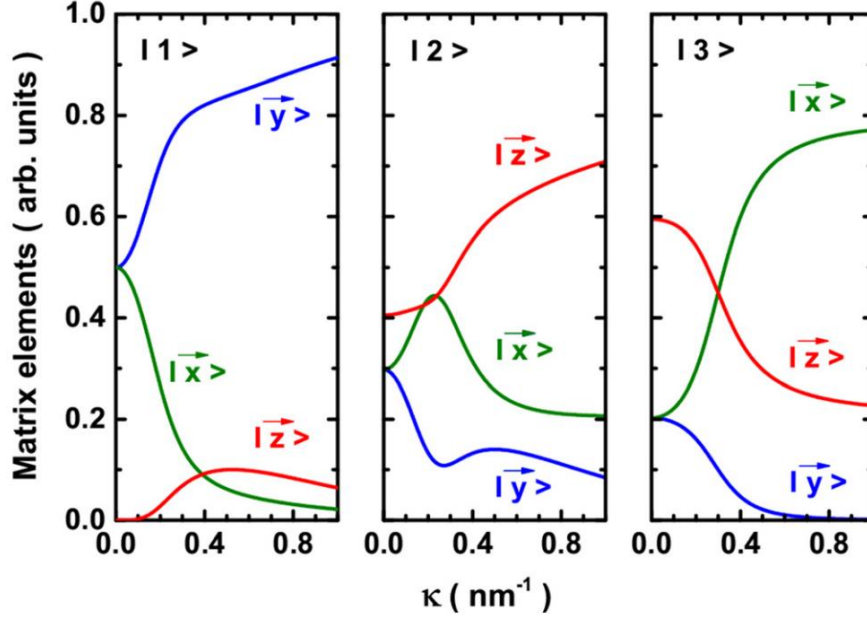
Figure 6.10. The eigenvectors expanded in terms of $|\vec{x}\rangle$, $|\vec{y}\rangle$ and $|\vec{z}\rangle$ Bloch states. [Reprinted with Permission from Ref.[148]]

When the photon is polarized along the $\vec{U}$ direction ($\vec{y}$ -polarized photon, Poynting $\vec{\pi}$ vector along $\vec{W}$), the transitions between confined electron and hole levels can be observed with intensity that is proportional to the electron-hole envelope functions overlap multiplied by $\dfrac{|c_1^Y|^2}{2}$, or $\dfrac{|c_2^Y|^2}{2}$, or $\dfrac{|c_3^Y|^2}{2}$. When the photon is polarized along the $\vec{V}$ direction, on the other hand, this transition can be detected with intensities proportional to the electron-hole envelope functions overlap multiplied by $\dfrac{3a^2}{3a^2+4c^2}\dfrac{|c_1^X|^2}{2}$, or $\dfrac{3a^2}{3a^2+4c^2}\dfrac{|c_2^X|^2}{2}$, or $\dfrac{3a^2}{3a^2+4c^2}\dfrac{|c_3^X|^2}{2}$ for the x -polarized photons (Poynting $\vec{\pi}$ vector along $\vec{U}$) and to the electron-hole envelope functions overlap times

158

$$\frac{4c^2}{3a^2 + 4c^2} \frac{\left|c_1^z\right|^2}{2}, \quad \frac{4c^2}{3a^2 + 4c^2} \frac{\left|c_2^z\right|^2}{2}, \quad \text{or} \quad \frac{4c^2}{3a^2 + 4c^2} \frac{\left|c_3^z\right|^2}{2} \quad \text{for the } \vec{z} \text{-polarized photons (Poynting } \vec{\pi}$$

vector along $\vec{W}$).

Figure 6.11 demonstrates the contributions of *x*-, *y*- and *z*-polarized photons as a function of K with Poynting vectors along either $\vec{W}$ or $\vec{U}$, for the three eigenvectors (1, 2, and 3). According to the plot, the transition with highest intensity in $\vec{E} // \vec{U}$ polarization (*y*-polarization) corresponds to transition from confined electron to confined hole from the first valence band (from Γ_9) for small values of κ. However, the situation changes with increasing κ. For large values of κ, the most probable transition is the one from confined electrons state to the confined holes from third valence band. As for the $\vec{E} // \vec{V}$ configuration, most of the optical response comes from the z-polarized photons.

159
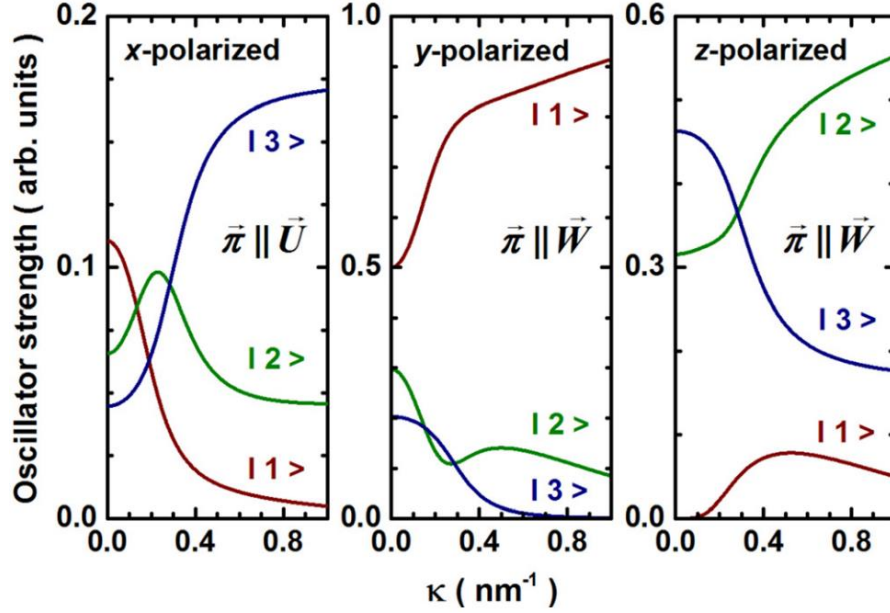
Figure 6.11. Calculated oscillator strength for the three band to band transitions (electrons confined states to confined holes in three valence band states) for different polarization of the photon: x polarization and Poynting $\vec{\pi}$ vector along $\vec{U}$ (left), polarization of the photon along y and z with Poynting $\vec{\pi}$ vector along $\vec{W}$ (middle and right, respectively). [Reprinted with Permission from Ref.[148]]

The comparison of valence band dispersion relations for polar *c*-plane, nonpolar *m*-plane, and semipolar $(10\bar{1}1)$ planes are performed which is demonstrated in Figure 6.12. The interesting point is the overall identical shapes of dispersion curves regardless of the orientation of the crystallographic plane. The QCSE (whether present or absent) seems to be more critical for correlating PL energy and a decay time to the thickness of a wurtzite quantum well rather than the anisotropy of the materials used for growing the structure.
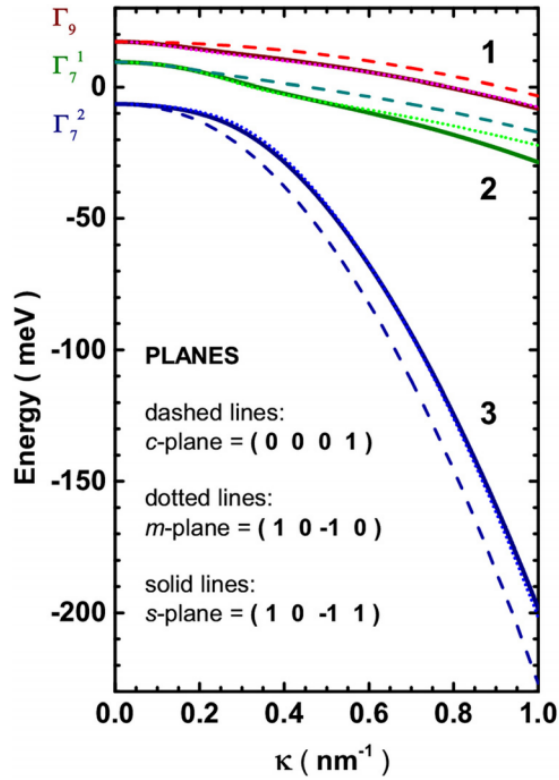
Figure 6.12. Dispersion relations calculated for the three GaN valence bands for κ orientation perpendicular to the polar (0001) plane (c-plane), the $(10\bar{1}0)$ nonpolar plane (m-plane), and the semipolar $(10\bar{1}1)$ plane (s-plane). Note the overall identical shapes of the dispersion curve for polar, nonpolar and semipolar planes. [Reprinted with Permission from Ref.[148]]

6.3.4. Excitonic Recombination Dynamics

Figure 6.13 demonstrates PL transients with mono-exponential decay times for various temperatures ranging from 8 to 295 K obtained from the m-plane GaN MQWs for photons polarized along y direction so that heavy-hole excitons can be probed.
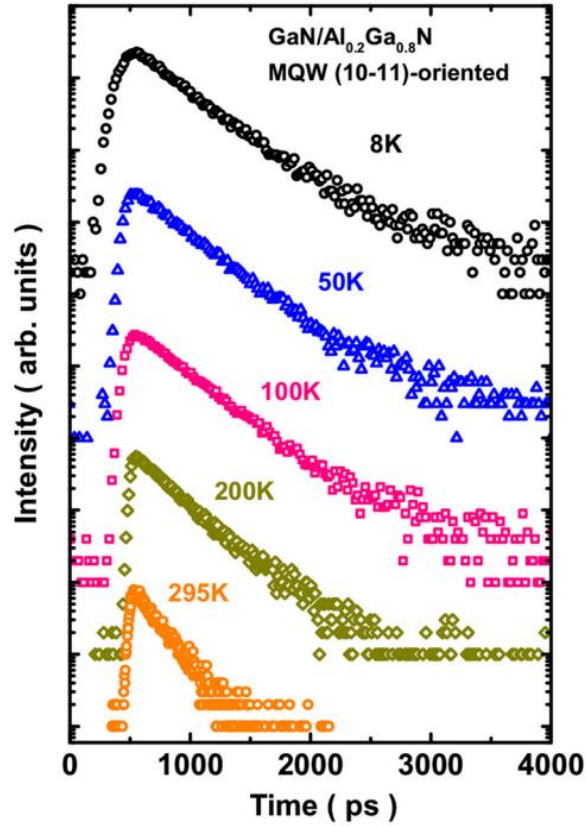
Figure 6.13. Several PL transients for various temperatures range from 8 to 295K with mono-exponential decays from the semipolar $(10\bar{1}1)$ AlGaN/GaN QWs measured for phonon polarization along y-direction. [Reprinted with Permission from Ref.[148]]

Here, we intend to separate the contributions of radiative and non-radiative recombination processes. The PL intensity decays exponentially with respect to time after the excitation pulse, based on

$$I \propto \Gamma_{rad} \cdot e^{-\Gamma t}, \qquad (6.1)$$

where Γ_{rad} is the radiative recombination rate and Γ, is the sum of the radiative and the nonradiative contribution Γ_{nonrad} of the recombination rate. Integrating over time gives us the following expression for the PL intensity for CW condition

$$I_{CW} \simeq \frac{\Gamma_{rad}}{\Gamma}. \qquad (6.2)$$

Normalizing the CW intensity with respect to the intensity obtained at 2 K we get

$$\frac{I_{CW}(T)}{I_{CW}(2K)} = \frac{\Gamma(2K)}{\Gamma_{rad}(2K)} \frac{\Gamma_{rad}(T)}{\Gamma(T)}. \qquad (6.3)$$

Assuming that decay mechanism at low temperature is purely of radiative origin, the expression simplifies to

$$\frac{I_{CW}(T)}{I_{CW}(2K)} \approx \frac{\Gamma_{rad}(T)}{\Gamma(T)}, \qquad (6.4)$$

Based on the literature studies,[130], [143], [149]–[152] we can assume that the recombination rate Γ being sum of recombination rates of free and localized weighted by their respective populations:

$$\Gamma = \frac{n_{free}}{n_{free} + n_{loc}} \Gamma_{free} + \frac{n_{loc}}{n_{free} + n_{loc}} \Gamma_{loc} \qquad (6.5)$$

As mentioned earlier, the localization energy, E_{loc}, has been been estimated as 12 meV. We can assume that this localization prevents the localized excitons from moving to the non-radiative recombination centers. Therefore, we assume that in this model, the recombination rate for the

163

localized excitons is the radiative recombination rate while the sum of two different contributions is assumed for free excitons; a radiative one $\Gamma_{free-rad}$ and a non-radiative one $\Gamma_{free-nonrad}$. Therefore, we can write

$$\Gamma = \left[\frac{n_{loc}}{n_{free} + n_{loc}} \Gamma_{loc} + \frac{n_{free}}{n_{free} + n_{loc}} \Gamma_{free-rad} \right] + \frac{n_{free}}{n_{free} + n_{loc}} \Gamma_{free-nonrad}, \tag{6.6}$$

$$\Gamma_{rad} = \left[\frac{n_{loc}}{n_{free} + n_{loc}} \Gamma_{loc} \frac{n_{free}}{n_{free} + n_{loc}} \Gamma_{free-rad} \right], \tag{6.7}$$

and

$$\Gamma_{nonrad} = \frac{n_{free}}{n_{free} + n_{loc}} \Gamma_{free-nonrad}. \tag{6.8}$$

The density of excitons with an energy E_{free} can be calculated as follows:

$$n_{free} = 4 \frac{Mm_0}{2\pi\hbar^2} \int_{E_{free}}^{\infty} \frac{dE}{1 + \exp\left(\frac{E - E_F}{kT} \right)}, \tag{6.9}$$

where $\frac{Mm_0}{2\pi\hbar^2}$ is the spinless two-dimensional areal density of states, m_0 is the electron mass at rest, E_F is the Fermi energy, and M is the translational mass of the exciton. The factor 4 accounts for electron and hole spins. Replacing the Fermi-Dirac distribution with a Maxwell-Boltzmann form in the above equation, it can be rewritten as

$$n_{free} = 2\frac{Mm_0}{\pi\hbar^2} \int_{E_{free}}^{\infty} \exp\left(-\frac{E-E_F}{kT}\right) \tag{6.10}$$

which then gives

$$n_{free} = 2\frac{Mm_0}{\pi\hbar^2} kT \exp\left(-\frac{E_{free}-E_F}{kT}\right) \tag{6.11}$$

or

$$n_{free}(cm^{-2}) \approx 7.2\times10^{10} \cdot M \cdot T \exp\left(-\frac{E_{free}-E_F}{kT}\right). \tag{6.12}$$

Similarly, the population of excitons which are localized by interfacial defects with density N_D at an energy E_{loc} below the free exciton band is given by

$$n_{loc} = N_D \exp\left(-\frac{E_{free}-E_{loc}-E_F}{kT}\right) \tag{6.13}$$

The recombination rates as the reciprocal analogs of each decay times (see Equation 12 of Ref.[143])

$$\frac{1}{\tau} = \left[\frac{n_{loc}}{n_{free}+n_{loc}}\frac{1}{\tau_{loc}} + \frac{n_{free}}{n_{free}+n_{loc}}\frac{1}{\tau_{free-rad}}\right] + \frac{n_{free}}{n_{free}+n_{loc}}\frac{1}{\tau_{free-nonrad}} = \frac{1}{\tau_{rad}} + \frac{1}{\tau_{nonrad}}, \tag{6.14}$$

which then leads to

165

$$\frac{I_{CW}(T)}{I_{CW}(2K)} \approx \frac{\tau(T)}{\tau_{rad}(T)} = \frac{\tau_{nonrad}(T)}{\tau_{rad}(T) + \tau_{nonrad}(T)}. \tag{6.15}$$

A plot of the effective decay time (or PL decay time) $\tau(T)$ (blue), non-radiative decay time $\tau_{nonrad}(T)$ (green), and radiative decay time $\tau_{rad}(T)$ (brown) are plotted in Figure 6.14. The non-radiative decay time is thermally activated: $\tau_{nonrad}(T) = \tau_1 \exp(T_a/T)$ with $T_a = 215$ K and τ_1 = 160 ps. It can be observed that the non-radiative decay time saturates to about 220 ps at room temperature. Such low non-radiative recombination rate could be indicative of relatively high crystalline quality of the layer.
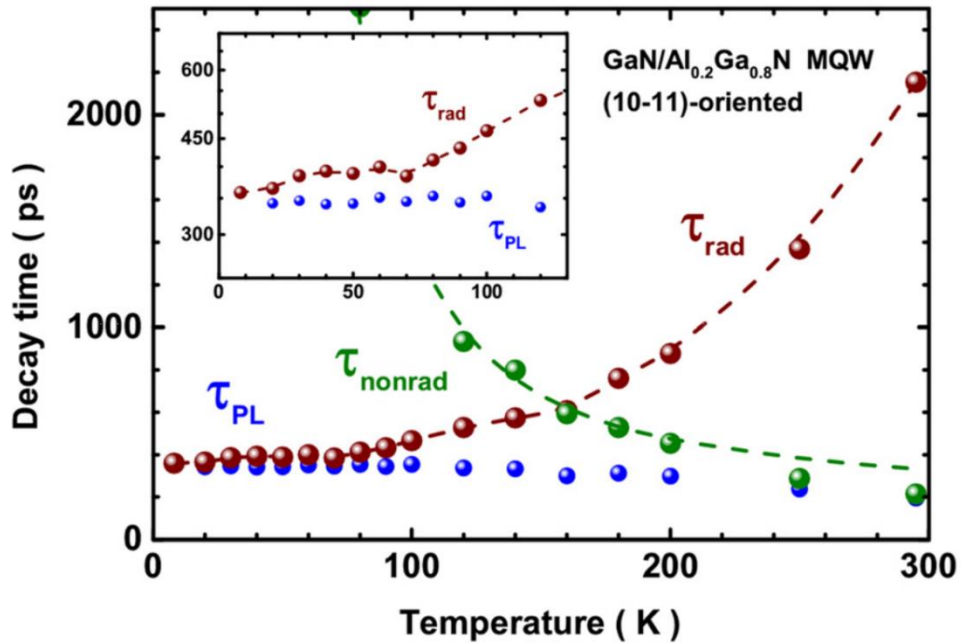
Figure 6.14. PL decay time (blue dots), nonradiative decay time (green dots), and radiative decay time (brown dots) including nonlinear fitting to the non-radiative component as well as radiative ones as dashed lines. The inset is logarithmic plot zoomed at low temperature region to display the effect of the transition of excitons from localized to free states on the radiative decay time. [Reprinted with Permission from Ref.[148]]

As mentioned before, in a two-dimensional system, the radiative decay time should be a linear function of temperature. For nonpolar oxides and nitrides with the wurtzite structure, the radiative decay time for free excitons increases linearly with T, with a slope of about 8 ps K^{-1} detailed discussion of which can be found in Refs.[144], [146] for various growth orientations.

The dependence of the radiative decay that is nonlinear in our case (see Figure 6.14) can be due to the contribution of both free and localized excitons in the PL spectrum. The radiative decay time of localized excitons τ_{loc} is independent of temperature and is attained from the low temperature decay time measurements as $\tau_{loc} = 355$ ps.

We tend to compute the relative populations of free and localized excitons versus temperature together with the contributions of the different recombination rates in order to gain a better insight into the evolution of the PL intensity and lifetime with temperature. Assuming an average value of 1.2 m_0 for the exciton translation mass, and localization energy $E_{loc} = 12$ meV measured as discussed earlier in this sub-subsection, the recombination rate can be calculated and the contributions of free and localized excitons using one fitting parameter, N_D. Figure 6.14 also shows the fitted curves for the non-radiative (dashed green curve) and radiative (dashed brown curve) components giving $N_D = 2.3\times10^{12}$ cm^{-2} for radiative component. This value is comparable to the ones reported by Corfdir et al.[153], [154] for a-plane GaN/Al$_{0.06}$Ga$_{0.94}$N quantum wells (N_D ranging from 2.2×10^{12} cm^{-2} to 4×10^{12} cm^{-2}) and a-plane GaN/Al$_{0.12}$Ga$_{0.88}$N quantum wells (1×10^{13} cm^{-2}). It is also comparable to our report for m-plane GaN/Al$_{0.14}$Ga$_{0.86}$N MQWs (0.2×10^{12} cm^{-2}) demonstrated earlier in this chapter. Since for all of these layers, GaN is the confined layer which is a binary compound, the localized exciton can be directly related with the interfacial defect density. For studying of InGaN-based heterostructures this is not the case as

167

InGaN is ternary and it is known that localization is also associated with presence of indium-rich regions.[155]

Figure 6.15 demonstrates a comparison between the variations of the radiative lifetimes obtained for the MQWs grown on nonpolar *m*-plane and *a*-plane as well as semipolar $(10\bar{1}1)$ orientation. The fitting values for the *m*-plane structure are E_{loc}=13 meV and $N_D = 2.2\times10^{11}$ cm^{-2} and the data corresponding to *a*-plane are taken from Refs.[130], [153], [154].
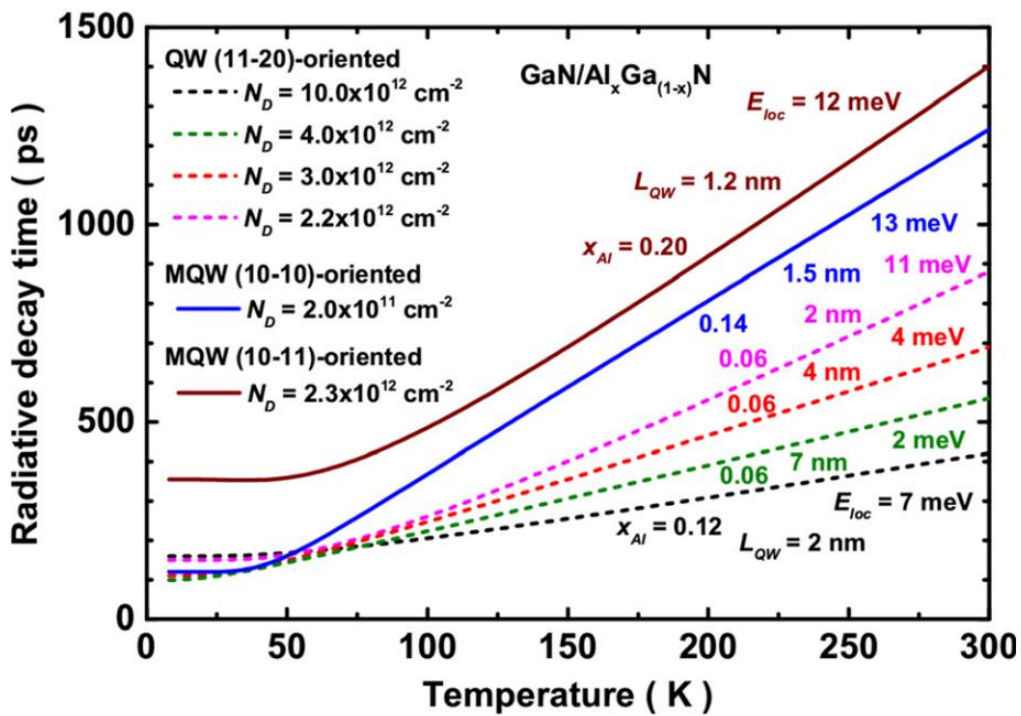
Figure 6.15. Radiative decay times as a function of temperature for nonpolar $(11\bar{2}0)$ *a*-plane and $(10\bar{1}0)$ *m*-plane and semipolar $(10\bar{1}1)$ orientations. The interfacial defect densities, aluminum compositions, well width, and localization energies are indicated for each curve separately in the plots. The data for $(10\bar{1}1)$ and $(10\bar{1}0)$ orientations are based on the works performed in this sub-subsection and our data presented in section 4.3.2, respectively, while the a-plane data are taken from Corfdir et al.[153], [154]. [Reprinted with Permission from Ref.[148]]

According to the plot of Figure 6.15, for all QW structures grown in nonpolar *m*-plane and *a*-plane orientations we have $\tau_{loc} \sim 100\text{–}160$ ps regardless of the aluminum content in the barriers and well widths (they change from 1.5 nm to 7 nm). This could mean that regardless of the growth methods and conditions, there is a universal behavior associated with the radiative decay time of localized excitons. Another point here is that, the higher value for the semipolar $(10\bar{1}1)$ orientation $\tau_{loc} = 355$ ps compared to all nonpolar structures indicate the presence of moderate internal electric field in the semipolar GaN layers which induces a slight shift of the electron and hole wave functions to the opposite interfaces producing an additional weak localization. Moreover, the slopes for the radiative decay time versus temperature depend on the relative populations of free and localized excitons. In order to demonstrate this dependency quantitatively, we plot the relative populations of free and localized excitons in Figure 6.16 for our samples together with the ones studied by Corfdir *et al*.[153], [154].

The temperature dependence of the relative populations of free and localized excitons for the GaN QWs with *m*-plane, *s*-plane, and the *a*-plane orientation are manifested in Figure 6.16. The temperature for the population crossover will affect the radiative decay time. Therefore, a global behavior is demonstrated in the study of the experiments obtained in both groups. However, the data for *a*-plane show that the population crossover can happen in various temperatures which at this point can be most likely due to growth conditions, substrate surface preparation, *etc*.

169
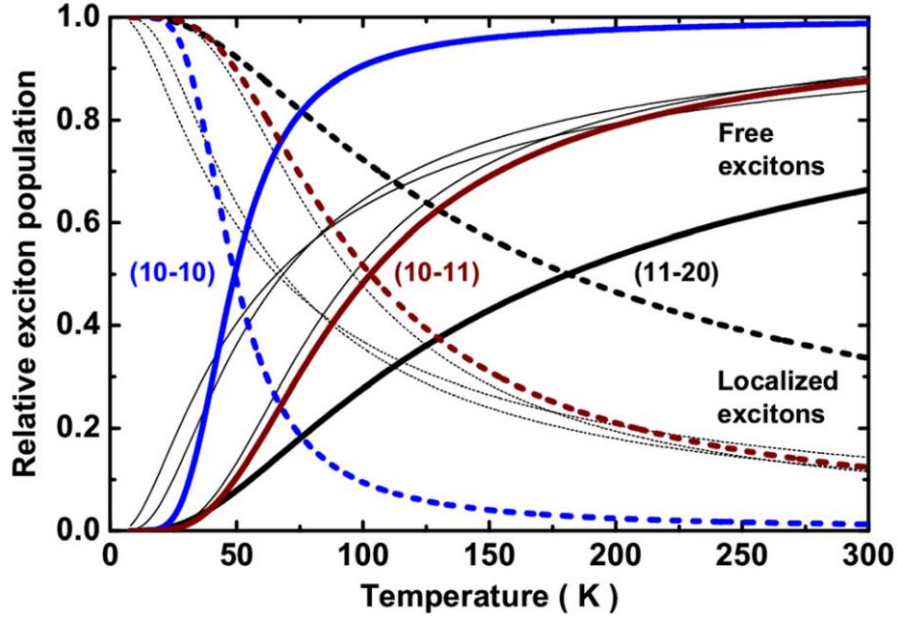
Figure 6.16. Relative populations of free (solid lines) and localized excitons (dashed lines) for semipolar *s*-plane (brown), nonpolar *m*-plane (blue), and nonpolar *a*-plane (black and grey), The data for $(10\bar{1}0)$ (discussed in subsection 5.3.3) and $(10\bar{1}1)$ (discussed here) orientations are our data, while the a-plane data are taken from Corfdir et al.[130], [153], [154]. [Reprinted with Permission from Ref.[148]]

6.3.5. Summary of Findings

As a summary of this sub-subsection, the semipolar $(10\bar{1}1)$ GaN/AlGaN MQWs gron on patterned Si (001) demonstrate low non-radiative recombination rates, robust temperature dependent PL, and a thermally stable population of free and localized excitons. This seems to be a promising approach for production of low-cost UV emitting devices. An effective density of interfacial defects of $N_D = 2.3 \times 10^{12}$ cm^{-2} and radiative recombination time for the localized excitons of $\tau_{loc} = 355$ ps was found for this semipolar orientation. The value for τ_{loc} for this semipolar plane is significantly larger than the reported values for the nonpolar *m*-plane and *a*-

plane structures (100–160 ps) which can be attributed to the presence of an internal electric field inducing an additional weak localization in the semipolar QWs.

6.4. Optical investigation of microscopic defect distribution in semi-polar $(10\bar{1}1)$ InGaN light emitting diodes

6.4.1. Overview

semipolar GaN growth often suffers from high density of extended defects such as threading dislocations and stacking faults, resulting in lower crystal quality.[156] Therefore, material quality needs to be improved further to take full advantage of semipolar orientation of GaN and comprehensive studies of effects of extended defects are required. In this work,[157] correlations between microscopic optical and structural properties in semipolar InGaN LEDs were investigated by means of spatially and spectrally resolved near-field scanning optical microscopy (NSOM).

6.4.2. Experimental details

Semipolar $(10\bar{1}1)$ GaN layers and InGaN LEDs were grown on patterned Si substrates in a low-pressure vertical metalorganic chemical vapor deposition (MOCVD) system. Si (001) substrates with an offcut by 7° toward the Si<110> direction were patterned to form grooves of 10 μm width separated by 3 μm terraces, the sidewalls of which were {111} facets. The 3 μm × 10 μm

pattern was chosen to prevent the coalescence of the growing wings which would result in inferior optical quality of the layers. The patterning procedure and initiation of GaN growth on the Si (111) facets exposed within the grooves have been described elsewhere.[120]
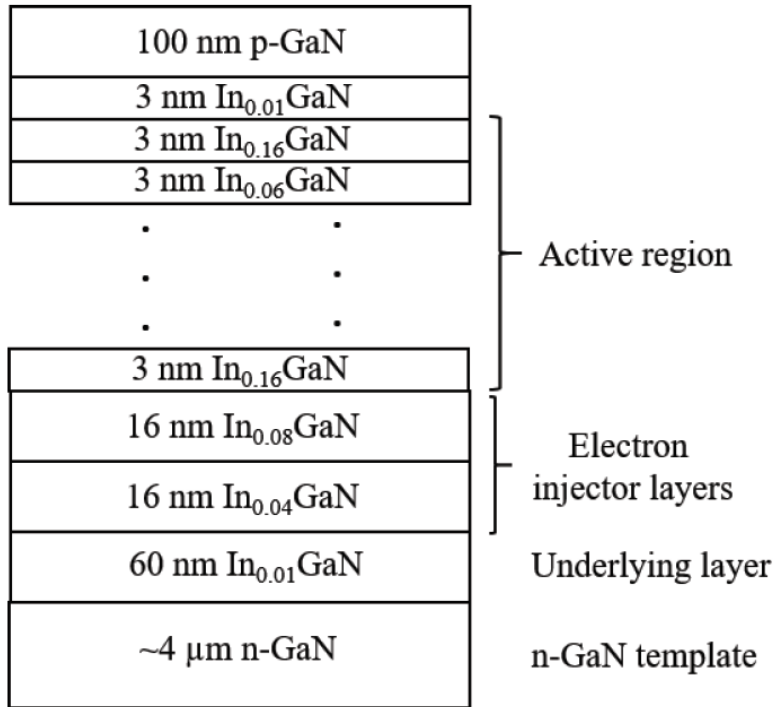
Figure 6.17. Cross-sectional schematic of the LED structures grown on semipolar $(1\bar{1}01)$ templates.[157]

LED structures incorporate, as shown schematically in Figure 6.17, a Si-doped $In_{0.01}Ga_{0.99}N$ underlying layer for improving the quality of overgrown layers, electron injectors composed of $In_{0.04}GaN$ and $In_{0.08}GaN$ layers for efficient thermalization of hot carriers prior to injection into the active region, six periods of 3 nm-thick In0.16GaN wells separated by 3 nm-thick $In_{0.06}GaN$ barriers as the active region, and a 100 nm-thick Mg-doped p-type GaN, grown

in the given order on top of $(10\bar{1}1)$ GaN templates. NSOM measurements were performed at 85

K using a Cryoview 2000 NSOM system (Nanonics Imaging Ltd) in the illumination mode

where HeCd (3.81 eV or 325 nm wavelength) and InGaN (3.06 eV or 405 nm wavelength) laser

excitation were used through a Cr-Al coated cantilevered optical fiber probe with 350 nm

aperture.

6.4.3. Results and Discussions: $(10\bar{1}1)$ GaN

Angled-view scanning electron microscope (SEM) image of a semipolar $(10\bar{1}1)$ GaN layer on

patterned Si is shown in Figure 6.18(a). One of the {111} Si sidewalls was coated with SiO_2 to

prevent nucleation and growth of GaN started from the other sidewall and continued in the GaN

[0001]$c+$ direction ($c+$ wing). Growth in the [0001] $c-$ direction ($c-$ wing) is very limited due to

the given geometry. It is evident that the layers did not coalesce and roughly 13 μm-wide GaN

stripes formed on patterned Si. Using 3.81 eV excitation, steady-state macroscopic (incident

laser beam diameter of 100 μm) PL spectrum was measured at 85K and is presented in Figure

6.18(b). Peaks at 3.457 eV, 3.406 eV and 3.296 eV correspond to the donor bound exciton

(D0X), basal-plane stacking fault (BSF), and donor-acceptor pair (DAP) emission, respectively.

Longitudinal optical (LO) phonon replicas of D0X emission as well as the yellow emission band

of GaN are also observed as indicated in the figure.

173
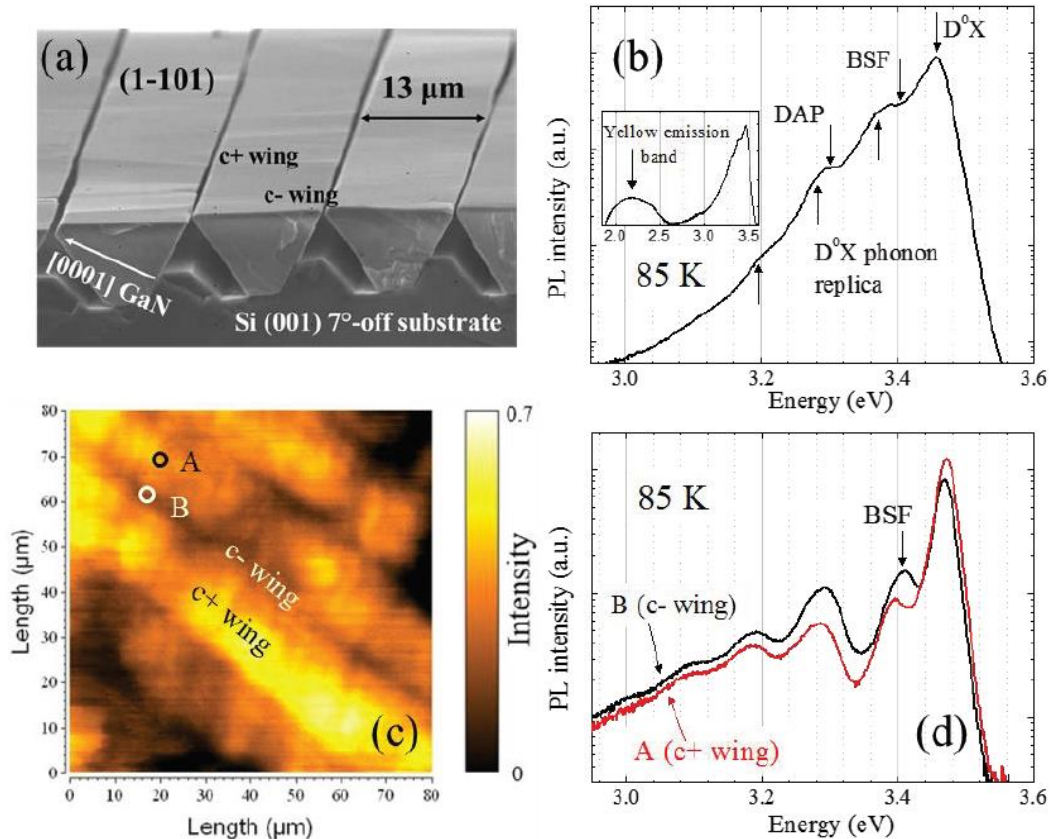
Figure 6.18. (a) Angled-view SEM image, (b) Macroscopic PL spectra (D0X, BSF, and DAP emission peaks are marked), and (c) NSOM PL intensity map of semipolar $(1\bar{1}01)$ GaN. (d) Local PL spectra for the points indicated in (c).[157]

Figure 6.18(c) shows the 85K NSOM PL intensity map where the PL spectra were integrated up to 3.54 eV (*i.e.* above 350 nm). It is evident that the intensity of PL emission from the $c+$ wings is stronger than the emission from $c-$ wings. For the particular section mapped, the darker regions observed in the bottom left and top right corner of the figure are due to presence of high density of threading dislocations and point defects which act as nonradiative recombination centers. Local PL spectra were collected at different points along and across the $c+$ and $c-$ wings. PL spectra of two representative points, A in the $c+$ wing and B in the $c-$ wing,

174

are shown in Figure 6.18(d). D0X peak intensity at point B is lower than that at point A. Moreover, B shows clear BSF emission peak at 3.41 eV whereas at point A, phonon replica of D0X dominates at 3.397 eV and BSF emission is not very clear. This implies that stacking fault density at point B, located on the c- wing, is higher than at point A, on c+ wing. Using spatially and spectrally resolved cathodoluminescence (CL) technique, Okur *et al.* [158] also reported that the optical quality of *c-* wings was much lower than *c+* wings because of the presence of higher density of TDs and BSFs.

6.4.4. Results and Discussions: $(10\bar{1}1)$ InGaN LED

Angled-view SEM image of the semipolar $(10\bar{1}1)$ InGaN LEDs is shown in Figure 6.19(a). Coating of one of the sidewalls with SiO_2 was not employed for this particular sample, which led to growth of GaN on both sidewalls. After establishing the lateral extension as shown in the SEM image, the LED active region and the p-GaN layers were grown. NSOM PL measurements were carried out using below GaN bandgap excitation (3.06 eV) to avoid influence of the top p GaN layer.
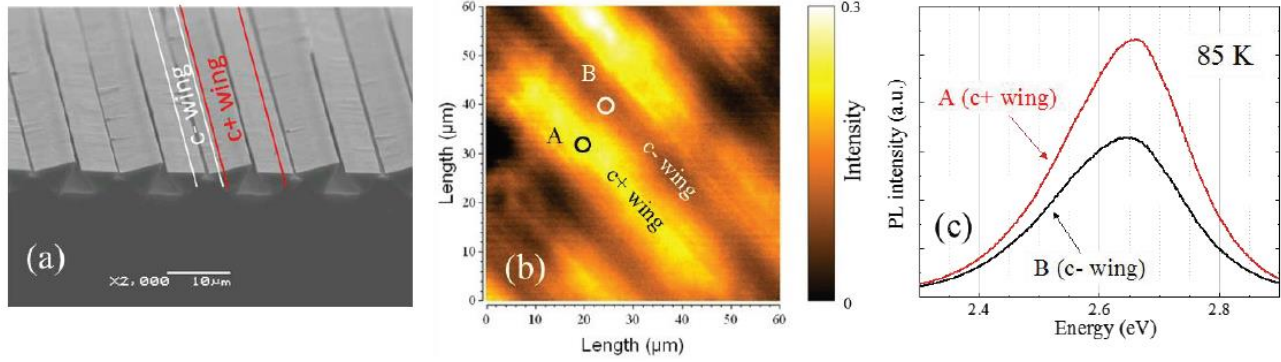
Figure 6.19. (a) Angled-view SEM image, and (b) NSOM PL intensity maps of semipolar $(1\bar{1}01)$ LEDs. (c) Local PL spectra for the two points indicated in (b).[157]

NSOM PL map (See Figure 6.19(b)) shows that $c+$ wings are dominated by strong active region emission whereas emission from $c-$ wings are relatively weaker. Local PL spectra were collected at multiple points along and across the $c+$ and $c-$ wings and two representative spectra are shown in Figure 6.19(c). It is evident that the PL intensity of $c+$ wing (point A) is stronger than that of $c-$ wing (point B), consistent with the observation in $(10\bar{1}1)$ GaN layers. Moreover the emission peak of $c-$ wing is 15 meV red-shifted compared to that of $c+$ wing indicating higher Indium incorporation in the $c-$ wing which could be induced by the presence of high density of stacking faults.

6.4.5. Summary of Findings

In summary, the spatial variations of extended defects, stacking faults and threading dislocations, and their effects on the optical quality for semi-polar $(10\bar{1}1)$ InGaN light emitting diodes (LEDs) were investigated by near-field scanning optical microscopy at 85 K. In case of $(10\bar{1}1)$

176

www.manaraa.com

GaN layers, the near-field PL from the $c+$ wings was found to be relatively strong and uniform across the sample but the emission from the $c-$ wings was substantially weaker due to the presence of high density of threading dislocations and basal plane stacking faults as shown by the local PL spectra. Similarly, in $(10\bar{1}1)$ InGaN LED structures, $c+$ wings showed comparatively stronger active region emission than $c-$ wings. Moreover, a slight red shift of active region PL peak emission in $c-$ wings compared to that in $c+$ wings could be due to presence of high stacking fault density in $c-$ wings.

6.5. Indium incorporation into semipolar $(10\bar{1}1)$ InGaN heterostructures

6.5.1. Overview

In order to better evaluate the $(10\bar{1}1)$ orientation for potential applications as alternatives for conventional c-plane green emitters, the enhancement in indium incorporation into $(10\bar{1}1)$-plane of GaN (predicted by theory) will be examined in this section. Although recent theoretical calculations have predicted more efficient indium incorporation in the semipolar orientations of wurtzite GaN with inclination angles of $\theta \sim 60°$,[20] preliminary experiments in regards to the In incorporation do not appear to be conclusive,[49], [159] which makes the said experimental investigation all the more important and urgent. Incisive experimental work is imperative to test the theory.

6.5.2. Experimental details

To study indium incorporation in semipolar $(1\bar{1}01)$ GaN in comparison with polar c-plane material, single and multiple $(1\bar{1}01)$ GaN/InGaN/GaN double heterostructures (DH) have been grown by MOCVD on patterned Si(001) substrates together with c-plane counterparts on Si(111) flat substrates in the same growth run. The thickness of InGaN layers was chosen to be no less than 4 nm to avoid the influence of quantum confinement. In case of multiple DHs, 4-nm $In_{0.01}Ga_{0.99}N$ barriers were used to separate the active regions. To provide the possibility to grow the whole structures including AlN nucleation layer, GaN buffer, and InGaN-based active

178

regions capped with GaN in one growth run, SiO$_2$ masking layers were not used in these experiments. Conventional planar layers were grown on Si(111) substrates, while the natural selectivity of GaN/AlN nucleation on Si(111) facets of the patterned Si(001) substrates gave rise to the structures with triangular cross-sections as seen in Figure 6.20. Note that no growth took place on the grove bottoms and only a thin layer is observed on top of Si terraces, because nucleation on Si(111) facets and consequent growth of GaN in the (0001)GaN direction proceed much faster than the growth of GaN nucleated on Si(001) facets (natural selectivity).
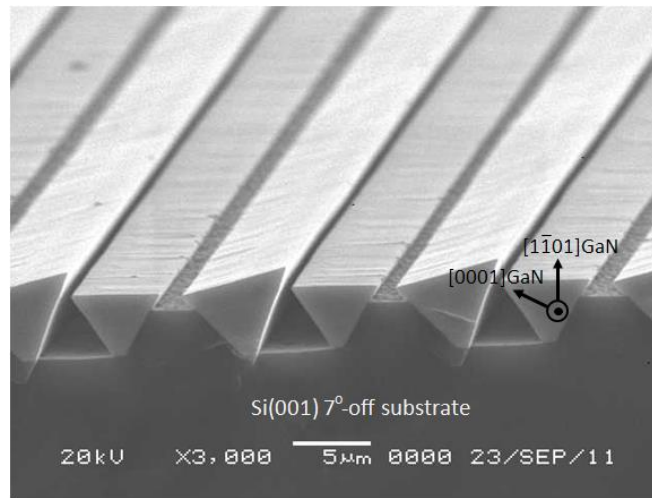
Figure 6.20. Cross-sectional inclined SEM image of $\left(10\overline{1}1\right)$ GaN/InGaN/GaN heterostructure grown on Si(001) substrate without SiO$_2$ masking layer. The surface undulations are likely due to strain caused by In incorporation.

6.5.3. Results and Discussions: Indium Content calculations, and QCSE induced Shifts

Indium content in the polar and semipolar samples was calculated from InGaN peak position in resonant micro-PL spectra measured using 380-nm excitation from a frequency-doubled pulsed Ti-sapphire laser for an excitation spot size of ~ 1 μm. Figure 6.21 shows the active region

179

structure and the excitation dependent spectra. As revealed from PL measurements, the GaN/InGaN/GaN heterostructures grown in the same run on patterned Si(001) substrates (semipolar) and Si(111) (*c*-plane) show comparable emission intensity. The indium content can be assessed using $E_{InGaN}(eV) = 3.493 - 2.843x - bx(1 - x)$, where *x* is In fraction, and *b* is the bowing parameter (*b* = 2.6 eV [160] used here). The wavelength of InGaN-related emission is larger for the *c*-plane GaN/InGaN/GaN structures, indicating higher (2.5-3%) In concentration in *c*-plane oriented heterostructures. Figure 6.1 compares In content in two sets of polar and semipolar samples, each set grown in the same MOCVD process. Because of very strong Stark effect in the polar structures, to make a fair comparison between the In incorporation into polar and semipolar structures, the wavelengths and corresponding In concentrations are listed for highest injection levels used when the strongest blue shifts of the emission line was observed. Indium incorporation into MOCVD growing layers is controlled by substrate temperature (the lower the temperature, the higher the In incorporation), TMI flow rate, and the reagent distribution in the gas phase. Since the growth conditions (flow rates of TMI and Si(001) and Si(111) substrate temperatures) were the same for each pair of polar and semipolar samples, our results point to slightly higher In incorporation rate into the polar *c*-plane material. However, the gas flow dynamics in MOCVD growth process which is different for the planar layers (*c*-plane layer) compared to patterned stripes (in case of semi-polar layers) could induce some variations in the results which make us to be unconfident about the said conclusion.

Excitation-power-dependent μ-PL
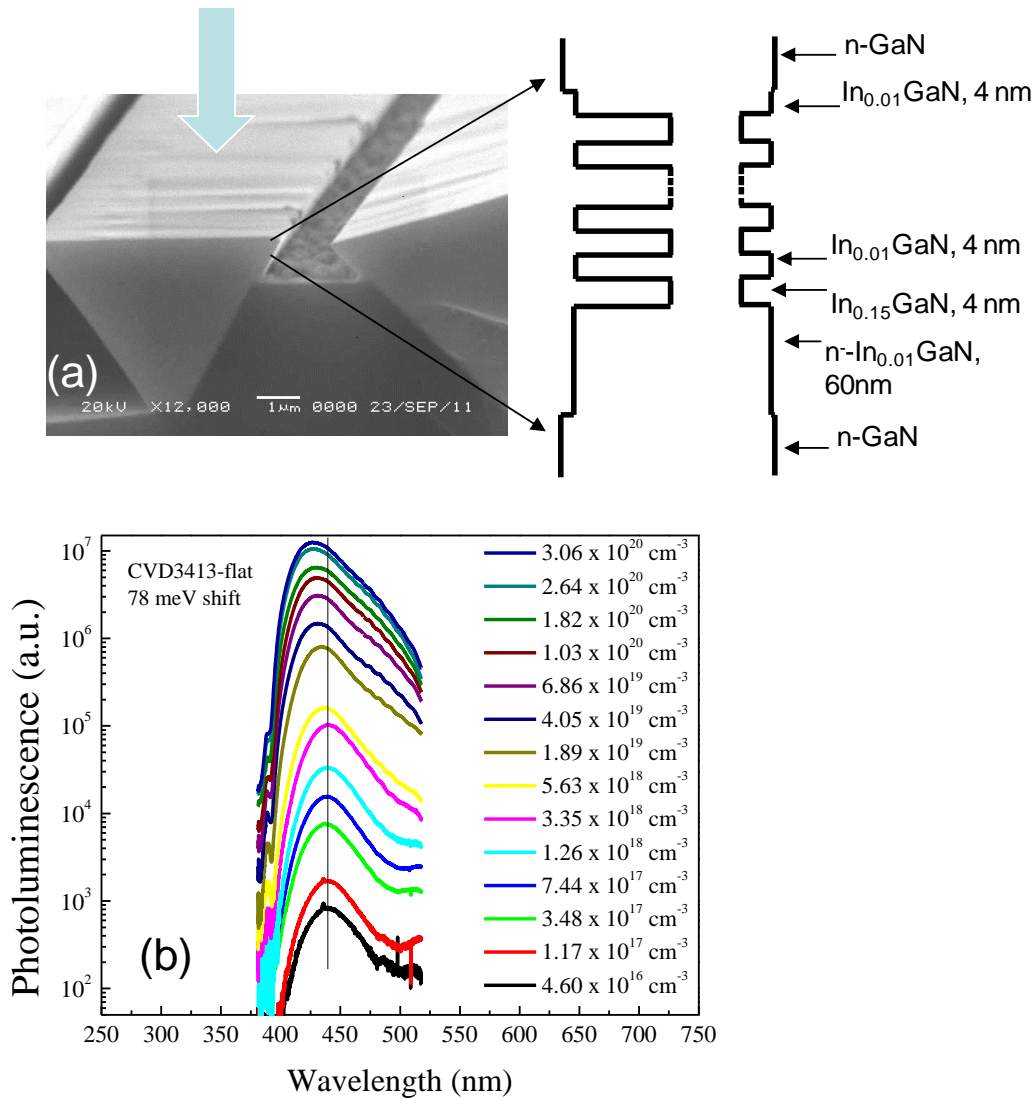
Figure 6.21. (a) Cross-sectional SEM image and the schematic of the $\left(1\bar{1}01\right)$ GaN/InGaN/GaN DH band structure. (Flat bands shown for simplicity) (b) Micro-PL spectra measured at different excitation power densities corresponding to the active region carrier densities indicated.

Table 6.1. Wavelength of InGaN-related emission and calculated In content in c-plane and $(1\bar{1}01)$ InGaN samples containing 8 DH/barrier pairs, which were grown at nominal substrate temperatures 693 ℃ (first row) and 680 ℃ (second row).

Sample	Emission Wavelength	Indium Content
Polar c-plane	450 nm	15.0%
Semi-polar (1-101)	430 nm	12.5 %
Polar c-plane	470 nm	17.0 %
Semi-polar (1-101)	440 nm	14.0 %

As seen from Figure 6.22 the amount of blue-shift in PL peak position with increasing optically excited carrier density is substantially smaller for $(1\bar{1}01)$-oriented structures as compared to c-plane counterparts (70 meV *vs.* 350 meV), thus suggesting smaller polarization field in $(1\bar{1}01)$ GaN, in agreement with theoretical predictions. It should be noted that DHs in the polar c-plane structures could be wider than those in the semipolar ones owing to higher growth rate in the c-direction; however, the very large difference in the blue shift observed in the experiment (5 times) cannot be explained by the difference in the width of active regions.
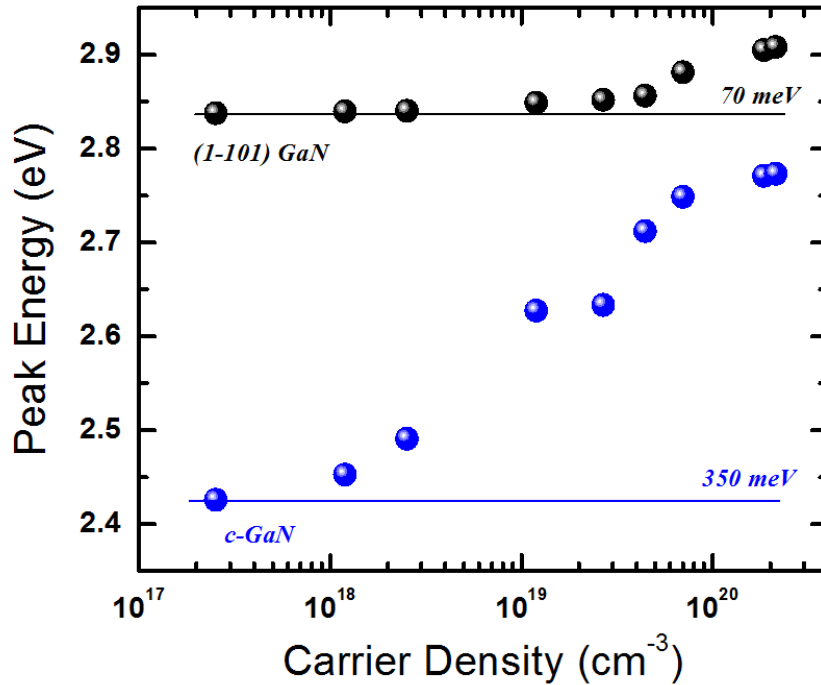
Figure 6.22. PL peak position vs. optically injected carrier density for semipolar $\left(1\bar{1}01\right)$ (black) and polar *c*-plane (blue) GaN/InGaN/GaN heterostructures.

Spatio-CL has revealed a strong geometrical effect on the In incorporation into semipolar $\left(1\bar{1}01\right)$ GaN facets. As seen from Figure 6.23, longer emission wavelength and, therefore, higher In content was observed for inclined GaN stripes than for those with the top surface parallel to the substrate surface. This finding can be explained by the effect of substrate geometry on the local distributions of gas flows in the MOCVD reactor. For instance, the inclined stripe may shadow the flat one since it is located higher with respect to the substrate surface (see Figure 6.20). Note that stacking faults are also observed on the *c+* wings in the structures (Figure 6.23(b) and Figure 6.23(c)), while they are present only in *c⁻* wings of non-coalesced $\left(1\bar{1}01\right)$

183

GaN. It is likely that the In incorporation into $(1\bar{1}01)$ GaN decreases the formation energy of stacking faults.
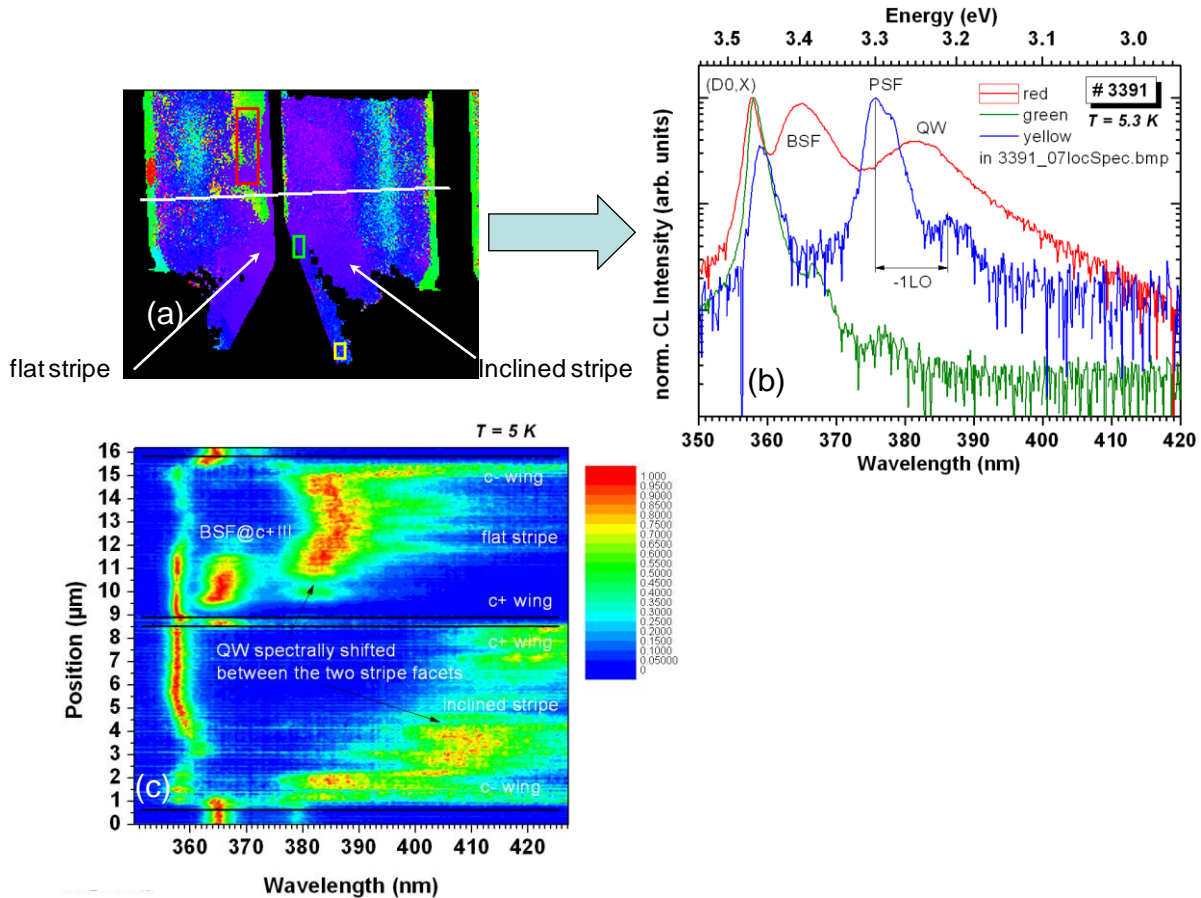
Figure 6.23. (a) Spatio-CL image showing two GaN stripes with GaN/InGaN/GaN DH on the top of s-plane surface, which are nucleated on Si(111) facets oriented at 47° and 61° with respect to 7° -off Si(001) surface. (b) Local CL spectra corresponding to the areas marked on image (a) with colored boxes. Colors of spectra match with the colors of boxes in (a) except for the blue spectrum which corresponds to the yellow box. (c) Line-scan CL spectrum recorded along the path indicated by the line shown in (a).

6.6. Limitations and alternatives

Application of this approach for heteroepitaxy of $(1\bar{1}01)$-plane heterostructures seems a promising approach for the production of low-cost UV and visible operating devices owing to substantial reduction in QCSE, low non-radiative recombination rates, robust temperature dependent PL, and theoretically predicted enhanced indium incorporation efficiency. However, difficult fabrication procedures on patterned substrates, as well as observation of reduced indium incorporation (as demonstrated in previous section) seems to be some of the challenges for manufacturing of LEDs based on $(1\bar{1}01)$-plane GaN on patterned Si.

Moreover, the search for finding the substrate orientation that exhibits the highest indium incorporation efficiency requires fair comparisons which could only be possible when comparing two orientations with similar substrate geometry. As discussed earlier in this chapter, theoretically, the orientation with $\theta \sim 60°$ should exhibit the highest indium incorporation. Study of semipolar $(11\bar{2}2)$ with $\theta = 58°$ which could be achieved as single phase on *m*-plane sapphire is of great interest owing to planar surface which is favorable for device fabrication. In addition, similar surface geometry as well as substrate thermal conductivity of these layers on *m*-sapphire compared to *c*-GaN on *c*-sapphire enables fair comparison of the two orientations in terms of indium incorporation efficiency.

In next chapter, the focus of our attention will be turned toward heteroepitaxy of single phase semi-polar $(11\bar{2}2)$ GaN heterostructures on planar *m*-plane sapphire as a promising approach for manufacturing of low cost efficient UV and visible LEDs. Such investigations will

enable us to have a fair comparison of c-plane and $(11\bar{2}2)$ in terms of indium incorporation efficiency as a crucial objective for solution of the so called 'green gap' problem.

Chapter 7

7. Semi-polar GaN-based Light Emitting Structures on Planar Substrates

7.1. Overview

As discussed previously, The possibility to achieve $(11\bar{2}2)$ GaN on planar m-plane sapphire substrates[161], [162] makes this semipolar orientation attractive for efficient and cost-effective light emitting devices. Moreover, the interest to the $(11\bar{2}2)$ orientation is additionally fueled by theoretical works[20], [21], [49] predicting enhanced In incorporation efficiency supported by recent experimental reports[22] which makes $(11\bar{2}2)$ structures particularly attractive for green light emitters. Despite of all the promises for future generations of long wavelength emitters based on semipolar $(11\bar{2}2)$, cost-effective heteroepitaxy of this orientation of GaN on m-plane sapphire suffers from high density of extended defects such as stacking faults (SFs) and threading dislocations (TDs) resulting in low optical quality.

Here, we demonstrate our investigation on semipolar $(11\bar{2}2)$ layers with applied defect reduction methods to reduce the extended defect. The investigations include optical and structural properties of the layers, nature of defects and their optical activity, exciton localization, and optical anisotropy in emissions from ternary InGaN QWs that are heteroepitaxially grown by

MOCVD. In addition, indium incorporation efficiency into these layers compared to reference *c*-plane layers will be discussed.

7.2. High quality semipolar $(11\bar{2}2)$ GaN on *m*-sapphire: a nano-ELO approach

7.2.1. Overview

Upon obtaining proper conditions for nitridation and nucleation leading to the growth of pure single-phase semipolar $(11\bar{2}2)$ GaN films on *m*-plane sapphire substrates, we continued our study of the $(11\bar{2}2)$ GaN layers with concentration on improvement of their structural and optical quality. Therefore, defect reduction methods such as epitaxial lateral overgrowth (ELO), inclusive both *in-situ*[101], [163], [164] and *ex-situ* [165], [166] techniques, which have been successfully used for *c*-plane, were paid attention to improve optical and structural quality of the semipolar structures intended for device applications.

Up to now, the most common approach to improve the quality of $(11\bar{2}2)$ GaN is growth on patterned sapphire[167]–[174] or Si[175] substrates. Although considerable progress was achieved in this field, the pattering process involves standard lithography, wet or reactive ion dry etching, and SiO_2 mask deposition, which is costly and time-consuming.

On the other hand, the *in-situ* ELO method, also referred to as "nano-ELO", relies on *in-situ* deposition of thin porous SiN_x which acts as a mask and blocks extended defects.[101],

188

[163], [164], [176] This method is of great interest, because it does not require special preparation of substrates and potentially reduces the production cost. Today *in-situ* nano-ELO growth of *c*-plane oriented GaN templates on sapphire and Si is widely used in LED industry. This approach has been demonstrated to be effective in case of polar *c*-plane,[101], [163], [164], [176] and nonpolar *a*-plane,[177], [178] while the reports on defect reduction for the $(11\bar{2}2)$ orientation with this method are rare.[174], [179]–[181]

In this sense, we performed two sets of experiments on *in-situ* nano-ELO to obtain highest optical quality of the semipolar $(11\bar{2}2)$ layers. In the first set of experiments,[102] we report the improvement of optical and structural quality of semipolar $(11\bar{2}2)$ GaN layers by means of inserting nano-porous SiN_x interlayers. In the second set, we demonstrate further optimization of the *in situ* nano-ELO technique with SiN_x interlayers deposited at higher temperatures (corresponding to higher crystallinity and lower porosity of the interlayers for same deposition time) in order to provide optical and structural quality required for device applications.

7.2.2. First Set of Experiments

7.2.2.1. Experimental Details

The nano-ELO approach involves in situ deposition of a porous SiNx interlayer that acts as a nano-mask for the subsequent lateral overgrowth. The overgrowth starts in the nanometer-sized pores and then progresses laterally, as in the case of conventional ELO. Thus, the inserted SiN_x

189

nano-mask prevents propagation of threading dislocations and stacking faults in the growth direction. The SiN_x nano-masks have been used successfully to block threading dislocations and thus improve optical properties of polar *c*-GaN layers.[101], [176] Defect reduction in nonpolar *a*-plane GaN layers grown with SiN_x interlayers has also been reported.[177], [178] However, reports on effectiveness of SiNx nano-ELO method in reducing defects in semipolar $(11\overline{2}2)$ GaN are scarce and contradictory.[179], [180]

From the experience with *c*-plane nano-ELO, it is known that the porosity of SiN_x interlayer is strongly dependent on the deposition temperature and time (*i.e.* thickness).[101] Usually the temperature during SiN_x deposition is kept constant and the deposition time is varied.[101] The longer is the deposition time of SiN_x, the lower is the pore density in the SiN_x non-coalesced layer (or the lower is the area of "seed regions") and the larger is the area of the overgrown GaN ("wing regions"), which results in more effective reduction of threading dislocations and potentially stacking faults.

However, in layers with very low porosity SiN_x, new stacking faults and dislocations may be introduced at the SiN_x/GaN interface. Therefore, depending on number of blocked and newly generated extended defects, the method may or may not lead to improvement of overgrown GaN quality. In addition, the time required for the GaN layer to coalesce increases as the porosity of the SiN_x interlayer is reduced which significantly increases the production cost. Thus there is a trade-off between blocking of the existing defects, generation of new ones, and the time required to coalesce the layer.

The growth of semipolar GaN layers was performed by MOCVD system (for details of growth technique see section 3.4). SiH_4 was employed both for Si-doping as well as SiN_x

190

interlayer deposition. The single phase $(11\overline{2}2)$ orientation of GaN was achieved on 2-inch *m*-sapphire wafers using a 20 nm-thick AlN buffer layer, which was grown at ~600ºC. Then, ~3µm–thick $(11\overline{2}2)$ GaN layers were grown by using the two-step growth approach. In the first step, the growth was carried out at a low reactor pressure of 30 Torr to ensure smooth surface morphology followed by the second step performed at a high pressure of 200 Torr to achieve high optical quality. The $(11\overline{2}2)$ GaN/*m*-sapphire wafers were cut into six pieces, which were used as templates for further in situ SiN_x nano-ELO experiments.

The *in situ* nano-ELO procedure used was as follows. First, a ~ 500 nm-thick GaN layer was grown on the template at 200 Torr followed by the deposition of a very thin, porous SiN_x layer under SiH_4 and ammonia flow, and growth of the GaN seed layer at a reactor pressure of 200 Torr at substrate temperature of about 1060ºC. Then, the overgrowth was carried out at 76 Torr (except sample D) and high substrate temperature of ~1080ºC. In the final stage, a growth of about 5-µm–thick GaN layer doped with Si to ~2×10^{18} cm^{-3} at a high reactor pressure of 200 Torr was employed to achieve high optical quality. Growth details of the samples investigated are listed in Table 7.1. To observe the improvement due to the SiN_x interlayer and for comparison with the *c*-plane variety, two reference samples were used: sample A with semipolar $(11\overline{2}2)$ orientation grown on *m*-sapphire without any SiN_x interlayer and sample E, which was grown with the same nano-ELO technique on *c*-sapphire under optimized conditions described in Ref. [101]. All the samples used in this study have total thicknesses of 10 to 12µm.

Scanning electron microscopy (SEM) was employed to characterize surface morphology. Room temperature and low temperature steady-state photoluminescence (PL) with HeCd laser

191

excitation (λ=325 nm) and X-ray diffractometery (XRD) were used to evaluate optical and structural quality of the samples.

Table 7.1. Growth conditions for the semi-polar nano-ELO samples investigated in the first set of experiments.[102]

Sample	SiN$_x$ deposition time (min)	Seed layer GaN growth time (min)	Recovery Pressure (Torr)
A $(11\bar{2}2)$ Reference	0	--	--
B $(11\bar{2}2)$ nano-ELO	4.5	10	76 + 200
C $(11\bar{2}2)$ nano-ELO	5.0	20	76 + 200
D $(11\bar{2}2)$ nano-ELO	7.0	5	200
E c-plane nano-ELO	4.0	20	76 + 200

7.2.2.2. Surface Morphologies

The surface morphology evolution of Sample B at different growth stages is illustrated in Figure 7.1. The SEM image of the template surface in Figure 7.1(a) shows a relatively flat surface with striations along the $\left[11\bar{2}3\right]$ direction of GaN. Such morphology is characteristic of the $\left(11\bar{2}2\right)$ GaN surface.[182] The sample surface upon 4.5-min deposition of the SiN$_x$ nano-mask followed by a 10-min GaN seed layer growth is presented in Figure 7.1(b). The surface is covered by triangular GaN islands with varying sizes, which were nucleated in the pores of the SiN$_x$ interlayer and then extended vertically and laterally. During the recovery stage performed at a reactor pressure of 76 Torr, the grains visible in Figure 7.1(b) coalesce and form a continuous film [Figure 7.1(c)]. Finally, after subsequent growth at 200 Torr, the sample surface becomes smooth again with the characteristic arrow-like features, as shown in Figure 7.1(d). The final

192

surface morphology is quite similar to that of the $(11\bar{2}2)$ GaN/*m*-sapphire template [Figure 7.1(a)], but the striations along the $\left[11\bar{2}3\right]$ direction are more prominent and longer. Figure 7.2 compares the surface morphology of the semipolar samples with different SiN$_x$ interlayer deposition times. One can see that sample B with 4.5-min SiN$_x$ nano-mask has the smoothest surface, while the other two samples suffer from shallow pits and rough V-shaped features. This observation can be explained by the fact that the longer is the SiN$_x$ deposition time, the lower is the density of pores and the larger are distances between the GaN nucleation islands, and therefore, the longer time is needed to achieve a fully coalesced layer with a smooth surface.
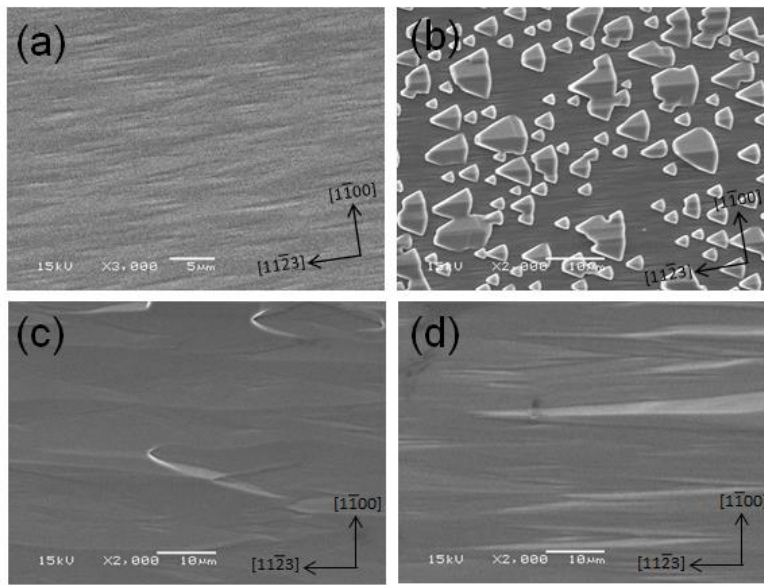
Figure 7.1. Plan-view SEM images of sample B at different stages of growth: (a) GaN/*m*-sapphire template, (b) after deposition of 4.5 min SiN$_x$ interlayer and 10 min GaN seed layer, (c) after additional 1.5 h of growth at 76 Torr, and (d) after an additional 1.5 h of growth at 200 Torr.[102]
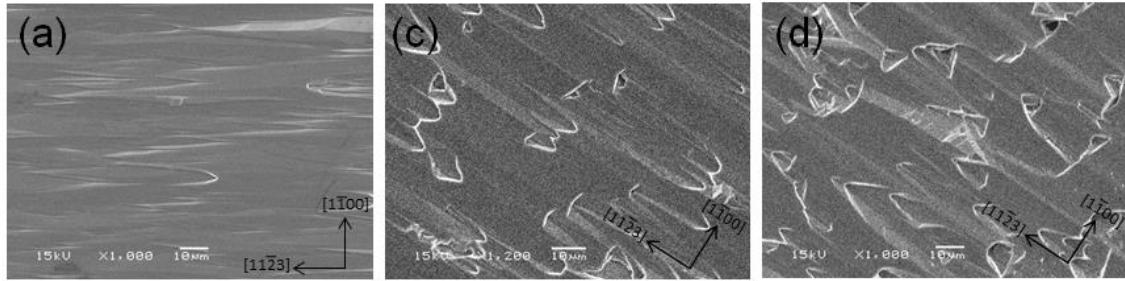
Figure 7.2. Plan-view SEM images of $(11\bar{2}2)$ GaN films grown with a SiN_x interlayers deposited for (a) 4.5 min (sample B), (b) 5 min (Sample C), and (c) 7 min (sample D).[102]

7.2.2.3. Structural Characterizations

To investigate the structural quality XRD measurements were carried out. Rocking curves of $(11\bar{2}2)$ reflection were measured along the $\left[11\bar{2}3\right]$ and $\left[1\bar{1}00\right]$ directions of GaN, as shown in the inset of Figure 7.3, which compares the derived full width at half maximum (FWHM) values for the samples A, B, C, and D. Insertion of the porous SiN_x interlayer is observed to results in a decrease in FWHM, *i.e.*, improvement of the structural quality of $(11\bar{2}2)$ GaN. Sample C with a SiN_x deposition time of 5 min shows the lowest FWHM and the smallest in-plane anisotropy.

194
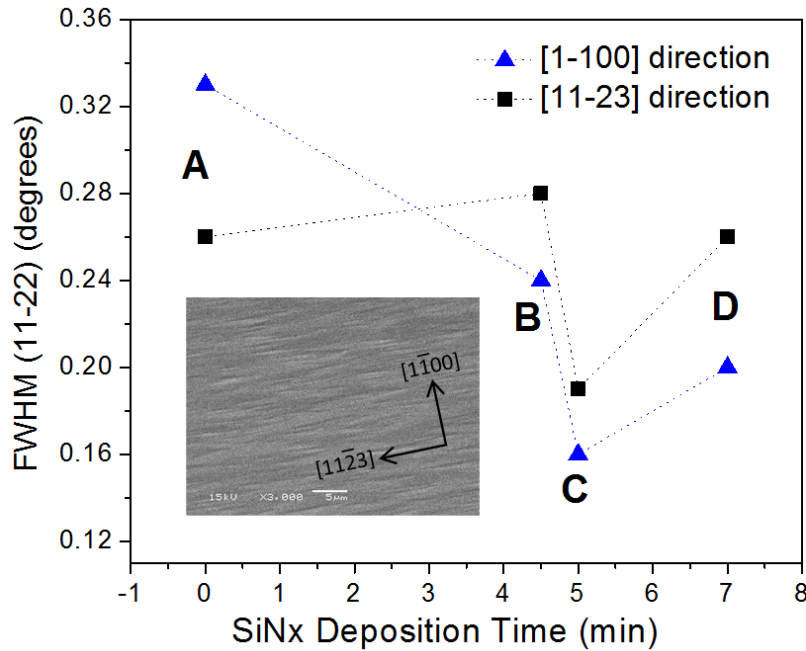
Figure 7.3. FWHM values of rocking curves measured along $\left[11\bar{2}3\right]$GaN and $\left[1\bar{1}00\right]$GaN directions *vs*. SiN$_x$ deposition time. The inset shows the plan-view SEM image and the two in-plane orientations.[102]

7.2.2.4. Optical Characterizations

Room-temperature PL measurements indicate the improvement of the optical quality of semi-polar $\left(11\bar{2}2\right)$ GaN grown with the nanoporous SiN$_x$ interlayers. Figure 7.4(a) illustrates the PL spectra for the semipolar samples with 4.5-min (blue), 5-min (green), and 7-min (magenta) SiN$_x$ interlayers in comparison with the semipolar reference sample without the SiN$_x$ interlayer (red) and the *c*-plane nano-ELO reference sample (black). The PL intensity for the samples with SiN$_x$ interlayers exceeds that of the $\left(11\bar{2}2\right)$ GaN reference film. The PL intensity rises with the SiN$_x$ deposition time, and the increase in intensity by more than 4 times is observed for sample D (7-min SiN$_x$). As we discussed above, the increased SiN$_x$ deposition time leads to lower porosity of

195

the SiN$_x$ interlayer, which should result in more effective reduction of threading dislocation density, and therefore, increase in radiative efficiency and PL emission intensity. The plot of integrated PL intensity vs. SiN$_x$ deposition time [Figure 7.4(b)] demonstrates this dependence.
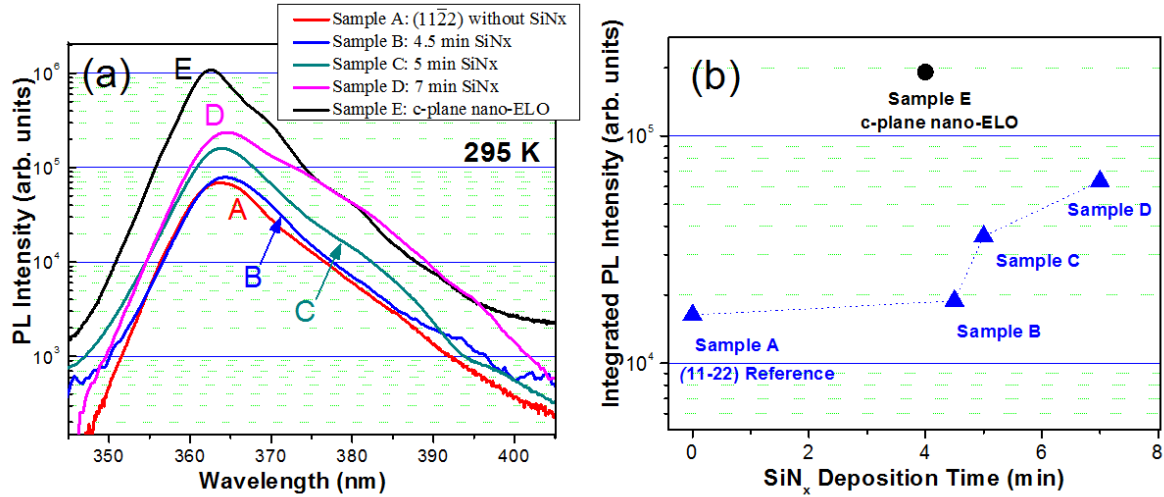
Figure 7.4. (a) Room temperature PL spectra for the $(11\bar{2}2)$ samples with various SiN$_x$ interlayers. Also shown are semipolar $(11\bar{2}2)$ (red) and *c*-plane nano-ELO (black) reference samples. (b) Room temperature integrated PL intensity as a function of SiN$_x$ deposition time. The integrated PL intensity for the *c*-plane nano-ELO reference is shown as a black circle.[102]

Low-temperature PL spectra for the samples are shown in Figure 7.5. The spectrum for the $(11\bar{2}2)$ GaN reference sample A (red) is dominated by peaks around 360 and 369 nm, which are assigned to basal-plane stacking faults (BSFs) and prismatic stacking faults (PSFs), respectively.[115], [121], [183] The donor-bound exciton (D^0X) emission is observed as a weak shoulder at 356 nm. The high intensities of the BSF- and PSF-related peaks are indicative of a large density of optically active stacking faults in the $(11\bar{2}2)$ GaN/*m*-sapphire template grown without SiN$_x$ interlayer. As compared to the reference layer, the samples grown with SiN$_x$ nano-

196

masks show considerable increase in the intensity of the D^0X emission, although it is still lower than that of the BSF related peak. The structure grown with 5-min deposition time of SiN_x interlayer exhibits the highest intensity of near band-edge emission in agreement with XRD data. The intensities of BSF PL line from nano-ELO semipolar samples decreases only slightly compared to the reference sample A, while the intensity of PSF-related emission diminishes more. These observations suggest the decrease in the density of threading dislocations and, possibly, partial dislocations associated with stacking faults, which are responsible for nonradiative recombination, while the total volume of optically active SFs does not change substantially. The latter finding can be consistent with the generation of new SFs at the GaN/ SiN_x interface during overgrowth, which virtually negates the effect of the SiNx interlayer, which blocks the propagation of SFs existent in the GaN template underneath.

197
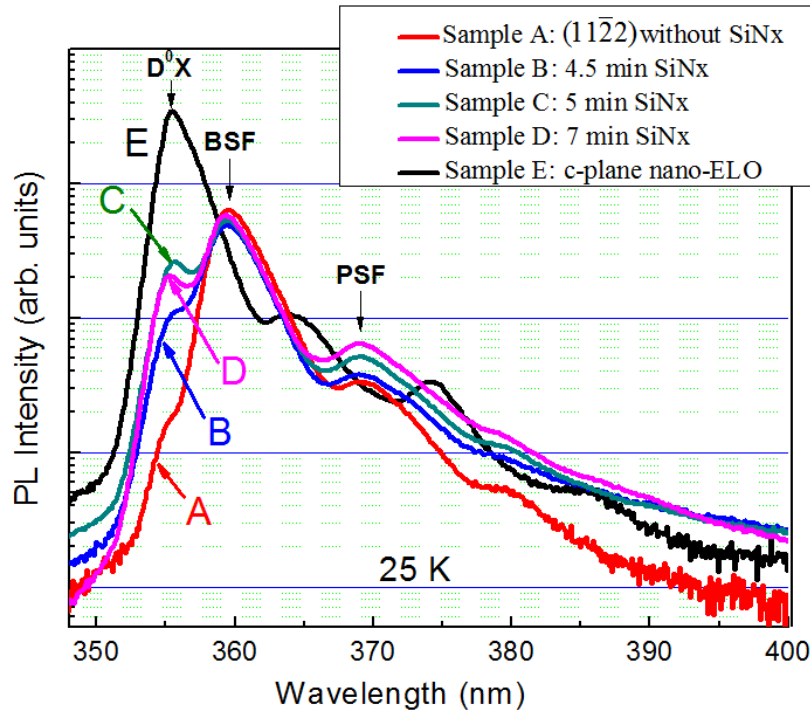
Figure 7.5. 25 K PL spectra for $(11\bar{2}2)$ GaN samples with SiN_x interlayers deposited for 4.5 min (blue), 5 min (green), and 7 min (magenta). The spectra for the *c*-plane nano-ELO reference (Sample E) (black) and $(11\bar{2}2)$ GaN reference without SiN_x (sample A) (red) are also shown for comparison.[102]

7.2.3. Second Set of Experiments

7.2.3.1. Overview

Later, as a second set of experiments,[184] we worked on further optimization of *in situ* SiN_x nano-ELO process with the use of SiN_x interlayers deposited at higher temperatures (which results in better crystallinity and lower porosity of the interlayers with same deposition time) in order to provide optical and structural quality required for device applications. For the sake of

that, $(11\bar{2}2)$-oriented semipolar GaN layers were grown on *m*-sapphire substrates by MOCVD using controlled seed layer and overgrowth conditions, meaning that, the seed distributions of the seed layers for different SiN_x deposition times were carefully studied and correlated to the overgrown GaN quality. For this set of experiment, growth pressure was kept constant (200 Torr) for all the samples for seed layer as well as overgrowth stages. Similar growth condition for growth of template was applied for the two sets of experiments.

7.2.3.2. Experimental Details

Here, for the subsequent nano-ELO, the growth was interrupted to deposit a very thin porous SiN_x layer in a flow of SiH_4 and ammonia at a substrate temperature of 1040°C and a reactor pressure of 200 Torr. A GaN seed layer was then grown for 20 min at the same pressure and temperature (stage 2 in Figure 7.6). As mentioned, compared to our previous work (Subsection 7.2.2), the SiN_x interlayer was deposited at an elevated substrate temperature, which resulted in lower pore density in the SiN_x interlayers for a given deposition time. In these experiments, we varied the SiN_x deposition time from 1 to 3 min, keeping all other conditions the same. For the same deposition temperature, the longer the SiN_x deposition time is, the lower the pore density will be in the nano-mesh. Thus, for this set of experiments, depending on the SiN_x deposition time, different porosity of the SiN_x layers and, consequently, various densities of GaN islands were obtained, as illustrated schematically in stage 2 of Figure 7.6 (a, b, c, and d). Finally, the GaN layers were overgrown at 200 Torr and 1040 ºC and doped with Si to $\sim2\times10^{18}$ cm^{-3} at 200 Torr reactor pressure to achieve the highest optical quality.

The total thickness of the GaN stack is 11.5 µm for all the samples. In this study, we used two reference samples. One is a *c*-plane GaN film which has been grown with the same *in-situ*

nano-ELO technique on *c*-sapphire.[101] The second reference sample is a semipolar ($11\bar{2}2$) GaN film grown on *m*-sapphire but without the SiN_x interlayer (referred to as the ($11\bar{2}2$) GaN template). To provide a fair comparison of semipolar nano-ELO structures, the total thickness of the reference films was chosen to be similar.

Scanning electron microscopy (SEM) and atomic forced microscopy (AFM) was used to examine surface morphology. Optical properties of the layers were evaluated using steady state and time-resolved photoluminescence (PL). The steady-state PL measurements were performed using HeCd laser excitation ($\lambda = 325$ nm) for which the samples were mounted on a closed-cycle He-cooled cryostat for low temperature measurements. For the time-resolved PL (TRPL) measurements, a frequency-tripled pulsed Ti-sapphire laser (265 nm excitation) with a pulse width of 150 fs and an excitation spot diameter of ~ 50 μm and a Hamamatsu streak camera with 25 ps resolution were utilized. Cross-sectional scanning transmission electron microscopy (STEM) was utilized to evaluate the role of SiN_x interlayer in blocking the extended defects. The STEM analyses were performed in a scanning transmission electron microscope FEI (S)TEM Tecnai F20 equipped with a bright-field annular detector (BF) by the Gatan company. The sample was prepared in cross-section by mechanical wedge polishing combined with Ar+ion milling. Detailed information about the experimental setup and sample preparation can be found elsewhere.[185], [186]
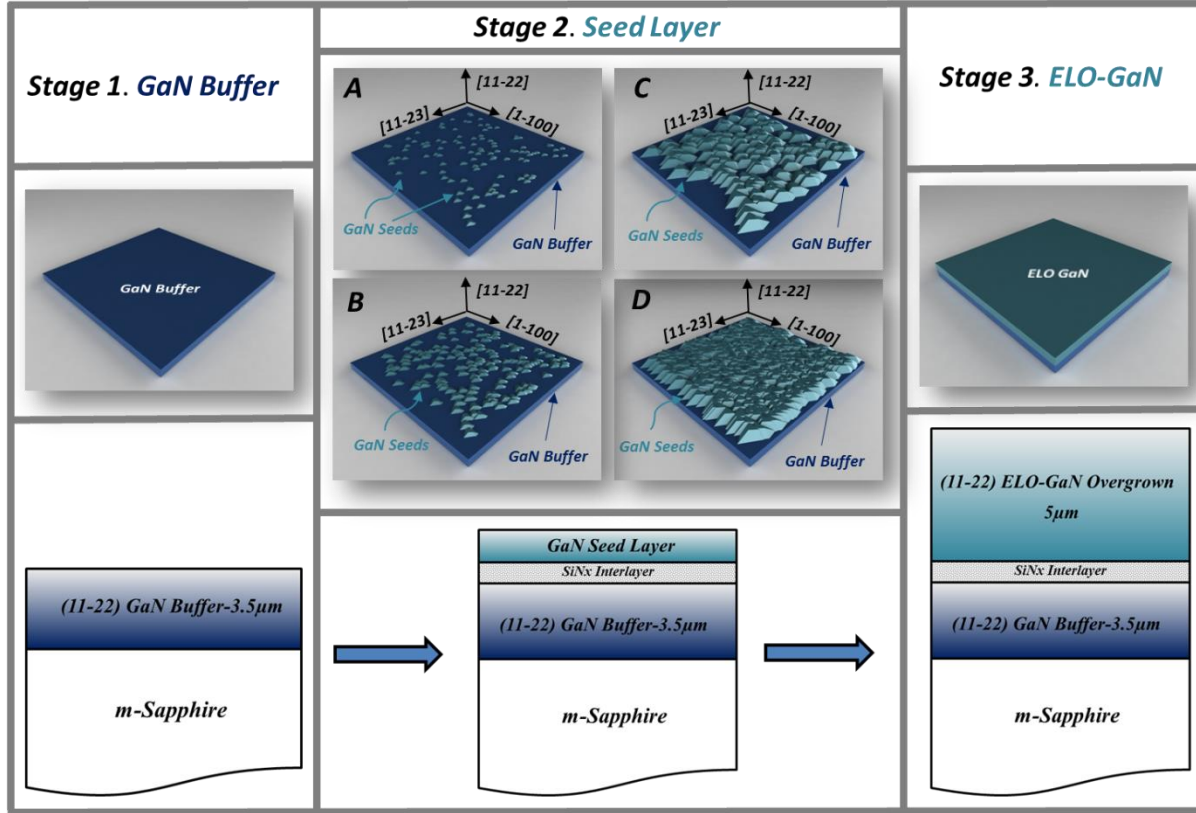
Figure 7.6. Schematics of the nano-ELO process including (Stage 1) the growth of GaN buffer (left panel), (Stage 2) deposition of SiNx nanomesh followed by seed layer (middle panel) and (Stage 3) ELO-GaN overgrown (right panel). Second stage is illustrated with four different seed layer morphologies (that is dependent on SiNx deposition conditions) with increasing density of nucleation islands from A to D.

7.2.3.3. Surface Morphologies

To study the initial stage of the overgrowth on the SiN_x nano-mesh (stage 2 in Figure 7.6), the growth was stopped after 20 min of GaN on SiN_x and the samples were unloaded for surface morphology investigation under an optical microscope and SEM. The samples were then loaded back into the MOVCD chamber and the growth was resumed. Figures 7.7(a)-7.7(c) compare the surface morphology of the semipolar GaN samples overgrown for 20 minutes on the templates

201

with different SiN$_x$ deposition times. To reiterate, the porosity of the SiN$_x$ layer is dependent on the deposition time: the shorter is the SiNx deposition time, the higher is the pore density in the nano-mesh, and GaN nucleates on the sites corresponding to pores in SiN$_x$ layer. Therefore, the density of nucleated GaN islands represents the porosity of the SiN$_x$ nano-porous mask. The GaN layer on the 1-min SiN$_x$ nano-mesh (Figure 7.7 (a)) is fully coalesced after 20 min of growth (similar to the case d in Figure 7.6), since the pore density, and consequently, the density of GaN nuclei, is the highest in this case. The GaN layer on the 1.5-min SiN$_x$ (Figure 7.7 (b)) is partially coalesced (similar to the case c in Figure 7.6), and the surface of the sample with 3-min SiN$_x$ (Figure 7.7 (c)) is covered with GaN islands that were nucleated in the pores with relatively low nucleation density (similar to the case b in Figure 7.6). Figure 7.7(d) shows an SEM image of the GaN islands on the template surface.
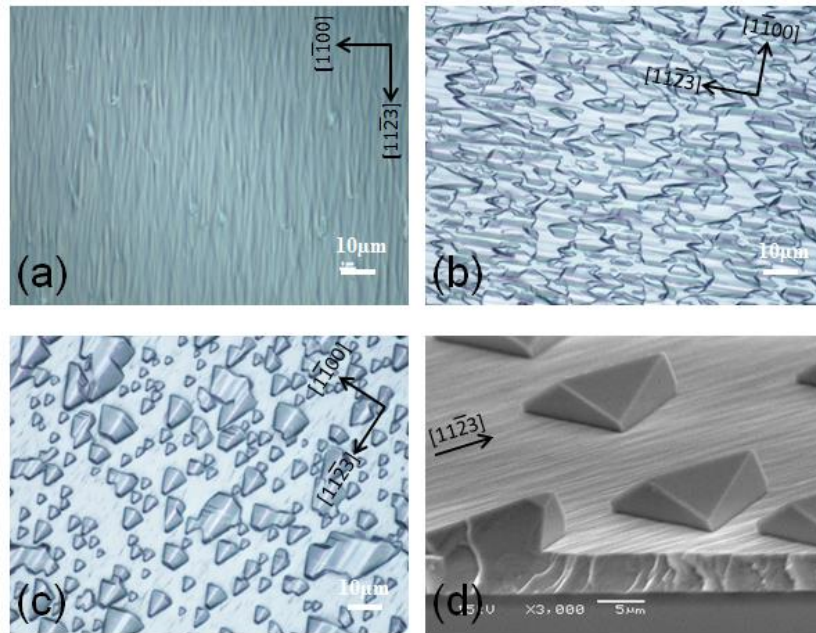
Figure 7.7. Optical microscopy images of $\left(11\bar{2}2\right)$ GaN layer surface after 20 min of GaN growth on (a) 1-min, (b) 1.5-min, and (c) 3-min SiNx interlayers. (d) Inclined view SEM image of

semipolar $(11\bar{2}2)$ GaN seeds on porous SiNx interlayer. [Reprinted with Permission from Ref.[184]]

Figures 7.8 shows optical microscope images of the final surfaces of the 11.5 µm-thick nano-ELO samples. One can see that the samples with 1- and 1.5-min SiN$_x$ interlayers have fully coalesced surface with arrow-like features elongated in the $[11\bar{2}3]$ direction of GaN (Figures 7.8(a) and (b)), which is a characteristic of $(11\bar{2}2)$ GaN layer surface.[182] The sample with 3-min SiN$_x$ interlayer, however, suffers from holes and rough V-shaped features (Figure 7.8(c)). AFM images of the samples with 1.0-, 1.5-, 3.0-min SiN$_x$ interlayers and the reference $(11\bar{2}2)$ GaN template are displayed in Figure 7.9. The root-mean-square (rms) values measured on 50 µm×50 µm areas are 53, 34, 50, and 251 nm for layers having 0, 1.0, 1.5, and 3.0 min SiN$_x$ deposition times, respectively. Thus, the sample with the shortest SiNx deposition time shows the best surface morphology.
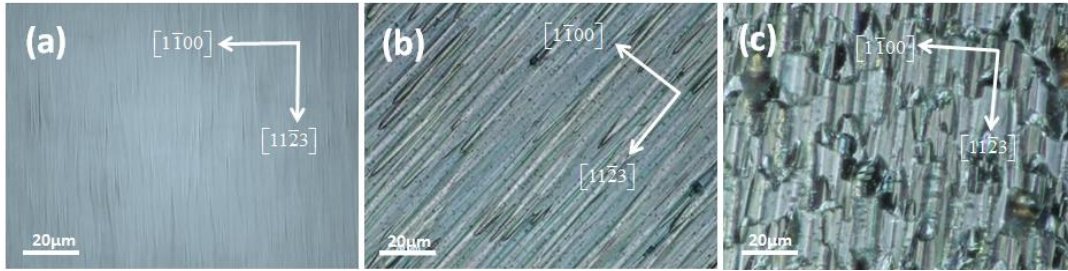
Figure 7.8. Optical microscopy images of the final surface morphologies of in-situ nano-ELO $(11\bar{2}2)$ GaN layers grown with SiNx interlayers deposited for (a) 1.0, (b) 1.5, and (c) 3.0 min. [Reprinted with Permission from Ref.[184]]
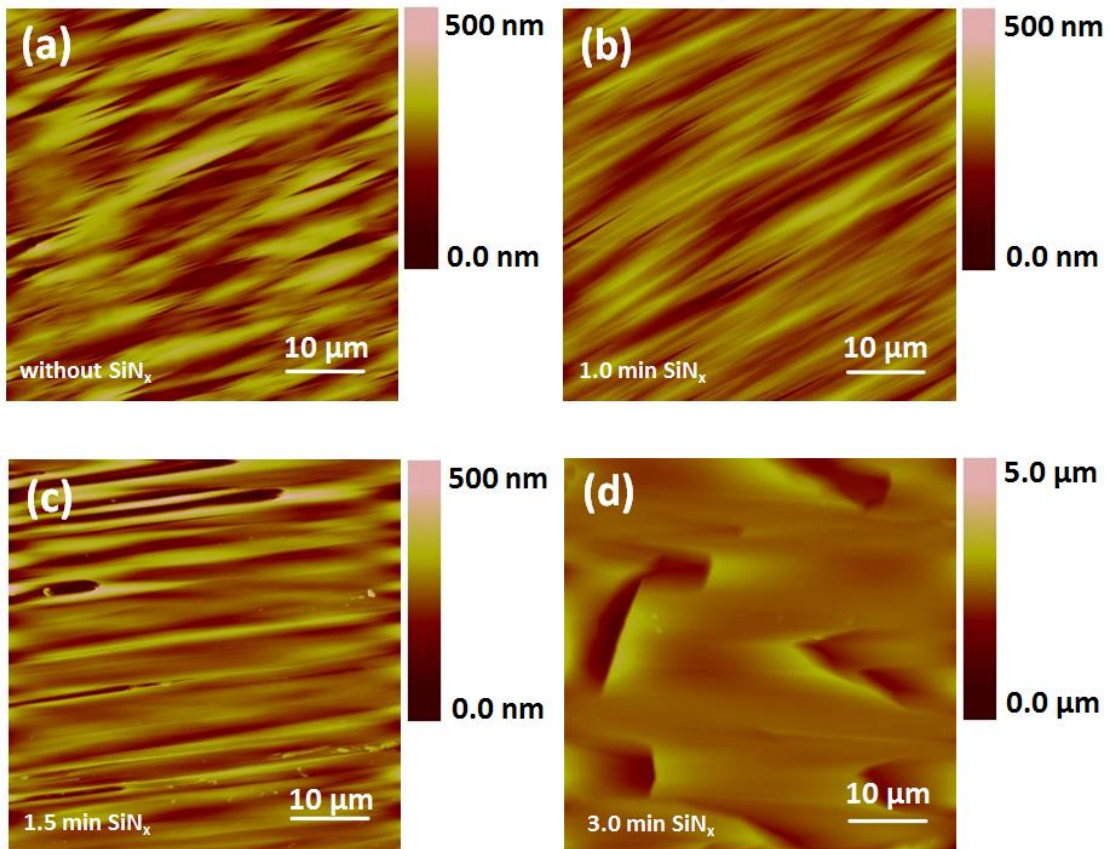
Figure 7.9. AFM images of the semipolar $(11\bar{2}2)$ GaN layers grown on m-sapphire using porous SiNx interlayer with (a) 0.0 min (reference), (b) 1.0 min, (c) 1.5 min, and (d) 3.0 min deposition times. Note the vertical scales are 500 nm except for (d) which is 5.0 μm. [Reprinted with Permission from Ref.[184]]

204

7.2.3.4. Optical and Structural Characterizations

Figure 7.10(a) shows low-temperature (25 K) PL spectra of the samples under study. One can see that the spectrum for the $(11\bar{2}2)$ GaN template grown without the SiN_x interlayer is dominated by a peak centered around 3.425 eV (362 nm) related to basal plane stacking faults (BSFs),[121], [183]while donor-bound exciton (D^0X) emission is seen only as a weak shoulder at 3.464 eV (358 nm). It should be mentioned that the BSF density in the layer can be correlated to the ratio of D^0X-to-BSF related intensities rather than to the BSF intensity by itself, as the BSF emission intensity can be also suppressed due to higher density of nonradiative centers, which include point defects and dislocations. The low value of the ratio of D^0X-to-BSF emission intensities is indicative of a large contribution from BSFs, thus suggesting their high density in the reference sample. It should be noted that the overall PL intensity, to the large extent, is limited by the density of dislocations (which are nonradiative defects), rather than stacking faults (which are optically active). For the sample grown with 1.5 min SiN_x, the intensity of both BSF-related and DX low-temperature PL lines as well as room-temperature PL intensity (Figure 7.10(a)) considerably increase compared to the reference sample grown without SiN_x, although the D^0X-to-BSF intensity ratio improved only slightly compared to the reference sample. This implies that the 1.5-min SiN_x nanomesh effectively blocks dislocations rather than BSFs. Employment of the 3-min SiN_x interlayer improves the D^0X-to-BSF intensity ratio, thus suggesting the reduction in the BSF density in this sample. However, as apparent from the low-temperature PL spectrum (Figure 7.10(a)), the BSF density is still high.

205
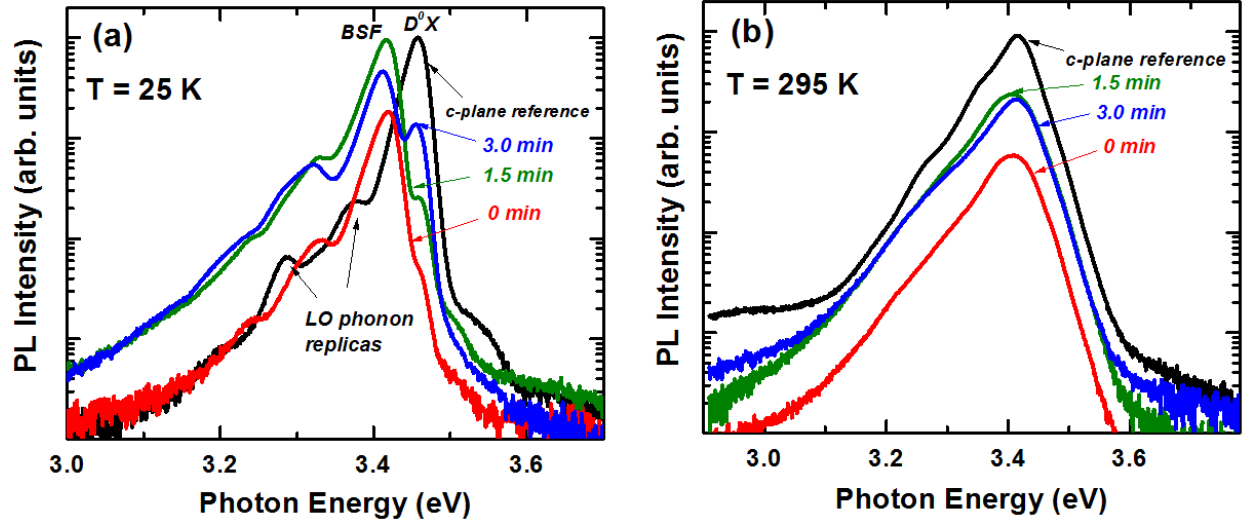
Figure 7.10. (a) Low-temperature (25 K) and (b) room-temperature PL spectra for in-situ nano-ELO $(11\bar{2}2)$ GaN structures with SiNx interlayers deposited for 1.5 min and 3 min in comparison with spectra for $(11\bar{2}2)$ GaN/m-sapphire template without SiNx interlayer and c-plane nano-ELO GaN film. [Reprinted with Permission from Ref.[184]]

Figure 7.10 (b) compares the room-temperature PL spectra obtained from the *in-situ* nano-ELO $(11\bar{2}2)$ GaN films with those from the $(11\bar{2}2)$ GaN reference sample without any SiN$_x$ interlayer and the *c*-plane nano-ELO reference sample. One can see that the introduction of the SiN$_x$ interlayer considerably improves the room-temperature PL intensity; the emission intensity from the sample with 1.5-min interlayer is only 3.8 times lower than that for the *c*-plane nano-ELO layer, while the PL intensity from the $(11\bar{2}2)$ GaN reference sample without the SiN$_x$ interlayer is approximately 20 times lower, suggesting that a PL intensity improvement by more than 5 times is obtained by applying the nano-ELO technique. It should be mentioned that the PL intensity is improved by a factor of 2 (on average) compared to the layers obtained in the previous study[102] (see subsection 7.2.2)which were grown at a lower SiN$_x$ deposition

206

temperature (by 15 °C). We can explain this improvement by the fact that the increase in SiN_x deposition temperature results in less porous nano-mesh, which more effectively blocks nonradiative defects. In addition, the surface morphology is significantly improved compared to our structures reported earlier.[102]

To investigate the effect of *in-situ* nano-ELO on carrier dynamics, we have performed time-resolved PL (TRPL) measurements. Figure 7.11 depicts PL transients for the $(11\overline{2}2)$ GaN samples with SiN_x interlayers measured with an excitation power density of 240 W/cm^2 at room temperature. As seen from the figure, the transients exhibit single exponential decay. We have found that, while $(11\overline{2}2)$ GaN layers grown without SiN_x interlayers but with identical total thickness exhibit a fast decay of about 0.15 ns, the PL decay times for the nano-ELO semipolar samples are longer by 35% to 85% (with 0.20 and 0.27 ns for the samples with 1.5- and 3.0-min SiN_x interlayers, respectively), although still shorter than that for the polar *c*-plane reference layer (0.66 ns). Thus, the TRPL data also indicate that the nano-ELO technique results in considerable improvement of the optical quality of semipolar material. Moreover, the increase in carrier lifetime as a function of SiN_x deposition time (demonstrated in the inset of Figure 7.11) is consistent with the reported data on the optimization of nano-ELO technique for case of *c*-plane GaN grown on *c*-sapphire.[101]
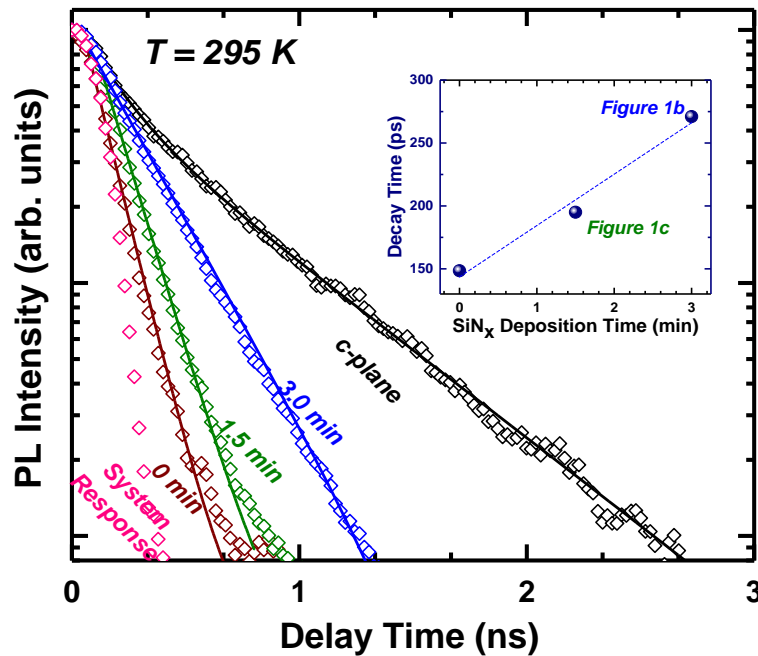
Figure 7.11. Time-resolved PL intensities for in-situ nano-ELO $(11\bar{2}2)$ GaN with SiNx interlayers deposited for 1.5 min and 3 min compared to reference layer without interlayer. The data for the c-plane GaN film prepared by the in situ nano-ELO technique is also shown for comparison. Solid lines are exponential fits. The inset demonstrates correlation between room temperature PL decay time and SiNx deposition time and consequently seed morphology. Reprinted with Permission from Ref.[184]]

The reduction in BSF density due to the SiN_x interlayer, as concluded from enhancement of the D^0X emission with respect to BSF-related PL line (see Figure 7.10(a)), is also supported by STEM data. Figure 7.12 shows a cross-sectional bright field STEM image of a semipolar nano-ELO structure grown at a lower SiN_x deposition temperature of 1025°C (more details can be found elsewhere[102]). A high density of basal plane stacking faults running at an angle of 58.4° with respect to semi-polar surface can be clearly seen in darker contrast in the bottom GaN layer. Importantly, it is clearly seen that the BSFs are locally blocked fairly efficiently at the

208

SiN$_x$ interlayer resulting in a significantly reduced BSF density in the upper semi-polar GaN layer. The improvement in BSF density for the nano-ELO layer (above the nano-mesh) compared to the semipolar template (below the nano-mesh) correlates with the improvement in the D^{0}X-to-BSF intensity ratio for the nano-ELO compared to the reference semipolar layer. In the low-temperature PL spectrum exhibited by this sample (not shown), the D^{0}X-to-BSF intensity ratio was improved by a factor of 4 compared to the reference $(11\bar{2}2)$ layer without nano-mesh.
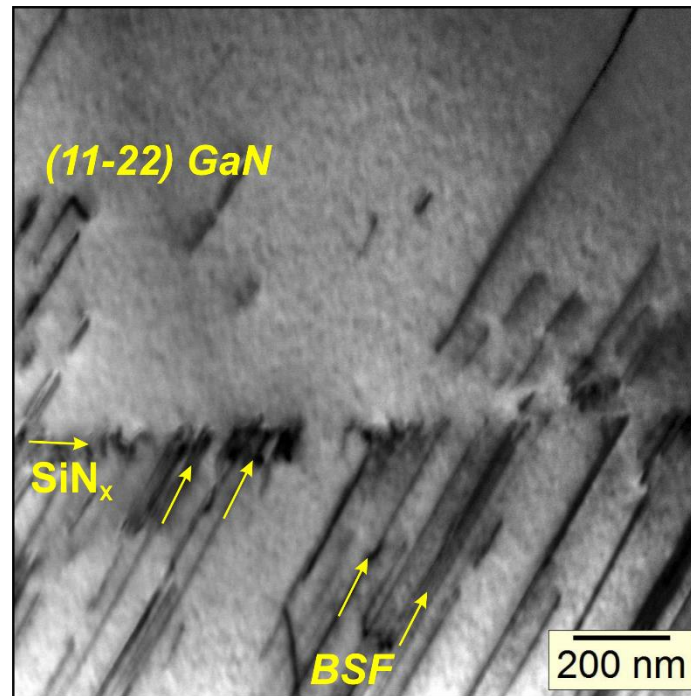
Figure 7.12. Cross-sectional STEM image in bright field contrast of in-situ nano-ELO$(11\bar{2}2)$- oriented semipolar GaN layer grown on 2-min SiNx nano-mesh deposited at 1025°C. [Reprinted with Permission from Ref.[184]]

The data obtained indicate that the insertion of the SiN$_x$ interlayer improves the surface morphology as well as optical properties of the overgrown $(11\bar{2}2)$ GaN layer. However, there is

209

a trade-off between surface morphology and optical quality; the increase in SiN_x deposition time improves the optical quality with the cost of increase in surface roughness. More extensive studies of the semipolar nano-ELO structures by means of cross sectional STEM in combination with spectrally and spatially resolved cathodoluminescence are in progress and the results will be reported elsewhere.

7.2.4. Summary and Conclusions

In summary, employment of the *in-situ* nano-ELO technique leads to semipolar $(11\bar{2}2)$ GaN layers with relatively smooth surface morphology and optical properties (PL intensity and carrier lifetimes) approaching to those of the *c*-plane GaN. An enhancement in the room-temperature photoluminescence intensity by a factor of 5 has been attained for layers with SiN_x nanomesh compared to the layer with identical total thickness but without the SiN_x interlayer. The recombination lifetime was found to increase from 150 to 270 ps with the deposition time of the SiN_x nanomesh when a 3 min SiN_x interlayer was used (in the second set of experiments).

Moreover, a trend has been observed for increase in carrier lifetime as a function of deposition time (or reduction in surface coverage in seed layer stage). Application of such trends in optimization of the semipolar GaN optical and structural quality in seed layer stage as well as the recovery stages could be helpful for utilizing the method to obtain highest quality as well as smooth surface morphology. Approaching the optical quality of the state of the art *c*-plane layers utilizing the nano-ELO technique presented here for semipolar $(11\bar{2}2)$ in one hand, and exhibition of higher indium incorporation efficiency for this semipolar orientation on the other hand (which will be demonstrated later), could pave the way toward cost-effective and efficient green emitters and beyond.

211

7.3. Optical activity of stacking faults in Heteroepitaxial $(11\bar{2}2)$ GaN/*m*-sapphire

7.3.1. Overview

In spite of the great improvement of semipolar $(11\bar{2}2)$ GaN obtained by applying SiN_x nanoporous interlayers, these layers still contain moderate density of basal plane and prismatic stacking faults. In general, depending on the effectiveness of nano-ELO process, the SiNx mask can block the threading dislocations, SFs, or both. As can be seen in previous section, the layer with better surface morphology still featured high BSF related emission line at low temperature PL spectrum, even though the TD density has been suppressed as evidenced by high integrated PL intensity at room temperature. Therefore, in order to study the intrinsic properties of this orientation and to understand optical performance of the overgrown light emitting heterostructures, it is worthy to somehow study defects (SFs) and their optical activity.

Stacking faults are regarded as interrupted stacking sequences in the crystal develop by slip. In wurtzite GaN, they form on (0001) basal plane and on $(11\bar{2}0)$ prismatic planes. The stacking sequence of the (0001) basal plane in wurtzite crystals is "ABABABABA..." where the letters A and B denote lattice structures consisting of atomic Ga-N bilayers. SFs are terminated by surfaces or heteroepitaxial interfaces, and propagated by dislocations within a crystal. I_1-type basal plane stacking fault (BSF) is the most common type observed in semipolar/nonpolar GaN templates which has the lowest formation energy compared to I_2-, I_3- and E-type basal plane stacking faults. It has recently been shown that the formation of I_1 type BSF is related to the

212

coalescence of islands in the Volmer-Weber growth mode.[187] Prismatic stacking fault (PSF)[188] is attached to basal plane stacking faults which usually fold into basal-plane faults. The atomic configuration of the PSFs is reported in a high-resolution transmission electron studies.[189] PSFs connect two I_1–type BSF with stair-rod dislocations forming at the intersections, leading to step-like features and loops.

The alignment of the conduction and valence bands is very important for heterostructures. The conduction and valence band offsets have opposite signs for type-I alignment, whereas type-II alignment has band offsets in the same sign. Both electrons and holes are confined in the QW for a type-I alignment, while the holes reside outside the QW for a type-II alignment. In a wurtzite GaN, BSFs are regarded as thin zinc-blende segments in wurtzite matrix, which are under high uniaxial compressive strain shifting the conduction band to form a potential well in the band diagram.[190] At low temperatures, the free exciton emission is found to be placed at 3.478 eV [191] and at 3.276 eV [192] for a wurtzite and zinc blende GaN, respectively. The wurtzite phase creates a significant spontaneous polarization compared to zinc-blende phase, which leads electric fields to across the SF quantum wells. In literature, the debate still continues about whether the band alignment for wurtzite/zinc-blende heterostructure in GaN is type-I [193] or type-II.[194] In a recent study, Lähnemann et al compared a type-I band alignment with a type-II band alignment taking the polarization field of $2.5 MV.cm^{-1}$ ($P_{sp} = -0.022\ Cm^{-2}$) into account for up to 3 nm thick cubic segments (BSFs) in a wurtzite GaN matrix. They carried out the calculations using the effective-mass approximation through a self-consistent solution of the one-dimensional Poisson and Schrodinger equations.[195] Their calculations predicted small differences in transition energies with increasing cubic segment thickness in the wurtzite matrix confirming similar behavior of a type-I band alignment and a

213

type-II alignment due to the fact that the spontaneous polarization dominate the emission energy change, and holes are confined in the triangular valence bands regardless of the actual band alignment.[195] Microscopic mechanisms governing the stacking fault formation as well as their effects on the optical quality are not well understood yet. There are limited studies in literature regarding recombination dynamics associated with basal plane stacking faults[196]–[199] and no studies are dedicated to recombination dynamics associated with the prismatic stacking faults. Therefore, comprehensive studies for the defects in nonpolar and semipolar nitrides and their influence on the optical quality through the recombination dynamics are essential for achieving device-quality material.

7.3.2. Strong carrier localization in stacking faults in semipolar (11-22) GaN

7.3.2.1. Overview

To date, there are only a few studies demonstrating stacking faults related emission at room temperature[128], [183] in which the BSF lines were observed to be quenching with increasing temperature and shifting together with the near band edge line. Here,[200] we intend to explore such optical behavior of stacking faults more comprehensively. Therefore, various optical techniques such as photoluminescence (PL), time- and polarization-resolved PL (TRPL and PRPL) were used to investigate the recombination dynamics of carriers in these extended defects. Moreover, influence of stacking faults on optical performance and recombination dynamics of semipolar $(11\overline{2}2)$ GaN will be discussed.

7.3.2.2. Experimental Procedure

Semipolar $(11\bar{2}2)$ GaN layer was grown on *m*-plane sapphire substrate by metal-organic chemical vapor deposition (MOCVD) applyed an in-situ epitaxial lateral overgrowth (or nano-ELO) method with SiNx used as nano-mask was utilized to obtain enhanced optical and structural quality. First, 500 nm thick GaN layer was grown on m-plane sapphire substrate with mass flow rates of 17 sccm and 9 L for TMGa and NH3, respectively, at a temperature of 1040 °C and a chamber pressure of 200 Torr. Then, a very thin nano-porous SiNx layer was deposited in a SiH_4 flow, followed by a 800 nm thick GaN growth at chamber pressure 200 Torr with mass flow rates of 17 sccm and 9 L for TMGa and NH3, respectively, at a temperature of 1050 °C. Detailed description of the nano-ELO process is provided in section 7.2. Figure 7.13(a) shows the growth schematic of the sample while Figure 7.13(b) displays the crystallographic planes and directions in wurtzite GaN. Photoluminescence measurements were performed using frequency-tripled Ti:Sapphire laser excitation (267 nm) with a pulse width of 150 fs. For temperature dependent measurements, the sample was mounted on a closed-cycle He-cooled cryostat where emission was collected from the cryostat window using an optical fiber focused into a spectrometer. The collected PL was analyzed by a liquid nitrogen cooled charge couple device (CCD) which was connected to the spectrometer. Time-resolved photoluminescence (TRPL) was measured between a temperature range of 15 K and 295 K to investigate the effects of defects on the carrier dynamics. Hamamatsu streak camera was used in order to analyze the time-resolved data. In polarization-dependent PL measurements, a linear polarization analyzer was used to resolve the polarization state of the PL and collected signal was analyzed using CCD.
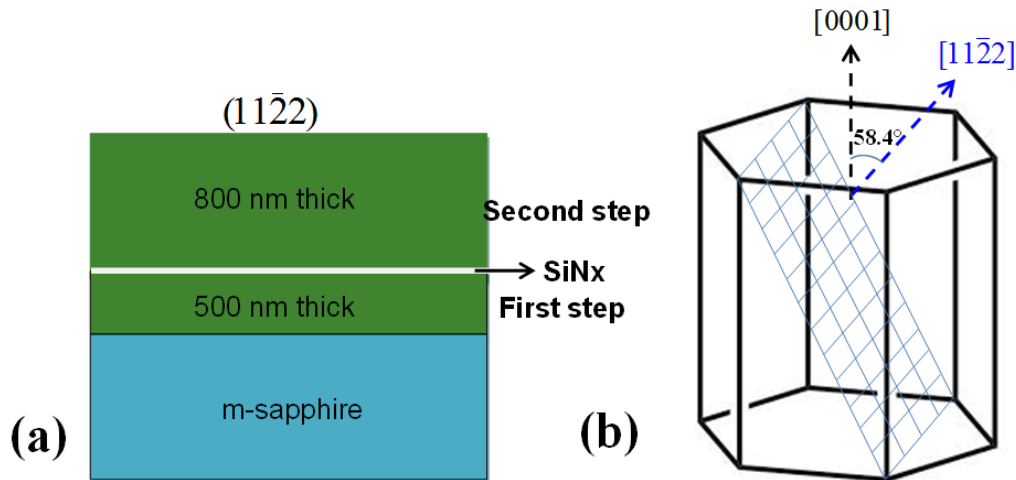
Figure 7.13. Schematic representation of growth procedure for $(11\bar{2}2)$ GaN (a) and Polar and semipolar crystallographic directions in wurtzite GaN structure (b). $(11\bar{2}2)$ GaN plane is shown in (b).[200]

7.3.2.3. Excitonics Recombination Dynamics in Stacking Faults

In order to explore the optical behavior of stacking faults, free exciton (FX), basal- plane stacking faults emission were evaluated in temperature dependent steady-state PL measurements. Figure 7.14 shows PL spectra for the semipolar $(11\bar{2}2)$ GaN sample collected a set of different temperature levels (from 15 to 295 K). The optical transitions from the stacking faults are clearly observed at 15 K PL spectra for the $(11\bar{2}2)$ GaN template, and indicated with different colored lines for their temporal evolution in Figure 7.14. These transitions occur at energies changing between 3.31 eV and 3.43 eV at 15 K. The I_1-type BSF (3.43 eV at 15 K) is found to have highest PL intensity for the given temperature range in the semipolar GaN compared to other types. Comparing the reported peak emission for the stacking faults it can be concluded that the stacking faults in this semipolar $(11\bar{2}2)$ GaN layer are under compressive strain which blue

216

shifts their peak energy by about 1-2 meV. The emission energies for the I_1, I_2 and E-type BSFs (or PSF) at room temperature are found to be 3.38, 3.30 and 3.24 eV, respectively, which are in a very good agreement with the values reported by Lähnemann et al.[195] One should note that the BSF related emissions quenched at room temperature indicating that nonradiative recombination paths become dominant with increasing the temperature. This claim can be supported by the huge reduction in integrated PL intensity for the spectra at room temperature compared to that measured at low temperature (see Figure 7.14). These nonradiative recombination centers are believed to be mainly Frank and Shockley dislocations surrounding the basal plane stacking faults.
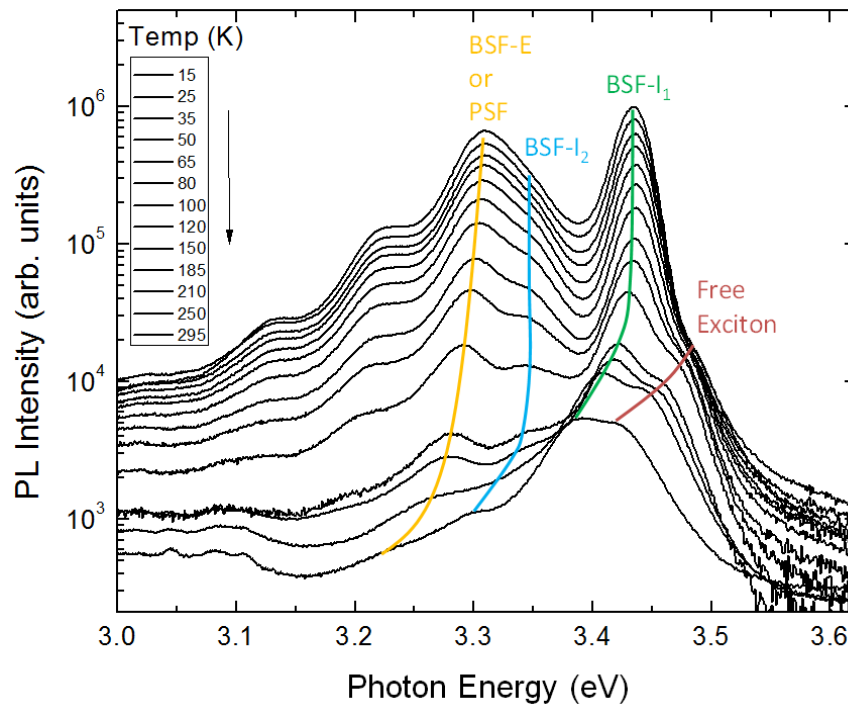
Figure 7.14. Temperature-dependent PL spectra for the semipolar $(11\bar{2}2)$ GaN layer.[200]

As reported by Rabane *et al*.,[201] the binding energy of an electron at a basal plane stacking fault is estimated to be nearly 25 meV from a solution of one-dimensional Schrodinger equation for a square quantum well. The calculation is obtained for the case of δ-potential well approximation where the binding energy is defined as $E_e = m_e (\Delta E_c L)^2 / 2\hbar^2$. The length of the basal plane stacking fault is taken as $L = 1nm$ and the electron effective mass as $m_e = 0.2m_0$. It is believed that the binding energy of an exciton bound to a stacking fault must be higher since the hole effective mass is much higher than that of a free electron's. Supporting this argument, the binding energy of a free exciton at a stacking fault is found to be 45 meV based on the theoretical calculations by Rebane *et al*.[201] According to the discussion, one can say that electrons can even bind to basal plane stacking fault at room temperature in either free or excitonic forms which is very consistent with the steady-state PL results shown in Figure 7.14(a) where the BSF emission is clearly observed at room temperature.

Evaluating earlier reports, it is found that 3.31 eV emission in the 15-K PL spectrum can be either from E-type basal plane stacking faults or prismatic stacking faults, which has PL intensities similar to I_1-type BSF at low temperatures. Due to high density of I_1-type BSF in the semipolar $(11\bar{2}2)$ GaN layer, the 3.31 eV line is likely due to PSF since PSFs are always associated with I_1–type BSF. However, transmission electron microscopy study is needed in order to state unambiguously, if this emission is originated from PSFs rather than from E-type BSFs. Both PL intensities for I_1-type BSFs and 3.31 eV emission show slight decrease between 15 K and 80 K following with a drastic droop with further temperature increase, as can be seen in Figure 7.15(a). It is believed that this behavior is closely related to donors which are acting as exciton capture sites up to 80 K. Excitons are fully delocalized from donors at temperatures

above 80 K (localization energy of the donors is 7 meV (~80K)).[198] PL ratio from these stacking faults showed slight increase from 15 K to 80 K (Figure 7.15(b)). However, the ratio significantly decreased by increasing the temperature above 80 K. The slight increase in the ratio up to 80 K might be due to either the carrier transfer between the stacking faults of different kinds or different radiative recombination efficiency of carriers in different type of stacking faults. The latter is supported by time-resolved PL results that will be discussed later. The fast decrease in the PL ratio after 80 K can be the indication of the carriers having lower binding energy at 3.31 eV SF compared to I_1-type BSF while we know that 3.31eV emission is deeper with respect to wurtzite matrix than I_1-type BSF. One can assume that an electron bound to a 3.31 eV SF can either bind to a basal plane stacking fault at low temperatures or become free when the substrate temperature is increased above 80 K. However, the effect of the nonradiative centers cannot be neglected in all processes affecting intensity of all stacking fault related emissions via carrier capture. This is very plausible assumption that the donors cannot prevent excitons from nonradiative recombination since the binding energy of excitons is insufficient to keep them localized near donors at room temperature.
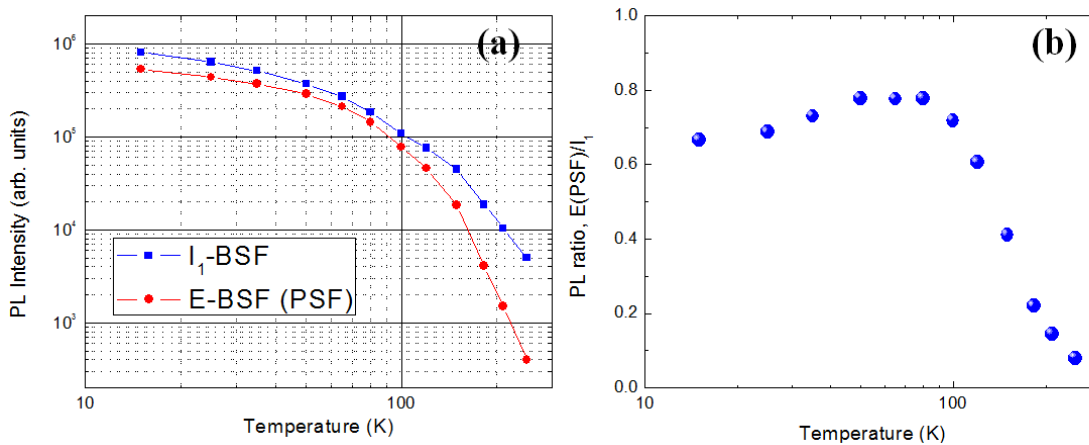
Figure 7.15. (a) PL intensity and (b) PL intensity ratio of 3.31 eV SF and I_1-type BSF with respect to temperature.[200]

219

Temperature dependent TRPL measurements were performed to better understand the effect of stacking faults on recombination dynamics. Figure 7.16 shows PL decay times obtained from biexponential fitting of PL transients for I_1-type BSF and 3.31 eV SF related emissions. It should be also mentioned here that recombination dynamics are affected by not only stacking faults, but also point defects and threading dislocations. However, the discussion here is limited to effects of longer decay times are taken as characteristic PL decay times since initial fast decays in transients are related to the carrier diffusion away from the surface deeper into the sample.[201], [202] Among the stacking fault emissions, higher PL intensity and faster decay times for I_1-type BSF compared to other stacking faults indicate that I_1-type BSF has larger density and larger contribution to overall recombination dynamics. It should be also mentioned here that recombination dynamics are affected by not only stacking faults, but also point defects and threading dislocations. However, the discussion here is limited to effects of stacking faults on the recombination dynamics deduced from their temperature dependent PL decay profiles. PL decay times of both I_1-type BSFs and 3.31 eV SFs do not show temperature dependence up to 80 K. After 80 K, PL decay times decreased as $\sim T^{-2}$ and $\sim T^{-1}$ for I_1-type BSFs and 3.31 eV SFs, respectively. One may conclude that the carrier delocalization with increasing temperature is higher in I_1-type BSF compared to 3.31 eV SF. This is consistent with position of the stacking faults related energy levels close to bottom of the conduction band. Obviously, the I_1-type BSFs energy level is closer to the conduction band bottom level of GaN wurtzite matrix compared to 3.31 eV SFs, which makes the carriers in 3.31 eV SF to be trapped more easily. This trapping can occur by either other basal plane stacking faults or conduction band by giving additional thermal energy. However, one should also consider the temperature effects where the probability

220

for the dissociation of excitons into free carriers increases with increasing the temperature. It must be also taken into account that the carrier localization will be different for the free excitons and donor bound excitons compared to free electrons. For example, when free excitons are around the vicinity of a BSF line, the probability of their capture by the BSF will be higher than that by donors. This is more effective up to 80 K since the excitons localized at the donors cannot bind to donors anymore above this temperature. Another mechanism related to electron localization in basal stacking faults was investigated by Confdir *et. al.*[203] They theoretically showed that presence of a donor in the vicinity of an I_1-type basal stacking fault localizes the electrons along the plane of the basal plane stacking fault. The localization becomes stronger when the distance between the donor and the basal stacking fault reduces, and reaches its maximum when the donor is placed inside the basal stacking fault.[203]
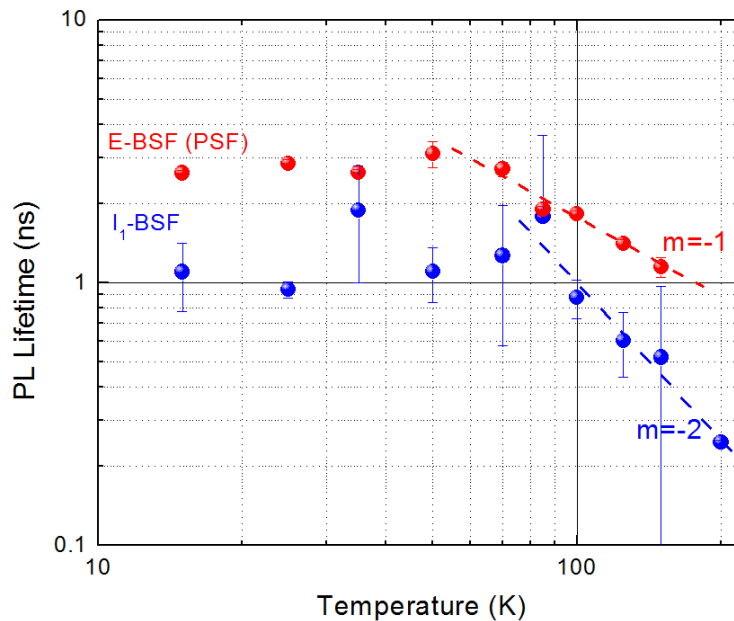
Figure 7.16. PL decay times for I_1-type BSF and 3.31 eV SF obtained from bi-exponential fits of the transients.[200]

Nevertheless, the most effective process for the dramatic decrease in PL decay time for the both types of stacking fault emissions at temperatures above 80 K is related to nonradiative recombination since increasing the temperature activates the nonradiative channels by delocalizing carriers from either donors or stacking faults and thus assisting them to reach the nonradiative-recombination centers. It can be understood from above discussion that the processes associated with the carrier recombination dynamics together with stacking faults are quite complicated and it is indeed difficult to distinguish all effects one by one using only optical techniques. However, optical techniques could provide strong evidence about the dominating mechanisms on the carrier recombination dynamics when temporal evolution of PL intensity and PL decay times for the stacking faults are investigated. One may conclude that exchange of carriers between the energy levels (conduction band, donor bound, and stacking faults) takes place via carrier trapping/detrapping processes and affects the carrier dynamics in addition to nonradiative recombination centers.

The temperature-dependent PL lifetimes and PL intensity ratios were used to separate the radiative and nonradiative lifetimes for both I_1-type BSF and 3.31 eV SF emissions. Figure 7.17 shows extracted radiative and nonradiative lifetimes. As seen from Figure 7.17 the radiative lifetime dominates the PL decay time at low temperatures and increases with increasing temperature. The theoretical value for the temperature dependence of radiative decay time is 1.5 for bulk samples, and 1 for two-dimensional structures as shown in Figure 7.17. However, the slopes obtained for the stacking fault emissions differs substantially from the theory as the stacking faults are expected to show two-dimensional character. This strongly implies that other mechanisms are affecting the radiative recombination dynamics. The slope for 3.31 eV SFs is

222

found to be steeper compared to I_1-type BSFs indicating that the density of carriers, which contribute the radiative recombination, in 3.31 eV SF decreases much faster with increasing the temperature compared to I_1-type BSF. As seen in Figure 7.17, the radiative lifetime at 200 K is ~20 ns and ~100 ns for I_1-type BSFs and 3.31 eV SFs, respectively. Assuming a radiative recombination coefficient B = 5×10^{-11} cm^3/s and using the $\tau_{Rad} = 1/BN$ one can find the carrier density, which is denoted by N in this equation. The carrier densities associated with I_1-type BSFs and 3.31 eV SFs at 200 K are calculated to be 10^{18} cm^{-3} and 2×10^{17} cm^{-3}, respectively. Based on the slopes, the radiative decay times for the I_1-type BSFs and 3.31 eV SFs at room temperature will be ~40 ns and ~300 ns, respectively. As noticed, the radiative decay for the I_1-type BSFs reduces to half at room temperature compared to 200 K, while the decay slowed down by factor 3 for 3.31 eV SF. Therefore, the carrier densities at room temperature will be 5×10^{17} cm^{-3} and 6.6×10^{16} cm^{-3} for the I_1-type BSF and 3.31 eV SF, respectively. This clearly shows that the escape rate of the carriers from the 3.31 eV SF are much faster than the I_1-type BSF supporting the earlier arguments and data. The electron bound to these stacking faults can either bind to another stacking fault or become a free electron when the substrate temperature is increased. However, the effect of the nonradiative centers, surrounding the stacking faults, should not be neglected in all processes.
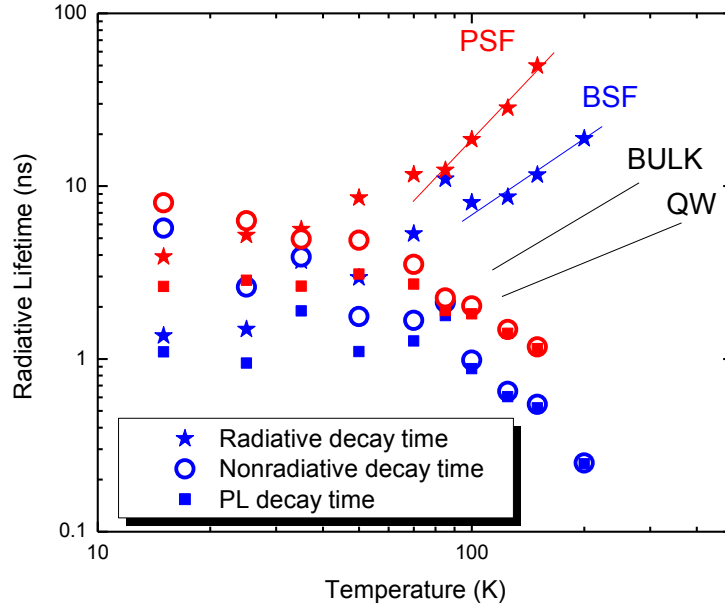
Figure 7.17. Temperature-dependent radiative and nonradiative decay times extracted from PL decay times. Stars, open circle and full square show radiative, nonradiative and PL decay times, respectively.[200]

7.3.2.4. Optical Anisotropy of Stacking Faults related emissions

Effects of stacking faults on optical processes are further investigated using polarization-resolved PL (PRPL) technique. Figure 7.18 shows the polar plot of normalized PL intensity for I_1-type BSF and 3.31 eV SF emissions from the semipolar GaN sample measured at 15 K. The directions of the excitation light wave vector k and the electric field E with respect to selected crystallographic directions in a wurtzite structure are indicated in the same figure. A linear polarization analyzer was used to resolve the polarization state of the PL with the light collected always normal to the sample surface. 90° for the polarizer corresponds to polarization parallel to the $\left[11\bar{2}0 \right]$ GaN axis. The degree of polarization is defined as $\rho = (I_h - I_l)/(I_h + I_l)$, where I_h and

224

I_l represent the highest and the lowest PL intensities resolved, respectively. The degree of polarization is found to be 0.30 and 0.15 at 15 K for the I_1-type BSF and 3.31 eV SF lines, respectively. Polarization may seem to diminish when carriers recombine through the 3.31 eV SFs compared to I_1-type BSFs. However, the two times decrease in degree of polarization can arise from different orientations of the stacking faults. This result is quite different from the PRPL results reported by Okur *et. al.*[204] where the degree of polarization clearly reduces when carriers recombine through basal plane stacking faults affecting adversely the optical quality of semipolar $(1\bar{1}01)$ GaN layers.
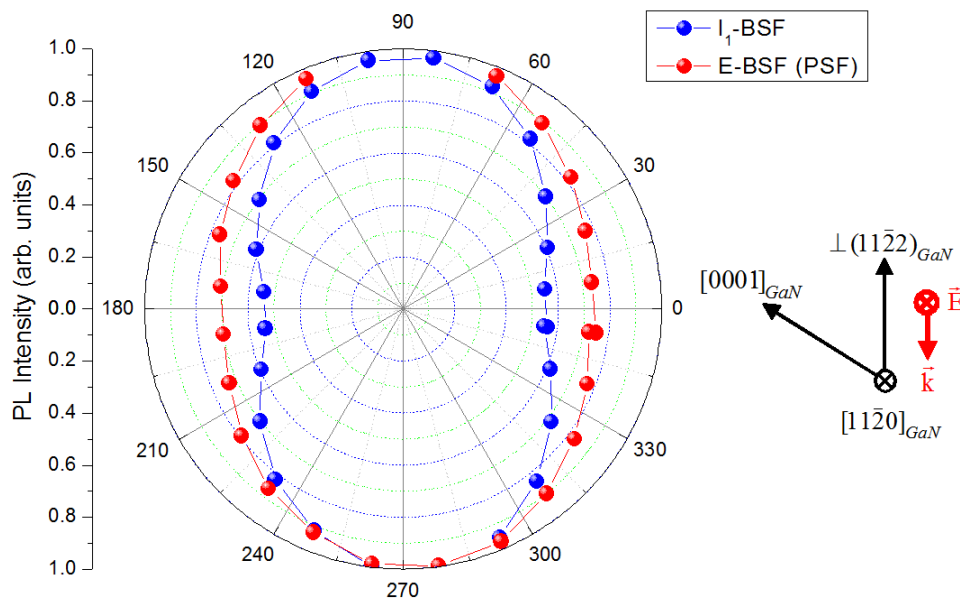
Figure 7.18. Normalized polarization-resolved PL intensity plot for the I_1-type BSF and 3.31 eV SF at 15 K together with directions for the excitation light wave vector k and the electric field E with respect to selected crystallographic directions in the wurtzite structure.[200]

225

www.manaraa.com

7.3.2.5. Summary and Conclusions

In summary, Stacking faults are found to be actively involved in optical processes substantially influencing the carrier dynamics in semipolar $\left(11\bar{2}2\right)$ GaN/*m*-sapphire. In addition to nonradiative recombination centers, carrier trapping/detrapping by stacking faults and carrier transfer between stacking faults and donor energy levels are found to be among those processes affecting the carrier recombination processes at different temperature levels. Temperature dependent steady-state PL results showed that carriers are loosely localized in 3.31 eV SF compared to I_1-type BSF. This is evidenced by strong I_1-type BSF PL appearing at room temperature while the 3.31 eV SF PL dies around 250 K. Temperature has a strong influence on the PL intensity ratio of those two which is believed to be closely related to exciton localization energy to donors (7 meV) where excitons are fully delocalized from donors after 80 K. Higher PL intensity and much faster radiative recombination decay times of I_1-type BSF compared to 3.31 eV SF showed that I_1-type BSF has larger density and larger contribution to recombination dynamics

7.3.3. Wurtzite/zinc-blende electronic-band alignment in basal-plane stacking faults in semi-polar GaN

7.3.3.1. Overview

As discussed before, heteroepitaxial semipolar and nonpolar GaN suffer from high densities of extended defects resulting in poor optical and structural quality.[102], [162], [183], [200], [205] Such extended defects significantly affect the layer properties by contributing in recombination

226

dynamics [122], [130], [148], emission characteristics (as nonradiative recombination centers[101] as well as sources of PL broadening by introducing emission lines[121], [200]), transport properties[57], [61], and impurity incorporation[106]. The understanding of the extended defects including stacking faults and their contributions to device properties is thus imperative. In order to develop a deep understanding of the effect of stacking faults on optical and transport properties of the heterostructures, the contributions of such defects and their electronic band structure needs to be realized.

As mentioned earlier in this section, basal plane stacking faults (BSFs) are considered as inclusions of the cubic zinc-blende phase in the GaN wutrzite matrix which result in band discontinuity at BSF interfaces because of different bandgaps of the cubic and the wurtzite GaN phase.[195] This provides a confinement in the lower bandgap phase and thus affects recombination dynamics[200] and emission spectra[121], [195]. Emission lines corresponding to recombination at BSFs have been reported between 3.29 to 3.42 eV at room temperature for Intrinsic (I_1, and I_2 types) and extrinsic (E type) BSFs the emission energy being dependent on the number of cubic layers (width of the quantum well (QW)) .[121], [183], [206]–[209] There is, however, still a debate on the type of band alignment, type I or type II, for this WZ/ZB QW system with atomically flat interfaces representing BSFs in III-Nitrides. Some calculations based on density functional theory (DFT) predict type I[193] while some others suggest type II[194] band alignment. Although the experimental reports, on the other hand, are more consistently in favour of a type II band alignment based on the amount of blue shift of PL with increasing excitation density,[210], [211] there is still no consensus.

227

Here,[212] we have employed time resolved differential transmission (TRDT) measurements[213] in order to shed more light onto the type of electronic band alignments at the WZ/ZB interfaces in BSFs. Semipolar $(11\overline{2}2)$ GaN layers were used for this exploration.

7.3.3.2. Experimental Procedure

The semipolar $(11\overline{2}2)$ GaN layer was grown on a planar *m*-plane sapphire substrate in a vertical design low pressure metal-organic chemical vapour deposition (MOCVD) system with trimethylgallium (TMGa) and NH_3 used as precursors for Ga and N, respectively, and H_2 as carrier gas. GaN nucleation was performed at a relatively high substrate temperature of 1060 ºC without inserting a buffer layer directly on *m*-sapphire. A nanoporous SiN_x interlayer with an estimated thickness of approximately 10 nm was employed as a mask for *in situ* epitaxial lateral overgrowth ('nano-ELO approach'[102]) to improve the optical quality of the GaN film. The total thickness of the structure was estimated to be 1.3 μm. The detail description of growth procedure can be found elsewhere.[102], [200] The cross-sectional schematics of the sample and the crystallographic orientation of semipolar $(11\overline{2}2)$ plane within the hexagonal wurtzite unit cell is displayed in Figure 7.19.

228
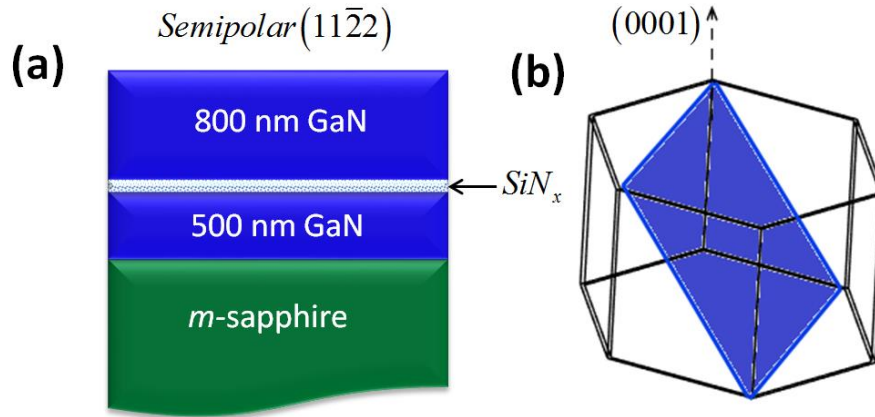
Figure 7.19. Cross-sectional schematic representation of (a) semipolar $(11\bar{2}2)$ GaN grown on *m*-sapphire using *in situ* nano-ELO[102] approach and (b) the crystallographic representation of the semipolar $(11\bar{2}2)$ plane with respect to *c*-direction within the hexagonal wurtzite unit cell.[212]

A CW He-Cd laser operating at 325 nm and focused to an excitation spot diameter of 50 μm was used for the photoluminescence (PL) measurements. The sample was mounted in a closed-cycle He-cooled cryostat and the emission was collected from the cryostat window using an optical fiber connected to a spectrometer with a liquid nitrogen cooled charge couple device (CCD) detector. The PL measurements were performed at 15 K and 295 K. In order to demonstrate high BSF density in the layers grown on m-sapphire the cross sectional STEM was employed in a scanning transmission electron microscope FEI (S)TEM Tecnai F20 equipped with a bright-field annular detector (BF).

Wavelength degenerate time-resolved differential transmission (TRDT) technique was employed to determine the band alignment of the BSFs in the semipolar GaN layer. Figure 7.20 displays the simplified schematic of set-up for the TRDT experiment. The primary beam

generated by a frequency doubled Ti-sapphire laser ($\lambda \sim 370 nm$) with a pulse width of 150 fs is divided into pump and probe beams where the pump beam has approximately one order of magnitude higher intensity than the probe beam. More detailed description of the TRDT experiment can be found elsewhere. [98]
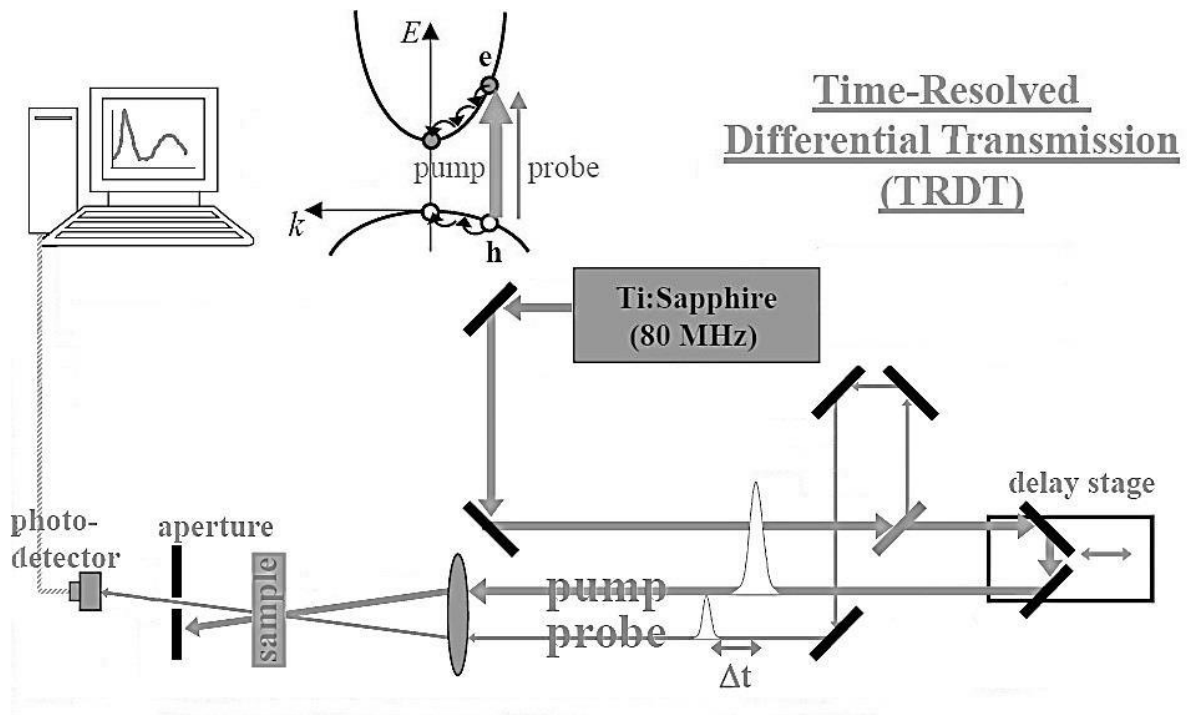
Figure 7.20. Simplified schematics of the TRDT experimental setup.[212]

7.3.3.3. Results and Discussions

The 15-K and 295-K PL spectra of the semipolar $(11\bar{2}2)$ GaN layer are shown in Figure 7.21.

The two emission peaks at 3.43 eV and 3.31 eV in the low temperature spectrum correspond to excitons bound to I_1 and E BSFs, respectively, while the donor bound exciton (D^0X) line can be

230

observed only as a shoulder at 3.48 eV. The significant contributions of BSFs to low temperature PL compared to D^0X are indicative of their large density.[102] The BSF related emission line survives even up to room temperature and is still visible as a peak at 3.38 eV next to the free exciton line (FX) at 3.41 eV. The temperature evolution of the PL of this structure published earlier[200] also supports the existence of BSF related lines at room temperature. The presence of large density of BSFs in semipolar $(11\bar{2}2)$ GaN layers grown on m-sapphire is verified by crosssectional STEM image shown in Figure 7.22.
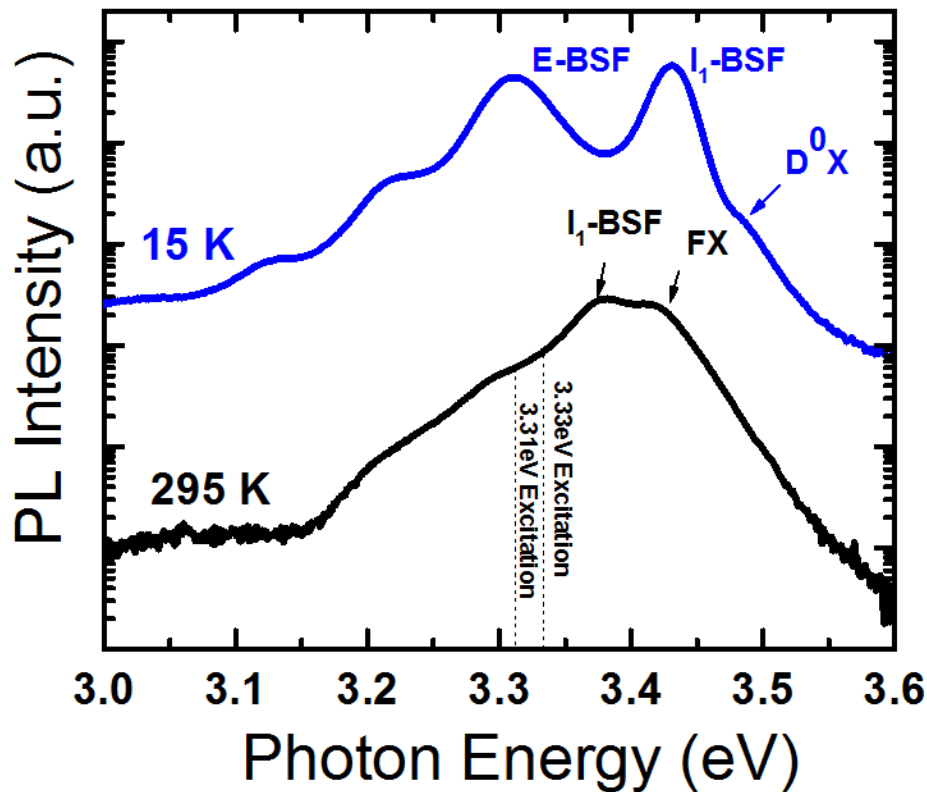
Figure 7.21. PL spectra for the semipolar $(11\bar{2}2)$ GaN layer obtained at 15 K and 295 K. The vertical dashed lines correspond to excitation photon energies used for TRDT measurement.[212]

231
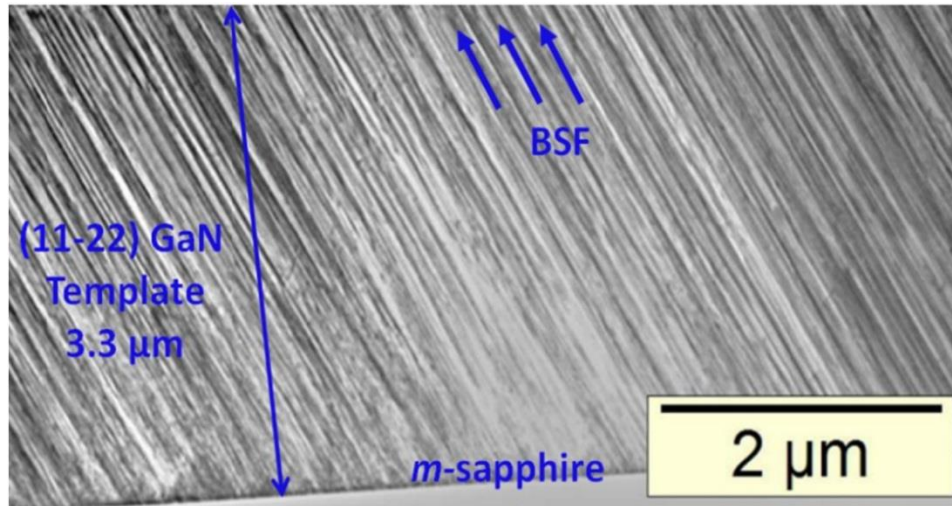
Figure 7.22. Cross-sectional STEM image in bright field contrast of a selected semipolar $(11\bar{2}2)$ GaN layer grown on *m*-sapphire indicating presence of large BSF density in the layers.[212]

The robust temperature dependence of BSF-related PL is crucial for exploration of BSFs by the TRDT technique at room temperature. The TRDT measurements were performed at two different photon energies of the pump and probe beams ($E_{pump} = E_{probe}$) of 3.33, and 3.31 eV, as marked by the vertical dashed lines in Figure 7.21. The aim is to mainly excite the I_1-type BSF related emission lines at room temperature and avoid excitation of the FX band to the extent possible.

For type I band alignment, under resonant excitation an initial rise in probe differential transmission ($DT \equiv \dfrac{\Delta T}{T_0}$) at t = 0 followed by a decay caused by carrier recombination and thermalization through carrier-carrier scattering should be observed.[213] For type II band alignment, the initial rise at t = 0 will be followed by a very fast decay (faster than 1 ps) and then, In contrast to the type I case, the differential transmission starts to increase until it reaches a

saturation (a few picoseconds after t = 0). In longer time (couple of hundreds of picoseconds), the transmission should decay until completely vanishes. [213] This behavior for the type II band alignment arises from relaxation of electron-hole plasma to thermal equilibrium (initial decay) accompanied by spatial separation of the plasma components (electrons and holes), providing an increase in differential transmission.[214] Finally, the carrier recombination takes place at a slower rate because of spatial separation of electrons and holes thus resulting in a slow decay of differential transmission. The decay behaviour of type I (in InGaN/GaN [98] and GaAs/AlGaAs[213] QWs) and type II (GaAs/AlAs QWs[213]) band alignments can be found in literature reports.

Figure 7.23 shows the results of TRDT experiment performed under two different excitation energies of 3.33 eV [Figures 7.23(a) and (b)] and 3.31 eV [Figures 7.23(c) and (d)]. The two photon energies (3.33 and 3.31 eV) below near band-edge (NBE) emission was performed to avoid intermixing of GaN NBE and and I_1 BSF absorption and to ensure absorption by only BSFs. DT transients excited with both photon energies of 3.33, 3.31 eV exhibit a rise followed by a decay lasting longer than 300 ps (Figure 7.23(a) and (c)). In the shorter delay range (< 10 ps), the differential transmission shows a decrease immediately after the initial rise at t = 0 [Figures 7.23(b) and (d)]. This quick initial drop followed by a slow signal increase is seen more clearly in the insets showing the TRDT signal for even shorter ranges (< 2ps). Note that due to different time resolutions of the experimental setup for different delay ranges, the signal levels do not necessarily match each other for the short and long delay ranges (See Figure 7.23(a) and (b) for instance). For a reference c-plane GaN layer containing practically no BSFs, However, the DT signal is very small independent of excitation energies (not shown).

233
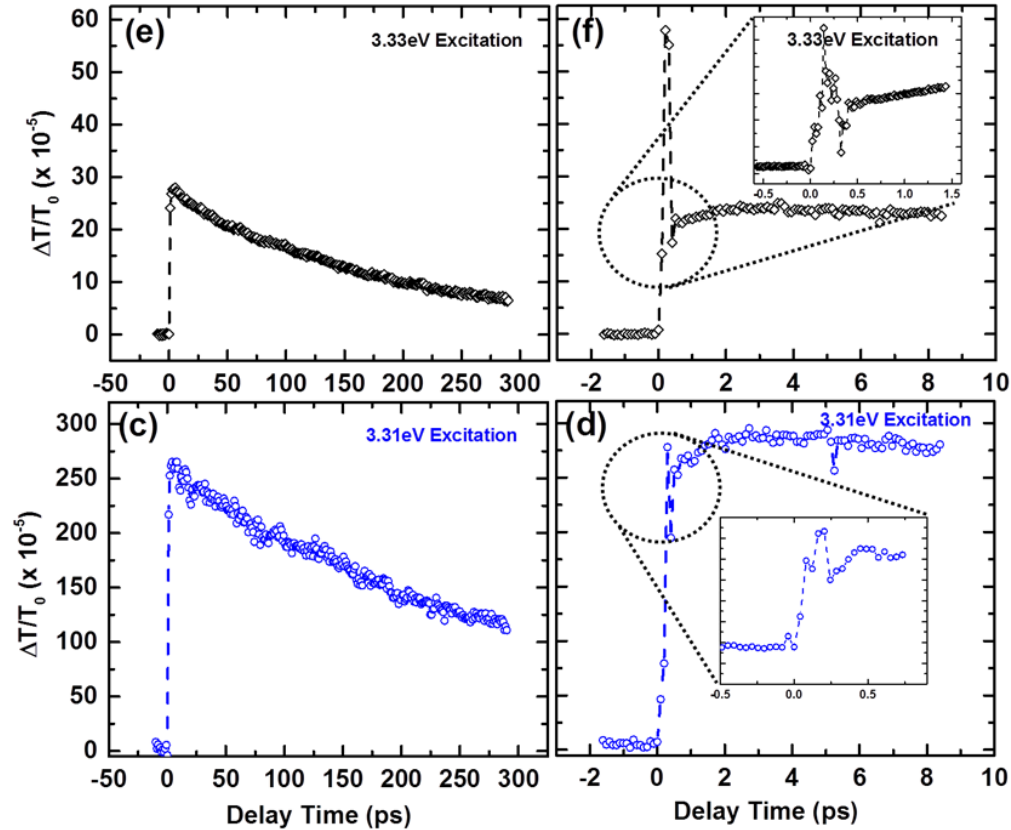
Figure 7.23. Probe differential transmission in the semipolar $(11\bar{2}2)$ GaN layer as a function of time delay between the pump and probe beams under 3.33 eV (a,b), and 3.31 eV (c,d) excitation for 300 ps (a,c) and 10 ps (b,d) delay ranges. The inset in (b,d) displays the zoomed in plot for 1 to 2 ps range.[212]

The results obtained for 3.31- and 3.33-eV excitations (exciting the BSFs of type I_1) point to type II band alignment in BSFs. Therefore, our findings are consistent with earlier experimental studies indicating type II band alignment at the BSF interfaces in GaN. [210], [211] Further investigations including excitation dependent and temperature dependent TRDT measurements are required for verifications of this finding which will be published elsewhere.

7.3.3.4. Summary of Findings

In summary, the type of band alignment of WZ/ZB GaN interfaces in BSFs was aimed to be determined to reach a consensus. A heteroepitaxial semipolar $(11\bar{2}2)$ GaN grown on *m*-plane sapphire with high density of BSFs having carriers strongly confined at room temperature are used for this study. The femtosecond pump-probe beam experiment in TRDT measurement shows the behaviour of type II band alignment in BSFs. Knowledge of band alignment type at the interfaces formed by BSFs representing zinc-blende inclusions in the wurtzite GaN matrix is critical for understanding their effects on optical and transport properties of electronic and optoelectronic devices based on nonpolar and semipolar orientations.

7.4. Optical investigation of microscopic defect distribution in semi-polar $(11\bar{2}2)$InGaN light emitting diodes

7.4.1. Overview

As stated earlier, semipolar $(11\bar{2}2)$InGaN LEDs grown on *m*-sapphire have been reported to show higher indium incorporation rate which would be beneficial for attaining efficient emission at longer wavelengths.[215] However, semipolar GaN growth often suffers from high density of extended defects such as threading dislocations and stacking faults, resulting in lower crystal quality.[156] Therefore, material quality needs to be improved further to take full advantage of

semipolar orientation of GaN and comprehensive studies of effects of extended defects are required. In this section, correlations between microscopic optical and structural properties in semipolar $(11\overline{2}2)$ InGaN LEDs were investigated by means of spatially and spectrally resolved near-field scanning optical microscopy (NSOM).[157]

7.4.2. Experimental Details

Semipolar $(11\overline{2}2)$ oriented GaN layers were grown on *m*-sapphire substrates by means of nano-epitaxial lateral overgrowth (ELO), details of which have been reported in Ref. [102].

LED structures incorporate, as shown schematically in Figure 7.24, a Si-doped $In_{0.01}Ga_{0.99}N$ underlying layer for improving the quality of overgrown layers, electron injectors composed of $In_{0.04}GaN$ and $In_{0.08}GaN$ layers for efficient thermalization of hot carriers prior to injection into the active region, six periods of 3 nm-thick $In_{0.16}GaN$ wells separated by 3 nm-thick $In_{0.06}GaN$ barriers as the active region, and a 100 nm-thick Mg-doped p-type GaN, grown in the given order on top of $(11\overline{2}2)$ GaN templates. NSOM measurements were performed at 85 K using a Cryoview 2000 NSOM system (Nanonics Imaging Ltd) in the illumination mode where HeCd (3.81 eV or 325 nm wavelength) and InGaN (3.06 eV or 405 nm wavelength) laser excitation were used through a Cr-Al coated cantilevered optical fiber probe with 350 nm aperture.

100 nm p-GaN

3 nm $In_{0.01}GaN$

3 nm $In_{0.16}GaN$

3 nm $In_{0.06}GaN$

⋮   ⋮   ⋮   — Active region

3 nm $In_{0.16}GaN$

16 nm $In_{0.08}GaN$ ⎤ Electron

16 nm $In_{0.04}GaN$ ⎦ injector layers

60 nm $In_{0.01}GaN$ Underlying layer

~4 μm n-GaN   n-GaN template
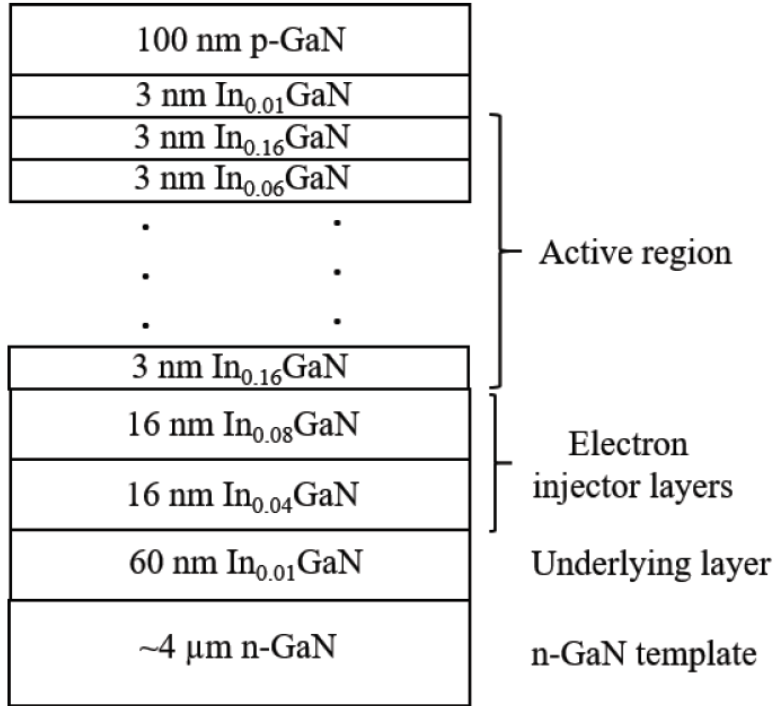
Figure 7.24. Cross-sectional schematic of the LED structures grown on semipolar $(11\bar{2}2)$ templates.[157]

7.4.3. Results and Discussion

The atomic force microscopy (AFM) image of $(11\bar{2}2)$ LED structure in Figure 7.25(a) shows striations along the $[11\bar{2}3]$ direction of GaN. Such morphology is characteristic of the $(11\bar{2}2)$ GaN surface.[216]–[218] Using cross-sectional SEM image, S. Y. Bae *et al.* [218] reported that the striated pattern consists of a "ridge-and-valley" shape which is formed due to the intersection of $\{10\bar{1}1\}$ planes. Moreover, from cross-sectional AFM image, the angle between the faceted and the flat surfaces was found to be ~26°, which is the angle between the $\{10\bar{1}1\}$ and $\{11\bar{2}2\}$ family of planes.
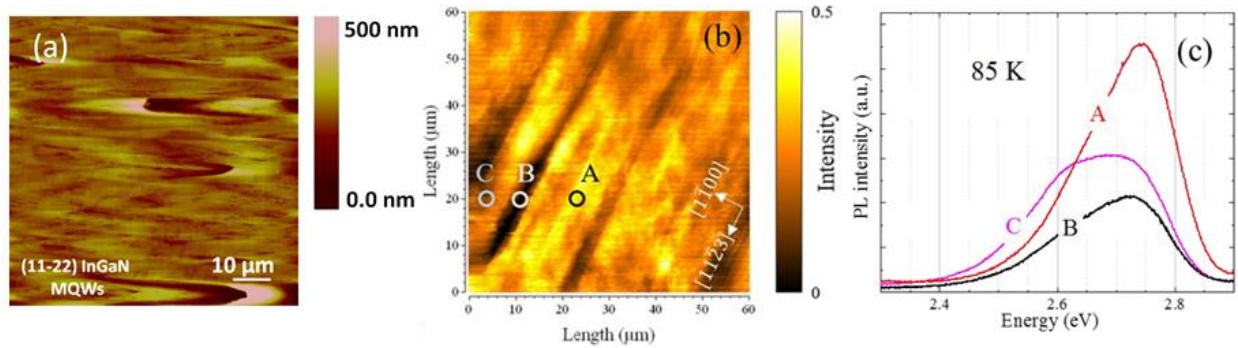
Figure 7.25. (a) AFM image and (b) NSOM PL intensity map of semipolar $(11\bar{2}2)$ InGaN LEDs. (c) Local PL spectra for the points indicated in (b).[157]

The spatial NSOM PL intensity map presented in Figure 7.25(b) shows similar surface features as observed in the AFM image. The striations are in general characterized by lower PL intensity, most likely due to the presence of threading dislocations and the associated defects, compared to the other regions. Local PL spectra were collected at multiple points on the sample and three representative spectra are shown in the figure. Point A located in a relatively flat region shows strong active region emission whereas point B located on one of the striations has weaker PL intensity. Point C located near the edge of the striation is characterized by intermediate PL intensity. In addition, appearance of an additional peak on the lower energy side as well as the red-shift of the main peak indicates higher indium content near the edge of the striations, where faceted surface meets the flat surface. Changes in the local strain may be the reason for different Indium incorporation efficiency and variations in the emission wavelength. Investigations of the $(11\bar{2}2)$ GaN templates are in progress in order to shed light on the effects of stacking faults on emission characteristics.

238

7.4.4. Summary of Findings

In summary, the spatial variations of extended defects, stacking faults and threading dislocations, and their effects on the optical quality for semi-polar $(11\bar{2}2)$ InGaN light emitting diodes (LEDs) were investigated by near-field scanning optical microscopy at 85 K. The striated regions showed weaker PL intensities compared to other regions and the meeting fronts of different facets were characterized by higher Indium content due to the varying internal field.

7.5. Indium incorporation efficiency to semi-polar $(11\bar{2}2)$ GaN on *m*-sapphire

7.5.1. Overview

In previous sections, we performed methods to improve crystal quality of the semipolar $(11\bar{2}2)$ GaN layers and discussed some general properties of the stacking faults. In the following sections (sections 7.5 and 7.6), we will turn our attention toward ternary InGaN systems grown on the semipolar $(11\bar{2}2)$ layers having reduced defect densities. Here, the indium incorporation efficiency in this orientation will be compared with that in *c*-plane. In the next section, the

239

semipolar $(11\bar{2}2)$-oriented InGaN heterostructures will be evaluated in terms of exciton localization, recombination dynamics, and optical anisotropy.

As noted, Yamada *et al.*[18] reported the reduction in indium contents by a factor of two to three for the layers grown on nonpolar *m*-plane compared to those on conventional *c*-plane substrates under similar growth conditions.[19] This caused significant reduction in LED output power for devices with emission wavelength longer than 400 nm possibly due to increase in nonradiative recombination rates.[19] Semipolar orientations featured by substantially reduced polarization fields represent another alternative to the polar structures for producing efficient LEDs in a wide range of wavelengths from blue to yellow, in particular in the light of theoretical predictions of enhanced indium incorporation efficiency relying on effects of strain[20] and surface atomic configurations[21]. According to the theoretical studies, planes with inclination angle of $\theta \sim 60°$ with respect to *c*-axis should exhibit the highest In incorporation efficiency among all the planes of GaN (about 4% higher indium compared to than in *c*-plane),[20] drawing attention to the $(11\bar{2}2)$ orientation with $\theta = 58°$.

Experimental data on In incorporation available in literature for the $(11\bar{2}2)$ orientation are, however, scarce and contradictory. Both reduced[219] and similar,[28], [220] incorporation efficiency of indium on $(11\bar{2}2)$ plane compared to the *c*-plane have been reported. Zhao *et al.*[22] found out higher indium incorporation for the $(11\bar{2}2)$-oriented InGaN heterostructures compared to other studied semipolar and nonpolar orientations grown on high quality bulk substrates. However, this study did not report any direct comparison with the conventional *c*-plane structures.[22]

240

In this section, we compare efficiencies of indium incorporation to InGaN LED active regions on semipolar $(11\bar{2}2)$ and conventional c-plane GaN templates on sapphire grown by metal-organic chemical vapor deposition (MOCVD) in the same run to ensure identical growth conditions.

7.5.2. Experimental Details

GaN/InGaN LED structures of semipolar $(11\bar{2}2)$ and polar (0001) orientations were grown on m- and c-sapphire substrates, respectively, utilizing our MOCVD system (see section 3.4). It is well known that indium incorporation rate is highly sensitive to growth temperature.[37], [67] Therefore, to ensure identical growth conditions for fair comparison of the two orientations, (0001)- and $(11\bar{2}2)$-oriented GaN templates were placed side by side in the reactor chamber at the same radial position on the holder. This will avoid any potential error due to radial non-uniformity of growth temperature in the MOCVD system. The GaN growth rates in (0001) and $(11\bar{2}2)$ orientations were found to be similar from $in\text{-}situ$ reflectometry measurements of respective GaN templates grown separately.

The semipolar $(11\bar{2}2)$GaN templates were grown on m-plane sapphire substrates using a thin (~20nm) AlN layer deposited at 600ºC. Thereafter, a 3μm semipolar GaN was grown at high temperature using a two-step approach involving deposition of 1.5 μm layer at 30 Torr followed by growth of GaN layer of higher optical quality at 200 Torr (details of two step growth

241

approach can be found elsewhere [102], [106], [119]). The *c*-plane GaN templates were grown on *c*-sapphire with the conventional three-step technique (low temperature deposition of GaN nucleation layer, followed by annealing and high temperature growth). Utilizing the *in-situ* nano-ELO technique, insertion of SiN_x nano-mesh was performed under optimized conditions for both *c*-plane and $(11\bar{2}2)$ GaN layers to improve optical and structural quality. The details of optimization of the *in-situ* epitaxial lateral overgrowth (ELO) process for *c*-plane[101] and $(11\bar{2}2)$ GaN[102] are discussed elsewhere. The total thicknesses of the polar and semipolar GaN layers were about 10µm.

The next stage was the growth of InGaN active layers on the prepared semipolar $(11\bar{2}2)$ and *c*-plane GaN templates. After loading the wafers into the MOCVD reactor, first a 60-nm thick Si-doped InGaN underlying layer with nominal indium content of 1% was grown to improve quality of active layers, followed by the deposition of staircase or graded electron injector (SEI or GEI)[76] segments with total thickness of 40 nm, which were inserted prior to the active regions (see Figure 7.26 for schematics). The following designs of the active region have been used: (1) two 4.5-nm-thick InGaN layers, (2) four 3-nm thick InGaN layers, and (3) six 3-nm thick InGaN layers, separated by 3-nm-thick $In_{0.06}Ga_{0.94}N$ barriers. The structures will be referred to hereafter as dual 4.5-nm double heterostructure (DH), quad 3-nm DH, and hex 3-nm DH, and respectively. The nominal indium contents for the InGaN active regions were 15% based on data obtained for *c*-plane LED structures deposited in separate experiments. The structures were completed with 3-nm $In_{0.01}Ga_{0.99}N$ cap layer and 100-nm Mg-doped p-type GaN. The schematics and flat-band conduction band structure of the samples are shown in Figure 7.26. Except for the c-plane reference layer of the second set (Figure 7.26(b)) that is grown on a

242

regular GaN template, the substrates for the other *c*-plane reference layers are grown using in-situ nano-ELO.
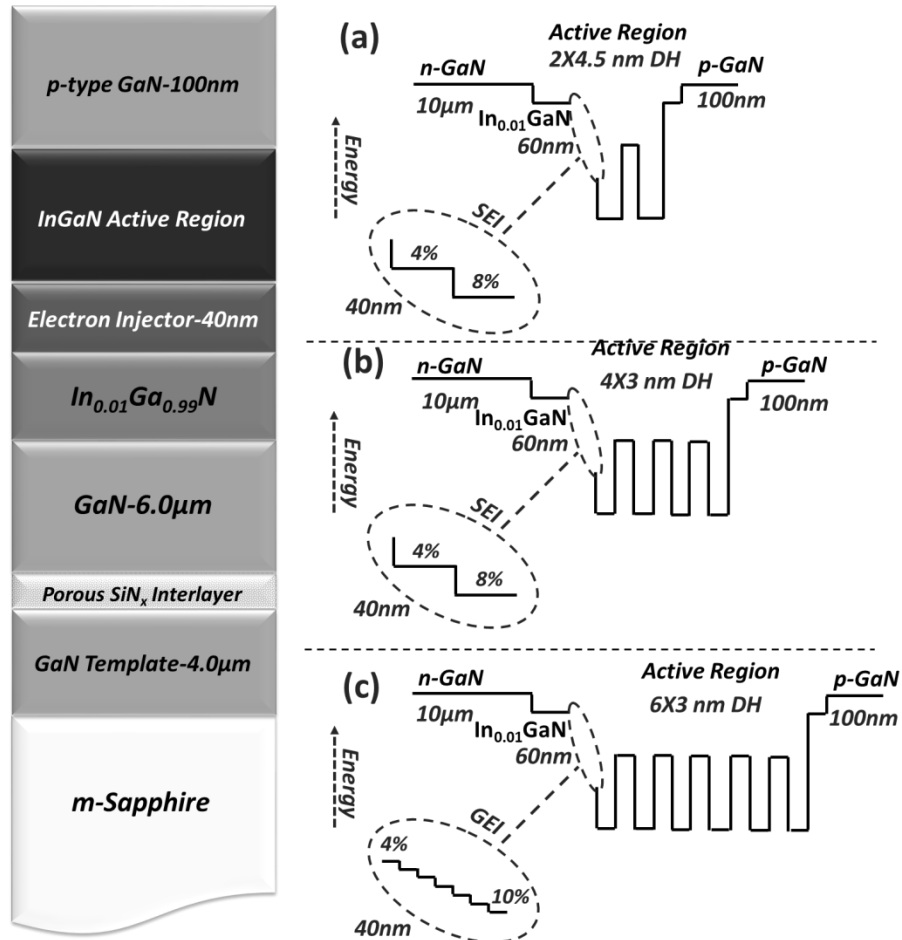
Figure 7.26. Schematic diagram (left) and the flat-band conduction band schematics (right) of the designed (a) dual 4.5nm DH, (b) quad 3nm DH (4×3nm DH), and (c) hex 3nm DH (6×3nm DH), LED structures used for comparison of indium incorporation efficiency between semipolar (11-22) LED and c-plane counterparts. [Submitted for Publication in Journal of Crystal Growth]

The actual indium contents for semipolar and polar structures were assessed from peak positions in steady-state micro-PL spectra measured at room temperature. At the excitation density used for the determination of In contents QCSE-induced red shift was confirmed to be

diminished. For steady-state micro-PL measurements a He-Cd laser with 325 nm wavelength was used as an excitation source, and the excited region was ~2 μm in diameter. Frequency doubled Ti-sapphire laser with 150 fs pulse width and period of 12.5 ns was used in combination with a Hamamatsu streak camera for the time-resolved photoluminescence (TRPL) measurements and to study time evolution of PL peak position and the QCSE induced shift in emission wavelength for selected samples. Spatially-resolved cathodoluminescence (CL) was employed to study the indium distribution in the layers.

7.5.3. Results and Discussions

Figure 7.27 compares room temperature micro-PL spectra from the semipolar and polar LED for dual 4.5-nm (Figure 7.27(a)), quad 3-nm (Figure 7.27(b)), and hex 3-nm (Figure 7.27(c)) InGaN structures (see Figure 7.26 for the schematics) excited with the highest excitation power of 8.0 kW/cm^2 corresponding to photo-generated carrier concentrations of $n = 1.67 \times 10^{18} cm^{-3}$. The shift of the whole PL spectra from LED structures (emissions from active region and underlying InGaN layers) to the longer wavelengths for the semipolar InGaN LED spectra relative to the polar structures is clearly seen from the figure. This indicates that semipolar structures exhibit higher In contents for both compressively strained (InGaN active layers) and relaxed or partially relaxed (InGaN under-layers layers) layers.

244
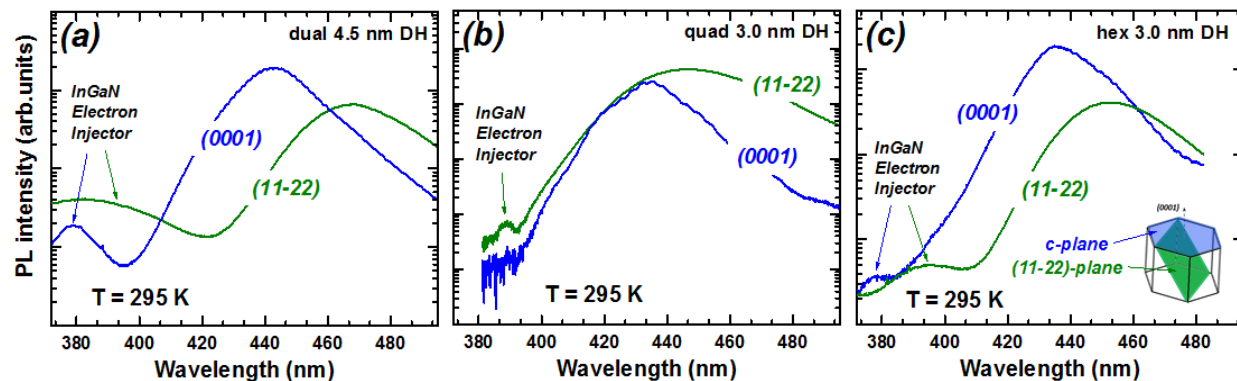
Figure 7.27. PL spectra for semipolar (green) and polar (blue) LEDs structures grown side by side with (a) 2×4.5 nm DH, (b) 4×3nm DH, and (c) 6×3nm DH active region designs. The inset shows the crystallographic orientations of the layers. [Submitted for Publication in Journal of Crystal Growth]

The In content in the layers was then calculated from the PL peak positions at highest excitation levels. Following the theoretical study by Moses *et al.*[107] reporting the bowing parameter, *b,* of InGaN as a function of InN molar fraction, the bowing parameter value of 1.73 was used to calculate In content in the active regions. The bandgap values of 0.7 eV[108] and 3.42 eV[1] for InN and GaN, respectively, were used for the calculations. The estimated indium concentrations for InGaN wells and underlying layers are listed in Table 7.2.

Table 7.2. Estimated indium contents from optical measurements in the DH layers for the structures used in this experiment. [Submitted for Publication in Journal of Crystal Growth]

Structure Design	In content (%) Semipolar $(11\bar{2}2)$	In content (%) Polar *c*-plane
2×4.5nm DH	18.6	14.8
4×3.0nm DH	15.7	13.0
6×3.0nm DH	16.6	13.7

In order to ensure saturations in the peak emission wavelength and flat-band condition for the micro-PL measurements, we evaluated the amount of Stark shift for polar and semipolar layers for one of the structures by comparing PL emission wavelength at low and high photo-generated carrier concentrations in the time-resolved PL measurement. Figure 7.28 shows a time evolution of PL spectra under pulsed excitation for the polar *c*-plane and semipolar $\left(11\overline{2}2\right)$ hex 3-nm InGaN LED structures. The highest photo-generated carrier concentration (estimated to be $n = 4.54 \times 10^{19} cm^{-3}$) corresponds to the pulse arrival and peak emission intensity of the active layers (violet and red horizontal lines in Figure 7.28(a) and (c)), while the low photo-generated carrier density at 1 to 1.5 ns after the pulse (pink dashed lines in Figure 7.28(a) and (c)) when most of the carriers had already been recombined. The QCSE-induced shifts in emission energy of $\Delta E_{QCSE} = 71 meV$ and $\Delta E_{QCSE} = 34 meV$ were observed for the polar and semipolar layers emitting at 2.87 eV(432 nm) and 2.73 eV(454 nm), respectively, with 3-nm well width with nominal 15.0% and 6.0% indium contents in DHs and barriers, respectively. This measured value for nominal $In_{0.15}Ga_{0.85}N/In_{0.06}Ga_{0.94}N$ 6×3nm DH structure is higher than the theoretically calculated values for $In_{0.1}Ga_{0.9}N/GaN$ 3×3nm DH with practically identical amount of DH/barrier lattice mismatch in which the maximum blue shifts were reported for structure emitting at 417 nm as $\Delta E_{QCSE} = 90 meV$ and $\Delta E_{QCSE} = 45 meV$ for and polar *c*-plane and semipolar $\left(11\overline{2}2\right)$, respectively.[46]
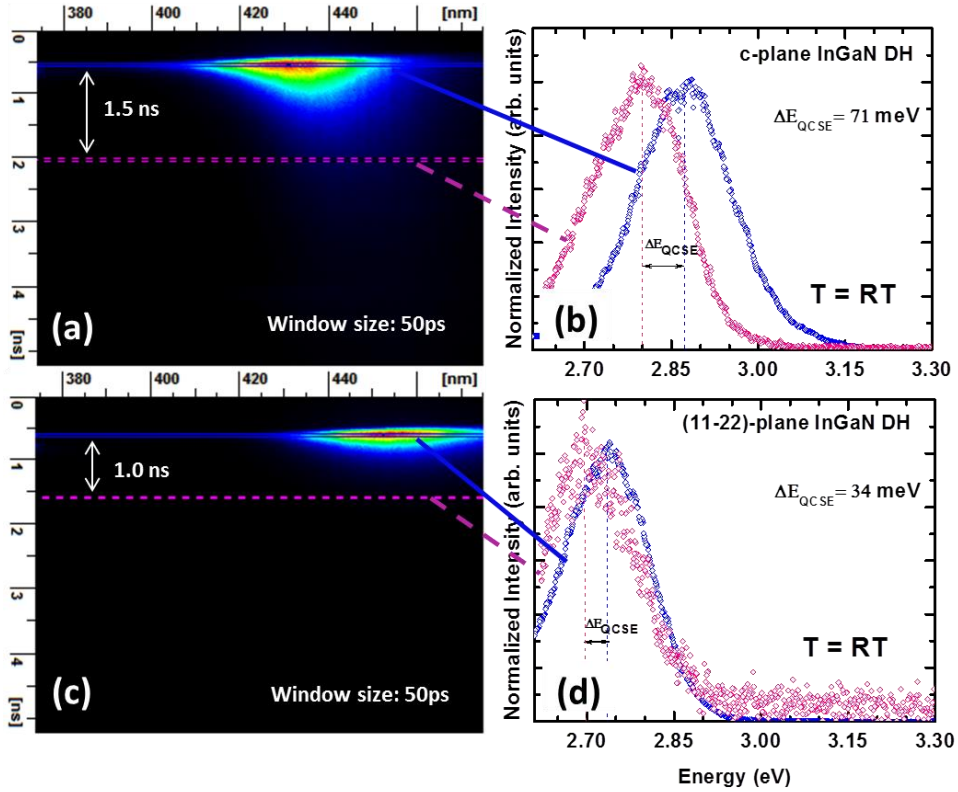
Figure 7.28. Time evolution of PL spectra for polar (a) and semipolar $\left(11\bar{2}2\right)$(c) 6×3nm (hex 3-nm DH) with delay time in vertical and emission wavelength in horizontal axis. The solid violet and dashed green horizontal lines in (a) and solid red and dashed blue horizontal lines in (c) indicate the 50 ps time windows at peak intensity (corresponding to highest photo-generated carrier density) and 1.5 ns (a) and 1.0 ns (c) afterwards (corresponding to low photo-generated carrier density), respectively. The PL spectra associated with the time windows indicated in (a,c) are shown in (b) and (d) for polar and semipolar structures, respectively. [Submitted for Publication in Journal of Crystal Growth]

The emission wavelengths for the highest excitation in TRPL match well with that of the micro-PL (Figure 7.27(b)) within 1 to 2 nm accuracy (which could also be explained by slight non-uniformity of indium contents for the different measurement points). This means that the carrier concentration for the highest excitations in micro-PL is high enough to perfectly screen

the electric field and ensure flat-band condition. Therefore, the calculated indium contents are sufficiently accurate within 0.2% of indium.

Liquid-helium-temperature (T = 5.5 K) spatially resolved-CL measurements revealed the uniformity of indium distribution on the semipolar surface. Figure 7.29 represents CL mapping for the hex 3-nm $(11\overline{2}2)$ LED structure. Relatively uniform intensity distribution from CL intensity image (CLI) for the range of active region emission can be observed (Figure 7.29(b)). There are some local increase in emission wavelength associated with the surface features in CL wavelength image (CLWI) (Figure 7.29(c)) that appear only at some spots and are very low in intensity (see Figure 7.29(b)) and thus do not contribute significantly to the integral optical properties. Except those local features, the distribution of indium is found to be uniform which makes our findings on enhanced incorporation of indium on the semipolar $(11\overline{2}2)$ surface more reliable.
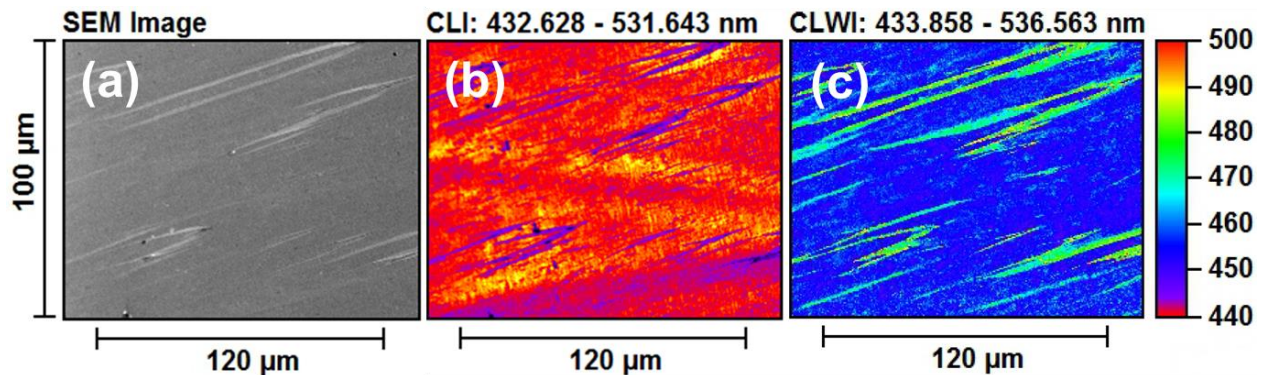
Figure 7.29. SEM image (a), spatially resolved CL intensity (b) as well as wavelength image (c) of semipolar 6×3 nm DH LED structures (see figure 1(b) for schematics of the structure). The scan size is 100 μm ×150μm. [Submitted for Publication in Journal of Crystal Growth]

248

Our findings suggest higher indium incorporation efficiency for the semipolar $(11\bar{2}2)$ orientation, which agrees well with the theoretical predictions.[20], [21], [49] This can be due to lower strain associated with In incorporation into the lattice due to more favorable atomic configuration in case of $(11\bar{2}2)$ compared to polar c-plane (similar to comparison of $(11\bar{2}2)$ with *m*-plane using first principle calculations by Northrup[21]). Another possible mechanism which can enhance the indium incorporation is the presence of stacking faults in the heteroepitaxial semipolar layers grown on non-native substrates.[200] It should be noted that stacking faults can be considered as inclusions of cubic phase in the wurtzite lattice, and In solubility in the cubic GaN lattice may be different from that in the hexagonal phase. High density of stacking faults in heteroepitaxial layers could also result in large density of type-II quantum wells[195] formed between the cubic inclusion into the InGaN layers and cause reduction in active region emission wavelength. [221] The situation can be more understandable due to our previous observation of strong localizations of carriers in stacking faults even at room temperature.[200]This way, the longer emission wavelength from semipolar InGaN structures compared to c-plane layers grown under similar growth conditions can be partially explained. However, we should mention here that the spatio-CL is sensitive to stacking faults[222] while the CL mapping of the semipolar structure demonstrates a uniform emission proving of low stacking fault density in the InGaN layers. Moreover, observation of very high indium incorporation efficiency for $(11\bar{2}2)$ planes for high quality layers grown on native substrates with low density of extended defects[219] could remove this possibility and ensure the highest indium incorporation efficiency in this semipolar GaN plane.

249

7.5.4. Summary and Conclusions

Substantial enhancement of In incorporation (by 3 to 4%) in semipolar $(11\bar{2}2)$ LED structures compared to polar counterparts has been observed for In contents in the range of 15 to 18%. Spatially resolved CL images for semiplar hex 3-nm DH LED indicates uniform indium distribution for the areas of 100 μm × 120μm supporting uniformly enhanced indium incorporation into semipolar $(11\bar{2}2)$ surface. In agreement with the theory predicting the highest incorporation for plane with inclination angle of about 60°[20], [21] and following the reports of incorporation comparison of semipolar $(11\bar{2}2)$ and other nonpolar and semipolar planes,[219] and based on our data demonstrated here, it can be concluded that indium incorporation efficiency is indeed the highest in this semipolar plane among the crystallographic orientations of GaN. Our findings suggest that semipolar $(11\bar{2}2)$ GaN plane holds a promise for addressing the green gap problem for future generation of efficient green and yellow LEDs.

7.6. Optical Anisotropy and Exciton Localization in Semipolar $(11\bar{2}2)$-oriented InGaN multi-quantum wells

7.6.1. Overview

As stated earlier, the optical properties of the nonpolar and semipolar heterostructures are limited by the presence of high densities of extended defects[61], [200] despite the substantial progress in improving their structural quality through employment of defect-eliminating methods [223], [102], [119], [224]. As a result, the recombination dynamics in these orientations are mainly governed by localized states[122], [148], [225], [226] due to presence of potential fluctuations which were found to correlate directly with densities of interfacial defects in binary quantum wells[1], [122], [130], [147], [148]. In case of InGaN ternary system, the presence of indium-rich regions also contribute to carrier localization.[155] Such exciton localization, in case of *c*-plane LEDs, has been found to isolate the carriers from dislocations and thus reduce nonradiative recombination[227], [228] while it can also have detrimental effect on device performance by causing current crowding[229]. Therefore, understanding exciton localization is crucial to analyze recombination dynamics as well as carrier transport properties in light emitter applications.

In this section, excitonic localization, recombination dynamics, and optical anisotropy in semipolar $(11\bar{2}2)$ InGaN multi-quantum wells (MQWs) grown on *m*-plane sapphire substrates will be discussed.[230]

7.6.2. Experimental Details

The MQW structure was grown using our MOCVD system (see section 3.4 for details about the system). As shown in section 7.2, the single-phase $(11\bar{2}2)$-oriented semipolar GaN templates

251

were grown on planar *m*-plane sapphire substrates using *in situ* nano epitaxial lateral overgrowth (nano-ELO)[102] for improved optical quality. Thereafter, a 60 nm-thick $In_{0.01}GaN$ layer and a compositionally graded ($In_{0.04}GaN$ to $In_{0.10}GaN$) electron injector (EI) were grown followed by the active region consisting of 6 periods of 3 nm-thick $In_{0.20}Ga_{0.80}N$ QWs separated by 3nm $In_{0.06}Ga_{0.94}N$ barriers as displayed in Figure 7.30. The details of the MOCVD growth of InGaN active region and electron injector (EI)[76] on planar *m*-sapphire can be found in section 7.5[106].
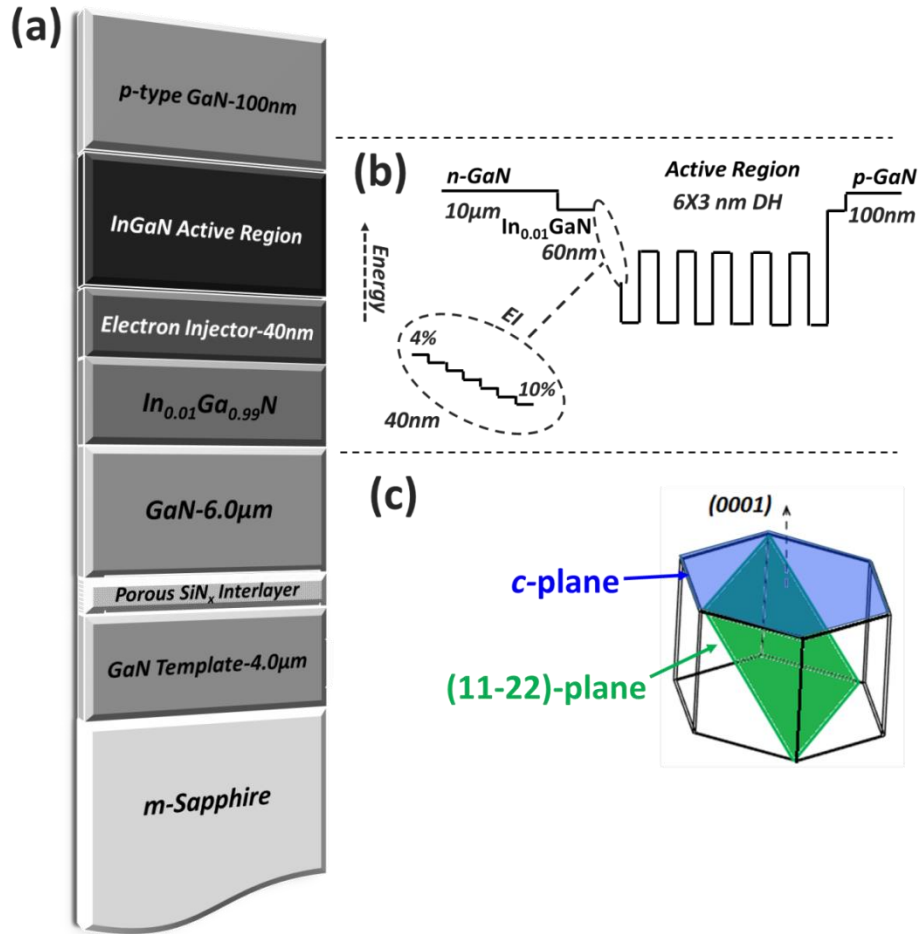
Figure 7.30. (a) Cross-sectional schematic diagram and (b) corresponding flat-band conduction band schematics of the semipolar $(11\bar{2}2)$-oriented InGaN MQWs structure. (c) Semipolar $(11\bar{2}2)$ plane within the hexagonal wurtzite unit cell.[230]

The optical properties of the semipolar InGaN MQWs were explored using steady state photoluminescence (PL) and time-resolved photoluminescence (TRPL). A 325 nm wavelength He-Cd laser excitation with a spot size of ~2 μm was employed to acquire the steady-state PL spectra. Frequency doubled Ti-sapphire laser (380 nm) having pulse width and period of 150 fs and 12.5 ns, respectively, in combination with a Hamamatsu streak camera was utilized for the TRPL measurements. Samples were mounted in a closed-cycle He-cooled cryostat and the

253

steady-state and TRPL measurements were performed in the temperature range from 15K to 295K. The emission was collected from the cryostat window through an optical fiber attached to a spectrometer having a liquid nitrogen cooled charge couple device (CCD) detector. In polarization-dependent PL measurements, a linear polarization analyzer was used to resolve the polarization state of the PL and collected signal was analyzed using CCD.

254

7.6.3. Results and Discussions: Optical Anisotropy

Similar to what we reported on subsection 5.3.2 in case of non-polar m-plane, and in subsection 6.3.2 for $(10\bar{1}1)$-plane for GaN MQWs, optical anisotropy of the $(11\bar{2}2)$-oriented InGaN MQW-related emission is investigated. This optical anisotropy for the semipolar $(11\bar{2}2)$-oriented ternary InGaN heterostructures is also confirmed by the data presented in Figure 7.31. The spectra consists of three main emission lines; QW, electron injector (EI), and yellow emission (YE). According to this plot which is a series of 15K photoluminescence spectra for different orientations of the electric field of the emitted photon radiation obtained using a polarization analyzer in the emitted beam path before reaching the detector, the intensity of the QWs, and the Electron Injector (EI) seems to be changing by changing the orientation of the polarization analyzer. This indicates the presence of optical anisotropy for both emissions.
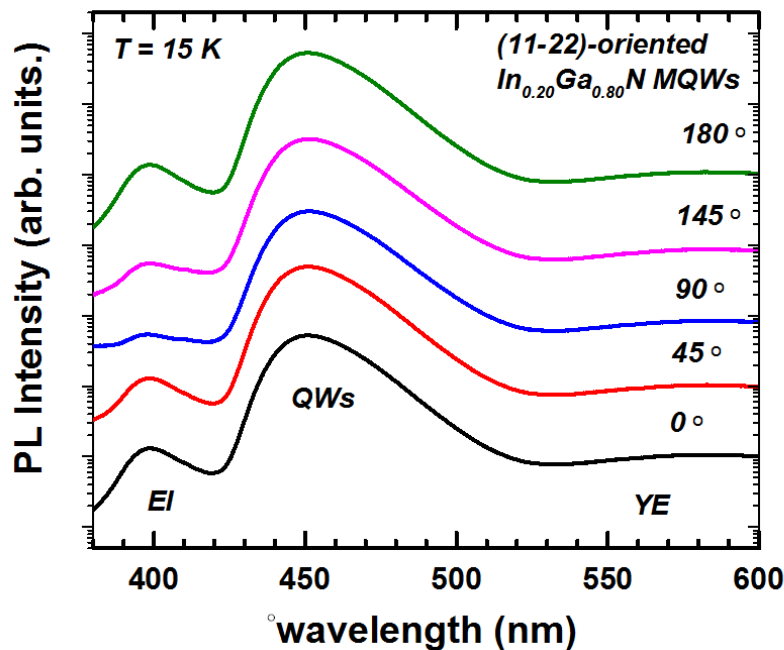
Figure 7.31. Photoluminescence spectra for various polarizations of the emitted photons with0º being taken parallel to the y direction of the Cartesian coordinate system.

This optical anisotropy in the emission lines can be seen more clearly in the polar plot illustrated in Figure 7.32. The experimental value for degree of polarization (DOP) was found to be 33% for QW related emission, 43% for the EI, and 15 % for the YE. These values are significantly lower than the DOP measured for $(10\bar{1}1)$-oriented GaN MQWs which was 58%. Also, the DOP for EI is found to be higher compared to QW which can be either related to differences in indium concentrations or the effect of strain as they are both different for QW and EI. One more interesting observation is the polarized emission with 15 % DOP for the YE. This observation could be better explained in case the origin of YE for this layer is known.
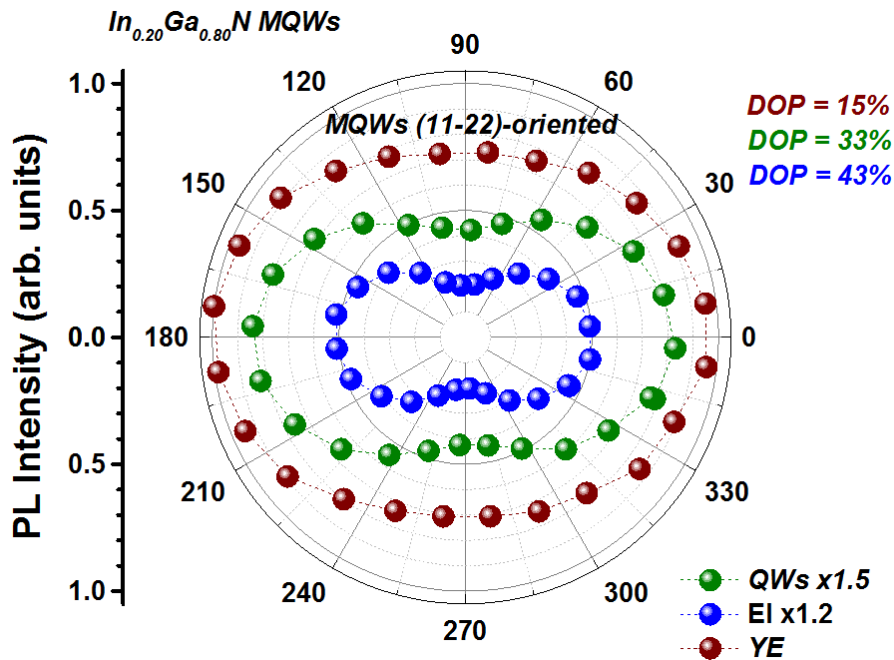
Figure 7.32. Polar plot of the PL intensity for the MQWs (green), for the electron injectors (blue), and for the yellow emission (wine).

Finally, comparison of the optical anisotropy for semipolar structure and the *c*-plane counterpart grown side by side (see section 7.5 for more information about the structures) shows the polarized emission for the semipolar structure in contrast to the practically isotropic behavior in case of polar structure (see Figure 7.33). Seemingly, the semipolar structures are promising candidates for applications in polarized light emitters.
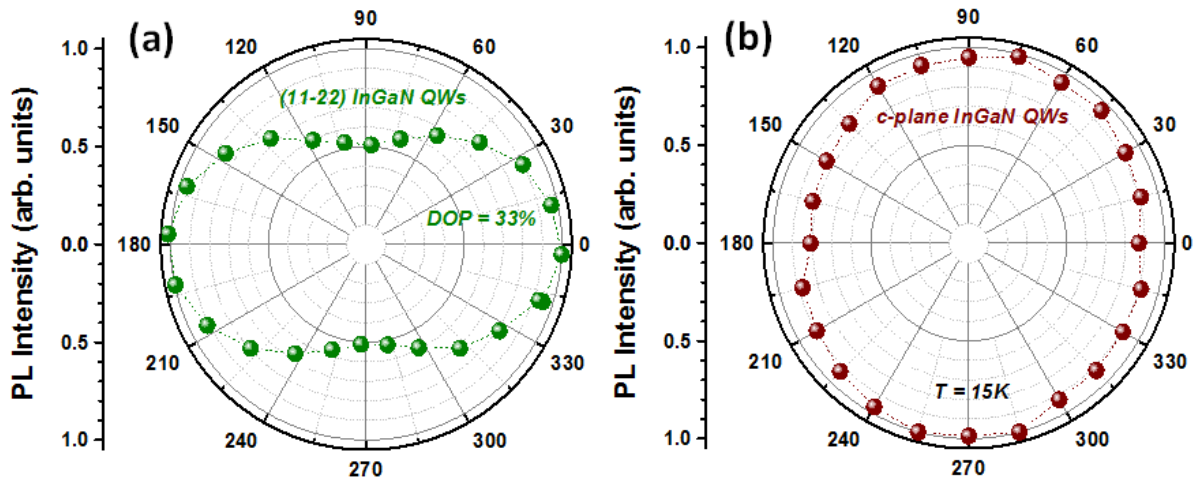
Figure 7.33. Polar plot of the PL intensity integrated over the InGaN MQWs emission of (a) $(11\bar{2}2)$ and (b) *c*-plane orientations.

7.6.4. Results and Discussions: Exciton Localization

7.6.4.1. Room Temperature PL Analysis

The room temperature micro-PL spectra of the semipolar $(11\bar{2}2)$ InGaN MQWs structure measured at the highest excitation of 8.0 kW/cm^2 and excitation wavelength of 325nm are shown

in Figure 7.34(a). The average photo-generated carrier concentration for the employed excitation level was estimated as $n = 1.67 \times 10^{18} \, cm^{-3}$. Beside the active-region emission in the blue wavelength range (~ 452 nm), the 394-nm emission from the InGaN electron injector and 366-nm GaN near band edge emission are also observed in the spectra of Figure 7.34(a).

Assuming perfect screening of the internal electric field (at the excitation power used) and considering quantum confinement, the indium content in the active layers can be determined from the MQW PL peak using

$$E_{PL} = E_g^{InGaN}(x) + E_{Confinement}, \tag{7.1}$$

where E_{PL} denotes the MQW PL peak emission energy, $E_g^{InGaN}(x)$ is the InGaN bandgap calculated using[107]

$$E_g^{InGaN}(x) = xE_g^{InN} + (1-x)E_g^{GaN} - bx(1-x), \tag{7.2}$$

where E_g^{InGaN}, E_g^{InN} (0.7 eV), and E_g^{GaN} (3.42 eV) are the bandgaps of InGaN, InN, and GaN [106], respectively, and b (1.73[107]) is the bowing parameter. The confinement component of the PL emission energy can be found considering ground state energy solution of electron and heavy holes in a finite rectangular potential well having width of L, starting from infinite barrier solution as

$$E_1^\infty = \frac{\hbar^2}{2m^*}\left(\frac{\pi}{L}\right)^2, \tag{7.3}$$

and defining dimensionless parameters for energy and barrier height

258

$$\varepsilon \equiv \frac{E}{E_1^{\infty}} \tag{7.4}$$

$$\nu_0 \equiv \frac{V_0}{E_1^{\infty}} \tag{7.5}$$

Thus, the symmetric solution for the allowed energies for finite barrier height problem should satisfy[109]

$$\sqrt{\varepsilon}\,\tan\left(\frac{\pi}{2}\sqrt{\varepsilon}\right) = \sqrt{\nu_0 - \varepsilon} \tag{7.6}$$

Therefore, the indium content x in the active layer wells was estimated to be around 20% ($\pm 0.2\%$),
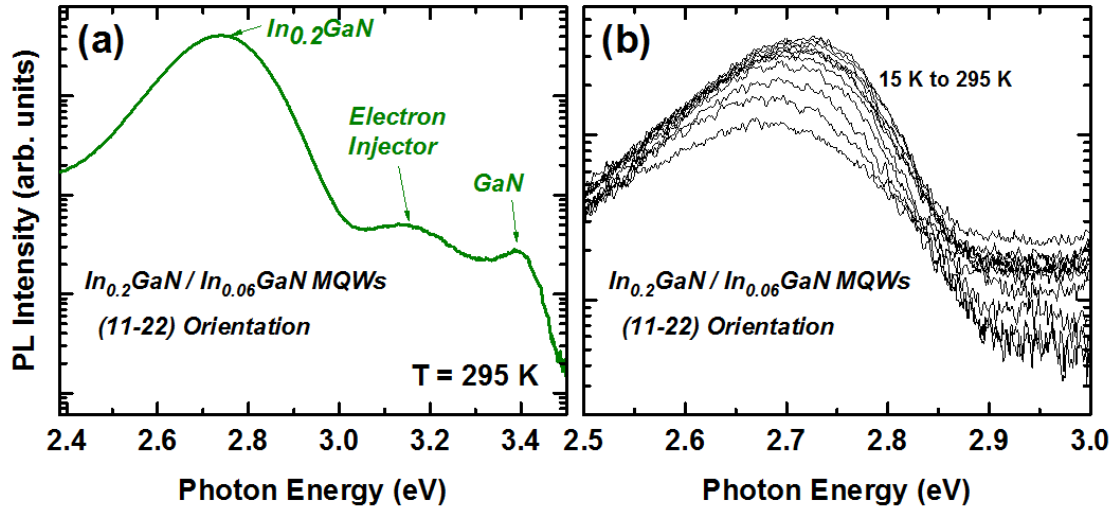
Figure 7.34. PL spectrum of the semipolar $(11\bar{2}2)$ $In_{0.165}Ga_{0.835}N/In_{0.06}Ga_{0.94}N$ MQWs at (a) room temperature (295 K) and (b) temperatures varying from 15 to 295 K. Besides the active region emission, luminescence from InGaN underlayers and GaN buffer can also be observed in (a).[230]

The evolution of emission from the active region with temperature in the range from 15 K to 295 K is displayed in the Figure 7.34(b). As the temperature increases from 15 K to 295 K, integrated PL intensity decreases by a factor of about 3 owing to increase in nonradiative recombination rates. With increase in temperature, the spectrum redshifts by about 40 meV.

7.6.4.2. Exciton localization from temperature dependent PL

In order to gain insight into the exciton spectral distributions and any localization, we plotted the temperature dependences of peak emission intensity and peak energy in Figure 7.35. This measurement is performed under pulsed excitation (380 nm) with excitation average power of $p_{avg} = 38.2 W/cm^2$, corresponding to an average photo-generated carrier density of $n = 6.52 \times 10^{12} cm^{-3}$. The PL intensity slowly decreases with temperature up to approximately 150 K, where there occurs an increase in intensity followed by a much faster decrease from 160 K to 295 K [Figure 7.35(a)]. Similarly, only small redshift in the PL peak from 2.712 to 2.705 eV is observed when temperature increases from 15 K to 150 K followed by a slight blueshift and then a more rapid redshift to 2.674 eV when temperature increases further to 295 K [Figure 7.35(b)]. This behavior could be explained by transfer of carriers between shallow and deep localization states as temperature rises.[231] As temperature rises from 15 K, carriers gain thermal energy to move out from shallow localized states and transfer to deeper ones. As the deepest localized states are occupied, further increase in temperature results in delocalization from those states and transfer to some shallower ones, at a rate higher than that of the bandgap shrinkage, and that is

260

why the slight blueshift occurs. As the carriers are redistributed across localized states of different depth, rate of bandgap shrinkage takes over and the redshift is observed again.
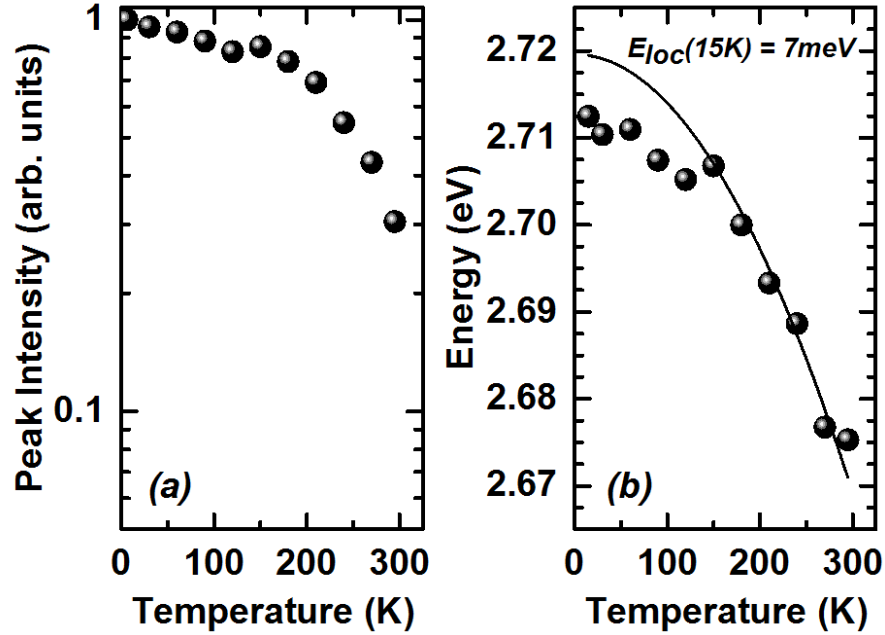
Figure 7.35. Temperature dependent peak PL intensity (a) and emission energy (b) for semipolar $(11\bar{2}2)$ 6×3nm InGaN MQWs. The experimental data points above 150 K in (b) are fitted (solid line) using Varshni's[232] empirical formula.[230]

The temperature dependence of energy bandgap for semiconductors can be described by Varshni's empirical formula[232]

$$E_{Varshni}(T) = E_0 - \frac{\alpha T^2}{T + \beta},$$
(7.7)

where α and β are the fitting parameters characteristic to a material. The localization energy is then defined as

261

$$E_{loc} = E_{\exp}(15K) - E_{Varshni}(15K), \tag{7.8}$$

where $E_{\exp}(15K)$ is the experimental bandgap at 15 K, $E_{Varshni}(15K)$ denotes the energy (at 15 K) deduced from the fit to high temperature data points using Varshni's empirical formula, and E_{loc} represents the localization energy (at 15 K). The deviation of the experimental data shown in Figure 7.35(b) from Varshni fit to data points above 150 K (defined as localization energy), is notable below 150 K. This deviation from the fitting curve can be attributed to exciton localization with localization energy estimated to be $E_{loc} = 7meV$ at 15 K. The value of localization energy is close to that reported for GaN QW (5 meV) on $(11\overline{2}2)$ [231] and smaller than 12 meV reported on $(1\overline{1}01)$ [148] and 20-60 meV in a recent report on c-plane InGaN QWs[233].

7.6.4.3. Exciton localization from temperature dependent time-resolved PL

To shed more light on the localization phenomena in InGaN LEDs of the $(11\overline{2}2)$ semipolar orientation, we performed temperature dependent TRPL. Figure 7.36 displays time transients of the PL integrated over the active region emission for temperatures from 15 to 295 K. The reduction in PL decay time with increasing temperature (as evident from the plots in Figure 7.36) can be attributed to the increase in nonradiative recombination rate.
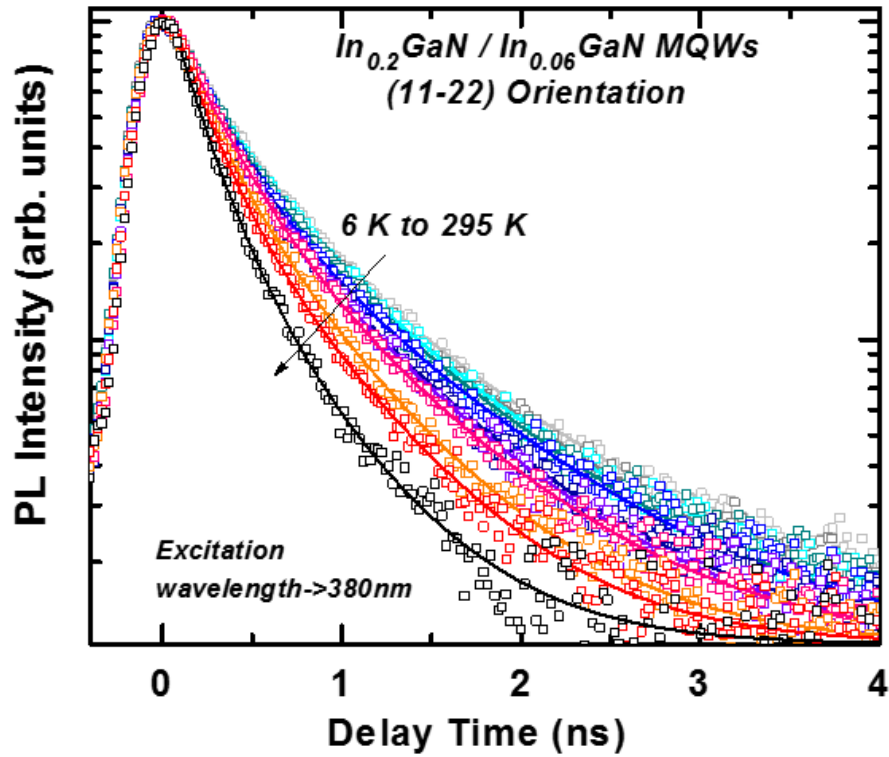
Figure 7.36. Time evolution of PL intensity integrated over the active region emission for temperatures from 15 to 295 K for the semipolar $(11\overline{2}2)$ 6×3nm InGaN MQWs. The inset displays each plot separately.[230]

Under the assumption of 100% internal quantum efficiency at 15 K and the equations [234]

$$\frac{1}{\tau_{PL}} = \frac{1}{\tau_r} + \frac{1}{\tau_{nr}} \,, \tag{7.9}$$

$$IQE = \frac{I(T)}{I(15K)} = \frac{1}{1 + \dfrac{\tau_r}{\tau_{nr}}} \,. \tag{7.10}$$

where τ_{PL}, τ_r, and τ_{nr} are PL, radiative, and nonradiative decay times, and $I(T)$ is the PL intensity at temperature T, the radiative (τ_r) and the nonradiative lifetimes (τ_{nr}) for the active region emission are calculated from the measured PL decay times (τ_{PL}) and plotted as a function of temperature in Figure 7.37. As seen from the figure, the radiative recombination is dominant at low temperature and radiative recombination lifetime remains close to 1 ns below 200 K and increases at higher temperatures with the slope of 5.8 $ps.K^{-1}$. This finding suggests that the carriers start to delocalize and contribute more into nonradiative recombination at temperatures above 200 K. In addition to the carrier delocalization, the increase in radiative decay time with increasing temperature could also originate from reduction in transition oscillator strength as a result of reduction in Coulombic interaction.
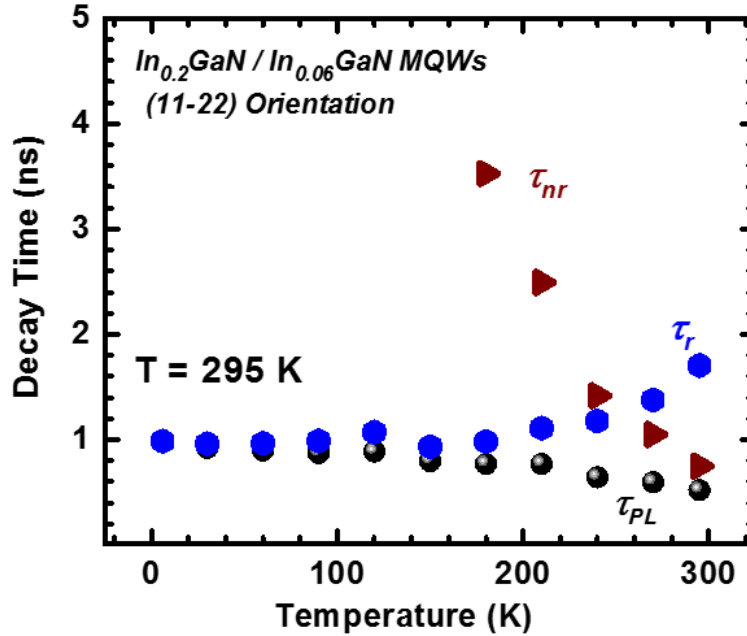
Figure 7.37. PL lifetime (τ_{PL}), and corresponding calculated radiative (τ_r) and nonradiative lifetimes (τ_{nr}) as a function of temperature from 15 to 295 K for the semipolar $(11\bar{2}2)$ 6×3nm InGaN MQWs.[230]

The results indicate the coexistence of free and localized excitons, in particular, for temperatures below 200 K. This supports our hypothesis that excitons are localized for temperatures below 200 K which is based on temperature dependent PL intensity and peak energy positions. In comparison to the previously reported *c*-plane polar structures with identical design[234] of the active regions, the delocalization temperature (T_{deloc}) for this semipolar orientation is significantly higher (200 K versus 100 K for *c*-plane).

The existence of carrier localization in semipolar $(11\bar{2}2)$ -oriented LED structure could be partially explained by presence of high density of extended defects including basal-plane stacking faults (BSFs)[200] in which case would not be desirable. Moreover, In contrast to

265

binary GaN QWs discussed in our previous studies[122], [148], where the density of localization centers was directly correlated to density of interfacial defects, the degree of carrier localization in ternary InGaN QWs can also be attributed to potential fluctuations associated with inhomogeneity in indium distribution in addition to interfacial defects and presence of BSFs.

7.6.5. Summary and Conclusions

In summary, polarized emission with degree of polarization of 33% (QW), 44% (EI), and 15% (YE) has been observed for the semipolar $(11\bar{2}2)$ -oriented 6×3nm In$_{0.20}$Ga$_{0.80}$N multi-quantum well (MQW) structure grown on GaN/m-sapphire.

Also, excitonic recombination in this semipolar $(11\bar{2}2)$ ternary QW structure was studied by means of temperature dependent steady-state and time resolved PL. The temperature dependent PL reveals exciton localization at low temperatures with localization energy of $E_{loc}(15K) = 7\ meV$. The value of localization energy is close to that reported on binary GaN QW (5 meV) with the same orientation[231] and smaller than our previous report of GaN MQWs on $(1\bar{1}01)$ (12 meV) [148] and lower than an earlier report of *c*-plane InGaN systems[233].

The temperature dependent radiative lifetime also indicates exciton localization with delocalization temperature $T_{deloc} = 200K$. The comparison of delocalization temperatures for the $(11\bar{2}2)$ InGaN MQWs with *c*-plane LED structures with the identical active-region design[234] reveals a significantly higher delocalization temperature (200K versus 100K) for the semipolar

266

counterpart. Correlation of exciton delocalization temperatures extracted from the temperature dependence of radiative and non-radiative decay times with the temperature dependences of PL intensity and energy position of the PL maximum consistently support the presence of exciton localization in the semipolar structures. Both interfacial defect-induced potential fluctuations and inhomogeneity in indium distribution in InGaN ternary alloy are likely responsible for the presence of localization centers in semipolar $(11\bar{2}2)$ InGaN MQWs. Exploration of the temperature dependence of localization energy and correlating it with those for excitonic transitions on certain defect states can provide a deeper insight into the genesis of the exciton localization in these semipolar structures.

Chapter 8

8. Summary and Conclusions

The conventional light emitting diodes have limited efficiencies at high injection current (known as 'Efficiency Droop') and long wavelengths (known as 'The Green Gap'). The latter is caused by polarization induced QCSE and limited indium incorporation while the origin of the former efficiency retention is not completely understood yet.

In order to shed some light on the carrier spillover as one of the main mechanisms that could be responsible for the efficiency droop, the photocurrent method for estimation of carrier leakage was studied. In addition, the improvement of carrier injection symmetry as another potential cause for efficiency retention at low and high injection for LEDs having MQW structures was paid attention. It was shown that utilizing delta doping of Mg (as *p*-type acceptor) to dope the barriers closer to the *n*-side could significantly improve the hole injection symmetry and quantum efficiency.

A novel design to alleviate the compressive strain in the InGaN MQWs which is responsible for both reductions of radiative recombination as well as indium incorporation efficiency was explored. With this aim, AlN/GaN periodic multilayers were designed as substrates for the InGaN QWs to introduce strain relaxations and thus improvement in indium incorporation. The data indicated a substantial enhancement in indium incorporation using this

268

technique. This approach allowed us to obtain efficient emission in variety of colors from purple to green.

The major focus of my work was on finding solution to the 'green gap' problem with the aim of finding suitable substrate orientation which could be potential candidate for future lighting technologies. First, the orientation dependent optical and structural properties based on theoretical and experimental studies available in literature were studied. Based on this foundation, we have explored the the effect of substrate orientation on stress and polarization, carrier transport, light emission, and indium incorporation. Then, we started our quest for finding suitable substrates for future lighting applications.

To evaluate the current status of the technology, I compared the reported peak EQE values for LEDs grown on polar, semipolar, and nonpolar planes reported in literature. The reported data indicates that EQE values of some orientations are approaching that of the *c*-plane which is promising. However, all the reported high EQE values are demonstrated for semipolar and nonpolar LED structures grown on free-standing GaN substrates which are expensive. On the other hand, the heteroepitaxial nonpolar and semipolar GaN films on inexpensive sapphire and Si substrates contain high densities of defects. My goal was to develop a cost-effective method of preparing high performance LEDs on inexpensive foreign substrates (GaN-on-Si, and GaN-on-sapphire technologies), although we will discuss some homoepitaxial structures (*m*-plane) too.

First, my research was concentrated on employing nonpolar planes that feature eliminated polarization field. Both homoepitaxy and heteroepitaxy of nonpolar *m*-plane GaN substrates was investigated. For heteroepitaxial nonpolar *m*-plane GaN on patterned Si (112), the improvement

269

of optical and structural quality using a two-step growth approach was achieved. For study of the homoepitaxial nonpolar structures, m-plane GaN MQWs on freestanding m-plane GaN substrates provided by Kyma Technology was investigated and optical anisotropy and excitonic recombination dynamics was demonstrated for this orientation. However, the observation of substantial reduction of indium incorporation for nonpolar m-plane InGaN structures turned our attention toward the semipolar LEDs.

Motivated by theoretical works predicting maximum indium incorporation efficiency at $\theta \sim 60°$ (θ being the tilt angle of the orientation with respect to c-plane), I explored the semipolar orientations with inclination angles close to 60º. Hence, I studied $\left(11\overline{2}2\right)$ and $\left(1\overline{1}01\right)$ semipolar orientations featured by $\theta = 58°$ and $\theta = 62°$, respectively, as promising candidates for green emitters. The $\left(11\overline{2}2\right)$-oriented GaN layers were grown on planar m-plane sapphire, while the semipolar $\left(1\overline{1}01\right)$ GaN were grown on patterned Si (001).

The semipolar $\left(10\overline{1}1\right)$ GaN MQWs on patterned Si (001) demonstrated strongly polarized (having degree of polarization close to 58%) with low nonradiative components. structure shows promising results in optical anisotropy and excitonic recombination dynamics. However, the efficiency of indium incorporation in the InGaN MQWs grown on semipolar $\left(10\overline{1}1\right)$-oriented GaN/patterned Si was found to be lower than that of the c-plane layer having the same structural design grown side by side in the same growth run. Moreover, the fabrication procedures on such structures would be challenging. Thus, the attention was turned toward planar semipolar $\left(11\overline{2}2\right)$ GaN which could be obtained on m-sapphire.

270

For semipolar $(11\bar{2}2)$ orientation, first, the efforts were concentrated on improving the structural quality of the semipolar GaN/*m*-sapphire. Thus we utilized *in-situ* epitaxial lateral overgrowth approach (ELO) using porous SiN_x interlayer which is also known as 'nano-ELO'. The data indicates the improvement of photoluminescence intensity by a factor of 5, and carrier lifetime by 35 to 85% by employing the *in-situ* ELO technique. Although the SiN_x interlayer could effectively block the extended defects, the efficiency of blocking the Stacking Faults was not optimum. As a result, there are still high densities of Stacking Faults in the overgrown layers.

In order to understand the optical activities and recombination of carriers in the basal-plane stacking faults, we studied carrier recombination dynamics of excitons bound to these structural defects. Different types of BSFs both intrinsic (I_1 and I_2) and extrinsic (E) was studied and the first conclusion was that the carriers are highly localized in BSFs (of any kind) even at room temperature. This allowed us to study band alignment in the QWs associated with the BSFs. Here we should mention tha SFs can be considered as QWs formed by inclusions of cubic material in the wurtzite matrix. The TRDT results pointed to type II band alignment for BSFs which is consistent with several experimental reports based on other optical techniques.

The InGaN MQW structures were then grown on the semipolar $(11\bar{2}2)$ GaN templates and side by side in the same run on *c*-plane templates. The results of PL comparison for three sets of LED structures with different active region designs indicated higher indium incorporation efficiency for the semipolar counterpart. This finding, which is extremely important as it can provide evidences for a solution to the green gap issue, was supported by uniform distribution of indium in the growth plane confirmed by spatio-CL and NSOM scans performed on the layers.

271

Exciton localization, recombination dynamics, and optical anisotropy in the semipolar $(11\bar{2}2)$ InGaN MQW structures were studied by temperature dependent steady-state, time-resolved, and polarization-resolved PL meaurements. The investigations revealed the presence of exciton localization having a relatively small localization energy compared to binary GaN MQWs system grown on $(10\bar{1}1)$ GaN/patterned Si. Such low carrier localization is an indirect proof of the uniform distributions of indium in the growth plane for the semipolar $(11\bar{2}2)$ structures.

In summary, the semipolar $(11\bar{2}2)$ GaN grown on planar *m*-sapphire with reduced defect density using the nano-ELO technique holds great promises for future generation of green LEDs having substantially reduced polarization and improved indium incorporation efficiency. The future works to realize this goal and to better understand this orientation will be discussed in next chapter.

Chapter 9

9. Future Research

9.1. Overview

The research presented in this dissertation can be extended to more detailed studies of various aspects including orientation dependence electronic and optoelectronic properties (such as carrier diffusion length, impurity incorporations, *etc.*), evaluation of quantum efficiency of devices, and improvement of the crystal quality and surface morphology to obtain level of conventional *c*-plane structures. It is intended to briefly discuss some of these potential studies as future research throughout this chapter.

9.2. Semipolar $(1\bar{1}01)$ structures on patterned Si

One potential study that will be performed as future research is the semipolar $(1\bar{1}01)$ GaN single quantum well (SQW) structures on patterned Si (001). The structures were designed for the purpose of determination of internal electric field. The idea is to have three layers with three different SQW structure having various well widths. Then, the QW transition energy or radiative decay time as a function of well width can be obtained. This will provide information about the internal electric field in the direction perpendicular to QW plane based on QCSE as have been illustrated for c-plane earlier[52].

Figure 9.1 schematically shows the $(1\bar{1}01)$ SQW structures which have been designed for this investigations. As can be seen in this schematics, the top barrier is designed to be AlGaN while for the bottom the AlN/GaN superlattice having around 43% average composition was used. The reason for using superlattice instead of AlGaN for barrier was to improve crystal quality of the GaN QW layer.
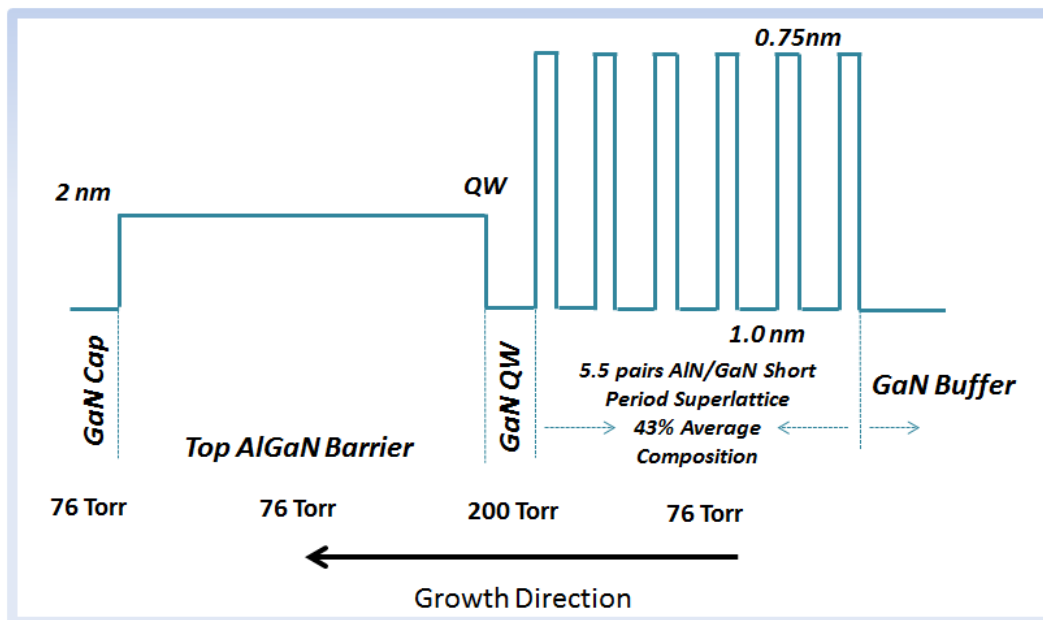
Based on such schematics, we performed SILVACO simulations considering 100% and 20% polarizations in the hetero-interfaces for polar c-plane and semipolar $(1\bar{1}01)$ structures. The simulation results are brought in Figure 9.2. The top 1 monolayer (ML)-thick AlN transition layer is inserted for the sake of avoiding the GaN layer to be etched by H_2 during the transition from GaN QW to AlGaN top barrier layer.
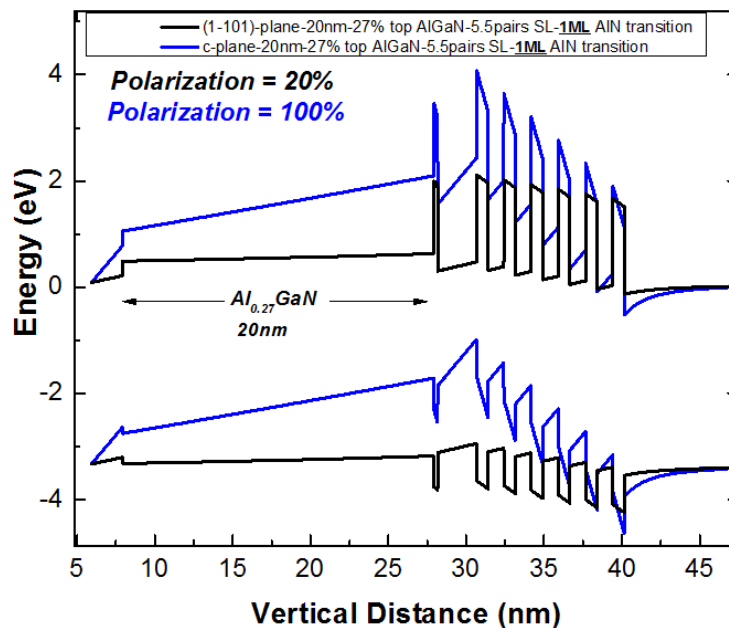
Figure 9.2. Band structure Simulations of the semipolar $(1\bar{1}01)$ and polar c-plane GaN SQW on patterned Si. 20% and 100 % polarizations were assumed for the semipolar and polar structures, respectively.

Three semipolar layers were grown with different GaN well widths; 5 MLs (Sample A); 8 MLs (Sample B); and 11 MLs (Sample C). The details of the patterning process and growth

conditions can be found in section 6.2. The SEM Images of the layers (See Figure 9.3) shows smooth surface morphologies for the stripes in all three semipolar layers.
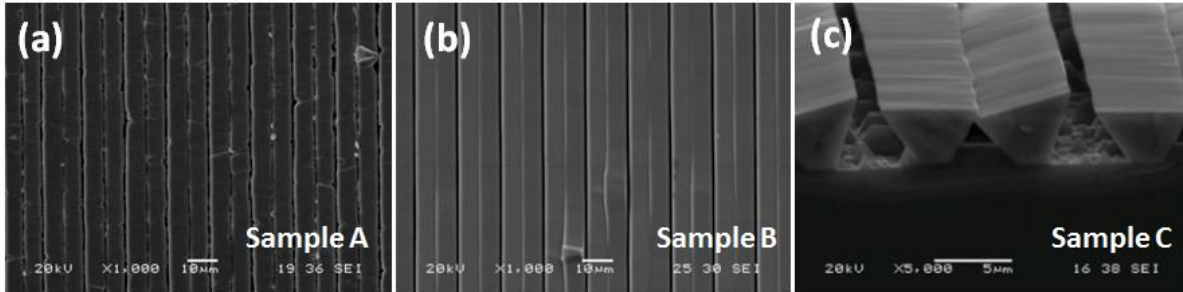
Figure 9.3. Planar and inclined-view SEM images of the stripe-shape semipolar $(1\bar{1}01)$ GaN SQW having well width of (a) 5MLs, (b) 8MLs, and (c) 11MLs.

The preliminary micro-PL investigations using He-Cd (325nm) excitation demonstrates carrier confinement and recombination in GaN SQW resulting in efficient emission at room temperature (see Figure 9.4). The PL peak positions for the QW emissions are consistent with theoretical calculations. In addition, it is observed that the PL intensity increases as the quantum well width reduces. This can be due to both strain relaxations and/or enhanced spatial separation of electrons and holes wavefunctions (QCSE) for the thicker wells both contributing to reduction in radiative recombination efficiency in the SQW. The GaN NBE is shifted to longer wavelengths for sample B. This can be due to the strain affecting the PL. Higher BSF-related emission line (at 370nm) for sample B compared to other two samples could mean that the measurement is performed closer to the *c-* wing for sample B.

276
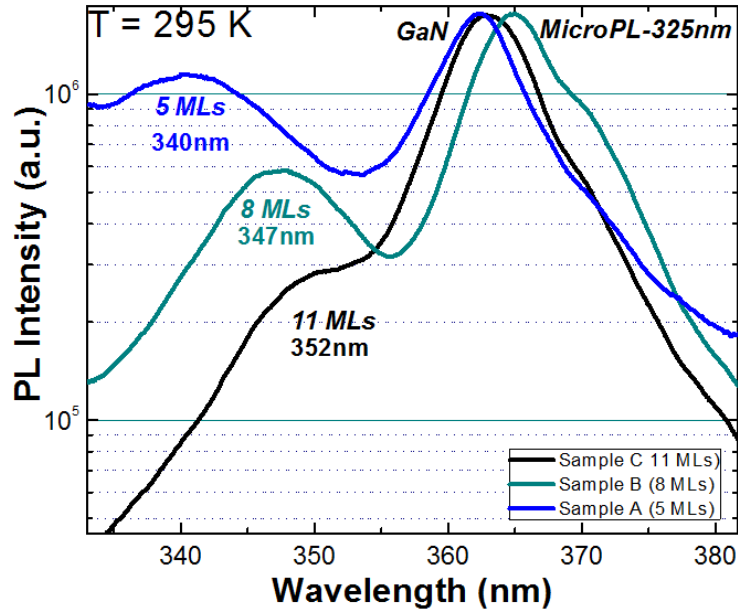
Figure 9.4. Room temperature micro-PL spectra of semipolar $(1\bar{1}01)$ GaN SQW on patterned Si with 5, 8, and 11MLs well widths.

The investigations of well width dependence of emission energy and radiative recombination lifetime using temperature dependent steady state and time-resolved PL will be performed in future to determine the internal electric field along the structure. Moreover, using the sets of layers grown here, the insight into the effect of strain in the GaN SQW on degree of optical polarization of QW emission can be gained.

9.3. Semipolar $(11\bar{2}2)$ structures on planar *m*-sapphire

277

9.3.1. Quantum efficiency evaluations of semipolar $(11\bar{2}2)$ InGaN MQW LEDs

In order to evaluate the external quantum efficiency of the semipolar $(11\bar{2}2)$ InGaN LED with the structure design demonstrated in section 7.6 we proceeded to fabrication process. First, the etching condition was tested on separate c-plane and semipolar $(11\bar{2}2)$ GaN templates and no significant changes in surface roughness after etching in either orientation was observed. Also the etching rate was found to be higher by around 40% for semipolar layer compared to polar counterpart siting side by side on the same holder in the ICP chamber.

However, after etching of the polar and semipolar $(11\bar{2}2)$ LEDs, the surface roughness was significantly increased for the semipolar layer while there was no notable surface roughness change was observed for c-plane LED. This could be explained by variations in etching rates of the different exposed facets for the semipolar LED layer.

Therefore, in order to overcome this problem, we need to optimize nano-ELO growth conditions for improving the surface morphology keeping optical quality in the same level. Other way would be to try alternative defect reduction methods such as insertion of AlN interlayers to improve surface morphology of the final layers.[235] Also, using thermal annealing to improve surface morphology is something that could be studied in future.

For fabricated devices, EQE versus current density of the semipolar layer compared to polar counterparts could provide interesting information about the efficiency droop, peak EQE value, and current density correspond to peak EQE. Moreover, the photocurrent measurement discussed in section 4.2 for estimation of carrier spillover can be perfomed on the polar and

278

semipolar LEDs to estimate carrier leakage as well as carrier transport properties for these two orientations.

9.3.2. Further Improving crystal quality using dual nano-ELO structures

With the aim of further improve the optical properties and at the same time surface morphology of the $(11\overline{2}2)$ GaN layers, we propose the structures with two SiN_x interlayers (referred to as dual nano-ELO). The layer schematics of such structures is demonstrated in Figure 9.5.
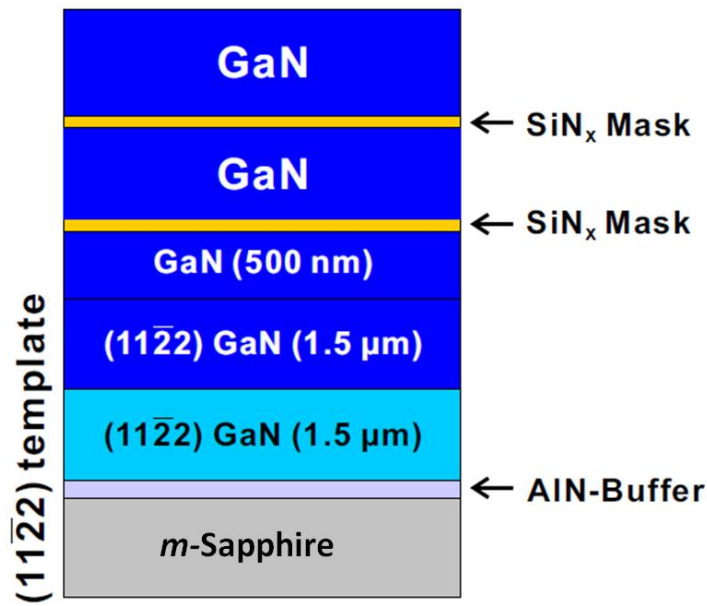
Figure 9.5. Schematics of the semipolar $(11\overline{2}2)$ GaN template on m-sapphire using dual nano-ELO for defect reduction.

Our preliminary investigation is presented here and further studies for better understanding and optimizations will be performed in future. Figure 9.6 shows the evolution of the surface morphology during growth of $(11\overline{2}2)$ GaN layer with two 1-min SiN_x interlayers on

279

m-sapphire substrate. One can see that at the end of the growth, the surface morphology was completely restored (Figure 9.6(c)). The layer grown with two 2-min SiN$_x$ interlayers was however not fully coalesced and had a rougher surface.
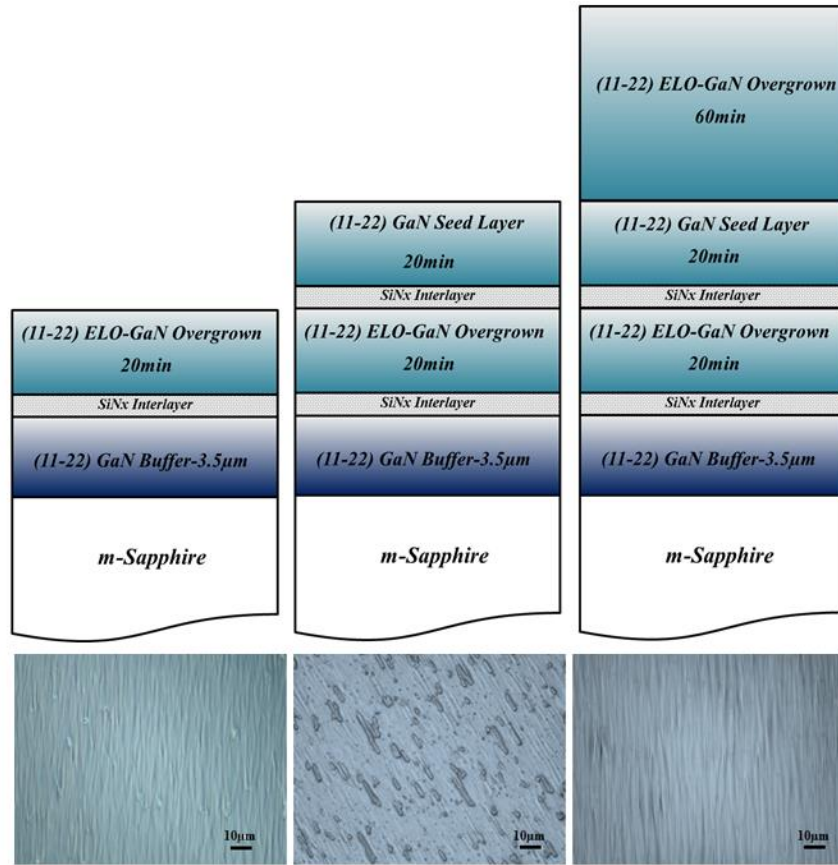
Figure 9.6. Growth schematics (top figures) and optical microscope images of $\left(11\bar{2}2\right)$ GaN layer surface after growth of first 1-min SiN$_x$ interlayer and 20 min GaN overgrowth (left), second 1-min SiN$_x$ interlayer and 20 min GaN seed layer (middle), and additional ELO-GaN overgrowth for another 60 min (right).

Figure 9.7 shows PL spectra measured from the two dual nano-ELO samples in comparison with the ($11\bar{2}2$) GaN reference layer without SiN$_x$ interlayers and the *c*-plane nano-

ELO reference layer. From low-temperature PL data (Figure 9.7 (a)) we can see that the use of dual nano-mesh leads to the increase of the donor-bound exciton (D^0X) emission and decrease of the stacking fault-related emission bands, and this improvement is more pronounced for the 2-min SiN_x interlayers. However, room-temperature PL from these samples shows little improvement (Figure 9.7 (b)). The sample with two 2-min SiN_x interlayers shows higher intensity, but it is more than 7 times lower than that of the polar nano-ELO layer. Moreover, as was mentioned above, the surface of this sample is not fully coalesced. Thus, the dual nano-ELO approach did not provide improvement as compared to single SiN_x interlayers. This finding can be attributed to the possible generation of new stacking faults and dislocations at the SiN_x/GaN interface and, depending on number of blocked and generated extended defects, the method may or may not lead to improvement of optical and structural quality of the material.
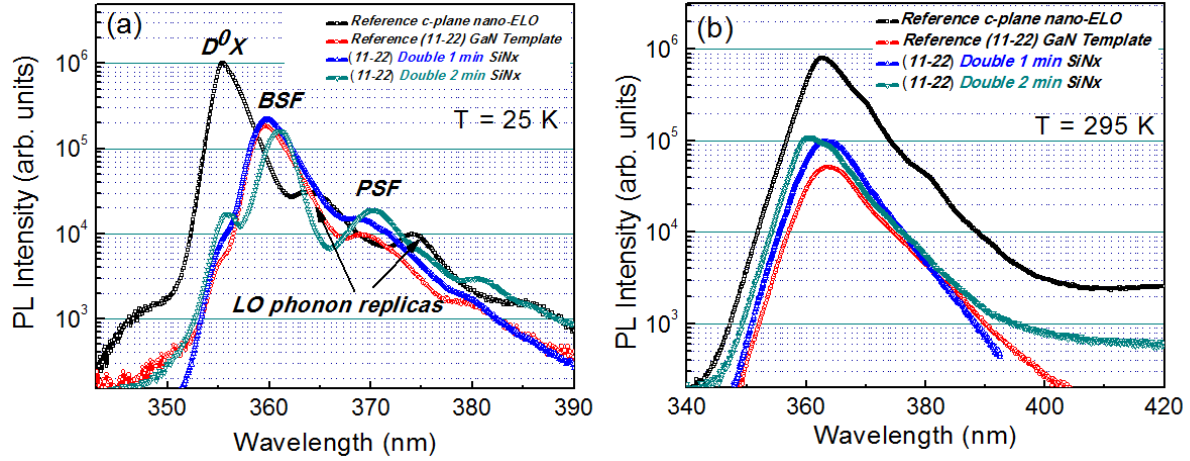
Figure 9.7. (a) Low-temperature and (b) room-temperature PL spectra for *in situ* dual nano-ELO $\left(11\bar{2}2\right)$ GaN samples with SiN_x interlayers deposited for 1 min (blue) and 2 min (green) in comparison with spectra for $\left(11\bar{2}2\right)$ GaN/*m*-sapphire template without SiN_x interlayer (red) and state-of-the-art *c*-plane nano-ELO GaN film (black).

Further studies involving growth optimizations and more extensive studies of the semipolar dual nano-ELO structures by means of cross sectional STEM in combination with spectrally and spatially resolved CL will be performed in future.

282

9.3.3. Other studies proposed

There are other investigations that will be performed in future on binary GaN and ternary InGaN QWs on semipolar $(11\bar{2}2)$ and $(1\bar{1}01)$ layers for the aim of more understanding these orientations and their optical, electronic, physical, and chemical properties and optimizing growth and device fabrication which are listed below.

1) Investigations of Mg incorporation (as *p*-type dopant) for semipolar $(11\bar{2}2)$ orientation including optimization of growth and activation condition to enhance the hole concentrations; Correlation of hole concentration from Hall Measurement and ABE emission in LTPL.

2) For semipolar $(11\bar{2}2)$ LED structures having smoth surface morphologies, the minority carrier diffusion length can be estimated using PL and CL techniques in the way similar to what we performed for conventional *c*-plane structures reported earlier [236], [237].

3) Further studies of optical properties by temperature dependent, excitation dependent steady-state, time-resolved, and polarization-resolved PL; theoretical and experimental study of degree of optical polarization in semipolar $(11\bar{2}2)$ and $(1\bar{1}01)$ compared to other orientations investigated; correlation of DX/BSF emission intensity ratio in LTPL and BSF density from (S)TEM (3 to 4 data points are required for a comprehensive analysis).

References

[1]   B. Gil, *III-Nitride Semiconductors and Their Modern Devices*. OUP Oxford, 2013.

[2]   S. Nakamura, M. Senoh, and T. Mukai, "High-power InGaN/GaN double-heterostructure violet light emitting diodes," *Appl. Phys. Lett.*, vol. 62, no. 19, pp. 2390–2392, May 1993.

[3]   S. Nakamura, T. Mukai, and M. Senoh, "Candela-class high-brightness InGaN/AlGaN double-heterostructure blue-light-emitting diodes," *Appl. Phys. Lett.*, vol. 64, no. 13, pp. 1687–1689, Mar. 1994.

[4]   S. Nakamura, T. Mukai, and M. Senoh, "High-brightness InGaN/AlGaN double-heterostructure blue-green-light-emitting diodes," *J. Appl. Phys.*, vol. 76, no. 12, pp. 8189–8191, Dec. 1994.

[5]   I. Akasaki and H. Amano, "Crystal Growth and Conductivity Control of Group III Nitride Semiconductors and Their Application to Short Wavelength Light Emitters," *Jpn. J. Appl. Phys.*, vol. 36, no. 9R, p. 5393, Sep. 1997.

[6]   V. Avrutin, S. A. Hafiz, F. Zhang, and Ü. Özgür, "Saga of efficiency degradation at high injection in InGaN light emitting diodes," *Turk. J. Phys.*, vol. 38, no. 3, pp. 269–313, 2014.

[7]   H. Morkoç, *Nitride Semiconductor Devices, Fundamentals and Applications*, 1 vols. Wiley-VCH, 2013.

[8]   *LED Inside Website*. [Online]. Available: http://www.ledinside.com.

[9]   R. Chu, "Asian Manufacturers Spur Low Priced Lighting Era." [Online]. Available: http://energy.gov/sites/prod/files/2015/02/f19/chu_global-trends_sanfrancisco2015.pdf.

[10]   V. Avrutin, S. din A. Hafiz, F. Zhang, Ü. Özgür, H. Morkoç, and A. Matulionis, "InGaN light-emitting diodes: Efficiency-limiting processes at high injection," *J. Vac. Sci. Technol. A*, vol. 31, no. 5, p. 50809, Sep. 2013.

[11]   "Osram achieves record figures with green LEDs | OSRAM Opto Semiconductors." [Online]. Available: http://www.osram-os.com/osram_os/en/press/press-releases/led-for-automotive,-consumer,-industry/2014/osram-achieves-record-figures-with-green-leds/index.jsp. [Accessed: 12-Apr-2016].

[12] V. Fiorentini, F. Bernardini, F. Della Sala, A. Di Carlo, and P. Lugli, "Effects of macroscopic polarization in III-V nitride multiple quantum wells," *Phys. Rev. B*, vol. 60, no. 12, pp. 8849–8858, Sep. 1999.

[13] Y. Kawaguchi, C.-Y. Huang, Y.-R. Wu, Q. Yan, C.-C. Pan, Y. Zhao, S. Tanaka, K. Fujito, D. Feezell, C. G. V. de Walle, S. P. DenBaars, and S. Nakamura, "Influence of polarity on carrier transport in semipolar (2021⁻) and (202⁻1) multiple-quantum-well light-emitting diodes," *Appl. Phys. Lett.*, vol. 100, no. 23, p. 231110, Jun. 2012.

[14] S. Pleasants, "LEDs: Overcoming the 'green gap,'" *Nat. Photonics*, vol. 7, no. 8, pp. 585–585, Aug. 2013.

[15] F. Scholz, "Semipolar GaN grown on foreign substrates: a review," *Semicond. Sci. Technol.*, vol. 27, no. 2, p. 24002, 2012.

[16] A. Chakraborty, B. A. Haskell, S. Keller, J. S. Speck, S. P. Denbaars, S. Nakamura, and U. K. Mishra, "Demonstration of Nonpolar m-Plane InGaN/GaN Light-Emitting Diodes on Free-Standing m-Plane GaN Substrates," *Jpn. J. Appl. Phys.*, vol. 44, no. 1L, p. L173, Jan. 2005.

[17] N. F. Gardner, J. C. Kim, J. J. Wierer, Y. C. Shen, and M. R. Krames, "Polarization anisotropy in the electroluminescence of m-plane InGaN–GaN multiple-quantum-well light-emitting diodes," *Appl. Phys. Lett.*, vol. 86, no. 11, p. 111101, Mar. 2005.

[18] H. Yamada, K. Iso, M. Saito, H. Masui, K. Fujito, S. P. DenBaars, and S. Nakamura, "Compositional Dependence of Nonpolar m-Plane InxGa1-xN/GaN Light Emitting Diodes," *Appl. Phys. Express*, vol. 1, no. 4, p. 41101, Mar. 2008.

[19] S. Nakamura and M. R. Krames, "History of Gallium-Nitride-Based Light-Emitting Diodes for Illumination," *Proc. IEEE*, vol. 101, no. 10, pp. 2211–2220, Oct. 2013.

[20] M. V. Durnev, A. V. Omelchenko, E. V. Yakovlev, I. Y. Evstratov, and S. Y. Karpov, "Indium incorporation and optical transitions in InGaN bulk materials and quantum wells with arbitrary polarity," *Appl. Phys. Lett.*, vol. 97, no. 5, p. 51904, Aug. 2010.

[21] J. E. Northrup, "GaN and InGaN(112$\underline{2}$) surfaces: Group-III adlayers and indium incorporation," *Appl. Phys. Lett.*, vol. 95, no. 13, p. 133107, Sep. 2009.

[22] Y. Zhao, Q. Yan, C.-Y. Huang, S.-C. Huang, P. S. Hsu, S. Tanaka, C.-C. Pan, Y. Kawaguchi, K. Fujito, C. G. V. de Walle, J. S. Speck, S. P. DenBaars, S. Nakamura, and

D. Feezell, "Indium incorporation and emission properties of nonpolar and semipolar InGaN quantum wells," *Appl. Phys. Lett.*, vol. 100, no. 20, p. 201108, May 2012.

[23]   Y. Narukawa, M. Ichikawa, D. Sanga, M. Sano, and T. Mukai, "White light emitting diodes with super-high luminous efficacy," *J. Phys. Appl. Phys.*, vol. 43, no. 35, p. 354002, 2010.

[24]   T. Jeong, H.-J. Park, J.-W. Ju, H. S. Oh, J.-H. Baek, J.-S. Ha, G.-H. Ryu, and H.-Y. Ryu, "High Efficiency InGaN Blue Light-Emitting Diode With Output Power at 3 A," *IEEE Photonics Technol. Lett.*, vol. 26, no. 7, pp. 649–652, Apr. 2014.

[25]   L. Jun-Lin, Z. Jian-Li, W. Guang-Xu, M. Chun-Lan, X. Long-Quan, D. Jie, Q. Zhi-Jue, Wang Xiao-Lan, P. Shuan, Z. Chang-Da, W. Xiao-Ming, F. Wen-Qing, and J. Feng-Yi, "Status of GaN-based green light-emitting diodes," *Chin. Phys. B*, vol. 24, no. 6, p. 67804, 2015.

[26]   R. Hashimoto, J. Hwang, S. Saito, and S. Nunoue, "High-efficiency green-yellow light-emitting diodes grown on sapphire (0001) substrates," *Phys. Status Solidi C*, vol. 10, no. 11, pp. 1529–1532, Nov. 2013.

[27]   H. Sato, H. Hirasawa, H. Asamizu, N. Fellows, A. Tyagi, M. Saito, K. Fujito, J. S. Speck, S. P. Denbaars, and S. Nakamura, "High Power and High Efficiency Semipolar InGaN Light Emitting Diodes," *J. Light Vis. Environ.*, vol. 32, no. 2, pp. 107–110, 2008.

[28]   H. Sato, A. Tyagi, H. Zhong, N. Fellows, R. B. Chung, M. Saito, K. Fujito, J. S. Speck, S. P. DenBaars, and S. Nakamura, "High power and high efficiency green light emitting diode on free-standing semipolar (11$\bar 2$2) bulk GaN substrate," *Phys. Status Solidi RRL – Rapid Res. Lett.*, vol. 1, no. 4, pp. 162–164, Jul. 2007.

[29]   S. Yamamoto, Y. Zhao, C.-C. Pan, R. B. Chung, K. Fujito, J. Sonoda, S. P. DenBaars, and S. Nakamura, "High-Efficiency Single-Quantum-Well Green and Yellow-Green Light-Emitting Diodes on Semipolar (2021) GaN Substrates," *Appl. Phys. Express*, vol. 3, no. 12, p. 122102, Nov. 2010.

[30]   M. C. Schmidt, K.-C. Kim, H. Sato, N. Fellows, H. Masui, S. Nakamura, S. P. DenBaars, and J. S. Speck, "High Power and High External Efficiency m-Plane InGaN Light Emitting Diodes," *Jpn. J. Appl. Phys.*, vol. 46, no. 2L, p. L126, Feb. 2007.

[31]   I. L. Koslow, J. Sonoda, R. B. Chung, C.-C. Pan, S. Brinkley, H. Ohta, S. Nakamura, and S. P. DenBaars, "High Power and High Efficiency Blue InGaN Light Emitting Diodes on

Free-Standing Semipolar (3031) Bulk GaN Substrate," *Jpn. J. Appl. Phys.*, vol. 49, no. 8R, p. 80203, Aug. 2010.

[32] D. L. Becerra, Y. Zhao, S. H. Oh, C. D. Pynn, K. Fujito, S. P. DenBaars, and S. Nakamura, "High-power low-droop violet semipolar (303⁻1⁻) InGaN/GaN light-emitting diodes with thick active layer design," *Appl. Phys. Lett.*, vol. 105, no. 17, p. 171106, Oct. 2014.

[33] D. F. Feezell, J. S. Speck, S. P. DenBaars, and S. Nakamura, "Semipolar InGaN/GaN Light-Emitting Diodes for High-Efficiency Solid-State Lighting," *J. Disp. Technol.*, vol. 9, no. 4, pp. 190–198, Apr. 2013.

[34] Y. Zhao, S. Tanaka, C.-C. Pan, K. Fujito, D. Feezell, J. S. Speck, S. P. DenBaars, and S. Nakamura, "High-Power Blue-Violet Semipolar (2021) InGaN/GaN Light-Emitting Diodes with Low Efficiency Droop at 200 A/cm2," *Appl. Phys. Express*, vol. 4, no. 8, p. 82104, Jul. 2011.

[35] Y. Zhao, J. Sonoda, C.-C. Pan, S. Brinkley, I. Koslow, K. Fujito, H. Ohta, S. P. DenBaars, and S. Nakamura, "30-mW-Class High-Power and High-Efficiency Blue Semipolar (1011) InGaN/GaN Light-Emitting Diodes Obtained by Backside Roughening Technique," *Appl. Phys. Express*, vol. 3, no. 10, p. 102101, Sep. 2010.

[36] P. Ruterana, rtin Albrecht, and J. Neugebauer, Eds., "Front Matter," in *Nitride Semiconductors*, Wiley-VCH Verlag GmbH & Co. KGaA, 2003, pp. I–XXII.

[37] Y. R. Wu, C. Y. Huang, Y.- Zhao, and J. S. Speck, "Nonpolar and semipolar LEDs. In Nitride Semiconductor Light-Emitting Diodes (LEDs): Materials, Technologies and Applications.," presented at the Elsevier Ltd., 2013, pp. 250–275.

[38] A. E. Romanov, T. J. Baker, S. Nakamura, J. S. Speck, and E. U. Group, "Strain-induced polarization in wurtzite III-nitride semipolar layers," *J. Appl. Phys.*, vol. 100, no. 2, p. 23522, Jul. 2006.

[39] J. A. del Alamo and J. Joh, "GaN HEMT reliability," *Microelectron. Reliab.*, vol. 49, no. 9–11, pp. 1200–1206, Sep. 2009.

[40] U. M. E. Christmas, A. D. Andreev, and D. A. Faux, "Calculation of electric field and optical transitions in InGaN⁄GaN quantum wells," *J. Appl. Phys.*, vol. 98, no. 7, p. 73522, Oct. 2005.

287

[41] E. Pan and F. Tonon, "Three-dimensional Green's functions in anisotropic piezoelectric solids," *Int. J. Solids Struct.*, vol. 37, no. 6, pp. 943–958, Feb. 2000.

[42] E. Pan, "Elastic and piezoelectric fields around a quantum dot: Fully coupled or semicoupled model?," *J. Appl. Phys.*, vol. 91, no. 6, pp. 3785–3796, Mar. 2002.

[43] F. Bernardini and V. Fiorentini, "Spontaneous versus Piezoelectric Polarization in III–V Nitrides: Conceptual Aspects and Practical Consequences," *Phys. Status Solidi B*, vol. 216, no. 1, pp. 391–398, Nov. 1999.

[44] T. Takeuchi, H. Amano, and I. Akasaki, "Theoretical Study of Orientation Dependence of Piezoelectric Effects in Wurtzite Strained GaInN/GaN Heterostructures and Quantum Wells," *Jpn. J. Appl. Phys.*, vol. 39, no. 2R, p. 413, Feb. 2000.

[45] D. A. B. Miller, *Quantum Mechanics for Scientists and Engineers*. Cambridge University Press, 2008.

[46] S. Morawiec, R. P. Sarzała, and W. Nakwaski, "A method used to overcome polarization effects in semi-polar structures of nitride light-emitting diodes emitting green radiation," *Appl. Phys. A*, vol. 113, no. 3, pp. 801–809, Feb. 2013.

[47] Y. Enya, Y. Yoshizumi, T. Kyono, K. Akita, M. Ueno, M. Adachi, T. Sumitomo, S. Tokuyama, T. Ikegami, K. Katayama, and T. Nakamura, "531 nm Green Lasing of InGaN Based Laser Diodes on Semi-Polar {2021} Free-Standing GaN Substrates," *Appl. Phys. Express*, vol. 2, no. 8, p. 82101, Jul. 2009.

[48] M. Funato, M. Ueda, Y. Kawakami, Y. Narukawa, T. Kosugi, M. Takahashi, and T. Mukai, "Blue, Green, and Amber InGaN/GaN Light-Emitting Diodes on Semipolar {11-22} GaN Bulk Substrates," *Jpn. J. Appl. Phys.*, vol. 45, no. 7L, p. L659, Jun. 2006.

[49] A. Strittmatter, J. E. Northrup, N. M. Johnson, M. V. Kisin, P. Spiberg, H. El-Ghoroury, A. Usikov, and A. Syrkin, "Semi-polar nitride surfaces and heterostructures," *Phys. Status Solidi B*, vol. 248, no. 3, pp. 561–573, Mar. 2011.

[50] A. Strittmatter, M. Teepe, Z. Yang, C. Chua, J. Northrup, N. M. Johnson, P. Spiberg, R. G. W. Brown, V. Ivantsov, A. Syrkin, L. Shapovalov, and A. Usikov, "Optically-pumped lasing of semi-polar InGaN/GaN(1122) heterostructures," *Phys. Status Solidi C*, vol. 7, no. 7–8, pp. 1814–1816, Jul. 2010.

[51] R. Sharma, P. M. Pattison, H. Masui, R. M. Farrell, T. J. Baker, B. A. Haskell, F. Wu, S. P. DenBaars, J. S. Speck, and S. Nakamura, "Demonstration of a semipolar (10(1)over-

bar(3)over-bar) InGaN/GaN green light emitting diode," *Appl. Phys. Lett.*, vol. 87, no. 23, Dec. 2005.

[52] M. Leroux, N. Grandjean, J. Massies, B. Gil, P. Lefebvre, and P. Bigenwald, "Barrier-width dependence of group-III nitrides quantum-well transition energies," *Phys. Rev. B*, vol. 60, no. 3, pp. 1496–1499, Jul. 1999.

[53] S. Jung, S.-N. Lee, and H. Kim, "Surface states and carrier transport properties at semipolar (11–22) n-type GaN planes," *Appl. Phys. Lett.*, vol. 102, no. 15, p. 151603, Apr. 2013.

[54] S. Jang, H. Kim, D. S. Kim, S.-M. Hwang, J. Kim, and K. H. Baik, "Investigation of carrier transport properties in semipolar (112‾2) GaN films with low defect density," *Appl. Phys. Lett.*, vol. 103, no. 16, p. 162103, Oct. 2013.

[55] K. Fujii, Y. Iwaki, H. Masui, T. J. Baker, M. Iza, H. Sato, J. Kaeding, T. Yao, J. S. Speck, S. P. DenBaars, S. Nakamura, and K. Ohkawa, "Photoelectrochemical Properties of Nonpolar and Semipolar GaN," *Jpn. J. Appl. Phys.*, vol. 46, no. 10R, p. 6573, Oct. 2007.

[56] S. Jung, S.-N. Lee, K.-S. Ahn, and H. Kim, "Carrier Transport Mechanism of a Low Resistance Ti/Al Ohmic Contact on (112̄2) Semipolar n-Type GaN," *Jpn. J. Appl. Phys.*, vol. 51, no. 6R, p. 61001, May 2012.

[57] A. Konar, A. Verma, T. Fang, P. Zhao, R. Jana, and D. Jena, "Charge transport in non-polar and semi-polar III-V nitride heterostructures," *Semicond. Sci. Technol.*, vol. 27, no. 2, p. 24018, 2012.

[58] M. McLaurin, T. E. Mates, F. Wu, and J. S. Speck, "Growth of p-type and n-type m-plane GaN by molecular beam epitaxy," *J. Appl. Phys.*, vol. 100, no. 6, p. 63707, Sep. 2006.

[59] M. McLaurin and J. S. Speck, "p-type conduction in stacking-fault-free m-plane GaN," *Phys. Status Solidi RRL – Rapid Res. Lett.*, vol. 1, no. 3, pp. 110–112, May 2007.

[60] K. H. Baik, Y. G. Seo, S. K. Hong, S. Lee, J. Kim, J. S. Son, and S. M. Hwang, "Effects of Basal Stacking Faults on Electrical Anisotropy of Nonpolar a-Plane ( ) GaN Light-Emitting Diodes on Sapphire Substrate," *IEEE Photonics Technol. Lett.*, vol. 22, no. 9, pp. 595–597, May 2010.

[61] A. Konar, T. Fang, N. Sun, and D. Jena, "Charged basal stacking fault scattering in nitride semiconductors," *Appl. Phys. Lett.*, vol. 98, no. 2, p. 22109, Jan. 2011.

[62]   E. Wimmer, H. Krakauer, M. Weinert, and A. J. Freeman, "Full-potential self-consistent linearized-augmented-plane-wave method for calculating the electronic structure of molecules and surfaces: O2 molecule," *Phys. Rev. B*, vol. 24, no. 2, pp. 864–875, Jul. 1981.

[63]   O. Gunnarsson and B. I. Lundqvist, "Exchange and correlation in atoms, molecules, and solids by the spin-density-functional formalism," *Phys. Rev. B*, vol. 13, no. 10, pp. 4274–4298, May 1976.

[64]   M. Suzuki and T. Uenoyama, "Theoretical Study of Momentum Matrix Elements of GaN," *Jpn. J. Appl. Phys.*, vol. 35, no. 2R, p. 543, Feb. 1996.

[65]   H.-H. Huang and Y.-R. Wu, "Light emission polarization properties of semipolar InGaN/GaN quantum well," *J. Appl. Phys.*, vol. 107, no. 5, p. 53112, Mar. 2010.

[66]   I. L. Koslow, M. T. Hardy, P. S. Hsu, P.-Y. Dang, F. Wu, A. Romanov, Y.-R. Wu, E. C. Young, S. Nakamura, J. S. Speck, and S. P. DenBaars, "Performance and polarization effects in (112¯2) long wavelength light emitting diodes grown on stress relaxed InGaN buffer layers," *Appl. Phys. Lett.*, vol. 101, no. 12, p. 121106, Sep. 2012.

[67]   F. Wu, Y.-D. Lin, A. Chakraborty, H. Ohta, S. P. DenBaars, S. Nakamura, and J. S. Speck, "Stacking fault formation in the long wavelength InGaN/GaN multiple quantum wells grown on m-plane GaN," *Appl. Phys. Lett.*, vol. 96, no. 23, p. 231912, Jun. 2010.

[68]   S. Keller, N. A. Fichtenbaum, M. Furukawa, J. S. Speck, S. P. DenBaars, and U. K. Mishra, "Growth and characterization of N-polar InGaN⁄GaN multiquantum wells," *Appl. Phys. Lett.*, vol. 90, no. 19, p. 191908, May 2007.

[69]   T. Zywietz, J. Neugebauer, and M. Scheffler, "Adatom diffusion at GaN (0001) and (0001¯) surfaces," *Appl. Phys. Lett.*, vol. 73, no. 4, pp. 487–489, Jul. 1998.

[70]   W. Kohn and L. J. Sham, "Self-Consistent Equations Including Exchange and Correlation Effects," *Phys. Rev.*, vol. 140, no. 4A, pp. A1133–A1138, Nov. 1965.

[71]   R. Stumpf and M. Scheffler, "Simultaneous calculation of the equilibrium atomic structure and its electronic ground state using density-functional theory," *Comput. Phys. Commun.*, vol. 79, no. 3, pp. 447–465, May 1994.

[72]   N. Troullier and J. L. Martins, "Efficient pseudopotentials for plane-wave calculations," *Phys. Rev. B*, vol. 43, no. 3, pp. 1993–2006, Jan. 1991.

[73] J. E. Northrup, "Impact of hydrogen on indium incorporation at m-plane and c-plane In0.25Ga0.75N surfaces: First-principles calculations," *Phys. Rev. B*, vol. 79, no. 4, p. 41306, Jan. 2009.

[74] F. Bertram, T. Riemann, J. Christen, A. Kaschner, A. Hoffmann, C. Thomsen, K. Hiramatsu, T. Shibata, and N. Sawaki, "Strain relaxation and strong impurity incorporation in epitaxial laterally overgrown GaN: Direct imaging of different growth domains by cathodoluminescence microscopy and micro-Raman spectroscopy," *Appl. Phys. Lett.*, vol. 74, no. 3, pp. 359–361, Jan. 1999.

[75] A. Urban, M. Müller, C. Karbaum, G. Schmidt, P. Veit, J. Malindretos, F. Bertram, J. Christen, and A. Rizzi, "Optical Emission of Individual GaN Nanocolumns Analyzed with High Spatial Resolution," *Nano Lett.*, vol. 15, no. 8, pp. 5105–5109, Aug. 2015.

[76] X. Ni, X. Li, J. Lee, S. Liu, V. Avrutin, Ü. Özgür, H. Morkoç, A. Matulionis, T. Paskova, G. Mulholland, and K. R. Evans, "InGaN staircase electron injector for reduction of electron overflow in InGaN light emitting diodes," *Appl. Phys. Lett.*, vol. 97, no. 3, p. 31110, Jul. 2010.

[77] F. Zhang, X. Li, S. Hafiz, S. Okur, V. Avrutin, Ü. Özgür, H. Morkoç, and A. Matulionis, "The effect of stair case electron injector design on electron overflow in InGaN light emitting diodes," *Appl. Phys. Lett.*, vol. 103, no. 5, p. 51122, Jul. 2013.

[78] S.-H. Han, D.-Y. Lee, S.-J. Lee, C.-Y. Cho, M.-K. Kwon, S. P. Lee, D. Y. Noh, D.-J. Kim, Y. C. Kim, and S.-J. Park, "Effect of electron blocking layer on efficiency droop in InGaN/GaN multiple quantum well light-emitting diodes," *Appl. Phys. Lett.*, vol. 94, no. 23, p. 231123, Jun. 2009.

[79] X. Ni, X. Li, J. Lee, S. Liu, V. Avrutin, A. Matulionis, Ü. Özgür, and H. Morkoç, "Pivotal role of ballistic and quasi-ballistic electrons on LED efficiency," *Superlattices Microstruct.*, vol. 48, no. 2, pp. 133–153, Aug. 2010.

[80] X. Li, S. Okur, F. Zhang, S. A. Hafiz, V. Avrutin, Ü. Özgür, H. Morkoç, and K. Jarašiūnas, "Improved quantum efficiency in InGaN light emitting diodes with multi-double-heterostructure active regions," *Appl. Phys. Lett.*, vol. 101, no. 4, p. 41115, Jul. 2012.

[81] Y. C. Shen, G. O. Mueller, S. Watanabe, N. F. Gardner, A. Munkholm, and M. R. Krames, "Auger recombination in InGaN measured by photoluminescence," *Appl. Phys. Lett.*, vol. 91, no. 14, p. 141101, Oct. 2007.

[82] M.-H. Kim, M. F. Schubert, Q. Dai, J. K. Kim, E. F. Schubert, J. Piprek, and Y. Park, "Origin of efficiency droop in GaN-based light-emitting diodes," *Appl. Phys. Lett.*, vol. 91, no. 18, p. 183507, Oct. 2007.

[83] I. V. Rozhansky and D. A. Zakheim, "Analysis of processes limiting quantum efficiency of AlGaInN LEDs at high pumping," *Phys. Status Solidi A*, vol. 204, no. 1, pp. 227–230, Jan. 2007.

[84] J. Xie, X. Ni, Q. Fan, R. Shimada, Ü. Özgür, and H. Morkoç, "On the efficiency droop in InGaN multiple quantum well blue light emitting diodes and its reduction with p-doped quantum well barriers," *Appl. Phys. Lett.*, vol. 93, no. 12, p. 121107, Sep. 2008.

[85] J. Hader, J. V. Moloney, and S. W. Koch, "Density-activated defect recombination as a possible explanation for the efficiency droop in GaN-based diodes," *Appl. Phys. Lett.*, vol. 96, no. 22, p. 221106, May 2010.

[86] X. A. Cao, Y. Yang, and H. Guo, "On the origin of efficiency roll-off in InGaN-based light-emitting diodes," *J. Appl. Phys.*, vol. 104, no. 9, p. 93108, Nov. 2008.

[87] A. A. Efremov, N. I. Bochkareva, R. I. Gorbunov, D. A. Lavrinovich, Y. T. Rebane, D. V. Tarkhin, and Y. G. Shreter, "Effect of the joule heating on the quantum efficiency and choice of thermal conditions for high-power blue InGaN/GaN LEDs," *Semiconductors*, vol. 40, no. 5, pp. 605–610, May 2006.

[88] S. Hafiz, F. Zhang, M. Monavarian, S. Okur, V. Avrutin, H. Morkoç, and Ü. Özgür, "Estimation of carrier leakage in InGaN light emitting diodes from photocurrent measurements," in *Proc. SPIE*, 2014, vol. 9003, p. 90031R.

[89] Y. Y. Zhang, G. H. Fan, and T. Zhang, "Performance Enhancement of Blue Light-Emitting Diodes Without an Electron-Blocking Layer by Using p-Type Doped Barriers and a Hole-Blocking Layer of Low Al Mole Fraction," *IEEE J. Quantum Electron.*, vol. 48, no. 2, pp. 169–174, Feb. 2012.

[90] S.-H. Han, C.-Y. Cho, S.-J. Lee, T.-Y. Park, T.-H. Kim, S. H. Park, S. W. Kang, J. W. Kim, Y. C. Kim, and S.-J. Park, "Effect of Mg doping in the barrier of InGaN/GaN

292

multiple quantum well on optical power of light-emitting diodes," *Appl. Phys. Lett.*, vol. 96, no. 5, p. 51113, Feb. 2010.

[91] K. J. Vampola, M. Iza, S. Keller, S. P. DenBaars, and S. Nakamura, "Measurement of electron overflow in 450 nm InGaN light-emitting diode structures," *Appl. Phys. Lett.*, vol. 94, no. 6, p. 61116, Feb. 2009.

[92] H.-Y. Ryu and J.-M. Lee, "Effects of two-step Mg doping in p-GaN on efficiency characteristics of InGaN blue light-emitting diodes without AlGaN electron-blocking layers," *Appl. Phys. Lett.*, vol. 102, no. 18, p. 181115, May 2013.

[93] Y. K. Kuo, M. C. Tsai, S. H. Yen, T. C. Hsu, and Y. J. Shen, "Effect of P-Type Last Barrier on Efficiency Droop of Blue InGaN Light-Emitting Diodes," *IEEE J. Quantum Electron.*, vol. 46, no. 8, pp. 1214–1220, Aug. 2010.

[94] I. V. Rozhansky and D. A. Zakheim, "Analysis of the causes of the decrease in the electroluminescence efficiency of AlGaInN light-emitting-diode heterostructures at high pumping density," *Semiconductors*, vol. 40, no. 7, pp. 839–845, Jul. 2006.

[95] F. Zhang, N. Can, S. Hafiz, M. Monavarian, S. Das, V. Avrutin, Ü. Özgür, and H. Morkoç, "Improvement of carrier injection symmetry and quantum efficiency in InGaN light-emitting diodes with Mg delta-doped barriers," *Appl. Phys. Lett.*, vol. 106, no. 18, p. 181105, May 2015.

[96] Z. Yi, Z. Jin-Cheng, X. Jun-Shuai, Z. Xiao-Wei, X. Sheng-Rui, and H. Yue, "Influence of compressive strain on the incorporation of indium in InGaN and InAlN ternary alloys," *Chin. Phys. B*, vol. 24, no. 1, p. 17302, 2015.

[97] M. E. Aumer, S. F. LeBoeuf, S. M. Bedair, M. Smith, J. Y. Lin, and H. X. Jiang, "Effects of tensile and compressive strain on the luminescence properties of AlInGaN/InGaN quantum well structures," *Appl. Phys. Lett.*, vol. 77, no. 6, pp. 821–823, Aug. 2000.

[98] S. D. Hafiz, F. Zhang, M. Monavarian, V. Avrutin, H. Morkoç, and Ü. Özgür, "Enhancement of coherent acoustic phonons in InGaN multiple quantum wells," in *Proc. SPIE*, 2015, vol. 9363, p. 93632J.

[99] M. C. Johnson, E. D. Bourret-Courchesne, J. Wu, Z. Liliental-Weber, D. N. Zakharov, R. J. Jorgenson, T. B. Ng, D. E. McCready, and J. R. Williams, "Effect of gallium nitride template layer strain on the growth of InxGa1-xN∕GaN multiple quantum well light emitting diodes," *J. Appl. Phys.*, vol. 96, no. 3, pp. 1381–1386, Aug. 2004.

[100] M. Monavarian, S. Hafiz, S. Das, N. Izyumskaya, Ü. Özgür, H. Morkoç, and V. Avrutin, "Enhancement of indium incorporation to InGaN MQWs on AlN/GaN periodic multilayers," in *Proc. SPIE*, 2016, vol. 9748, p. 974825.

[101] J. Xie, Ü. Özgür, Y. Fu, X. Ni, H. Morkoç, C. K. Inoki, T. S. Kuan, J. V. Foreman, and H. O. Everitt, "Low dislocation densities and long carrier lifetimes in GaN thin films grown on a SiNx nanonetwork," *Appl. Phys. Lett.*, vol. 90, no. 4, p. 41107, Jan. 2007.

[102] M. Monavarian, S. Metzner, N. Izyumskaya, M. Müller, S. Okur, F. Zhang, N. Can, S. Das, V. Avrutin, Ü. Özgür, F. Bertram, J. Christen, and H. Morkoç, "Enhancement of optical and structural quality of semipolar (11-22) GaN by introducing nanoporous SiNx interlayers," in *Proc. SPIE*, 2015, vol. 9363, p. 93632I.

[103] D. J. Dunstan, "Strain and strain relaxation in semiconductors," *J. Mater. Sci. Mater. Electron.*, vol. 8, no. 6, pp. 337–375, Dec. 1997.

[104] H. Morkoç, *Nitride Semiconductors and Devices*, vol. 32. Berlin, Heidelberg: Springer Berlin Heidelberg, 1999.

[105] A. R. Denton and N. W. Ashcroft, "Vegard's law," *Phys. Rev. A*, vol. 43, no. 6, pp. 3161–3164, Mar. 1991.

[106] M. Monavarian, S. Metzner, N. Izyumskaya, S. Okur, F. Zhang, N. Can, S. Das, V. Avrutin, Ü. Özgür, F. Bertram, J. Christen, and H. Morkoç, "Indium-incorporation efficiency in semipolar (11-22) oriented InGaN-based light emitting diodes," in *Proc. SPIE*, 2015, vol. 9363, p. 93632P.

[107] P. G. Moses, M. Miao, Q. Yan, and C. G. V. de Walle, "Hybrid functional investigations of band gaps and band alignments for AlN, GaN, InN, and InGaN," *J. Chem. Phys.*, vol. 134, no. 8, p. 84703, Feb. 2011.

[108] P. Rinke, M. Scheffler, A. Qteish, M. Winkelnkemper, D. Bimberg, and J. Neugebauer, "Band gap and band parameters of InN and GaN from quasiparticle energy calculations based on exact-exchange density-functional theory," *Appl. Phys. Lett.*, vol. 89, no. 16, p. 161919, Oct. 2006.

[109] J. L. P. Castineira, J. R. Leite, L. M. R. Scolfaro, R. Enderlein, J. L. A. Alves, and H. W. Leite Alves, "First principles studies of point defects and impurities in cubic boron nitride," *Mater. Sci. Eng. B*, vol. 51, no. 1–3, pp. 53–57, Feb. 1998.

[110] H. Zhao, R. A. Arif, Y. K. Ee, and N. Tansu, "Self-Consistent Analysis of Strain-Compensated InGaN #x2013;AlGaN Quantum Wells for Lasers and Light-Emitting Diodes," *IEEE J. Quantum Electron.*, vol. 45, no. 1, pp. 66–78, Jan. 2009.

[111] H. Zhao, R. A. Arif, Y.-K. Ee, and N. Tansu, "Optical gain analysis of strain-compensated InGaN–AlGaN quantum well active regions for lasers emitting at 420–500 nm," *Opt. Quantum Electron.*, vol. 40, no. 5–6, pp. 301–306, Jan. 2008.

[112] P. Waltereit, O. Brandt, A. Trampert, H. T. Grahn, J. Menniger, M. Ramsteiner, M. Reiche, and K. H. Ploog, "Nitride semiconductors free of electrostatic fields for efficient white light-emitting diodes," *Nature*, vol. 406, no. 6798, pp. 865–868, Aug. 2000.

[113] Y. Saito, K. Okuno, S. Boyama, N. Nakada, S. Nitta, Y. Ushida, and N. Shibata, "m-Plane GaInN Light Emitting Diodes Grown on Patterned a-Plane Sapphire Substrates," *Appl. Phys. Express*, vol. 2, no. 4, p. 41001, Mar. 2009.

[114] X. Ni, M. Wu, J. Lee, X. Li, A. A. Baski, Ü. Özgür, and H. Morkoç, "Nonpolar m-plane GaN on patterned Si(112) substrates by metalorganic chemical vapor deposition," *Appl. Phys. Lett.*, vol. 95, no. 11, p. 111102, Sep. 2009.

[115] N. Izyumskaya, S. J. Liu, V. Avrutin, X. F. Ni, M. Wu, Ü. Özgür, S. Metzner, F. Bertram, J. Christen, L. Zhou, D. J. Smith, and H. Morkoç, "Epitaxial lateral overgrowth of non-polar GaN(1 Г0 0) on Si(1 1 2) patterned substrates by MOCVD," *J. Cryst. Growth*, vol. 314, no. 1, pp. 129–135, Jan. 2011.

[116] A. Bhattacharyya, I. Friel, S. Iyer, T.-C. Chen, W. Li, J. Cabalu, Y. Fedyunin, K. F. Ludwig Jr., T. D. Moustakas, H.-P. Maruska, D. W. Hill, J. J. Gallagher, M. C. Chou, and B. Chai, "Comparative study of GaN/AlGaN MQWs grown homoepitaxially on (1 Г0 0) and (0 0 0 1) GaN," *J. Cryst. Growth*, vol. 251, no. 1–4, pp. 487–493, Apr. 2003.

[117] H. Masui, H. Asamizu, T. Melo, H. Yamada, K. Iso, S. C. Cruz, Shuji Nakamura, and S. P. DenBaars, "Effects of piezoelectric fields on optoelectronic properties of InGaN/GaN quantum-well light-emitting diodes prepared on nonpolar (10 -10) and semipolar (11-22) orientations," *J. Phys. Appl. Phys.*, vol. 42, no. 13, p. 135106, 2009.

[118] N. Izyumskaya, S. J. Liu, S. Okur, M. Wu, V. Avrutin, Ü. Özgür, S. Metzner, F. Bertram, J. Christen, L. Zhou, D. J. Smith, and H. Morkoç, "Optical properties of nonpolar (1-100) and semipolar (1-101)GaN grown by MOCVD on Si patterned substrates," in *Proc. SPIE*, 2011, vol. 7939, p. 79391W.

[119] N. Izyumskaya, S. Okur, F. Zhang, M. Monavarian, V. Avrutin, Ü. Özgür, S. Metzner, C. Karbaum, F. Bertram, J. Christen, and H. Morkoç, "Optical properties of m-plane GaN grown on patterned Si(112) substrates by MOCVD using a two-step approach," in *Proc. SPIE*, 2014, vol. 8986, p. 898628.

[120] N. Izyumskaya, F. Zhang, S. Okur, T. Selden, V. Avrutin, Ü. Özgür, S. Metzner, C. Karbaum, F. Bertram, J. Christen, and H. Morkoç, "Optical studies of strain and defect distribution in semipolar (11¯01) GaN on patterned Si substrates," *J. Appl. Phys.*, vol. 114, no. 11, p. 113502, Sep. 2013.

[121] R. Liu, A. Bell, F. A. Ponce, C. Q. Chen, J. W. Yang, and M. A. Khan, "Luminescence from stacking faults in gallium nitride," *Appl. Phys. Lett.*, vol. 86, no. 2, p. 21908, Jan. 2005.

[122] D. Rosales, B. Gil, T. Bretagnon, B. Guizal, F. Zhang, S. Okur, M. Monavarian, N. Izyumskaya, V. Avrutin, Ü. Özgür, H. Morkoç, and J. H. Leach, "Excitonic recombination dynamics in non-polar GaN/AlGaN quantum wells," *J. Appl. Phys.*, vol. 115, no. 7, p. 73510, Feb. 2014.

[123] Y. J. Sun, O. Brandt, S. Cronenberg, S. Dhar, H. T. Grahn, K. H. Ploog, P. Waltereit, and J. S. Speck, "Nonpolar InxGa1−xN/GaN(11¯00) multiple quantum wells grown on γ−LiAlO2(100) by plasma-assisted molecular-beam epitaxy," *Phys. Rev. B*, vol. 67, no. 4, p. 41306, Jan. 2003.

[124] H. M. Ng, "Molecular-beam epitaxy of GaN/AlxGa1−xN multiple quantum wells on R-plane (10 1̄ 2) sapphire substrates," *Appl. Phys. Lett.*, vol. 80, no. 23, pp. 4369–4371, Jun. 2002.

[125] T. Paskova, V. Darakchieva, P. P. Paskov, J. Birch, E. Valcheva, P. O. A. Persson, B. Arnaudov, S. Tungasmitta, and B. Monemar, "Properties of nonpolar a-plane GaN films grown by HVPE with AlN buffers," *J. Cryst. Growth*, vol. 281, no. 1, pp. 55–61, Jul. 2005.

[126] T. Paskova, *Nitrides with Nonpolar Surfaces: Growth, Properties, and Devices*. Wiley Online Library, 2008.

[127] T. Onuma, A. Chakraborty, B. A. Haskell, S. Keller, S. P. DenBaars, J. S. Speck, S. Nakamura, U. K. Mishra, T. Sota, and S. F. Chichibu, "Localized exciton dynamics in

nonpolar (112¯0)InxGa1−xN multiple quantum wells grown on GaN templates prepared by lateral epitaxial overgrowth," *Appl. Phys. Lett.*, vol. 86, no. 15, p. 151918, Apr. 2005.

[128] P. P. Paskov, R. Schifano, T. Malinauskas, T. Paskova, J. P. Bergman, B. Monemar, S. Figge, D. Hommel, B. A. Haskell, P. T. Fini, J. S. Speck, and S. Nakamura, "Photoluminescence of a -plane GaN: comparison between MOCVD and HVPE grown layers," *Phys. Status Solidi C*, vol. 3, no. 6, pp. 1499–1502, Jun. 2006.

[129] S. Okur, K. Jarašiūnas, S. din A. Hafiz, J. Leach, T. Paskova, V. Avrutin, H. Morkoç, and Ü. Özgür, "Recombination dynamics in non-polar m-plane GaN investigated by time- and polarization-resolved photoluminescence," in *Proc. SPIE*, 2013, vol. 8625, p. 86252D.

[130] P. Corfdir, J. Levrat, A. Dussaigne, P. Lefebvre, H. Teisseyre, I. Grzegory, T. Suski, J.-D. Ganière, N. Grandjean, and B. Deveaud-Plédran, "Intrinsic dynamics of weakly and strongly confined excitons in nonpolar nitride-based heterostructures," *Phys. Rev. B*, vol. 83, no. 24, p. 245326, Jun. 2011.

[131] R. Mata, A. Cros, J. A. Budagosky, A. Molina-Sánchez, N. Garro, A. García-Cristóbal, J. Renard, S. Founta, B. Gayral, E. Bellet-Amalric, C. Bougerol, and B. Daudin, "Reversed polarized emission in highly strained a-plane GaN/AlN multiple quantum wells," *Phys. Rev. B*, vol. 82, no. 12, p. 125405, Sep. 2010.

[132] S. Schulz, T. J. Badcock, M. A. Moram, P. Dawson, M. J. Kappers, C. J. Humphreys, and E. P. O'Reilly, "Electronic and optical properties of nonpolar a-plane GaN quantum wells," *Phys. Rev. B*, vol. 82, no. 12, p. 125318, Sep. 2010.

[133] M. Funato, K. Matsuda, R. G. Banal, R. Ishii, and Y. Kawakami, "Strong optical polarization in nonpolar (1-100) AlxGa1−xN/AlN quantum wells," *Phys. Rev. B*, vol. 87, no. 4, p. 41306, Jan. 2013.

[134] T. J. Ochalski, B. Gil, P. Lefebvre, N. Grandjean, J. Massies, and M. Leroux, "Photoreflectance spectroscopy as a powerful tool for the investigation of GaN–AlGaN quantum well structures," *Solid State Commun.*, vol. 109, no. 9, pp. 567–571, Feb. 1999.

[135] T. J. Ochalski, B. Gil, P. Lefebvre, N. Grandjean, M. Leroux, J. Massies, S. Nakamura, and H. Morkoç, "Photoreflectance investigations of the bowing parameter in AlGaN alloys lattice-matched to GaN," *Appl. Phys. Lett.*, vol. 74, no. 22, pp. 3353–3355, May 1999.

[136] B. Gil and A. Alemu, "Optical anisotropy of excitons in strained GaN epilayers grown along the ⟨10-10⟩ direction," *Phys. Rev. B*, vol. 56, no. 19, pp. 12446–12453, Nov. 1997.

[137] S.-H. Park and S.-L. Chuang, "Crystal-orientation effects on the piezoelectric field and electronic properties of strained wurtzite semiconductors," *Phys. Rev. B*, vol. 59, no. 7, pp. 4725–4737, Feb. 1999.

[138] B. Gil, O. Briot, and R.-L. Aulombard, "Valence-band physics and the optical properties of GaN epilayers grown onto sapphire with wurtzite symmetry," *Phys. Rev. B*, vol. 52, no. 24, pp. R17028–R17031, Dec. 1995.

[139] P. Rinke, M. Winkelnkemper, A. Qteish, D. Bimberg, J. Neugebauer, and M. Scheffler, "Consistent set of band parameters for the group-III nitrides AlN, GaN, and InN," *Phys. Rev. B*, vol. 77, no. 7, p. 75202, Feb. 2008.

[140] S.-H. Park, "Optical anisotropy in nonpolar (10-10)-oriented m-plane GaN/AlGaN quantum wells and comparison with experiment," *Appl. Phys. A*, vol. 91, no. 3, pp. 361–364, Mar. 2008.

[141] L. Viña, S. Logothetidis, and M. Cardona, "Temperature dependence of the dielectric function of germanium," *Phys. Rev. B*, vol. 30, no. 4, pp. 1979–1991, Aug. 1984.

[142] R. Pässler, "Dispersion-related assessments of temperature dependences for the fundamental band gap of hexagonal GaN," *J. Appl. Phys.*, vol. 90, no. 8, pp. 3956–3964, Oct. 2001.

[143] L. C. Andreani, "Optical Transitions, Excitons, and Polaritons in Bulk and Low-Dimensional Semiconductor Structures," in *Confined Electrons and Photons*, E. Burstein and C. Weisbuch, Eds. Springer US, 1995, pp. 57–112.

[144] L. Béaur, T. Bretagnon, B. Gil, A. Kavokin, T. Guillet, C. Brimont, D. Tainoff, M. Teisseire, and J.-M. Chauveau, "Exciton radiative properties in nonpolar homoepitaxial ZnO/(Zn,Mg)O quantum wells," *Phys. Rev. B*, vol. 84, no. 16, p. 165312, Oct. 2011.

[145] P. Lefebvre, J. Allègre, B. Gil, A. Kavokine, H. Mathieu, W. Kim, A. Salvador, A. Botchkarev, and H. Morkoç, "Recombination dynamics of free and localized excitons in GaN/Ga0.93Al0.07N quantum wells," *Phys. Rev. B*, vol. 57, no. 16, pp. R9447–R9450, Apr. 1998.

[146] D. Rosales, T. Bretagnon, B. Gil, A. Kahouli, J. Brault, B. Damilano, J. Massies, M. V. Durnev, and A. V. Kavokin, "Excitons in nitride heterostructures: From zero- to one-dimensional behavior," *Phys. Rev. B*, vol. 88, no. 12, p. 125437, Sep. 2013.

[147] P. Corfdir, A. Dussaigne, H. Teisseyre, T. Suski, I. Grzegory, P. Lefebvre, E. Giraud, M. Shahmohammadi, R. T. Phillips, J.-D. Ganiere, N. Grandjean, and B. Deveaud, "Temperature-Dependence of Exciton Radiative Recombination in (Al,Ga)N/GaN Quantum Wells Grown on *a* -Plane GaN Substrates," *Jpn. J. Appl. Phys.*, vol. 52, no. 8S, p. 08JC01, Aug. 2013.

[148] D. Rosales, B. Gil, T. Bretagnon, B. Guizal, N. Izyumskaya, M. Monavarian, F. Zhang, S. Okur, V. Avrutin, Ü. Özgür, and H. Morkoç, "Recombination dynamics of excitons with low non-radiative component in semi-polar (10-11)-oriented GaN/AlGaN multiple quantum wells," *J. Appl. Phys.*, vol. 116, no. 9, p. 93517, Sep. 2014.

[149] L. C. Andreani and A. Pasquarello, "Accurate theory of excitons in GaAs-Ga1−xAlxAs quantum wells," *Phys. Rev. B*, vol. 42, no. 14, pp. 8928–8938, Nov. 1990.

[150] M. Colocci, M. Gurioli, and A. Vinattieri, "Thermal ionization of excitons in GaAs/AlGaAs quantum well structures," *J. Appl. Phys.*, vol. 68, no. 6, pp. 2809–2812, Sep. 1990.

[151] L. C. Andreani, F. Tassone, and F. Bassani, "Radiative lifetime of free excitons in quantum wells," *Solid State Commun.*, vol. 77, no. 9, pp. 641–645, Mar. 1991.

[152] D. S. Citrin, "Radiative lifetimes of excitons in quantum wells: Localization and phase-coherence effects," *Phys. Rev. B*, vol. 47, no. 7, pp. 3832–3841, Feb. 1993.

[153] P. Corfdir, A. Dussaigne, H. Teisseyre, T. Suski, I. Grzegory, P. Lefebvre, E. Giraud, M. Shahmohammadi, R. T. Phillips, J.-D. Ganiere, N. Grandjean, and B. Deveaud, "Temperature-Dependence of Exciton Radiative Recombination in (Al,Ga)N/GaN Quantum Wells Grown on a-Plane GaN Substrates," *Jpn. J. Appl. Phys.*, vol. 52, no. 8S, p. 08JC01, May 2013.

[154] P. M. Corfdir, "Physics of the Ultrafast Dynamics of Excitons in GaN Nanostructures," 2011.

[155] T. j. Ochalski, B. Gil, P. Bigenwald, M. Bugajski, A. Wojcik, P. Lefebvre, T. Taliercio, N. Grandjean, and J. Massies, "Dual Contribution to the Stokes Shift in InGaN–GaN Quantum Wells," *Phys. Status Solidi B*, vol. 228, no. 1, pp. 111–114, Nov. 2001.

[156] R. M. Farrell, E. C. Young, F. Wu, S. P. DenBaars, and J. S. Speck, "Materials and growth issues for high-performance nonpolar and semipolar light-emitting devices," *Semicond. Sci. Technol.*, vol. 27, no. 2, p. 24001, 2012.

[157] S. Hafiz, N. Andrade, M. Monavarian, N. Izyumskaya, S. Das, F. Zhang, V. Avrutin, H. Morkoç, and Ü. Özgür, "Optical investigation of microscopic defect distribution in semipolar (1-101 and 11-22) InGaN light-emitting diodes," in *Proc. SPIE*, 2016, vol. 9748, p. 974828.

[158] S. Okur, S. Metzner, N. Izyumskaya, F. Zhang, V. Avrutin, C. Karbaum, F. Bertram, J. Christen, H. Morkoç, and Ü. Özgür, "Microscopic distribution of extended defects and blockage of threading dislocations by stacking faults in semipolar (1 1 ¯ 01) GaN revealed from spatially resolved luminescence," *Appl. Phys. Lett.*, vol. 103, no. 21, p. 211908, Nov. 2013.

[159] D. F. Feezell, M. C. Schmidt, S. P. DenBaars, and S. Nakamura, "Development of Nonpolar and Semipolar InGaN/GaN Visible Light-Emitting Diodes," in *MRS Bulletin*, 2009, vol. 34, pp. 318–323.

[160] C. Wetzel, T. Takeuchi, S. Yamaguchi, H. Katoh, H. Amano, and I. Akasaki, "Optical band gap in Ga1−xInxN (0<x<0.2) on GaN by photoreflection spectroscopy," *Appl. Phys. Lett.*, vol. 73, no. 14, pp. 1994–1996, Oct. 1998.

[161] P. Vennéguès, T. Zhu, D. Martin, and N. Grandjean, "Study of the epitaxial relationships between III-nitrides and M-plane sapphire," *J. Appl. Phys.*, vol. 108, no. 11, p. 113521, Dec. 2010.

[162] T. J. Baker, B. A. Haskell, F. Wu, J. S. Speck, and S. Nakamura, "Characterization of Planar Semipolar Gallium Nitride Films on Sapphire Substrates," *Jpn. J. Appl. Phys.*, vol. 45, no. 2L, p. L154, Feb. 2006.

[163] S. Haffouz, V. Kirilyuk, P. R. Hageman, L. Macht, J. L. Weyher, and P. K. Larsen, "Improvement of the optical properties of metalorganic chemical vapor deposition grown GaN on sapphire by an in situ SiN treatment," *Appl. Phys. Lett.*, vol. 79, no. 15, pp. 2390–2392, Oct. 2001.

[164] J. Hertkorn, F. Lipski, P. Brückner, T. Wunderer, S. B. Thapa, F. Scholz, A. Chuvilin, U. Kaiser, M. Beer, and J. Zweck, "Process optimization for the effective reduction of

threading dislocations in MOVPE grown GaN using in situ deposited masks," *J. Cryst. Growth*, vol. 310, no. 23, pp. 4867–4870, Nov. 2008.

[165] P. Vennéguès, "Defect reduction methods for III-nitride heteroepitaxial films grown along nonpolar and semipolar orientations," *Semicond. Sci. Technol.*, vol. 27, no. 2, p. 24004, 2012.

[166] N. Kriouche, P. Vennéguès, M. Nemoz, G. Nataf, and P. De Mierry, "Stacking faults blocking process in (1 1 −2 2) semipolar GaN growth on sapphire using asymmetric lateral epitaxy," *J. Cryst. Growth*, vol. 312, no. 19, pp. 2625–2630, Sep. 2010.

[167] P. Vennéguès, F. Tendille, and P. D. Mierry, "Study of defect management in the growth of semipolar (11-22) GaN on patterned sapphire," *J. Phys. Appl. Phys.*, vol. 48, no. 32, p. 325103, 2015.

[168] F. Tendille, M. Hugues, P. Vennéguès, M. Teisseire, and P. D. Mierry, "Successive selective growth of semipolar (11-22) GaN on patterned sapphire substrate," *Semicond. Sci. Technol.*, vol. 30, no. 6, p. 65001, 2015.

[169] H. Furuya, N. Okada, and K. Tadatomo, "Growth of {11-22} GaN on shallowly etched r - plane patterned sapphire substrates," *Phys. Status Solidi C*, vol. 9, no. 3–4, pp. 568–571, Mar. 2012.

[170] N. Okada, A. Kurisu, K. Murakami, and K. Tadatomo, "Growth of Semipolar (1122) GaN Layer by Controlling Anisotropic Growth Rates in r-Plane Patterned Sapphire Substrate," *Appl. Phys. Express*, vol. 2, no. 9, p. 91001, Aug. 2009.

[171] Q. Sun, C. D. Yerino, B. Leung, J. Han, and M. E. Coltrin, "Understanding and controlling heteroepitaxy with the kinetic Wulff plot: A case study with GaN," *J. Appl. Phys.*, vol. 110, no. 5, p. 53517, Sep. 2011.

[172] F. Scholz, T. Meisch, M. Caliebe, S. Schörner, K. Thonke, L. Kirste, S. Bauer, S. Lazarev, and T. Baumbach, "Growth and doping of semipolar GaN grown on patterned sapphire substrates," *J. Cryst. Growth*, vol. 405, pp. 97–101, Nov. 2014.

[173] D. V. Dinh, M. Akhter, S. Presa, G. Kozlowski, D. O'Mahony, P. P. Maaskant, F. Brunner, M. Caliebe, M. Weyers, F. Scholz, B. Corbett, and P. J. Parbrook, "Semipolar (112―2) InGaN light-emitting diodes grown on chemically–mechanically polished GaN templates," *Phys. Status Solidi A*, vol. 212, no. 10, pp. 2196–2200, Oct. 2015.

[174] M. Caliebe, T. Meisch, B. Neuschl, S. Bauer, J. Helbing, D. Beck, K. Thonke, M. Klein, D. Heinz, and F. Scholz, "Improvements of MOVPE grown (11-22) oriented GaN on pre-structured sapphire substrates using a SiNx interlayer and HVPE overgrowth," *Phys. Status Solidi C*, vol. 11, no. 3–4, pp. 525–529, Feb. 2014.

[175] J. Bai, X. Yu, Y. Gong, Y. N. Hou, Y. Zhang, and T. Wang, "Growth and characterization of semi-polar (11-22) GaN on patterned (113) Si substrates," *Semicond. Sci. Technol.*, vol. 30, no. 6, p. 65012, 2015.

[176] J. Xie, Y. Fu, X. Ni, S. Chevtchenko, and H. Morkoç, "I-V characteristics of Au∕Ni Schottky diodes on GaN with SiNx nanonetwork," *Appl. Phys. Lett.*, vol. 89, no. 15, p. 152108, Oct. 2006.

[177] J. L. Hollander, M. J. Kappers, C. McAleese, and C. J. Humphreys, "Improvements in a-plane GaN crystal quality by a two-step growth process," *Appl. Phys. Lett.*, vol. 92, no. 10, p. 101104, Mar. 2008.

[178] T. S. Ko, T. C. Wang, H. M. Huang, J. R. Chen, H. G. Chen, C. P. Chu, T. C. Lu, H. C. Kuo, and S. C. Wang, "Characteristics of a-plane GaN with the SiNx insertion layer grown by metal-organic chemical vapor deposition," *J. Cryst. Growth*, vol. 310, no. 23, pp. 4972–4975, Nov. 2008.

[179] J. Jeong, J. Jang, J. Hwang, C. Jung, J. Kim, K. Lee, H. Lim, and O. Nam, "Improved performance of semi-polar (11-22) GaN-based light-emitting diodes grown on SiNx interlayer," *J. Cryst. Growth*, vol. 370, pp. 114–119, May 2013.

[180] Y. A. R. Dasilva, M. P. Chauvat, P. Ruterana, L. Lahourcade, E. Monroy, and G. Nataf, "Defect structure in heteroepitaxial semipolar (11-22) (Ga, Al)N," *J. Phys. Condens. Matter*, vol. 22, no. 35, p. 355802, 2010.

[181] M. Pristovsek, M. Frentrup, Y. Han, and C. J. Humphreys, "Optimizing GaN (112̄2) hetero-epitaxial templates grown on (101̄0) sapphire," *Phys. Status Solidi B*, vol. 253, no. 1, pp. 61–66, Jan. 2016.

[182] S. Ploch, J. Bum Park, J. Stellmach, T. Schwaner, M. Frentrup, T. Niermann, T. Wernicke, M. Pristovsek, M. Lehmann, and M. Kneissl, "Single phase GaN on sapphire grown by metal-organic vapor phase epitaxy," *J. Cryst. Growth*, vol. 331, no. 1, pp. 25–28, Sep. 2011.

302

[183] P. P. Paskov, R. Schifano, B. Monemar, T. Paskova, S. Figge, and D. Hommel, "Emission properties of a-plane GaN grown by metal-organic chemical-vapor deposition," *J. Appl. Phys.*, vol. 98, no. 9, p. 93519, Nov. 2005.

[184] M. Monavarian, N. Izyumskaya, M. Müller, S. Metzner, P. Veit, N. Can, S. Das, Ü. Özgür, F. Bertram, J. Christen, H. Morkoç, and V. Avrutin, "Improvement of optical quality of semipolar (11-22) GaN on m-plane sapphire by in-situ epitaxial lateral overgrowth," *J. Appl. Phys.*, vol. 119, no. 14, p. 145303, Apr. 2016.

[185] M. Müller, G. Schmidt, S. Metzner, P. Veit, F. Bertram, R. A. R. Leute, D. Heinz, J. Wang, T. Meisch, F. Scholz, and J. Christen, "Nanoscale cathodoluminescene imaging of III-nitride-based LEDs with semipolar quantum wells in a scanning transmission electron microscope," *Phys. Status Solidi B*, vol. 253, no. 1, pp. 112–117, Jan. 2016.

[186] G. Schmidt, M. Müller, P. Veit, F. Bertram, J. Christen, M. Glauser, J.-F. Carlin, G. Cosendey, R. Butté, and N. Grandjean, "Nano-scale luminescence characterization of individual InGaN/GaN quantum wells stacked in a microcavity using scanning transmission electron microscope cathodoluminescence," *Appl. Phys. Lett.*, vol. 105, no. 3, p. 32101, Jul. 2014.

[187] P. Vennéguès, J. M. Chauveau, Z. Bougrioua, T. Zhu, D. Martin, and N. Grandjean, "On the origin of basal stacking faults in nonpolar wurtzite films epitaxially grown on sapphire substrates," *J. Appl. Phys.*, vol. 112, no. 11, p. 113518, Dec. 2012.

[188] J. Mei, S. Srinivasan, R. Liu, F. A. Ponce, Y. Narukawa, and T. Mukai, "Prismatic stacking faults in epitaxially laterally overgrown GaN," *Appl. Phys. Lett.*, vol. 88, no. 14, p. 141912, Apr. 2006.

[189] D. N. Zakharov, Z. Liliental-Weber, B. Wagner, Z. J. Reitmeier, E. A. Preble, and R. F. Davis, "Structural TEM study of nonpolar a-plane gallium nitride grown on (11-20) 4H-SiC by organometallic vapor phase epitaxy," *Phys. Rev. B*, vol. 71, no. 23, p. 235334, Jun. 2005.

[190] C. Stampfl and C. G. Van de Walle, "Energetics and electronic structure of stacking faults in AlN, GaN, and InN," *Phys. Rev. B*, vol. 57, no. 24, pp. R15052–R15055, Jun. 1998.

[191] K. P. Korona, "Dynamics of excitonic recombination and interactions in homoepitaxial GaN," *Phys. Rev. B*, vol. 65, no. 23, p. 235312, May 2002.

[192] J. Menniger, U. Jahn, O. Brandt, H. Yang, and K. Ploog, "Identification of optical transitions in cubic and hexagonal GaN by spatially resolved cathodoluminescence," *Phys. Rev. B*, vol. 53, no. 4, pp. 1881–1885, Jan. 1996.

[193] A. Belabbes, L. C. de Carvalho, A. Schleife, and F. Bechstedt, "Cubic inclusions in hexagonal AlN, GaN, and InN: Electronic states," *Phys. Rev. B*, vol. 84, no. 12, p. 125108, Sep. 2011.

[194] M. Murayama and T. Nakayama, "Chemical trend of band offsets at wurtzite/zinc-blende heterocrystalline semiconductor interfaces," *Phys. Rev. B*, vol. 49, no. 7, pp. 4710–4724, Feb. 1994.

[195] J. Lähnemann, U. Jahn, O. Brandt, T. Flissikowski, P. Dogan, and H. T. Grahn, "Luminescence associated with stacking faults in GaN," *J. Phys. Appl. Phys.*, vol. 47, no. 42, p. 423001, 2014.

[196] A. Dussaigne, P. Corfdir, J. Levrat, T. Zhu, D. Martin, P. Lefebvre, J.-D. Ganière, R. Butté, B. Deveaud-Plédran, N Grandjean, Y. Arroyo, and P. Stadelmann, "One-dimensional exciton luminescence induced by extended defects in nonpolar GaN/(Al,Ga)N quantum wells," *Semicond. Sci. Technol.*, vol. 26, no. 2, p. 25012, 2011.

[197] T. J. Badcock, M. J. Kappers, M. A. Moram, P. Dawson, and C. J. Humphreys, "Modification of carrier localization in basal-plane stacking faults: The effect of Si-doping in a-plane GaN," *Phys. Status Solidi B*, vol. 249, no. 3, pp. 498–502, Mar. 2012.

[198] P. Corfdir, P. Lefebvre, J. Levrat, A. Dussaigne, J.-D. Ganière, D. Martin, J. Ristić, T. Zhu, N. Grandjean, and B. Deveaud-Plédran, "Exciton localization on basal stacking faults in a-plane epitaxial lateral overgrown GaN grown by hydride vapor phase epitaxy," *J. Appl. Phys.*, vol. 105, no. 4, p. 43102, Feb. 2009.

[199] P. Corfdir, J. Ristić, P. Lefebvre, T. Zhu, D. Martin, A. Dussaigne, J. D. Ganière, N. Grandjean, and B. Deveaud-Plédran, "Low-temperature time-resolved cathodoluminescence study of exciton dynamics involving basal stacking faults in a-plane GaN," *Appl. Phys. Lett.*, vol. 94, no. 20, p. 201115, May 2009.

[200] S. Okur, M. Monavarian, S. Das, N. Izyumskaya, F. Zhang, V. Avrutin, H. Morkoç, and Ü. Özgür, "Strong carrier localization in stacking faults in semipolar (11-22) GaN," in *Proc. SPIE*, 2015, vol. 9363, p. 93632N.

[201] Y. T. Rebane, Y. G. Shreter, and M. Albrecht, "Stacking Faults as Quantum Wells for Excitons in Wurtzite GaN," *Phys. Status Solidi A*, vol. 164, no. 1, pp. 141–144, Nov. 1997.

[202] P. Ščajev, K. Jarašiūnas, S. Okur, Ü. Özgür, and H. Morkoç, "Carrier dynamics in bulk GaN," *J. Appl. Phys.*, vol. 111, no. 2, p. 23702, Jan. 2012.

[203] P. Corfdir, P. Lefebvre, J. Ristić, J.-D. Ganière, and B. Deveaud-Plédran, "Electron localization by a donor in the vicinity of a basal stacking fault in GaN," *Phys. Rev. B*, vol. 80, no. 15, p. 153309, Oct. 2009.

[204] S. Okur, N. Izyumskaya, F. Zhang, V. Avrutin, S. Metzner, C. Karbaum, F. Bertram, J. Christen, H. Morkoç, and Ü. Özgür, "Impact of extended defects on optical properties of (1-101)GaN grown on patterned Si," in *Proc. SPIE*, 2014, vol. 8986, p. 89862B.

[205] M. D. Craven, S. H. Lim, F. Wu, J. S. Speck, and S. P. DenBaars, "Structural characterization of nonpolar (11$\bar{2}$0)a-plane GaN thin films grown on (1$\bar{1}$02)r-plane sapphire," *Appl. Phys. Lett.*, vol. 81, no. 3, pp. 469–471, Jul. 2002.

[206] Y. J. Sun, O. Brandt, U. Jahn, T. Y. Liu, A. Trampert, S. Cronenberg, S. Dhar, and K. H. Ploog, "Impact of nucleation conditions on the structural and optical properties of M-plane GaN(1$\bar{1}$00) grown on γ-LiAlO2," *J. Appl. Phys.*, vol. 92, no. 10, pp. 5714–5719, Nov. 2002.

[207] M. Albrecht, S. Christiansen, G. Salviati, C. Zanotti-Fregonara, Y. T. Rebane, Y. G. Shreter, M. Mayer, A. Pelzmann, M. Kamp, K. J. Ebeling, M. D. Bremser, R. F. Davis, and H. P. Strunk, "Luminescence Related to Stacking Faults in Heterepitaxially Grown Wurtzite GaN," in *Symposium D – Gallium Nitride and Related Materials II*, 1997, vol. 468.

[208] T. Paskova, R. Kroeger, P. P. Paskov, S. Figge, D. Hommel, B. Monemar, B. Haskell, P. Fini, J. S. Speck, and S. Nakamura, "Microscopic emission properties of nonpolar a-plane GaN grown by HVPE," 2006, vol. 6121, pp. 612106-612106–7.

[209] I. Tischer, M. Feneberg, M. Schirra, H. Yacoub, R. Sauer, K. Thonke, T. Wunderer, F. Scholz, L. Dieterle, E. Müller, and D. Gerthsen, "${I}_{2}$ basal plane stacking fault in GaN: Origin of the 3.32 eV luminescence band," *Phys. Rev. B*, vol. 83, no. 3, p. 35314, Jan. 2011.

305

[210] X. H. Lu, P. Y. Yu, L. X. Zheng, S. J. Xu, M. H. Xie, and S. Y. Tong, "Evidence for a Type-II band alignment between cubic and hexagonal phases of GaN," *Appl. Phys. Lett.*, vol. 82, no. 7, pp. 1033–1035, Feb. 2003.

[211] G. Jacopin, L. Rigutti, L. Largeau, F. Fortuna, F. Furtmayr, F. H. Julien, M. Eickhoff, and M. Tchernycheva, "Optical properties of wurtzite/zinc-blende heterostructures in GaN nanowires," *J. Appl. Phys.*, vol. 110, no. 6, p. 64313, Sep. 2011.

[212] M. Monavarian, S. Hafiz, N. Izyumskaya, S. Das, Ü. Özgür, H. Morkoç, and V. Avrutin, "Wurtzite/zinc-blende electronic-band alignment in basal-plane stacking faults in semi-polar GaN," in *Proc. SPIE*, 2016, vol. 9748, p. 974827.

[213] K. Meissner, B. Fluegel, R. Binder, S. W. Koch, G. Khitrova, and N. Peygambarian, "Comparison of optical nonlinearities of type II and type I quantum wells," *Appl. Phys. Lett.*, vol. 59, no. 3, pp. 259–261, Jul. 1991.

[214] R. Binder, I. Galbraith, and S. W. Koch, "Theory of band-edge optical nonlinearities in type-I and type-II quantum-well structures," *Phys. Rev. B*, vol. 44, no. 7, pp. 3031–3042, Aug. 1991.

[215] P. D. Mierry, T. Guehne, M. Nemoz, S. Chenot, E. Beraudo, and G. Nataf, "Comparison between Polar (0001) and Semipolar (1122) Nitride Blue–Green Light-Emitting Diodes Grown on c- and m-Plane Sapphire Substrates," *Jpn. J. Appl. Phys.*, vol. 48, no. 3R, p. 31002, Mar. 2009.

[216] D.-S. Oh, J.-J. Jang, O. Nam, K.-M. Song, and S.-N. Lee, "Study of green light-emitting diodes grown on semipolar (11–22) GaN/m-sapphire with different crystal qualities," *J. Cryst. Growth*, vol. 326, no. 1, pp. 33–36, Jul. 2011.

[217] B. Leung, Y. Zhang, C. D. Yerino, J. Han, Q. Sun, Z. Chen, S. Lester, Kuan-Yung Liao, and Y.-L. Li, "Optical emission characteristics of semipolar (11-22) GaN light-emitting diodes grown on m-sapphire and stripe-etched r-sapphire," *Semicond. Sci. Technol.*, vol. 27, no. 2, p. 24016, 2012.

[218] S. Y. Bae, D. S. Lee, B. H. Kong, H. K. Cho, J. F. Kaeding, S. Nakamura, S. P. DenBaars, and J. S. Speck, "Electroluminescence enhancement of (11-22) semipolar GaN light-emitting diodes grown on miscut m-plane sapphire substrates," *Curr. Appl. Phys.*, vol. 11, no. 3, pp. 954–958, May 2011.

[219] D. A. Browne, E. C. Young, J. R. Lang, C. A. Hurni, and J. S. Speck, "Indium and impurity incorporation in InGaN films on polar, nonpolar, and semipolar GaN orientations grown by ammonia molecular beam epitaxy," *J. Vac. Sci. Technol. A*, vol. 30, no. 4, p. 41513, Jul. 2012.

[220] H. Jönen, H. Bremers, U. Rossow, T. Langer, A. Kruse, L. Hoffmann, J. Thalmair, J. Zweck, S. Schwaiger, F. Scholz, and A Hangleiter, "Analysis of indium incorporation in non- and semipolar GaInN QW structures: comparing x-ray diffraction and optical properties," *Semicond. Sci. Technol.*, vol. 27, no. 2, p. 24013, 2012.

[221] H. Jönen, U. Rossow, H. Bremers, L. Hoffmann, M. Brendel, A. D. Dräger, S. Metzner, F. Bertram, J. Christen, S. Schwaiger, F. Scholz, J. Thalmair, J. Zweck, and A. Hangleiter, "Indium incorporation in GaInN/GaN quantum well structures on polar and nonpolar surfaces," *Phys. Status Solidi B*, vol. 248, no. 3, pp. 600–604, Mar. 2011.

[222] N. Izyumskaya, F. Zhang, S. Okur, T. Selden, V. Avrutin, Ü. Özgür, S. Metzner, C. Karbaum, F. Bertram, J. Christen, and H. Morkoç, "Optical studies of strain and defect distribution in semipolar (11¯01) GaN on patterned Si substrates," *J. Appl. Phys.*, vol. 114, no. 11, p. 113502, Sep. 2013.

[223] F. Tendille, P. De Mierry, P. Vennéguès, S. Chenot, and M. Teisseire, "Defect reduction method in (11-22) semipolar GaN grown on patterned sapphire substrate by MOCVD: Toward heteroepitaxial semipolar GaN free of basal stacking faults," *J. Cryst. Growth*, vol. 404, pp. 177–183, Oct. 2014.

[224] C. F. Johnston, M. J. Kappers, M. A. Moram, J. L. Hollander, and C. J. Humphreys, "Assessment of defect reduction methods for nonpolar a-plane GaN grown on r-plane sapphire," *J. Cryst. Growth*, vol. 311, no. 12, pp. 3295–3299, Jun. 2009.

[225] D. Rosales, B. Gil, M. Monavarian, F. Zhang, S. Okur, N. Izyumskaya, V. Avrutin, Ü. Özgür, and H. Morkoç, "Temperature-dependent time-resolved photoluminescence measurements of (1-101)-oriented semi-polar AlGaN/GaN MQWs," in *Proc. SPIE*, 2015, vol. 9363, p. 93630J.

[226] D. Rosales, B. Gil, T. Bretagnon, F. Zhang, S. Okur, M. Monavarian, N. Izioumskaia, V. Avrutin, Ü. Özgür, H. Morkoç, and J. H. Leach, "Polarized time-resolved photoluminescence measurements of m-plane AlGaN/GaN MQWs," in *Proc. SPIE*, 2014, vol. 8986, p. 89860L.

307

[227] F. Hitzel, G. Klewer, S. Lahmann, U. Rossow, and A. Hangleiter, "Localized high-energy emissions from the vicinity of defects in high-efficiency GaInN/GaN quantum wells," *Phys. Rev. B*, vol. 72, no. 8, p. 81309, Aug. 2005.

[228] A. Kaneta, M. Funato, and Y. Kawakami, "Nanoscopic recombination processes in InGaN/GaN quantum wells emitting violet, blue, and green spectra," *Phys. Rev. B*, vol. 78, no. 12, p. 125317, Sep. 2008.

[229] A. Pinos, S. Marcinkevičius, J. Yang, Y. Bilenko, M. Shatalov, R. Gaska, and M. S. Shur, "Aging of AlGaN quantum well light emitting diode studied by scanning near-field optical spectroscopy," *Appl. Phys. Lett.*, vol. 95, no. 18, p. 181914, Nov. 2009.

[230] M. Monavarian, D. Rosales, B. Gil, N. Izyumskaya, S. Das, Ü. Özgür, H. Morkoç, and V. Avrutin, "Exciton localization in (11-22)-oriented semi-polar InGaN multiple quantum wells," in *Proc. SPIE*, 2016, vol. 9748, p. 974826.

[231] D. Rosales, B. Gil, T. Bretagnon, J. Brault, P. Vennéguès, M. Nemoz, P. de Mierry, B. Damilano, J. Massies, and P. Bigenwald, "Optical properties and structural investigations of (11-22)-oriented GaN/Al0.5Ga0.5N quantum wells grown by molecular beam epitaxy," *J. Appl. Phys.*, vol. 118, no. 2, p. 24303, Jul. 2015.

[232] Y. P. Varshni, "Temperature dependence of the energy gap in semiconductors," *Physica*, vol. 34, no. 1, pp. 149–154, 1967.

[233] Q. Mu, M. Xu, X. Wang, Q. Wang, Y. Lv, Z. Feng, X. Xu, and Z. Ji, "Influence of the InGaN/GaN quasi-superlattice underlying layer on photoluminescence in InGaN/GaN multiple quantum wells," *Phys. E Low-Dimens. Syst. Nanostructures*, vol. 76, pp. 1–5, Feb. 2016.

[234] N. Can, S. Okur, M. Monavarian, F. Zhang, V. Avrutin, H. Morkoç, A. Teke, and Ü. Özgür, "Active region dimensionality and quantum efficiencies of InGaN LEDs from temperature dependent photoluminescence transients," in *Proc. SPIE*, 2015, vol. 9363, p. 93632U.

[235] M. Pristovsek, M. Frentrup, Y. Han, and C. J. Humphreys, "Optimizing GaN (11-22) hetero-epitaxial templates grown on (10-10) sapphire," *Phys. Status Solidi B*, vol. 253, no. 1, pp. 61–66, Jan. 2016.

[236] S. Hafiz, F. Zhang, M. Monavarian, V. Avrutin, H. Morkoç, Ü. Özgür, S. Metzner, F. Bertram, J. Christen, and B. Gil, "Determination of carrier diffusion length in GaN," *J. Appl. Phys.*, vol. 117, no. 1, p. 13106, Jan. 2015.

[237] S. Hafiz, S. Metzner, F. Zhang, M. Monavarian, V. Avrutin, H. Morkoç, C. Karbaum, F. Bertram, J. Christen, B. Gil, and Ü. Özgür, "Determination of carrier diffusion length in p- and n-type GaN," in *Proc. SPIE*, 2014, vol. 8986, p. 89862C.

Biography

Morteza Monavarian received the B.S. degree in electrical engineering from Sharif University of Technology, Tehran, Iran in 2012 and the M.S. and Ph.D. in electrical engineering from Virginia Commonwealth University (VCU), Richmond, VA in 2014 and 2016, respectively. He joined the Microelectronic Materials and Devices Laboratory (MMDL) at VCU School of Engineering, as a Research Assistant in 2012 working with Professors Hadis Morkoç, Ümit Özgür, and Vitaliy Avrutin on the development of efficient III-Nitride based light emitting devices. His field of research mainly involves growth, fabrication, and characterization of III-Nitride electronic and optoelectronic devices including high electron mobility transistors (HEMTs), light emitting diodes (LEDs), vertical cavity surface emitting lasers (VCSELs), and acoustic phonon emitting applications. He has been contributing to the field of semiconductor optoelectronics and photonics for four years and has authored or co-authored over 20 peer-reviewed journal and conference proceeding publications. Morteza is a member of American Physical Society (APS), Institute for Electrical and Electronics Engineers (IEEE), Eta Kappa Nu (The honor society branch of the IEEE), the international Society for Optics and Photonics (SPIE), Golden Key international honor society, and Honorsociety.org.

Education

- Ph.D., Electrical Engineering, Virginia Commonwealth University, Richmond, VA, 2016

- M.S., Electrical Engineering, Virginia Commonwealth University, Richmond, VA, 2014

- B.S., Electrical Engineering, Sharif University of Technology, Tehran, Iran, 2012

Publications

Peer-reviewed journal papers:

1) **M. Monavarian**, S. Metzner, N. Izyumskaya, S. Das, V. Avrutin, Ü. Özgür, F. Bertram, J. Christen, and H. Morkoç, "*Enhanced indium incorporation in semipolar (11-22)-oriented InGaN light emitting diodes*" Journal of Crystal Growth (***Under Review***).

2) M. A. Reshchikov, J. D. McNamara, F. Zhang, **M. Monavarian**, A. Usikov, H. Helava, Yu. Makarov, and H. Morkoç, "*Zero-phonon line and fine structure of the yellow luminescence band in GaN*", Physical Review B (***Under Review***).

3) Md B. Ullah, V. Avrutin, S. Li, S. Das, **M. Monavarian**, M. Toporkov, Ü. Özgür, Pierre Ruterana, and Hadis Morkoç. "*Polarity Control and Residual Strain in ZnO Epilayers Grown by Molecular Beam Epitaxy on (0001)-GaN/Sapphire*", Applied Physics Letters (***Under Review***).

4) D. Rosales, B. Gil, T. Bretagnon, **M. Monavarian**, F. Zhang, S. Okur, N. Izyumskaya, V. Avrutin, Ü. Özgür, H. Morkoç, "*Optical properties of semi-polar (Al,Ga)N/GaN multiple quantum wells*", Japanese Journal of Applied Physics (***Under Review***).

5) **M. Monavarian**, S. Hafiz, N. Izyumskaya, S. Das, Ü. Özgür, H. Morkoç, and V. Avrutin, "*Evidence for type-II band alignments of WZ/ZB in basal-plane stacking faults in semipolar GaN*", Applied Physics Letters (***Under Preparation***).

6) **M. Monavarian**, M. Müller, S. Metzner, N. Izyumskaya, N. Can, S. Das, V. Avrutin, Ü. Özgür, F. Bertram, J. Christen, and H. Morkoç, "*Microscopic study of nucleation and coalescence of semipolar (11-22) GaN/m-sapphire layers grown by MOCVD using in-situ epitaxial lateral overgrowth*", Physical Status Solidi (b) (***Under Preparation***).

7) **M. Monavarian**, "*Comment on "Experimental study of the orientation dependence of indium incorporation in GaInN" [J. Cryst. Growth 433 (2016) 7–12]*", Journal of Crystal Growth **445** (2016) 63-64.

8) **M. Monavarian**, M. Müller, S. Metzner, N. Izyumskaya, N. Can, S. Das, V. Avrutin, Ü. Özgür, F. Bertram, J. Christen, and H. Morkoç, "*Improvement of optical quality of semipolar (11-22) GaN on m-plane sapphire by in-situ epitaxial lateral overgrowth*", Journal of Applied Physics **119**, 145303 (2016).

9) F. Zhang, N. Can, S. Hafiz, **M. Monavarian**, S. Das, V. Avrutin, Ü. Özgür, and H. Morkoç, "*Improvement of carrier injection symmetry and quantum efficiency in InGaN light-emitting diodes with Mg delta-doped barriers*", Applied Physics Letters **106**, 181105 (2015).

10) S. Hafiz, F. Zhang, **M. Monavarian**, V. Avrutin, H. Morkoç, Ü. Özgür, S. Metzner, F. Bertram, J. Christen, B. Gil, "*Determination of carrier diffusion length in GaN*", Journal of Applied Physics **117**, 013106 (2015).

311

11) D. Rosales, B. Gil, T. Bretagnon, B. Guizal, N. Izyumskaya, **M. Monavarian**, F. Zhang, S. Okur, V. Avrutin, Ü. Özgür, H. Morkoç, "*Recombination dynamics of excitons with low non-radiative component in semi-polar (10-11)-oriented GaN/AlGaN multiple quantum wells* ", Journal of Applied Physics **116**, 093517 (2014).

12) D. Rosales, B. Gil, T. Bretagnon, B. Guizal, F. Zhang, S. Okur, **M. Monavarian**, N. Izyumskaya, V. Avrutin, Ü. Özgür, H. Morkoc, J.H. Leach, "*Excitonic recombination dynamics in non-polar GaN/AlGaN quantum wells*", Journal of Applied Physics **115**, 073510 (2014).

Peer-reviewed Proceeding papers:

13) **M. Monavarian**, D. Rosales, B. Gil, N. Izyumskaya, S. Das, Ü. Özgür, H. Morkoç, and V. Avrutin, "*Exciton localization in (11-22)-oriented semi-polar InGaN multiple quantum wells*", Proc. SPIE 9748, Gallium Nitride Materials and Devices XI, 974826 (2016).

14) **M. Monavarian**, S. D. A. Hafiz, N. Izyumskaya, Ü. Özgür, H. Morkoç, and V. Avrutin, "*Wurtzite/zinc-blende electronic-band alignment in basal-plane stacking faults in semipolar GaN*", Proc. SPIE 9748, Gallium Nitride Materials and Devices XI, 974827 (2016).

15) **M. Monavarian**, S. Hafiz, Ü. Özgür, H. Morkoç, and V. Avrutin, "*Enhancement of indium incorporation to InGaN MQWs on AlN/GaN periodic multilayers*", Proc. SPIE 9748, Gallium Nitride Materials and Devices XI, 974825 (2016).

16) S. Hafiz, N. Andrade, **M. Monavarian**, F. Zhang, V. Avrutin, H. Morkoç, and Ü. Özgür, "*Optical investigation of microscopic defect distribution in semi-polar (1-101 and 11-22) light emitting diodes*", Proc. SPIE 9748, Gallium Nitride Materials and Devices XI, 974828 (2016).

17) **M. Monavarian**, S. Metzner, N. Izyumskaya, M. Müller, S. Okur, F. Zhang, N. Can, S. Das, V. Avrutin, Ü. Özgür, F. Bertram, J. Christen, H. Morkoç, "*Enhancement of optical and structural quality of semipolar (11-22) GaN by introducing nanoporous SiNx interlayers*", Proc. SPIE 9363, Gallium Nitride Materials and Devices X, 93632I (2015).

18) **M. Monavarian**, S. Metzner, N. Izyumskaya, S. Okur, F. Zhang, N. Can, S. Das, V. Avrutin, Ü. Özgür, F. Bertram, J. Christen, H. Morkoç, "*Indium-incorporation efficiency in semipolar (11-22) oriented InGaN-based light emitting diodes*" Proc. SPIE 9363, Gallium Nitride Materials and Devices X, 93632P (2015).

19) S. Okur, **M. Monavarian**, N. Izyumskaya, F. Zhang, V. Avrutin, H. Morkoc, U. Ozgur, S. Das, "*Strong carrier localization in stacking faults in semipolar (11-22) GaN*", Proc. SPIE 9363, Gallium Nitride Materials and Devices X, 93632N (2015).

20) S. D. Hafiz, F. Zhang, **M. Monavarian**, V. Avrutin, H. Morkoç, Ü. Özgür, "*Enhancement of coherent acoustic phonons in InGaN multiple quantum wells*", Proc. SPIE 9363, Gallium Nitride Materials and Devices X, 93632J (2015).

21) N. Can, S. Okur, **M. Monavarian**, F. Zhang, V. Avrutin, H. Morkoç, A. Teke, Ü. Özgür, "*Active region dimensionality and quantum efficiencies of InGaN LEDs from temperature-dependent photoluminescence transients*", Proc. SPIE 9363, Gallium Nitride Materials and Devices X, 93632U (2015).

22) D. Rosales, B. Gil, **M. Monavarian**, F. Zhang, S. Okur, N. Izyumskaya, V. Avrutin, Ü. Özgür, H. Morkoç, "*Temperature-dependent time-resolved photoluminescence measurements of (1-101)-oriented semi-polar AlGaN/GaN MQWs*", Proc. SPIE 9363, Gallium Nitride Materials and Devices X, 93630J (2015).

23) S. Hafiz, S. Metzner, F. Zhang, **M. Monavarian**, V. Avrutin, H. Morkoç, C. Karbaum, F. Bertram, J. Christen, B. Gil, Ü. Özgür, "*Determination of carrier diffusion length in p-and n-type GaN*", Proc. SPIE 8986, 89862C (2014).

24) N. Izyumskaya, S. Okur, F. Zhang, **M. Monavarian**, V. Avrutin, Ü. Özgür, S. Metzner, C. Karbaum, F. Bertram, J. Christen, H. Morkoç, "*Optical properties of m-plane GaN grown on patterned Si (112) substrates by MOCVD using a two-step approach*", Proc. SPIE 8986, 898628 (2014).

25) D. Rosales, B. Gil, T. Bretagnon, F. Zhang, S. Okur, **M. Monavarian**, N. Izioumskaia, V. Avrutin, Ü. Özgür, H. Morkoç, J.H. Leach, "*Polarized time-resolved photoluminescence measurements of m-plane AlGaN/GaN MQWs*", Proc. SPIE 8986, 89860L (2014).

26) S. Hafiz, F. Zhang, **M. Monavarian**, S. Okur, V. Avrutin, H. Morkoç, Ü. Özgür, "*Estimation of carrier leakage in InGaN light emitting diodes from photocurrent measurements*", Proc. SPIE 9003, 90031R (2014).